Delivery and Release of [^{125}I]Iododeoxyuridine via Nanocarriers for Auger-radiotherapy of Glioblastoma

Tang, Qing

Publication date:
2023

Document Version
Publisher's PDF, also known as Version of record

Doctor of Philosophy
Doctoral thesis in Radiopharmaceutical Sciences

DTU Health Tech
Department of Health Technology

Delivery and Release of [^{125}I]Iododeoxyuridine via Nanocarriers for Auger-radiotherapy of Glioblastoma

Qing Tang

September, 2023

DTU

Supervisor: Andreas T.I. Jensen
Co-supervisors: Helge Thisgard & Natan Startorf

Hevesy Lab
Department of Health Technology Technical
University of Denmark
RISØ Campus
4000 Roskilde, Denmark

Preface

In this thesis, the major work conducted during my last 3 years at the Hevesy Laboratory of DTU Health Tech, Risø campus, was presented. The project was funded by DFF Sapere Aude Grant.

This thesis was carried out under the main supervision of Andreas Tue Ingemann Jensen, my co-supervisors Natan Johannes Willem Straathof and Helge Thisgaard, as well as Matthias Barz during my external research stay in Leiden University.

The work is presented in five separate chapters. Chapter 1 is a general introduction of targeted radionuclide therapy and the use of nanoparticles in the field of radiopharmaceuticals. Chapter 2 focus on the delivery and release of [^{125}I]Iododeoxyuridine ([^{125}I]IUdR) using liposomes. Chapter 3 further describes the delivery and release of [^{125}I]IUdR with polymeric micelles. Chapter 4 focus on a polypept(o)ides based nanocarrier used for delivery and release of [^{125}I]IUdR. Chapter 5 is a description of work regarding the biodistribution of nanoparticles using Convection Enhanced Delivery (CED) in pig brain. A general conclusion & perspectives are given in the end.

Roskilde, September 2023

Qing Tang

Abstract

This PhD thesis provides a comprehensive exploration into the realm of targeted drug delivery systems, with a particular emphasis on the potential of [^{125}I]IUdR-deoxyuridine ([^{125}I]IUdR) for Auger radiotherapy in the treatment of glioblastoma multiforme (GBM). The thesis is structured into five separate chapters:

Chapter 1: This chapter was a general introduction of the thesis. It started with the treatment and challenges of GBM, and the explorations of novel treatment approaches. It continued deeply into the Targeted Radionuclide Therapy (TRT), exploring the utilization of α emitters, β- emitters, and Auger electron emitters as the radiopharmaceutical agents for cancer therapy, with a special emphasis on Auger electrons, exemplified by [^{125}I]IUdR. This chapter also introduced the applications of nanoparticles in TRT, including both organic and inorganic nanoparticles. The radiolabelling strategies of nanoparticles is discussed subsequently. Furthermore, the chapter described the delivery methods of nanoparticles to the tumor sites, including passive, active delivery and local administration, with CED detailed as an example of local administration. Finally, the chapter provided a short rationale for the entire study.

Chapter 2: In this chapter, the study embarked on the development of drug delivery systems, particularly focusing on liposomes. As nanoscale vesicles, liposomes have garnered attention for their ability to encapsulate and deliver therapeutic agents directly to tumor sites, enhancing the efficacy and reducing systemic side effects. Therefore, they are promising candidates for the delivery of Auger radiotherapy agent

[^{125}I]IUdR. Given the rapid degradation of free [^{125}I]IUdR in the body, strategic structural modifications were introduced. A key innovation was the incorporation of an ester linker, facilitating the creation of prodrugs with varying carbon chain lengths, referred as [^{125}I]IUdR-C_n. This design allowed for a controlled release of [^{125}I]. The loading and release study of the prodrug loaded liposomes were carried out. The *in vitro* efficacy study and *in vivo* biodistribution study were conducted.

Chapter 3. In this chapter, the exploration of [^{125}I]IUdR-C_n prodrugs was continued, with a focus on using polymeric micelles (PMs) as the nanocarrier. PMs, with their unique core-shell structure and small sizes, simple preparation methods and prolonged retention time in blood, have shown their abilities as the vesicle in the drug delivery system for cancer treatment. Therefore, in this chapter, the preparation methods of blank PMs, the loading of the prodrugs and the release of [^{125}I]IUdR from the loaded PMs were evaluated. Furthermore, DNA incorporation efficiency and *in vitro* efficacy study were investigated.

Chapter 4: The focus here was shifted to the exploration of polypept(o)ides, specifically a so called PeptoBrush (PB), for GBM's Auger radiotherapy. Peptobrush, with their unique brush-like architecture, offer advantages in drug loading and release dynamics. The

absence of PEG in PB make them particularly attractive, minimizing potential immune responses, such as the accelerated blood clearance (ABC) phenomenon. The chapter detailed the synthesis of PB and the use of click chemistry for drug loading, achieving remarkable drug loading efficiency. The relevant drug release and *in vitro* efficacy studies were investigated.

Chapter 5: In the last chapter, the research delved into the relationship between nanoparticle sizes, distribution and retention in the brain, utilized by PET-guided intracranial CED administration. Understanding the distribution dynamics of nanoparticles is crucial, as it directly impacts therapeutic efficacy and safety. Therefore, two different nanoparticles, liposomes (130 nm) and gold nanoparticles (AuNPs, 8 and 40 nm), were prepared and investigated. The findings distinctly underscore the advantages of sizes in terms of distribution, setting the stage for future studies to optimize the *in vivo* characteristics of [^{125}I]IUdR-C_{18}-LIPs for GBM treatment.

Resumé (Danish)

Denne ph.d.-afhandling giver en omfattende undersøgelse af målrettede lægemiddelleveringssystemer, med særlig vægt på potentialet af [^{125}I]IUdR-deoxyuridin ([^{125}I]IUdR) til Auger-radioterapi i behandlingen af glioblastoma multiforme (GBM). Afhandlingen er struktureret i fem separate kapitler:

Kapitel 1: Dette kapitel var en generel introduktion til afhandlingen. Det begyndte med behandlingen og udfordringerne ved GBM og undersøgelserne af nye behandlingsmetoder. Det fortsatte dybt ind i den målrettede radionuklidterapi (TRT), hvor det udforskede anvendelsen af α-emittere, β-emittereog Auger-elektron emittere som radiopharmaceutiske midler til kræftterapi, med særlig vægt på Auger-elektroner, eksemplificeret ved [^{125}I]IUdR. Dette kapitel introducerede også anvendelsen af nanopartikler i TRT, inklusive både organiske og uorganiske nanopartikler. Radiomærkningsstrategier for nanopartikler blev efterfølgende diskuteret. Desuden beskrev kapitlet leveringsmetoderne for nanopartikler til tumorsites, inklusive passiv, aktiv levering og lokal administration, med CED detaljeret som et eksempel på lokal administration. Endelig gav kapitlet en kort begrundelse for hele studiet.

Kapitel 2: I dette kapitel begyndte studiet udviklingen af lægemiddelleveringssystemer, med særlig fokus på liposomer. Som nanoskalavesikler har liposomer fået opmærksomhed for deres evne til at indkapsle og levere terapeutiske midler direkte til tumorsites, hvilket forbedrer effektiviteten og reducerer systemiske bivirkninger. Derfor er de lovende kandidater til levering af Auger-radioterapimiddel [^{125}I]IUdR. Givet den hurtige nedbrydning af fri [^{125}I]IUdR i kroppen blev der introduceret strategiske strukturmodifikationer. En nøgleinnovation var inkorporeringen af en esterlinker, hvilket muliggjorde skabelsen af prodrugs med varierende kulstofkædelængder, omtalt som [^{125}I]IUdR -Cn. Dette design tillod en kontrolleret frigivelse af [^{125}I]IUdR. Studiet af lastning og frigivelse af de prodrug-loaded liposomer blev udført. *In vitro* effektivitetsstudiet og *in vivo* biodistributionsstudiet blev gennemført.

Kapitel 3: I dette kapitel fortsatte udforskningen af [^{125}I]IUdR-Cn prodrugs, med fokus på brugen af polymeric micelles (PMs) som nanobærer. PMs, med deres unikke kerne-skalstruktur og små størrelser, enkle forberedelsesmetoder og forlænget tilbageholdelsestid i blodet, har vist deres evner som vesikel i lægemiddelleveringssystemet til kræftbehandling. Derfor blev i dette kapitel forberedelsesmetoderne for blanke PMs, lastningen af prodrugs og frigivelsen af [^{125}I]IUdR fra de loaded PMs evalueret. Desuden blev DNA inkorporeringseffektivitet og *in vitro* effektivitetsstudie undersøgt.

Kapitel 4: Fokusset blev her skiftet til udforskningen af polypept(o)ider, specifikt en såkaldt PeptoBrush (PB), til GBM's Auger-radioterapi. PeptoBrush, med deres unikke børsteligende arkitektur, tilbyder fordele ved lægemiddellastning og frigivelsesdynamik. Fraværet af PEG i PB gør dem særligt attraktive, hvilket minimerer potentielle immunreaktioner,

såsom det accelererede blodclearance (ABC) fænomen. Kapitlet detaljerede syntesen af PB og brugen af click-kemi til lægemiddellastning, hvilket opnåede bemærkelsesværdig lægemiddellastningseffektivitet. De relevante lægemiddelfrigivelses- og in vitro effektivitetsstudier blev undersøgt.

Kapitel 5: I det sidste kapitel gik forskningen ind i forholdet mellem nanopartikelstørrelser, distribution og tilbageholdelse i hjernen, anvendt af PET-guidet intrakraniel CED-administration. Forståelsen af nanopartiklers distributionsdynamik er afgørende, da det direkte påvirker terapeutisk effektivitet og sikkerhed. Derfor blev to forskellige nanopartikler, liposomer (130 nm) og guld nanopartikler (AuNPs, 8 og 40 nm), forberedt og undersøgt. Resultaterne understreger tydeligt fordelene ved størrelser med hensyn til distribution, hvilket lægger grundlaget for fremtidige studier for at optimere de *in vivo* karakteristika af [^{125}I]IUdR-C_{18}-LIPs til GBM-behandling.

Overview of contributions

Manuscript 1:

Tuneable Release of [^{125}I]Iododeoxyuridine ([^{125}I]IUdR) From Liposomes Administered by Convection Enhanced Delivery for Auger Radiotherapy of Glioblastoma (In preparation)

Qing Tang[1], Natan Johannes Willem Straathof[1], Aaraby Yoheswaran Nielsen[2], Katharina Ravn,[1] Vigga Sand Gammelsrød[2,3], Mikkel C Schou Andersen[3,4,5], Fedor Zhuravlev[1], Bo Halle[6], Helge Thisgaard*[,2], Andreas Ingemann Jensen*[,1]

The structure of the manuscript was designed and written by the PhD student and Natan J.W. Straathof. Main revision was conducted by Andreas I. Jensen. All experiments related to liposomes were conducted and evaluated by the PhD student, including drug loading, drug release and cell based studies. The *in vivo* experiments were executed and analyzed by Aaraby Nielsen.

Manuscript 2:

[^{125}I]Iododeoxyuridine ([^{125}I]IUdR) Prodrugs Loaded Polymeric Micelles: A Novel Approach for Glioblastoma Treatment via Auger Radiotherapy (In preparation)

Qing Tang[1], Alina Hossain[1], Natan Johannes Willem Straathof[1], Katharina Ravn,[1] Andreas Ingemann Jensen*[,1]

The structure of the manuscript was designed and written by the PhD student. Main revision was conducted by Natan J.W. Straathof and Andreas I. Jensen. Most of the experiments were conducted and evaluated by Alina Hossain under the supervision of the PhD student. Some of the drug loading and cell based studies were conducted by the PhD student.

Manuscript 3:

Continuous & Sustained Release of Cytotoxic [^{125}I]IUdR from a Modified Cyclononyne-Functionalized PeptoBrush for Auger-Radiotherapy of Glioblastoma (In preparation)

Qing Tang,[1] Gabriela Schäfer,[3] Heyang Zhang,[3] Matthias Barz,[3*] Natan J.W. Straathof,[1,2,*] Andreas I. Jensen[1,2,*]

The outline of the manuscript was designed and written by Natan J.W. Straathof and the PhD student. The draft was revised by Natan J.W. Straathof and Andreas I. Jensen. The experiments related to [^{125}I]IUdR loaded PeptoBrush were conducted and analyzed by the PhD student, including drug loading, drug release and cell based studies. The synthesis of the PeptoBrush was conducted by Gabriela Schäfer. The radiolabelled compound [^{125}I]IUdR-N_3 was synthesized by Natan J.W. Straathof.

Manuscript 4:

The Influence of Size On The Intracranial Distribution of Biomedical Nanoparticles Administered by Convection Enhanced elivery in Pigs (In preparation)

Mahsa Amirrashedi [a,b,c], Andreas Ingemann Jensen [d*], **Qing Tang** [d], Natan Johannes Willem Straathof [d], Katharina Ravn [d], Christian G.T. Pedersen [a], Louise Langhorn [e], Frantz R. Poulsen [f,g], Max Woolley [h], David Johnson [h], Julia Williams [h], Helge Thisgaard [a,f*], Bo Halle [f,g*]

The main manuscript was written by Mahsa Amirrashedi and revised by Andreas I. Jensen and Bo Halle. The PhD student wrote the experimental part related to the work she performed. All experiments related to the production of Cu-64 labelled liposomes were performed and evaluated by the PhD student. The production of the Cu-64 labelled gold nanoparticles was conducted by Katharina Ravn. Natan J.W. Straathof contributed a revised version of experimental section. The *in vivo* study was performed and analyzed by Mahsa Amirrashedi.

Other work:

The PhD student also participated in research based on DOTA-hEGF, including the production of DOTA-hEGF, and the radiolabelling of DOTA-hEGF using lanthanum-135.

This part of the work is outside the scope of this thesis, so it is not included in the thesis.

Patent:

Nanoparticle delivery system for intracranial distribution and release of drugs (In preparation)

Andreas Ingemann Jensen, Helge Thisgaard, Bo Halle, Natan Johannes Willem Straathof, **Qing Tang,** Aaraby Yoheswaran Nielsen

The patent application is in progress and therefore the manuscripts are not submitted yet.

Acknowledgements

During my Ph.D. studies, I have had the fortune to work with many friendly, memorable, and helpful individuals, for which I am profoundly grateful. I especially want to thank my main supervisor, Andreas I. Jensen. He has not only provided immense help with any issues related to my thesis but also offered timely and effective assistance when I felt lost and confused. I also appreciate his help in establishing a strong interdisciplinary network.

I also want to express my gratitude to my co-supervisor, Natan Straathof, who is a postdoctoral researcher in our group. I thank him for generously providing compounds whenever I needed, and actively helping me overcome challenges in experiments and thesis writing. I also want to thank my co-supervisor, Helge Thisgaard, and researchers such as Bo Halle, Aaraby Nielsen, etc., for extensive and in-depth collaboration in *in vivo* experiments. Additionally, I am thankful to Matthias Barz from Leiden University, my supervisor during my external stay period, Gabriela Schäfer and Heyang Zhang, for their support and fruitful collaboration.

Moreover, I want to thank Katharina Ravn from the Hevesy Laboratory, who, as a research technician, has provided me with a lot of help, support, and care, along with cheerful conversations. Also, Kristina Pedersen has always offered various help and care with a smile, and I really enjoyed the unforgettable trips during the conference with her. I also want to extend my thanks to the staff of the Hevesy Laboratory, especially Ghazal Torabi, Helle T. Holm, Trine Borre, for their generous help to make my research runs smoothly.

I also want to thank my friends, Zhimei Yu, Xiuqing Hao, for their support and care in the last three years, your words and companionship have made my life in Denmark better. I also enjoyed the weekly sports time with Xiaofeng Wang, Chunlei Wen, Tingting Chen, etc., and the pleasant game time during Covid times with Zhimei Yu, Qin Su and Qi Wu.

Last but not least, I want to express my gratitude to my parents, Zhen Li and Qianyou Tang. They have always respected my choices, especially when I decided to come to Denmark for my PhD; despite their worries, they expressed their support. I couldn't have completed my PhD studies without their love and support.

To my grandparents, I have always miss you.

Contents

Chapter 1

General Introduction

1 Glioblastoma

Glioblastoma, or glioblastoma multiforme (GBM), as shown in **Figure 1**, is the most aggressive type of primary brain tumor in adults. Originating from star-shaped glial cells called astrocytes, their rapid growth and tendency to infiltrate surrounding brain tissue make them particularly difficult to treat.[1] GBM has an estimated incidence of 2-3 cases per 100,000 people in the United States and Europe, with a higher occurrence in the 75-84 age group and slightly more common in men.[2] The overall incidence rate for the elderly population in the United States between 2000 and 2017 was 13.16 cases per 100,000, according to a study in 2021.[3] Glioblastoma's aggressive nature and resistance to treatment contribute to a high mortality rate. Median survival is typically around 15 months with standard treatment, and the 5-year survival rate is less than 10%.[4]

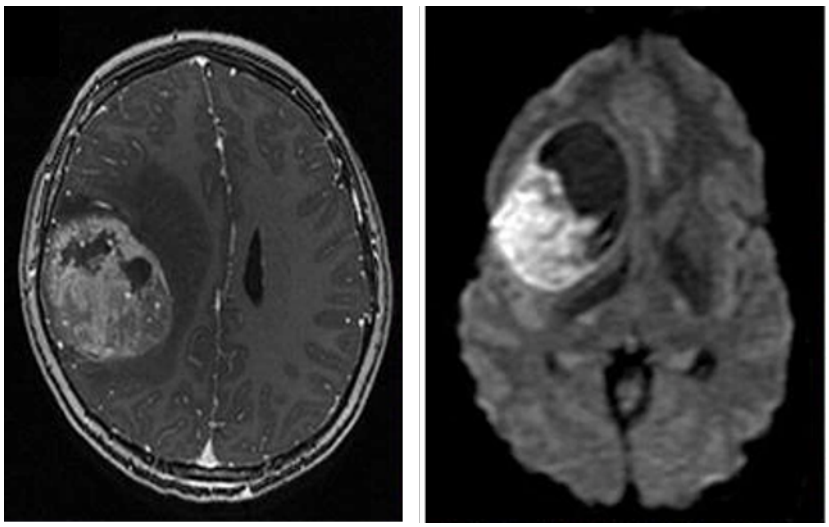

Figure 1. Representative MRI images of GBM. Figure adapted from Louis et al.[5]

Standard treatment involves a multimodal approach, starting with maximal safe surgical resection. This is followed by radiation therapy to kill remaining tumor cells and concurrent chemotherapy, often with the drug temozolomide (TMZ).[6] More specifically, external radiation is delivered in daily doses of 2 Gy along with 75 mg/m^2/day of TMZ, five days

a week for six weeks, for a total of 60 Gy. The treatment was then supplemented with TMZ at 150-200 mg/m^2/day for 5 days in each 28-day cycle, for a total of 6 cycles. This procedure is also known as Stupp's regimen, which was reported by Stupp et. al in 2005.[4] It is reported this method has improved the overall 5-year survival rate to 9.8% compared to 1.9 % for radiotherapy alone.[6]

Despite these interventions, GBM frequently recur because of its aggressive nature, especially infiltrating GBM cells, and resistance to treatment. The histopathological hallmarks of GBM are described in **Figure 2**. Consequently, there is a critical need for innovative therapeutic solutions. Over the past 20 years, several innovative approaches utilizing biotechnology have been evaluated in laboratory and clinical trials.[7–9] For example, tumour treating fields (TTF) use low-intensity (1–2 V/cm) and intermediate-frequency electric fields (100 kHz to 1 MHz) to kill cancer cells, and has been approved by FDA for GBM treatment.[10]When TTF was included into radiochemotherapy, it resulted in a notable improvement in the 5-year survival rate to 13 % and a prolonged progression-free survival, as compared to radiochemotherapy alone. However, the high cost, approximately 20,000 USD per month, poses a significant barrier to more clinical use.[11]

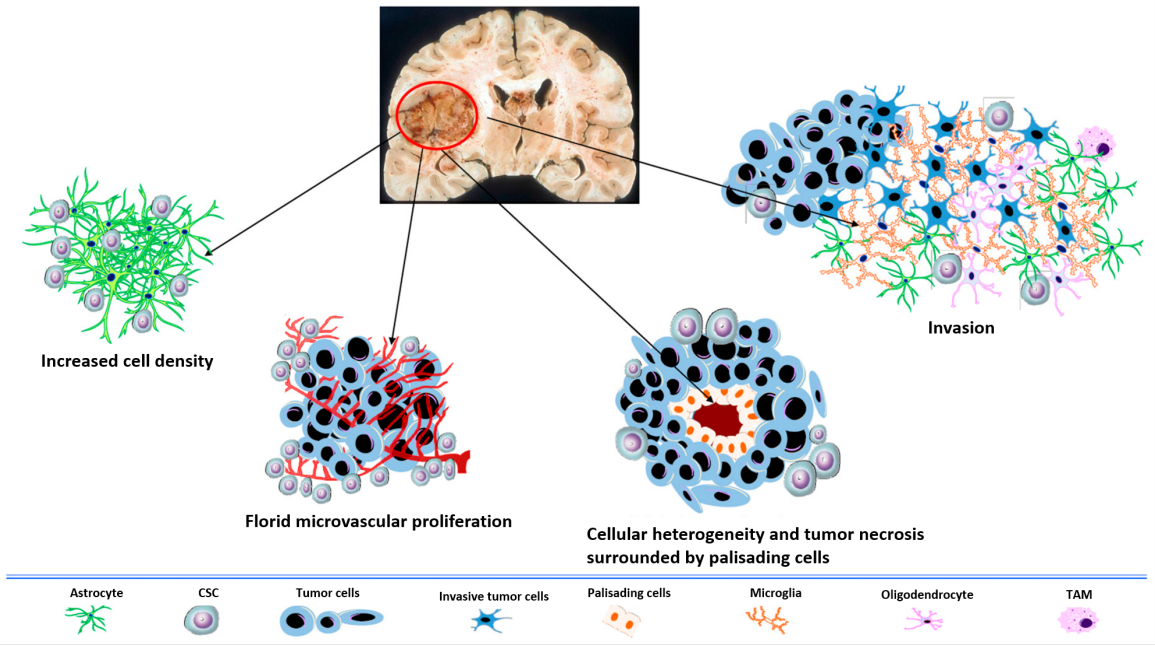

Figure 2. Schematic overview of the histopathological hallmarks of GBM. CSC: cancer stem cell; TAM: tumor-associated macrophage. Figure adapted from Angelucci et al.[12]

Meanwhile, recent advancements in nuclear medicine and nanotechnology have provided new opportunities for cancer treatment.[13,14] Specifically, the innovative idea of integrating nanotechnology with radiopharmaceutical has generated new promising approaches.[15] Therefore, the primary focus in this chapter is on targeted radionuclide therapy (TRT) and the nanoparticles employed in TRT.

2 Targeted radionuclide therapy

TRT is a unique approach exploits a specific biochemical pathway to guide radionuclides directly to the cancer site.[16]The components of TRT include a radionuclide-tagged molecule, a chelator, a vector, and a target.[17] **Figure 3** illustrates the components and applications of TRT in a comprehensible manner.

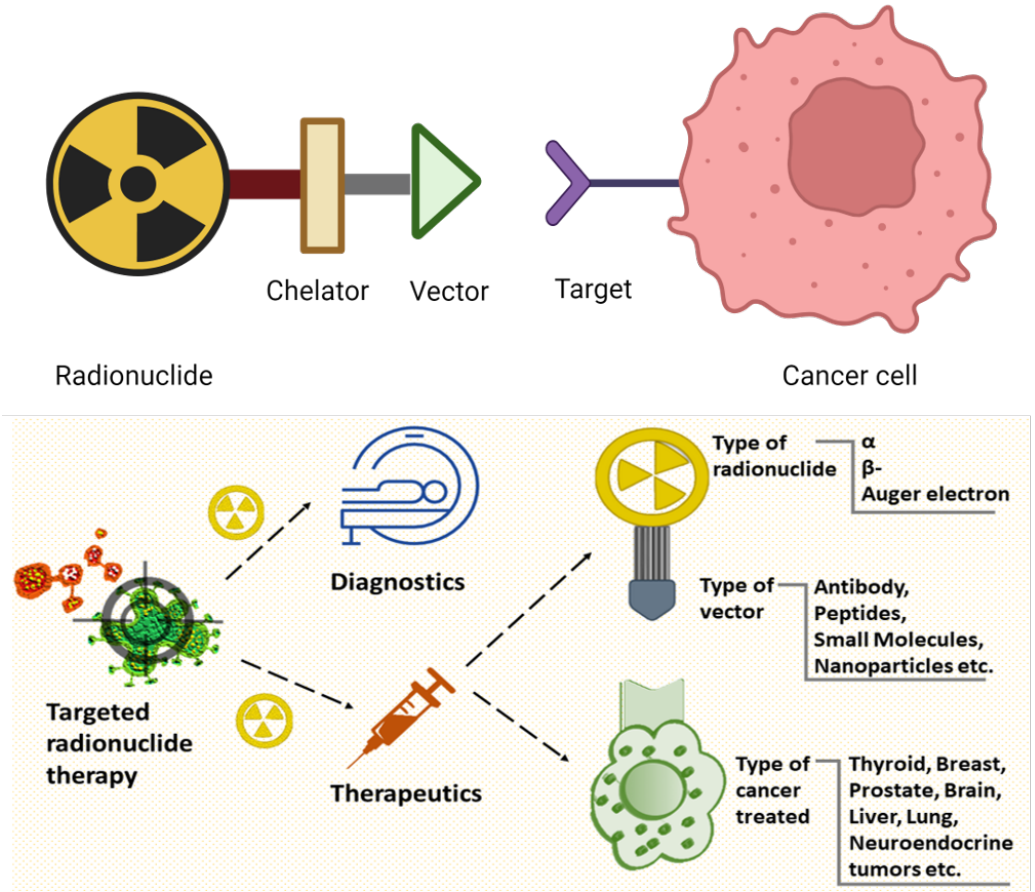

Figure 3. Illustration of the components and applications of TRT. a) A typical design of TRT components, b) The applications of TRT as diagnostics and therapeutics. Figure adapted from Goel et al. and recreate with Biorender.[16]

Table 1.1 Representative properties of α, β−, and AEs and their clinical applications[18,19]

Particles	Properties	Mechanism	Applications
Beta Particles	Range: 0.2-15 mm Energy: 0.05-2.5 MeV LET: 0.2 keV/µm	Cross fire effect half-life and radioactivity dependent oxygen dependent	mCRPC metastatic melanoma
Alpha Particles	Range: 50-100 µm Energy: 2-10 MeV LET: 80-300 keV/µm	Traversed path length in the cell nuclei oxygen independent	non-Hodgkin lymphoma mCRPC
Auger Emitters	Range: 2-500 nm Energy: 10 eV-10 keV LET: 4-26 keV/µm	Breaks in DNA strands (”Bystander” effect)	metastatic EGFR-positive breast cancer GBM

Abbreviations: LET, linear energy transfer; eV, electron volts; mCRPC, Metastatic castration resistant prostate cancer; EGFR, epidermal growth factor receptor

The primary goal of TRT is to deliver a high radiation dose to a specific site, thereby selectively eliminating tumor cells and minimizing damage to healthy cells. For therapeutic applications, alpha (α), beta (β-) particles, and Auger electrons are used, while β+, X-rays, and γ-rays are reserved exclusively for diagnostic purposes. **Table1.2** illustrates the representative properties of the radionuclides used for TRT. **Figure 4** provides a visual illustration of the properties of β-, α, and AEs in tumors or cells.

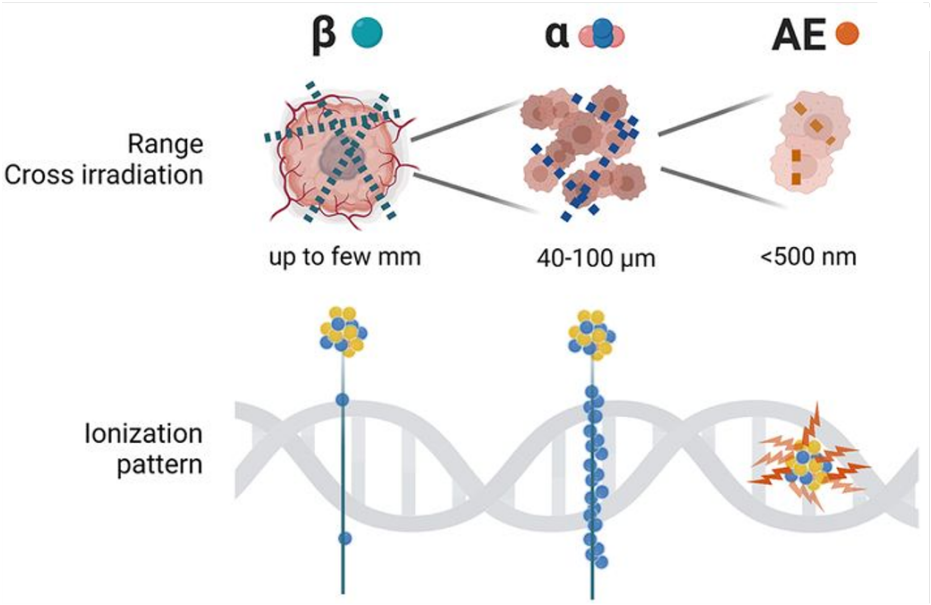

Figure 4. Illustration of the LET ranges, cross-irradiation, and ionization patterns of β-, α, and AEs in tumors or tumor cells (top) and DNA (bottom). Figure adapted from Bolcaen et al.[20]

2.1 α emitters

The α particle possesses a positive charge and a substantial mass as helium nucleus , with an energy range from 4 to 9 MeV. The α particle exhibits a slow speed and a limited range of 50 to 100 μm, accompanied by a high LET value of 100 keV/μm.[21] The treatment via α particles is known as target alpha therapy (TAT), with a milestone in 2013 when ^{223}Ra dichloride was approved by FDA for mCRPC treatment.[22]

As the α particle reaches the end of its trajectory, it approaches the maximum energy of the Bragg peak. It also demonstrates a high relative biological effectiveness (RBE) and therefore exerts significant damage on DNA.[23]Because of its high LET and high ionization density, the cell damage is normally caused by double strand break (DSB) and DNA cluster breaks.[19,24] Consequently, the DNA cannot be repaired, leading to lethally damage. Furthermore, α particles can induce indirect effects, such as the cross-fire effect, oxygen free radicals (ROS), and other off-target effects, which contribute to their ability to cause cell damage.[25]Thus, the potent, low-toxicity nature of α based formulations, have significance impact in tumor therapy. For instance, Liu et al. developed a heterodimeric peptide (iRGD-C6-lys-C6-A7R) that targets both VEGFR and integrin, serving as a novel molecule for ^{211}At radiolabelling, which resulted in an increased median survival period for tumor-bearing mice.[26] **Table 1.2** provides several common α particles and their clinical applications.

Table 1.2 α particles being investigated or approved in clinical trials

Isotope	Half-life	Energy(MeV)	Indication	Phase	Refs
Radium 223	11.4 days	5.58	CRPC	Xofigo ®	[27]
Thorium 227	18.7 days	6	NHL	1	[28]
Actinium 225	10 days	5.08	AML	½	[29]
Astatine 211	7.2 hours	5.09	AML, ALL,and MDS	½	[30]
Lead 212	10.6 hours	6.01	ERBB2/HER2-positive tumors	1	[31]

Abbreviations: CRPC, castration-resistant prostate cancer; AML, acute myeloid leukemia; ALL, acute lymphoblastic leukemia; MDS, myelodysplastic syndrome; NHL, non-Hodgkin lymphoma, ERBB2 (HER2) , human epidermal growth factor receptor 2.

2.2 β- emitters

Compared to α particles, TRT based on β- emitters have been wildly investigated. β- particles are negative charged high-energy electrons that are emitted from the nucleus of isotopes.[17]These small particles moves in complex and twisted paths before eventually stop. However, it should be mentioned that the capacity of β-particles to produce permanent DNA damage is occasionally limited due to their low LET of around 0.2 keV/µm.[32]To obtain the intended therapeutic effect, a large concentration of radionuclides is often needed in the target tissue, especially compared to α particles.

Furthermore, β-particles have a rather long travel range in tissues, reaching from 1 to 10 mm. Such a characteristic can lead to harm in adjacent healthy tissues as well as the 'cross-fire effect.'[33,34]This impact leads to the elimination of both the tumor and the neighboring healthy tissue, which provides a dangerous environment for cancer cells. Consequently, metastases that are invisible to the naked eye can be treated without the requirement to attach the radiopharmaceutical to each individual cancer cell. This technique offers potential benefits in terms of therapeutic effectiveness.

The first two radionuclides utilized are sodium-24 (^{24}Na) and phosphorus-32 (^{32}P) in 1936 to treat hematological disorders, while the most commonly used isotope is iodine-131(^{131}I) for the treatment of thyroid cancer.[35]At present, isotopes such as yttrium-90 (^{90}Y) and lutetium-177 (^{177}Lu) have been explored extensively.[36]Some of their radiopharmaceutical products have been available in market, for instance, FDA-approved ^{90}Y-ibritumomab tiuxetan, ^{177}Lu-DOTATATE as well as ^{177}Lu-PSMA-617. **Table 1.3** shows the most commonly used β- particles and their applications.

Table 1.3 Most commonly used β-emitting radionuclides and their applications[22]

Isotope	Half-life	Energy (MeV)	Range (mm)	Indication
Iodine-131	8.2 d	0.356	0.4	Thyroid Cancer
Lutetium-177	6.73 d	0.208	0.28	Synovitis, mCRPC
Samarium-153	46.5 d	0.1032	0.7	Bone Pain Palliation, Synovitis
Rhenium-188	17 d	1.592	2.1	Bone Pain Palliation, Arthritis
Phosphorus-32	14.26 d	0.356	2.6	Polycythemia vera, cystic craniopharyngioma

Abbreviations: mCRPC, metastatic castration-resistant prostate cancer

2.3 Auger electrons

During the process of radioactive decay, electron vacancies are often formed in the K shell layer of atoms through mechanisms known as electron capture (EC) or internal conversion (IC), as illustrated in **Figure5**.[37]This results in the movement of electrons from higher energy levels to fill these vacancies, creating new vacancies in their original layers. As a result, specific X-ray or electrons are subsequentially emitted, these generated electrons are called AEs. Therapies utilizing AEs are also referred to as Auger radiotherapy (ART).[38]

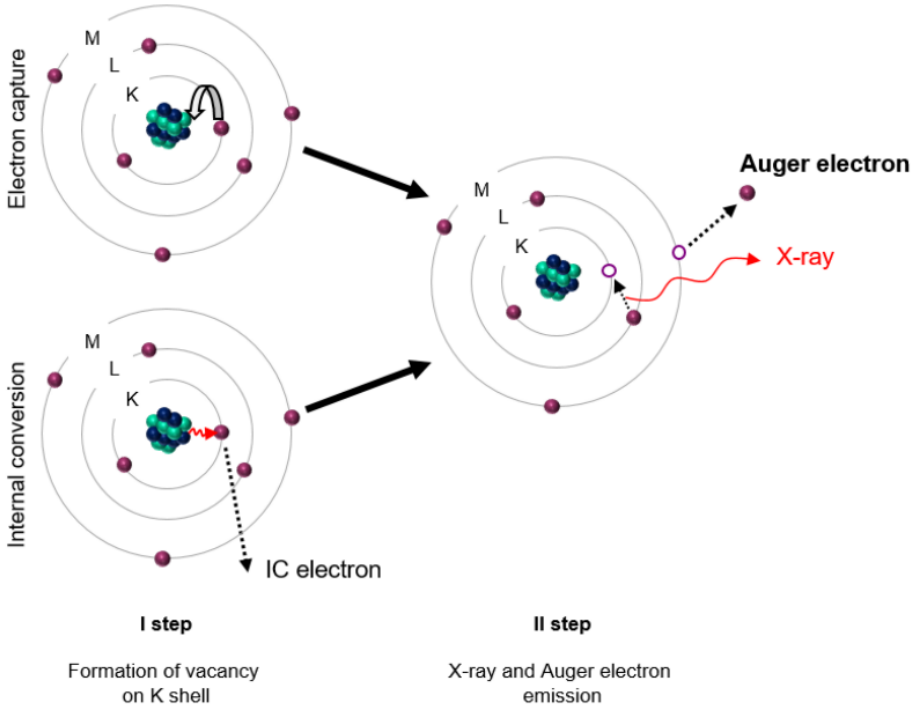

Figure 5. Emission of Auger electrons via electron capture or internal conversion. Figure adapted from Gharibkandi et al.[37]

Around 5-30 AEs with energy levels ranging from a few eV up to 1 keV were released in each transition. These AEs have irregular travelling paths ranging from a few nanometers to 0.5 micrometers. Their ionization, which is characterized by a LET of 4-26 keV/µm, occurs a few nanometers away from the origin.[39,40]Therefore, the close distance of AEs based radiopharmaceutical to the target, such as DNA, is crucial due to the rapid decrease in energy density over nanometric distances.

In addition to direct DNA damage caused by high LET, indirect damage to DNA also induced by ROS. Moreover, local cross-dose effects may still occur in cells neighboring the decay of the radionuclides and leads to the death of non-irradiated cells through bystander

effect.[22]Consequently, the internalization to cell DNA is crucial but not always required, targeting the cell membrane can be an effective approach to kill cancer cells as well.[39,41]For example, ^{125}I-anti-CEA monoclonal antibodies (mAbs) targeting the cancer cell membrane induce off-target effects through lipid rafts, demonstrating significant anti-cancer efficacy.[42]

Commonly used Aes include indium-111 (^{111}In), iodine-123 (^{123}I), and iodine-125 (^{125}I). Recently, the lanthanide isotope La-135 has gained interest due to its favorable physical properties and its ability to form stable complexes with the commonly used chelating agent, 1,4,7,10-tetraazacyclododecane-1,4,7,10-tetraacetic acid (DOTA).[43,44] **Table 1.4** listed the most commonly used AEs and their applications.

Table 1.4 Most commonly used AEs and their applications

Radionuclide	Half-life	Energy (keV)	Electrons	Applications	Reference
Technetium-99m	6.01 h	140	04.04	Breast cancer	[45]
Iodine-123	13.2 h	27.0	20	GBM	[46]
Iodine-125	59.4 d	27.2	21	GBM, prostate cancer	[4748]
Indium-111	2.80 d	6.78	5	Neuroendocrine cancers	[49]

Abbreviations: GBM, Glioblastoma

2.3.1 [^{125}I]IUdR

Iodine-125 is a low-energy electron emitter with a half-life of 59.6 days, releasing approximately 20 Auger electrons per decay. When ^{125}I placed close to DNA, its biological toxicity is identical to that of high LET radionuclides, therefore ^{125}I is often used in Brachytherapy.[50] The iodine-substituted analogue, IUdR, is a thymidine (dThd) analogue. IUdR undergoes phosphorylation to become IUdR monophosphate (IdUMP) and then further phosphorylated and integrated into DNA during the S phase.[51] Therefore, ^{125}I can be incorporated into DNA when IUdR is radiolabelled with ^{125}I. When cells incorporated with [^{125}I]IUdR, the radioactive decay of [^{125}I]IUdR, retained in the cells and their progeny, has been demonstrated to be extremely toxic.[52] The structure of [^{125}I]IUdR can be seen in **Figure 6**. For instance, Thisgaard et al. demonstrated that [^{125}I]IUdR significantly reduces the survival and-migration rate of GBM cells *in vitro*. Moreover, when combined with methotrexate(MTX) and/or TMZ, can further reduce cell viability.[53]

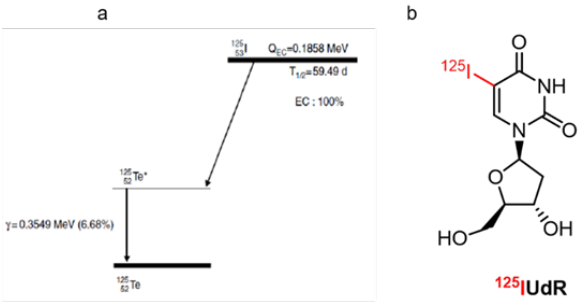

Figure 6. Decay scheme of ^{125}I and chemical structure of [^{125}I]IUdR. A. ^{125}I decay, B. [^{125}I]IUdR structure . Decay scheme adapted from Zeituni et al.[54]

Nevertheless, it should be noted that [^{125}I]IUdR is relatively unstable in vivo, as seen by its short biological half-life of about 5 minutes.[55] Additionally, [^{125}I]IUdR rapidly degrades to 5-iodouracil or dehalogenated, leading to a reduction of DNA integration properties, especially when administered intravenously.[51,56] Therefore, to enhance the therapeutic effect of [^{125}I]IUdR, one option is the structural modification or inject [^{125}I]IUdR directly to the tumor site.[52,53] Another alternative approach could be to utilize nanotechnology, such as [^{125}I]IUdR loaded nanoparticles, to extend the biological retention time.

3 Nanoparticles in TRT

The delivery of isotopes to the tumor site within the body presents a notable challenge.[50] This is especially the case for Aes, as they have a restricted travel range of a few nanometers. In order to successfully eradicate tumor cells, it is important to accurately deliver the radioactive agents in close proximity to the DNA.

One approach to achieve this is through labeling with monoclonal antibodies (mAbs).[39] However, studies have indicated that the specific activity obtained using this method could be insufficient for therapeutic purposes. For instance, the specific activity of ^{111}In-labeled trastuzumab was below 0.24 MBq/µg, indicating that only a small fraction of molecules are radiolabelled.[51] Consequently, a significant number of unlabeled mAbs bound to the HER2 receptor, thereby limiting cytotoxicity. Attempts to increase specific activity by increasing chelator-to-antibody ratios have yielded minimal gains, as they may lower the antibody immunoreactivity.[52]

Alternatively, nanomaterials offer a promising solution. The large surface area of nanoparticles allows for modification with appropriate carriers, such as antibodies, peptides, and small molecules, to target tumor cells.[57] Additionally, coating the surface with polymers, such as polyethylene glycol, can enhance their stability and pharmacokinetics in vivo by altering their surface properties.[58,59]

Various nanomaterials, including organic nanoparticles, such as liposomes, serum albumin, polydopamine, dendrimers, and polymeric micelles, as well as inorganic nanocarriers like AuNPs, magnetic nanoparticles, carbon nanoparticles, and silica nanoparticles (SiNPs), have been utilized as carriers for radionuclides.[60] The representative nanoparticles are listed in **Figure 7.**

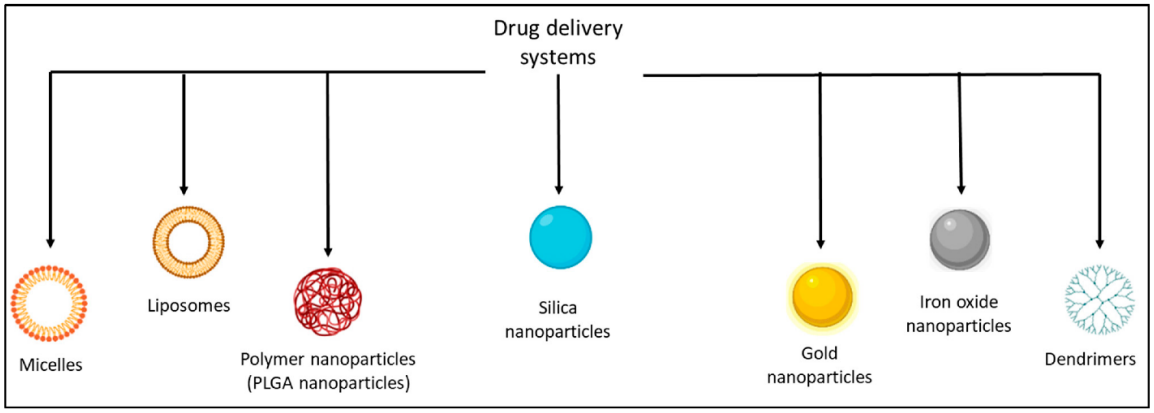

Figure 7. Representative nanoparticles that have been used in TRT. Figure adapted from Poletto et al.[61]

3.1 Organic nanoparticles

Organic nanoparticles, including liposomes, polymeric micelles, and dendrimers, have been employed in the field of radiopharmaceuticals.[62,63] Liposomes, in particular, are nanosized vesicles composed of phospholipid bilayers that resemble cell membranes. They are commonly used as carriers for drugs and have the ability to encapsulate both hydrophilic drugs within their aqueous core and hydrophobic drugs within their lipid bilayer.[64] In addition to their conventional use, liposomes can also be functionalized with radioactive nuclides. For example, Jensen and his colleagues reported a ^{52}Mn or ^{64}Cu loaded liposomes for PET imaging. In general, there are two main techniques for radiolabelling liposomes: surface labeling and internal labeling, which will be discussed in detail in section 3.3.

Similarly, micelles, which have a hydrophobic core and a hydrophilic shell, can also be radiolabelled using chelator and core-embedding strategies.[61,65] This approach allows for the labeling of micelles without affecting their corona and without interfering with their biodistribution and pharmacokinetic properties. Dendritic polymers, characterized by an exponential increase in the number of peripheral groups with each generation, can attach a large number of chelating molecules.[66] The labeling of dendritic polymers is typically achieved by introducing chelators and labeling with radiometals.[67]

In order to enhance the durability and systemic circulation duration of nanoparticles inside the human body, it is common practice to conjugate polyethylene glycol (PEG) chains to the nanoparticles, a process referred to as PEGylation.[68,69] So far, the U.S. Food and Drug Administration (FDA) has granted approval for clinical use to over 20 PEGylated nanoparticles, such as Doxil® and Genexol PM®, for cancer treatment.[70–72]

Although PEGylated nanoparticles have potential in augmenting medication delivery, there is a rising apprehension over their capacity to elicit immunological responses. According to recent research, it has been shown that the frequent application of pegylated therapies might potentially result in the production of anti-PEG antibodies, which can lead to rapid clearance of the nanoparticles from the bloodstream, also known as ”accelerated blood clearance (ABC) phenomenon”.[73,74] This phenomenon is further complicated by complement activation-related pseudo allergy (CARPA), a hypersensitivity reaction that can occur upon intravenous administration of some PEGylated products.[75] Their responses have the potential to undermine the effectiveness of the therapeutic treatment and give rise to concerns over the safety of PEGylated products.

In light of these aforementioned obstacles, it is important to investigate alternate materials that possess the benefits of PEGylation while circumventing its attendant drawbacks. Polypept(o)ides are a distinct category of hybrid polymers that possess a combination of characteristics derived from both polypeptides and polysarcosine.[76] Peptides provide a strong argument in favor of their use for drug administration owing to their inherent biocompatibility, ability to be tailored in terms of size, and capacity for surface functionalization.[77] Unlike PEGylated nanoparticles, polypept(o)ides have less tendency to provoke an immune response, making them intriguing candidates for repeated administration in therapeutic contexts.[78] **Figure 8** presents an overview of the structures and applications of polypept(o)ides.

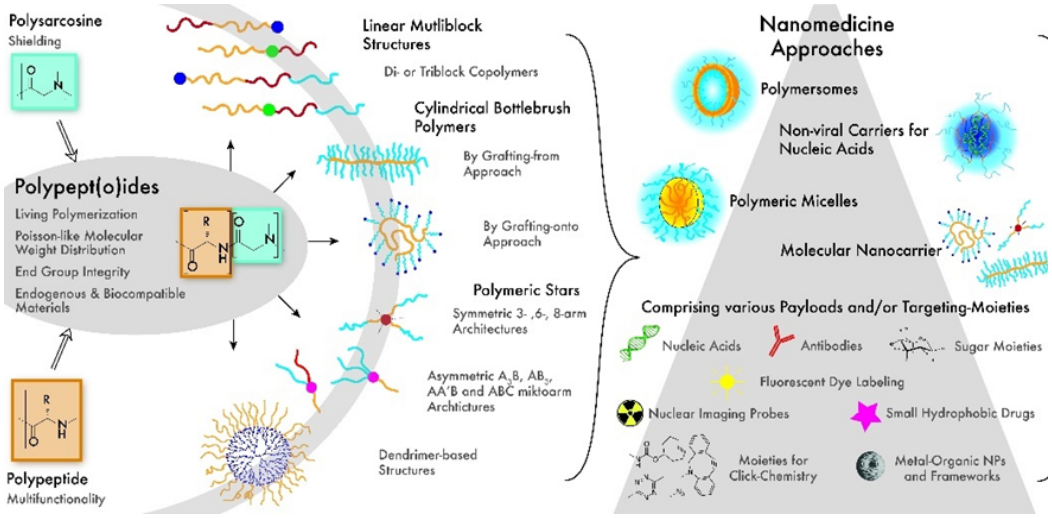

Figure 8. Overview on different polypept(o)ide architectures, nanoparticles and biomedical applications. Figure adapted from https://acs.digitellinc.com/sessions/579599/view

3.2 Inorganic nanoparticles

Inorganic nanoparticles have gained significant interest in the field of cancer treatment due to their unique size, chemical composition, and physical properties.[79] These nanoparticles can be utilized as therapeutic probes by incorporating or attaching radioactive nuclides with specific emission characteristics onto their surface, this enables their use in both radionuclide therapy and imaging.[80,81] Among the various types of inorganic nanoparticles that have been synthesized, gold nanoparticles (AuNPs) have emerged as the most widely used carriers for radionuclides in therapy.[57] For example, researchers have successfully developed ^{111}In -labeled gold nanoparticles modified with PEG chains and conjugated with

trastuzumab, which effectively bind to HER2-positive breast cancer cells and demonstrate tumor suppression.[82] Furthermore, the high affinity between gold atoms and heavy halogens allows for the adsorption of ^{125}I onto the gold surface. Researchers have synthesized ^{125}I -labeled AuNPs using the citrate reduction technique, resulting in highly stable particles with no significant leaching.[83] It is important to note that the anticancer effects of the radiolabelled AuNPs may not only because of the radionuclides, as AuNPs themselves can act as radiosensitizers, emitting AEs when exposed to external X- or ɣ- rays irradiation, such as those emitted by the ^{111}In radionuclides.[57]

3.3 Radiolabelling strategies of nanoparticles

Radiolabelling of nanoparticles can be achieved through various techniques, each with its unique advantages and challenges.[84] Direct labeling involves the incorporation of radionuclides into the nanoparticle matrix or onto the surface. This method is relatively straightforward and normally used for non-metallic radionuclides (such as fluorine-18, carbon-11 and iodine-125).[85] Indirect labeling, on the other hand, involves attaching radionuclides to a chelator or a bifunctional agent, which is then conjugated to the nanoparticle. This method is often used for metallic radionuclides, for instance, ^{64}Cu and ^{89}Zr.[86] The radiolabelling strategies of nanoparticles can be seen in **Figure 9**.

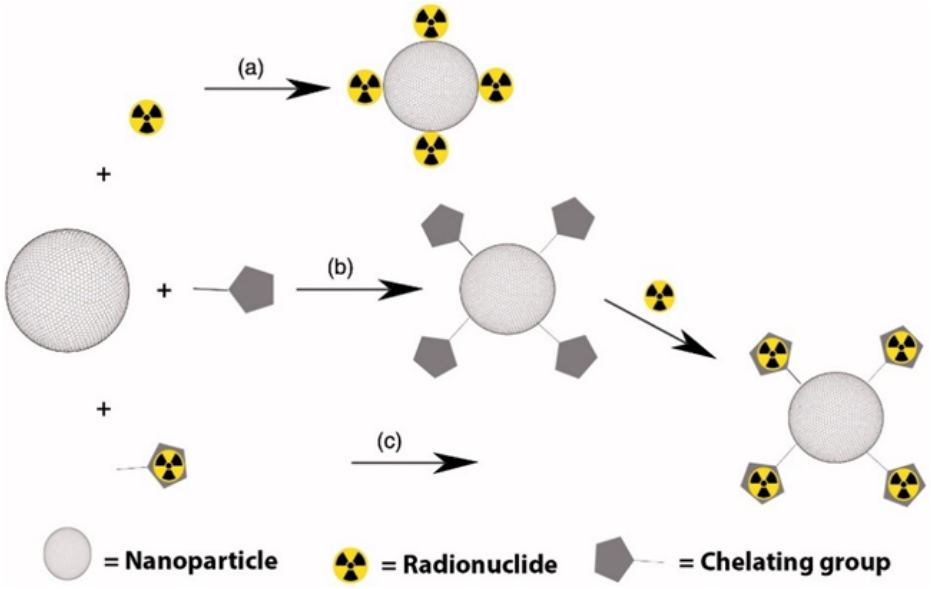

Figure 9. Strategies for radiolabelling nanoparticles include: (a) Direct radiolabelling; (c) Indirect radiolabelling where a chelator is first attached to the nanoparticle surface; and (b) Indirect labelling where chelating agents have been previously radiolabelled before conjugated to nanoparticles. Figure adapted from Enrique et al.[84]

Besides the 'doping' method applied to inorganic nanoparticles like AuNPs doped with ^{199}Au, radio-halogenation serves as another crucial strategy for direct radiolabelling.[85] Radio-halogenation is widely used for the radiolabelling of nanomaterials with ^{124}I, ^{125}I, or ^{131}I. Common iodination agents, such as iodobeads, iodogen, Chloramine-T, or Bolton-Hunter reagent, typically complete the procedure within a few seconds to minutes and are accompanied by high yields.[87] Some examples of radioactive halogenation can be found in **Figure 10.**

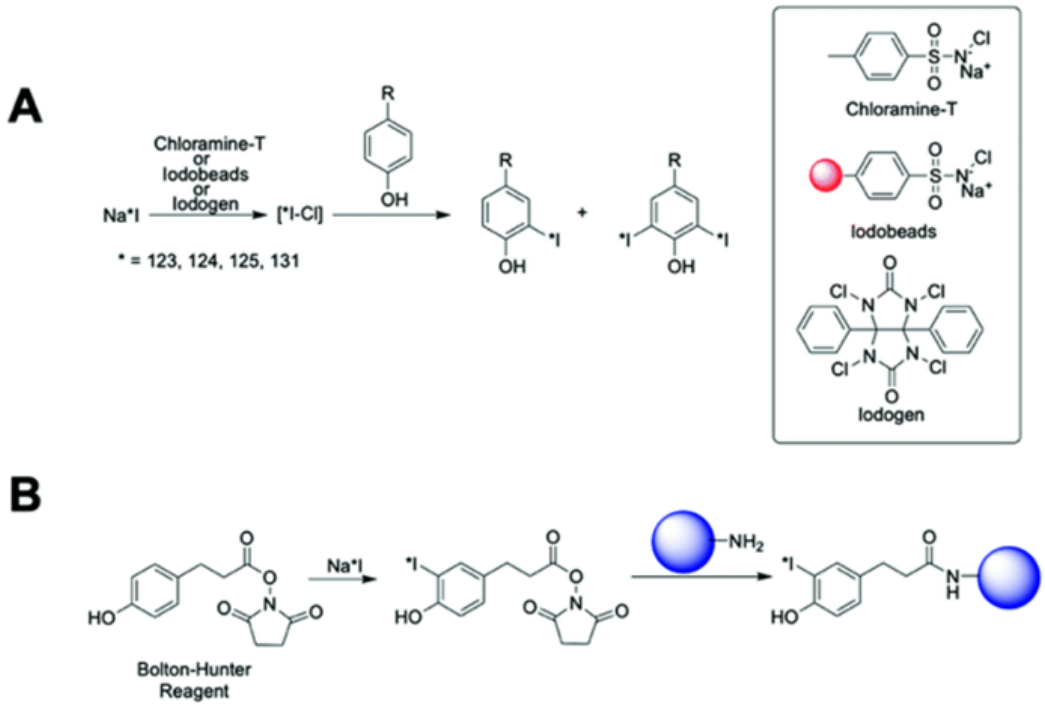

Figure 10. Representative radioiodination procedures. (A) Illustration of the radioiodination process facilitated by chloramine-T, iodobeads, or iodogen. (B) Illustration of the radioiodination of nanoparticles terminated with amine groups using Bolton–Hunter reagent. Figure adapted from Pellico et al.[85]

Regarding indirect radiolabelling of nanoparticles, the use of chelating agents is typically necessary to create highly stable metal-chelator complexes by means of coordination chemistry methods. Common chelating agents employed are often multidentate ligands, which, due to the ”chelate effect,” can form more stable complexes compared to monodentate ligands.[88] These chelating agents can be categorized into two categories: acyclic/linear chelating agents and macrocyclic chelating agents, as illustrated in **Figure 11**. Acyclic or linear chelating agents are typically utilized for rapid radiometal complexation. On the other hand, macrocyclic chelating agents exhibit slower complexation kinetics, often necessitating high temperatures and extended reaction times for radiolabelling but also bring higher complex stability, known as the macrocyclic effect.[85]

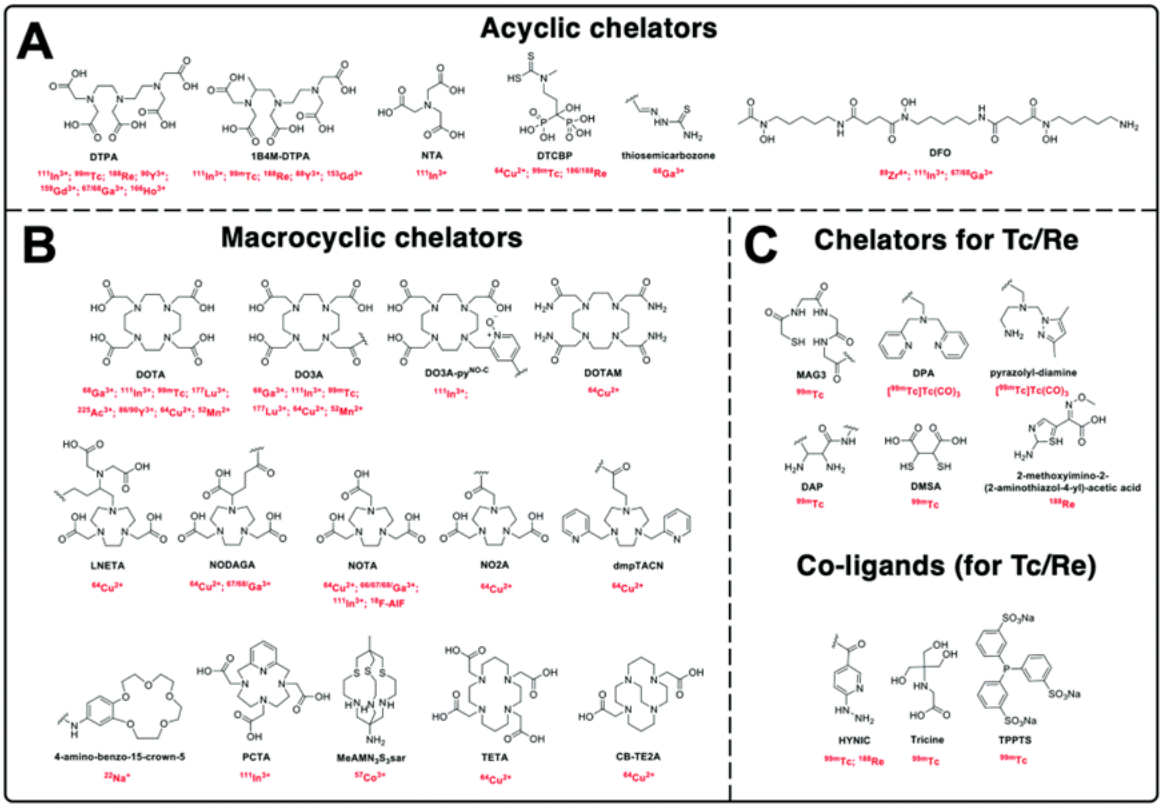

Figure 11. Chemical structures of the chelators used for radiolabelling nanomaterials with their corresponding radionuclides. (A) Acyclic chelators, (B) Macrocyclic chelators, (C) Chelators and co-ligands for Tc/Re. Figure adapted from Pellico et al.[85]

Among the nanoparticles, the radiolabelling strategies of liposomes have interesting and different methods compare to the classic chelator-based methodologies.[89] While liposomes can indeed be radiolabelled with radionuclides via chelator-based methods, as shown in **Figure 12A**, also known as surface labelling.[61] Apart from that, a passive encapsulation method is also used to encapsulate the radionuclides into the internal compartment of liposomes during preparation of the liposomes. For example, this method has been used to load [^{18}F]fluorodipalmitin ([^{18}F]FDP) into liposomes.[90] However, the loading efficacy is often less than 10%, thereby limiting the use in (pre)clinical studies.

Another widely used method is intraliposomal labelling (**Figure 12B**). Various strategies can be utilized for this purpose, including ionophore-chelator binding, unassisted loading, ionophore-drug binding and remote loading.[91] Commonly, ionophore-chelator binding is employed due to its ability to form stable complexes once the isotopes are encapsulated within the liposome core. For example, Petersen et al. reported the efficient loading of ^{64}Cu with or without the use of 2-hydroxyquinoline as ionophore into liposomes that encapsulated DOTA as copper chelator.[92]

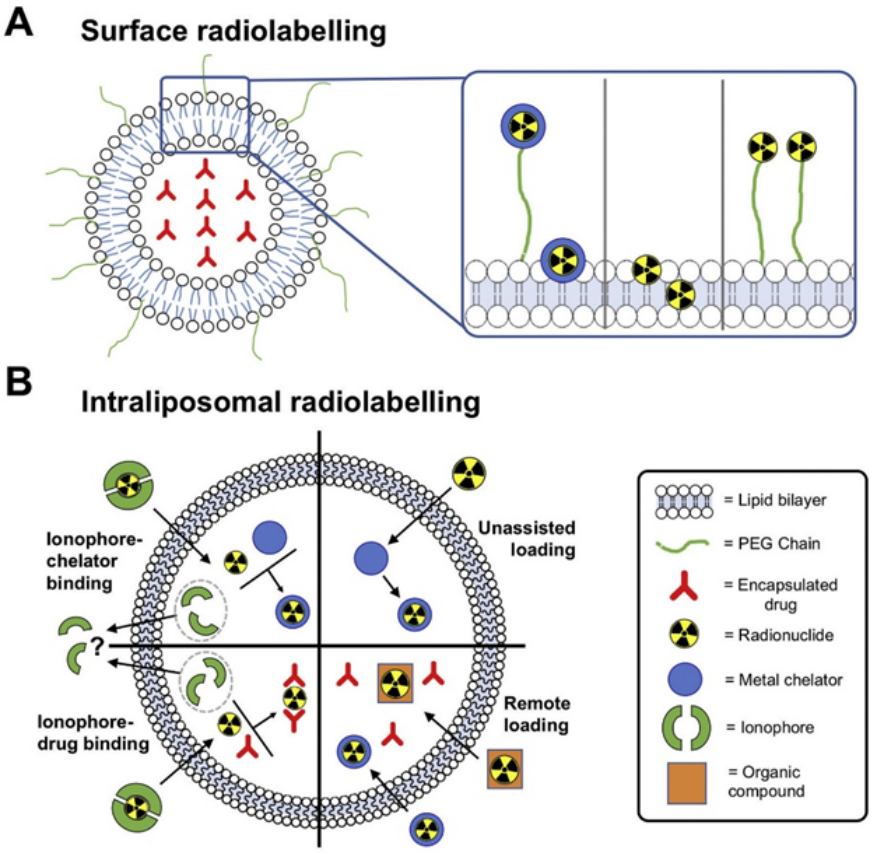

Figure 12. Radiolabelling strategies of liposomes. A) surface labelling, B) intraliposomal labelling. Figure adapted from Man et al.[91]

Similar to ionophore-chelator binding, remote loading involves the use of lipophilic radioactive tracers that can passively cross the lipid membrane of liposomes.[93] The loading process is normally driven by a pH or ion gradient, such as ammonium sulfate gradient.[94] This method is crucial as it maintains the *in vivo* stability of radiolabelled liposomes and preserves the original physicochemical properties of the liposomes, as it does not involve any surface modification. The complexes formed are designed to be stable within the liposome core and are captured due to the presence of functional groups that can carry a charge in the aqueous environment of the liposomes.[61] For example, Gokce et.al reported the successful loading of ^{124}I-labeled amino diatrizoic acid (ADA) compound via remote loading method with quantitative loading efficiency (>99%).[95]

4 Delivery of nanoparticles

4.1 Passive targeting

Nanoparticles can be delivered to tumor sites through three potential pathways. The first one is passive delivery, where nanoparticles of up to 250 nm can easily pass through the abnormal endothelial lining and remain in the tumor over time.[96] This phenomenon, as shown in **Figure 13**, known as the "enhanced permeability and retention (EPR) effect," serves as the foundation for the passive targeting of nanomedicines to tumors.[97] However, the effectiveness of passive targeting is hindered by the rapid uptake of nanoparticles in the liver and spleen, particularly when administered intravenously.[98] To overcome this limitation, nanoparticles can be effectively coated with a surface layer, commonly achieved through PEGylation, which prevents recognition by the reticuloendothelial system (RES) and thereby increases the circulation half-life of the nanoparticles.[99,100] Additionally, it is crucial for nanoparticles to circulate in the bloodstream for a longer retention time to reach to the tumor site. To this end, a nanoparticle with size of 10-100 nm, negative surface charge and invisible to RES, would be an ideal candidate for passive targeting.[96]

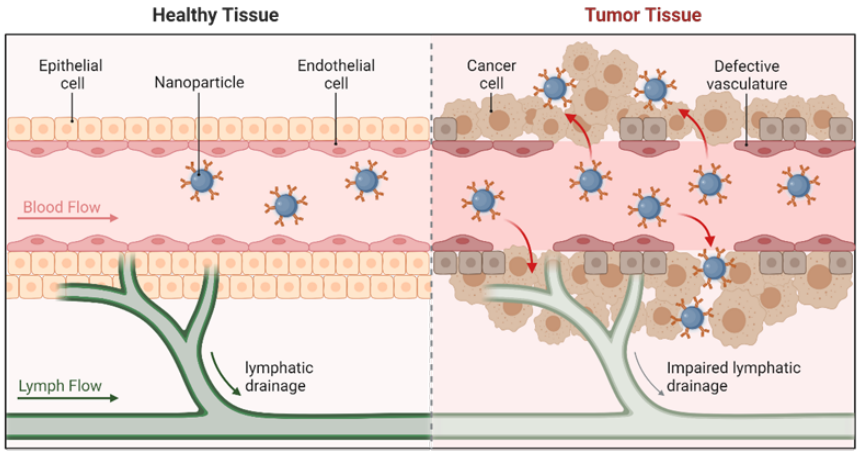

Figure 13. Illustration of passive targeting of nanoparticles in solid tumors via EPR effect. Figure created with Biorender.

4.2 Active targeting

Active targeting involves the application of various reagents with high affinity for specific target sites, such as receptors overexpressed by tumors or endothelial cells, onto the surface of nanoparticles.[101] These high affinity reagents can be ligands or antibodies. Commonly used targeting ligands include small molecules (e.g., folic acid),[102] peptides (e.g.,

RGD),[103,104] proteins (e.g., transferrin),[105,106] nanobodies,[107] and aptamers.[108] **Figure 14** presents the concept of active targeting delivery of radionuclides.

However, active targeting has its limitations. It primarily enhances the cellular internalization of the nanoparticles at the tumor site, but the accumulation of nanoparticles still relies on the EPR effect.[96] Therefore, actively targeted nanoparticles must meet the requirements of passive targeting mentioned earlier as well, such as appropriate particle size, stealthiness, sufficient stability, prolonged circulation, and effective drug retention.[109]

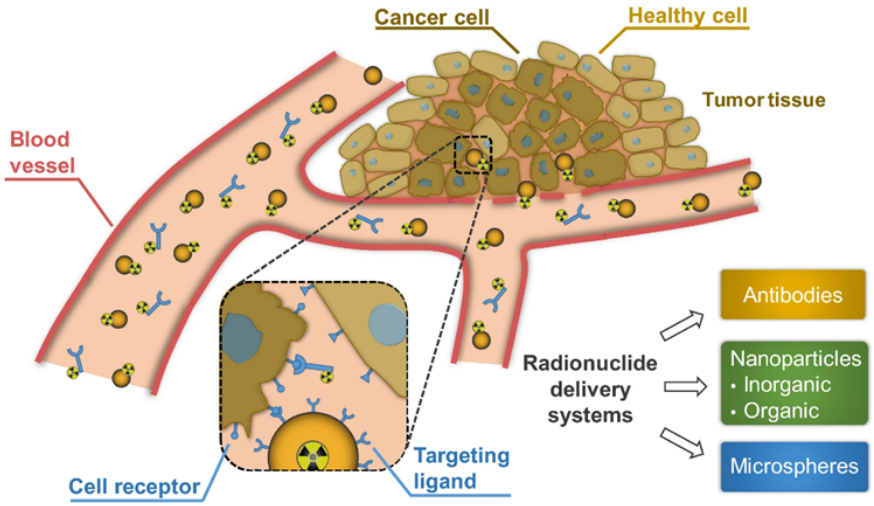

Figure 14. Administering radionuclide carriers at the tumor location and their subsequent accumulation through an active targeting strategy.Figure adapted from Peltek et al.[110]

4.3 Local administration

The delivery of nanoparticles to GBM is always a challenge.[111,112] The blood-brain barrier (BBB) is a sophisticated and distinctive membrane with selective permeability, functioning as a safeguarding mechanism to uphold homeostasis in the brain.[113] Therefore, NPs administrated systemically cannot cross the BBB sufficiently. The intratumor approach, or local administration, is a potential method for delivering drugs to tumors using nanoparticles in order to address challenges associated with drug delivery, such as dispersion, penetration, and retention.[114–116] The local administration method, specifically using convection-enhanced delivery (CED), will be used as an example in this context. A diagram illustrating the process of CED is provided in **Figure 15** .

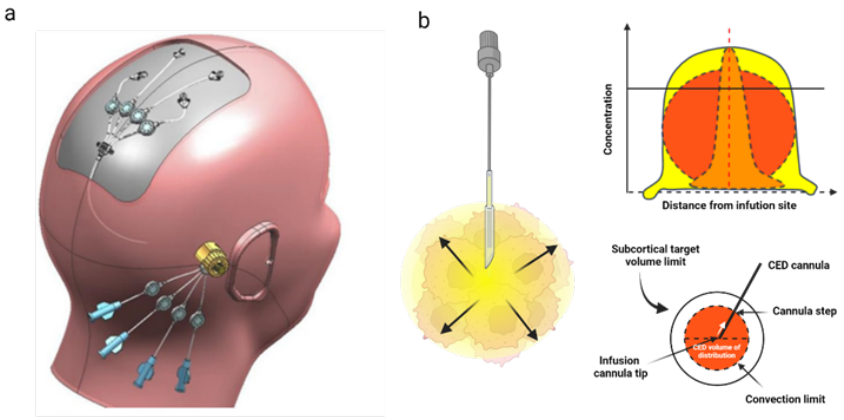

Figure 15. Illustration of convection-enhanced delivery (CED). a. 3D illustration of CED drug administration set-up in the brain; b. Distribution of therapeutical agents via CED to the tumor site. Figure adapted from Ruiz-Garcia et al.,[117] Barua et al.,[118] and recreate with Biorender.

CED was initially proposed by Bobo et al. in 1994 as a method for delivering drugs that are unable to penetrate the BBB or are too large to diffuse effectively over the required distances.[119] It involves the direct implantation of a cannula into the brain or tumor to deliver an infusion through a pressure gradient.[120].The key advantages of CED are it can achieve high local drug concentrations in the brain by dispersing the drug uniformly over the target area in a larger volume, more homogeneously and at a higher dose, and. occurs independently of either the molecular weight of the reagent or the diffusion rate.[121,122] Although there is no standardized protocol for implementing CED, key variables such as catheter design, placement, number, infusion rate, duration, and drug size are generally considered crucial for its success[123] It should be noted that the precise control of the V_d is crucial as it limits drug exposure to healthy brain tissue and safeguards neurological function.[124]

Successful applications of CED for nanoparticles in the brain have been reported, such as carboplatin-loaded or rhenium-186-loaded liposomes for GBM treatment.[125,126] Both approaches have demonstrated improvements in median survival times. Furthermore, when using CED to deliver nanoparticles, these particles must be of appropriate size and possess suitable surface chemistry to enhance penetration into the brain parenchyma and improve drug distribution and retention.[127] This ensures complete coverage of both the tumor mass and infiltrating cells, making this combined approach particularly suitable for applying Auger radiotherapy to GBM.

One of the primary factors influencing the distribution volume in CED is the size of the nanoparticles.[128,129] However, most CED studies have been conducted on small rodent models, which have significantly smaller brains compared to humans.[130] This raises the possibility of overestimating the effectiveness of CED.[123] Therefore, studies based on larger non-rodent animals, such as dogs, monkeys, or pigs, are essential for more accurate translation to human clinical applications.

5 Rationale of the thesis

Therefore, the motivation behind this thesis is rooted in the urgent need to develop innovative and effective therapeutic strategies for GBM. Traditional treatment methods have proven to be inadequate due to challenges such as the inability to traverse the blood-brain barrier, the infiltrative nature of GBM, and insufficient delivery to tumor sites. By exploring and optimizing advanced drug delivery systems and administration methodologies, with a special emphasis on nanoparticles loaded with [^{125}I]IUdR, such as liposomes, micelles and peptobrush, we hope to offer viable solutions for the aforementioned challenges. **Figure 16** gives a general illustration of the concept of the thesis. Within this framework, detailed explorations pertaining to liposomes and micelles will be elucidated in Chapter 2 and Chapter 3, the investigation on peptobrush will be presented in Chapter 4, the investigation of the behavior of liposomes in the pig brain via CED administration will be presented in Chapter 5. This structured approach aims to provide a comprehensive understanding and potentially pave the way for groundbreaking advancements in GBM treatment strategies.

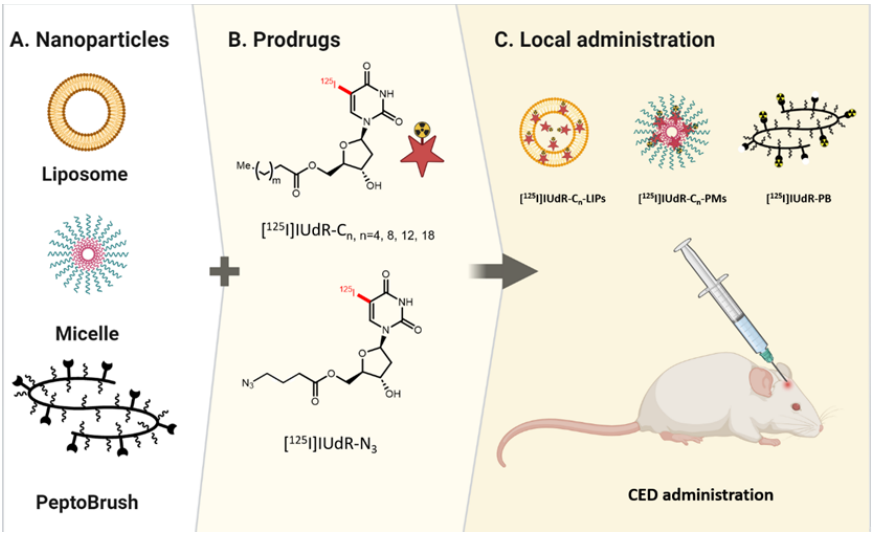

Figure 16. General illustration of the design of the researches that included in the thesis

Chapter 2

Tuneable release of [^{125}I]IUdR-deoxyuridine from liposomes administered by convection enhanced delivery for Auger radiotherapy of glioblastoma

---

Qing Tang[1], Natan Johannes Willem Straathof[1], Aaraby Yoheswaran Nielsen[2], Katharina Ravn,[1] Vigga Sand Gammelsrød[2,3], Mikkel C Schou Andersen[3,4,5], Fedor Zhuravlev[1], Bo Halle[6], Helge Thisgaard*[,2], Andreas Ingemann Jensen*[,1]

[1]DTU Denmark, Institut for Sundhedsteknologi, Risø Campus, Frederiksborgvej 399 (Bygning 202), 4000 Roskilde.

[2]Department of Nuclear Medicine, Odense University Hospital, Odense, Denmark

[3]Department of Clinical Research, University of Southern Denmark, Odense, Denmark

[4]Department of Neurosurgery, Odense University Hospital, Odense, Denmark

[5]BRIDGE (Brain Research - Inter Disciplinary Guided Excellence), University of Southern Denmark, Odense, Denmark

[6]The Danish Neurosurgical Society, Odense University Hospital Dept. of Neurosurgery, Odense C

The work in this chapter will be represented as manuscript.

1 Introduction

Glioblastoma (GBM) is the most common and aggressive malignant primary brain tumor,[1] accounting for 77%-81% of all primary malignancies of the central nervous system (CNS).[2] The incidence of GBM varies depending on the analysis, with an annual incidence rate of approximately 3-5 cases per 100,000 persons,[3–6] an average age at presentation of 62 years, and a predominance of males.[7] As a WHO grade IV glioma, the aggressive infiltrative growth of malignant glioma cells and the development of tumor angiogenesis are major impediments to effective treatment.[8] Additionally, the extensive intramolecular and phenotypic heterogeneity of GBM and glioma stem cells (GSC) makes complete surgical excision impossible.[9,10] As a result, the median survival of patients with GMB is approximately 14.6 months and the five-year survival rate is only 6.8%. [11,12]

The current standard treatment for GBM, the so-called Stupp's regimen, is surgical resection followed by external radiotherapy and chemotherapy with temozolomide (TMZ).[1,13,14,15] However, the recurrence of GBM is still unavoidable. The main reason is that while surgical treatment and external irradiation remove the main GBM tumor, it does not deal effectively with the infiltrating GBM cells. Additionally, although TMZ has proven to be widely distributed in all tissues, only 20% of this drug in systemic circulation is detected in the brain. This means that high systemic doses are required to achieve therapeutic levels, which in turn carry the risk of hematological toxicity. [16,17]

To address this, other treatments have been proposed. For example, FDA-approved carmustine-containing wafer (Gliadel®) can be implanted directly into the post-surgical resection cavity, thereby bypassing the blood-brain barrier (BBB).[18] However, the risk of infection and compromised wound healing limits its application.[19] Additionally, the FDA authorized Tumour Treating Fields (TTFields) as an adjuvant therapy for GBM treatment in 2011.[20] TTFields interferes with the cell cycle process of GBM cells by applying a low intensity, medium frequency, alternating electric field (100-300 kHz). [21,22] While the remaining novel therapies, such as boron neutron capture therapy (BNCT), anti-angiogenic therapy (with e.g. bevacizumab), immunotherapy, and gene therapy, have demonstrated promise in preclinical studies, their clinical outcomes remain ambiguous or discouraging. [20,23] In general, the limitations of the various treatments for GBM are strongly associated with the invasion and infiltration of the tumor itself.[24,25] Even a single glioblastoma cell can significantly invade and infiltrate into the brain parenchyma. [26] Furthermore, tumor cell infiltra-

tion has been seen in nearly one-third of the neighboring tissue around the surgical cavity.[27] Consequently, these infiltrating or invading GBM cells serve as the new starting points for recurrence.

Recent advances in nuclear medicine promise new tools for the fight against GBM. Auger electrons (AEs) emitting radionuclides, such as ^{99m}Tc, ^{125}I, ^{111}In, and ^{67}Ga have demonstrated high potential with therapeutic application in preclinical studies.[28–30] AEs are predominantly low-energy (<25 keV) electrons released by certain radionuclides during decay as a result of electron capture or internal conversion nuclear processes. The majority of AEs have ranges tissue of nano-to-micron distances, resulting in a high linear energy transfer (LET) of 4-25 keV/µm. [31,32] This makes AEs a potent modality for cancer treatment, particularly when the AEs are released near sensitive targets like DNA and cell membranes. Therefore, the close distance of AEs to cancer cell DNA is crucial for efficient cancer therapy. For example, Reiner *et al.* successfully developed ^{123}I-MAPi, an iodine-123 labeled Auger PARP1 inhibitor, inhibiting the overexpressed marker poly (ADP-ribose) polymerase 1 and killing GBM cells.[33] They demonstrated that ^{123}I-MAPi was capable of delivering a direct lethal payload at a distance of 50 Å from GBM cancer cell DNA.

Iodine-125 (^{125}I) releases approximately 20 AEs per decay and has a half-life of 59.6 days. Therefore, the efficacy of iodine-125 is significant when it is positioned close to DNA. The iodine-substituted thymidine (dThd) analog, 5-iodo-2'-deoxyuridine (IUdR), can be phosphorylated to IUdR monophosphate (IdUMP) by thymidine kinase and subsequently integrated into the DNA of cancer cells, making it a promising and viable option for targeted DNA destruction of cancer cells.[34] According to previous studies, [^{125}I]IUdR is integrated into DNA during cancer cell proliferation and the radioactive decay of [^{125}I]IUdR thus accumulated in cells and their progeny is exceedingly cytotoxic.[34–36] For example, Thisgaard *et al.* showed that when using intratumoral convection-enhanced delivery (CED) of [^{125}I]IUdR, DNA-incorporated [^{125}I]IUdR was found to have great therapeutic efficacy in rats with GBM, with and without temozolomide as adjuvant. [37]

CED is a local delivery approach that delivers therapeutics to the tumor site under positive pressure via an implanted catheter, thereby circumventing BBB constraints.[38–40] However, small molecular anti-GBM medications are ineffective and swiftly cleared from GBM tumors, whereas CED delivery of nanoformulations is reported to provide uniform distribution in the tumor with significantly prolonged retention compared to free drugs.[41,42] For instance, CED delivery of carboplatin was found to be possible and safe in a phase I clinical

study, but the free carboplatin was rapidly cleared within 24 hours.[43] Another study found that CED-delivered free carboplatin achieved a tumor tissue concentration of 34.4 µg/g after four hours of injection. In contrast, carboplatin encapsulated in PEGylated-liposomes exhibited 28 times higher concentration (963.7 µg/g tissue) at 4 hours and retained over 75% of the drug after 48 hours. [44] Moreover, numerous nanoparticle formulations, including magnetic nanoparticles, [45,46] liposomes,[41,47] and polymeric micelles,[48,49] have been reported to be administered using CED to increase the efficiency of delivery to brain tissue.

With this strategy in mind, we designed a liposome-based nanoparticle system for delivering [^{125}I]IUdR derivatives via CED for the efficient treatment of GBM. Four 5'-hydroxyl-mono-ester derivatives were elected as the first group of [^{125}I]IUdR-prodrug structures to be investigated. These prodrugs were envisaged to first undergo release from the liposomal lipid bilayers into the surrounding medium, followed by cleavage of the ester linkage by endogenous esterases (**Figure 1**). This study described a comprehensive investigation into the loading and release efficiency of these [^{125}I]IUdR derivatives ([^{125}I]IUdR-C_n) inserted liposomes ([^{125}I]IUdR-C_n-LIPs). Additionally, selected [^{125}I]IUdR-C_n-LIPs were investigated in vitro, with an assessment of DNA incorporation of ^{125}I and cytotoxicity. Furthermore, we examined the in vivo biodistribution as well as in vivo DNA incorporation of [^{125}I]IUdR-C_n-LIPs administered intracranially in rats. Finally, we evaluated the potential therapeutic efficacy of [^{125}I]IUdR-C_n-LIPs via CED in rats with GBM.

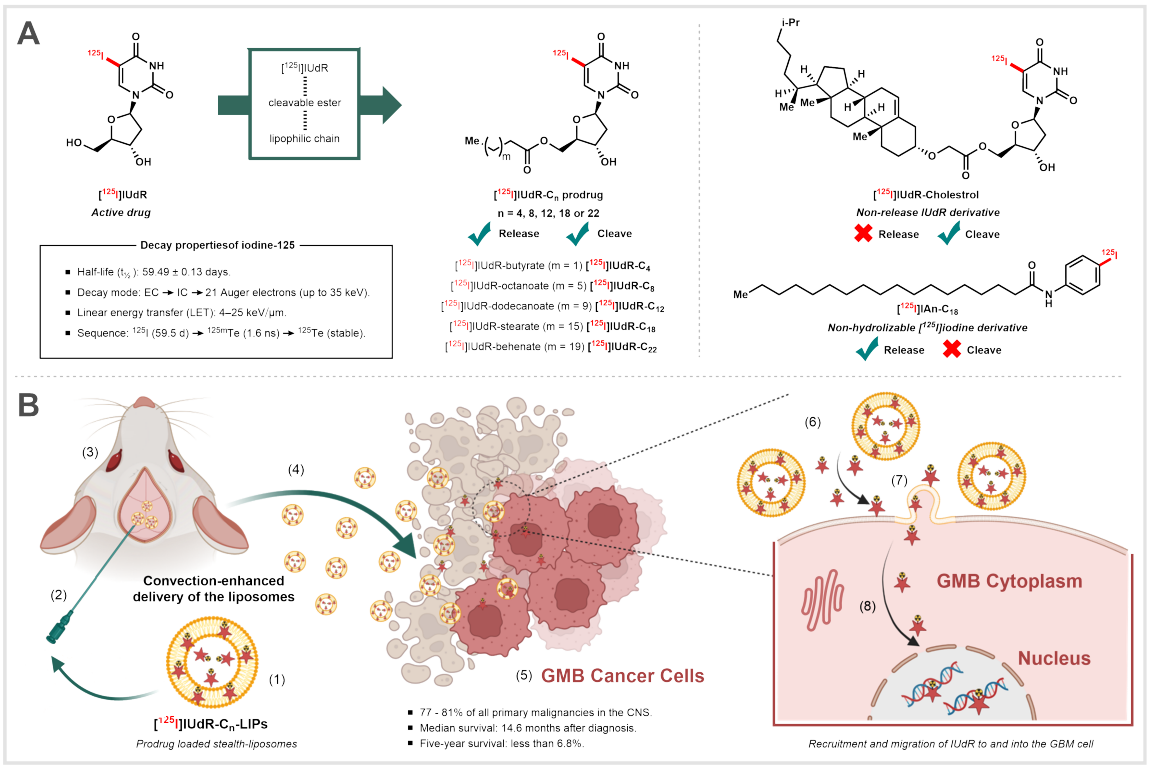

Figure 1. Rational design of the liposomal delivery platform. (a). The design of the [^{125}I]IUdR prodrugs for the object of efficient cleavage and release from the nanocarriers. (b). The illustration of the model-of-action of [^{125}I]IUdR-C$_n$-LIPs delivered to the cancer site.

2 Materials and methods

General considerations All reagents and solvents were bought from commercial suppliers; Sigma-Aldrich, ABCR Chemicals, FluoroChem or TCI Chemicals, and were used as received. Technical solvents were bought from VWR International and used as received. Solvents were distilled when necessary, following the procedures according to the method of Grubbs. Lyophilized esterase powder from porcine liver was obtained from Merck, 1 mg powder has 20 units(U) of esterase. Dulbecco's modified Eagle's medium (DMEM, high glucose) and fetal bovine serum (FBS) were obtained from Gibco and used as received. Celltiter Blue was purchased from Promega. All blank Salth liposome dispersions were produced using the Avanti mini-extruder with 100 nm filter.

Organic solutions were concentrated under reduced pressure on a Büchi rotary evaporator using a water bath. Flash column chromatography was performed by using Geduran Silica gel Si 60 (40-63 µm). Thin layer chromatography (TLC) was carried out on commercially pre-coated aluminium sheets (Merck Silica gel 60) and visualized using fluorescence quenching or relevant stain (e.g. $KMnO_4$, iodine, etc.). 1H-NMR and 13C-NMR spectra were recorded on a 400 MHz Bruker instrument using relevant deuterated solvents (e.g. $CDCl_3$ or DMSO-d6). Coupling constants are given in Hz. ^{1}H-NMR signals are reported in chemical shift (δ ppm), multiplicities are reported as; s = singlet, d = doublet, t = triplet, q = quartet, p = pentet, h = hextet, hept = heptet, m = multiplet, b = broad. ^{13}C-NMR signals are reported in chemical shift (δ ppm). Mass Spectrometry (MS) was measured on a Liquid Chromatography Shimadzu MS-2020 with an electrospray ionization spectrometer (ESI) or matrix-assisted laser desorption/ionization, coupled to a time-of-flight mass spectrometer (MALDI-TOF). HPLC analysis (HPLC) and radio-HPLC analysis were carried out on a Hitachi XYZ coupled with a XYZ autosampler injector coupled to a XYZ UV-VIS detector and a gamma-radio-detector (approx. 0.5 min signal delay).

The particle size and zeta potential (DLS) of the self-assembled micelles were measured by dynamic light scattering on a Malvern Zetasizer NANO ZS (Malvern Instruments Limited, UK) using a He-Ne laser -wavelength of 633 nm and a detector angle of 90°. Unless stated otherwise, particle size and zeta potential analysis were performed at 0.1 mg/mL in Phosphate-buffered saline (PBS, pH 7.4) at 25°C. Routine analysis of activity was performed on a Capintec CRC-55tR dose calibrator and reported in Becquerel (kBq or MBq). Liquid scintillation counting (LSC) measurements were performed on a HIDEX 425-034 LSC for routine analysis, or on a HIDEX 300-SL LSC for large batch analysis, and reported in Becquerel (kBq, MBq) or counts per minute (cpm). Radio TLC analysis was performed with a PerkinElmer Cyclone Plus phosphor imager on commercial pre-coated aluminium TLC sheets (4 x 10 cm, Merck Silica gel 60), and unless stated otherwise run in 10% MeOH in DCM and exposed overnight to a phosphor imaging plate. Unless stated otherwise, the radio chemical conversion (RCC) was determined by the following equation, RCC = (Radio chemical conversion TLC) x (Radio chemical conversion HPLC). The radiochemical yield (RCY) was calculated using the following, RCY = (Collected activity) / (Starting activity) x RCC.

Synthesis of IUdR references and [^{125}I]IUdR prodrug derivatives

General synthesis of IUdR-C$_n$ (n = 4, 8, 12 or 18) (2a, 2b, 2c or 2d). In a flask equipped with a stirring bar was placed iododeoxyuridine (**1**, 354 mg, 1.0 mmol) and alkyl carboxylic acid (mass determined by X, 2 mmol, 2 equiv.), followed by dissolution in DMF (15 mL). After this, the mixture was cooled down to 0 °C and DCC (216 mg, 1.05 mmol, 1.05 equiv.) was added in a single portion, together with a grain of N,N-dimethyl-4-aminopyridine (10 mg, 0.01 mmol). This flask was sealed with a rubber septum, the atmosphere was replaced with argon, and the mixture was stirred at 0 °C. After 3 hours, the reaction mixture was allowed to warm up to room temperature and stirred for another 18 hours. After complete consumption of iododeoxyuridine, the reaction was diluted with aq. LiCl (15 mL, 1.0 M), transferred to an extraction-funnel, and extracted with EtOAc (3 x 15 mL). The combined organic layers were collected and dried over $MgSO_4$ and then concentrated under reduced pressure. The crude was then further purified by silica column chromatography (0%-10% MeOH in DCM) to yield the title compound **2** as off-white solids ().

General synthesis of stannyl-IUdR-C$_n$ precursors (n = 4, 8, 12 or 18) (3). A flask with **2** (mass determined by starting material used, 0.2 mmol, 1 equiv.) in 1,4-dioxane (2 mL) and bis(triphenylphosphine) palladium dichloride (6 mg, 2.5 mol%). was prepared. The vial was sealed with a rubber septum, and argon was bubbled through the solvent for 10 minutes. To this solution was added, 1,1,1,2,2,2-hexabutyldistannane (256 mg, 0.44 mmol, 2.2 equiv.). The reaction mixture was heated to 120 °C and stirred for 12 hours. After this, the reaction mixture was cooled down to room temperature, diluted with EtOAc and filtered over a pad of Celite (0.5 cm). The combined organic layers were concentrated *in vacuo*, and further purified by silica column chromatography (0%-5% MeOH in DCM) to obtain the title compound **3** as an off-white solid (xyz% yield).

General radiosynthesis procedure of [^{125}I]IUdR-C$_n$ prodrugs (n = 4, 8, 12 or 18) ([^{125}I]2a – [^{125}I]2d). In a 2 mL HPLC-vial equipped with a small stirring bar was added a mixture of IUdR-stannyl precursor (0.13 - 0.17 µmol, 0.2 mg) in DMF (100 µL). To this was added in a sequential manner, acetic acid (5 µL), aq. chloramine-T solution (10 µL, 100 mg/mL) and then [^{125}I]NaI in 0.1 M NaOH (2-50 MBq). The vial was sealed with a screw cap and stirred for 30 min at 25 °C. After this, a solution of KI in H_2O (10 uL, 0.1 M) was added and the reaction was stirred for another 10 min at 25 °C. Hereafter, the reaction was terminated using a sodium meta-bisulfite solution (2 mg in 20 µL of H_2O). Hereafter, an aliquot was removed for radio-HPLC or radio-TLC analysis to give the radiochemical conversion (RCC).

Then, the reaction mixture was diluted with MeCN (2 mL) and transferred through a SiO_2 cartridge (Sep-Pak Silica Plus Light Cartridge, 120 mg sorbent per cartridge) and collected in different fractions of MeCN (1-3 mL) depending on the substrate or activity (see SI for more details). The mixture was then concentrated if needed, using a flow of nitrogen, a few vent-needles at a temperature of 65 °C. Then, the reaction mixture was diluted with H_2O (2-50 mL, with minimal amounts of MeCN depending on the compound, see specifics in the SI for details), taken up and trapped on a pre-activated C_{18} cartridge (Sep-Pak C_{18} Plus Short Cartridge, 360 mg sorbent). The C_{18} cartridge was slowly eluted with a series of MeCN/H_2O-mixtures to release the radio-iodinated compound from the cartridge; in consecutive order H_2O (2 mL), 20% MeCN in H_2O (2 mL), 70% MeCN in H_2O (2 mL), 100% MeCN (2 mL) or 100% EtOH (2 mL) were slowly eluted over the C_{18} cartridge (depending on the specific compound, see details below), and collected in different fractions. All fractions were analysed by radio-TLC. The desired fractions were collected and concentrated using a flow of N_2 (1 L/min) at 65 °C, with several ventilation needles. The obtained dried compound was analysed by dose-CAL, radio-TLC or radio-HPLC to give the final radiochemical yield and purity (typical yields, RCY = 65 ± 4%, RCP > 97 ± 2%, n > 25) and used directly for liposome loading (*vide infra*).

Preparation of [^{125}I]IUdR prodrug loaded liposomes ([^{125}I]IUdR-C$_n$-LIPs) by pre-insertion

In a glass vial with a stirring magnet, pre-mixed powder composed of HSPC:CHOL:DSPE-PEG_{2000} (14.68 mg, 3:1:1 mass ratio) and [^{125}I]IUdR-C_n (10 MBq, $1.2x10^{-6}$ mmol, mass range: 0.1- 1 mg) were dissolved in 1 mL of DCM/MeOH (2:1, v/v) and evaporated to dryness under a flow of argon at 70 °C for 30 mins. Using the thin film hydration method, the film was rehydrated with HEPES buffer (1 mL) for 1 hour at 65 °C and extruded by an Avanti® mini-extruder with 100 nm filter for 21 times at 65 °C to form single unilamellar vesicles (SUVs). Subsequently, the mixture underwent separation of the incorporated [^{125}I]IUdR-C_n-LIPs and non-incorporated [^{125}I]IUdR-C_n using a PD-10 desalting column (GE Healthcare) with HEPES buffer. The hydrodynamic diameter and size distribution of [^{125}I]IUdR-C_n-LIPs were determined by dynamic light scattering. Drug insertion efficiency (dI%) is calculated as the same as following: $dI\% = A_{final}/A_{initial} \times 100\%$. Where A_{final} is the final activity of [^{125}I]IUdR-C_n-LIPs. $A_{initial}$ is the initial activity of [^{125}I]IUdR-C_n prodrugs.

Preparation of [^{125}I]IUdR prodrug loaded liposomes ([^{125}I]IUdR-C$_n$-LIPs) by post-insertion 400 µL of radiolabelled [^{125}I]IUdR-C$_n$ (2 MBq, 1.2x10^{-6} mmol, mass range: 0.1- 1 mg) in MeCN was transferred to a glass vial and evaporated to dryness under argon flow for 30 mins at 70 °C. To this mixture, the pre-made blank Stealth liposome dispersion (32 mM, 1000 µL) was added and then incubated for 6 or 12 hours at 35 °C, 45 °C, or 55 °C under continuous stirring. Note that the molar ratio of the prodrug-to-lipid was below 5% in all cases. After incubation, the mixture of [^{125}I]IUdR-C$_n$-LIPs and [^{125}I]IUdR-C$_n$ were passed through a PD-10 size-exclusion chromatography column (GE Healthcare) with HEPES buffer to separate the [^{125}I]IUdR-C$_n$-LIPs from free [^{125}I]IUdR-C$_n$. The hydrodynamic diameter and size distribution of the loaded liposomes were determined by dynamic light scattering. Drug insertion efficiency (*dI%*) was calculated as above.

In vitro release of [^{125}I]IUdR from [^{125}I]IUdR-C$_n$-LIPs exposed to esterase Three HPLC vials containing [^{125}I]IUdR-C$_n$-LIPs dispersion (30 kBq, 1.0 mL) in iso-HEPES buffer were continuously stirred at 37 °C. Esterase powder (2 mg, 40 U) was dissolved in PBS (400 µL), resulting in a stock solution of 100 U/mL. Then to each vial, 10 µL of esterase stock solution was added for a final concentration of 1 U/mL. A series of aliquots (5 µL) were removed at different time points: 0, 0.5, 1, 3, 6, 24, 48, 168 and 336 hours, and then the aliquots were immediately mixed with THF (15 µL) to quench the enzymatic hydrolysis and dissolve the liposomes, which were then analyzed by radio-TLC. The ratios of [^{125}I]IUdR-C$_n$, [^{125}I]IUdR, and remaining unidentified spots (”others”) were quantified.

In vitro release of [^{125}I]IUdR from [^{125}I]IUdR-C$_n$-LIPs exposed to rat brain homogenate To obtain Brain homogenate (BH), rats were administered subcutaneous ketamine (100 mg/kg) and dexmedetomidine (0.5 mg/kg) for anesthesia. When the loss of response to painful stimuli was confirmed, the rats were then euthanized and their brains were promptly extracted and divided into four sections. Each section was then homogenized in 5 mL of PBS using a homogenizer. The resulting BH samples were stored at a temperature of -80 °C until further utilization. [50] Then BH (200 µL) was diluted 1:1 (v/v) with HEPES buffer (200 µL) in a HPLC vial. Penicillin-streptomycin solution (6 µL, 10,000 U/mL) was added, followed by [^{125}I]IUdR-C$_n$-LIPs dispersion in HEPES buffer (200 µL, 30 kBq). Then, aliquots (5 µL) were obtained at 0, 0.5, 1, 3, 6, 24, 48, 168, and 336 h and mixed with THF (15 µL) immediately after removal to quench the enzymatic hydrolysis and dissolve

the liposomes. All samples were analyzed by radio-TLC with ratios of [^{125}I]IUdR-C_n, free [^{125}I]IUdR and unidentified spots ('others') quantified.

Esterase mediated release in two compartments under simulated sink conditions A beaker with HEPES buffer (60 mL) was mixed with aq. esterase (600 µL, 100 U/mL) and stirred at 37 °C. Then a dialysis tube (MWCO 8-12 KDa) containing [^{125}I]IUdR-C_{18}-LIPs dispersion in HEPES buffer (2.0 mL, 265 kBq) was placed inside the beaker. Samples from the solution inside the dialysis tube (referred to as the "inside") and the surrounding solution in the beaker (referred to as the "outside") were sampled at 0, 0.5, 1, 3, 6, 24, 48, 168, and 336 hours in aliquots of 5 µL and 400 µL, respectively. The radioactivity of the samples was subsequently analyzed and calculated by liquid scintillation counting (LSC).

In vitro cell viability assay LN-229 cells were grown in DMEM growth medium with a pH = 7.4, supplemented with 10% FBS, 100 U/mL of penicillin, 2 mM glutamine, and 100 µg/mL of streptomycin according to supplier instructions. Cell cultures were maintained in flasks and grown at 37 °C in a humidified atmosphere of 5% CO_2 in air.

In vitro cytotoxicity of [^{125}I]IUdR-C_{18}-LIPs against LN-229 cells was determined by a cell viability assay using CellTiter-Blue from Promega. Briefly, cells were seeded in 96-well plates, 300 cells/well, and incubated for 24 hours at 37 °C in an incubator. Samples were grouped to evaluate cytotoxicity as (1) [^{125}I]IUdR-C_{18}-LIPs with/without esterase, (2) [^{125}I]IUdR-C_{18} prodrug with/without esterase, (3) [^{125}I]IUdR, and (4) IUdR-C_{18} prodrug with/without esterase. Appropriate amounts of [^{125}I]IUdR-C_{18}-LIPs, [^{125}I]IUdR-C_{18} (dissolved in DMSO) and [^{125}I]IUdR were diluted with complete DMEM culture medium to achieve the desired final radioactivity of 0.23, 0.49, 0.98, 1.97, 3.75, 7.5, 15, and 30 kBq/mL. The concentrations (µg/mL) of the negative control groups containing non-radiolabelled IUdR-C_{18}-LIPs and IUdR-C_{18} prodrug were the same as the corresponding radiolabelled groups. All groups with added esterase (E) were introduced post sample preparation and maintained a consistent concentration of 0.1 U/mL. The plates were incubated for 7 days before mixed with CellTiter-Blue solution (20 µL). After a 4 h incubation, the absorbance was recorded by microplate reader at 570 and 600 nm. The results were expressed as % cell viability = (mean optical density (OD) of treated cells/mean OD of untreated cells) × 100%.

In vitro clonogenic assay Flasks with 2× 10^5 cells per flask were cultured and applied to [^{125}I]IUdR-C_{18}-LIPs+E, [^{125}I]IUdR or free iodine-125 for two days with the activity of 0, 0.125, 0.25, 0.5, 1, 2 kBq/mL, respectively. Then the flasks were harvested individually and reseeded into new flasks at densities of 100, 100, 200, 250, 600, and 1000 cells per flask. While flasks treated with free iodine-125 were seeded at 100 cells per new flask. These densities corresponded to the aforementioned activity concentrations above ranging from 0 to 2 kBq/mL. The flasks were incubated for another 14 days, after which the cells were fixed and stained with crystal violet for 2 hours, the flasks were washed with water and air-dried. Visible colonies containing at least 50 cells were manually counted under a microscope. Plating Efficiency (PE) and Surviving Fraction (SF) were defined as: PE=Number of colonies counted / Number of cells seeded; SF = Number of colonies counted after treatment/ (Number of cells seeded* PE).

In vitro DNA incorporation LN229 cells were seeded in 24-well plates (200,000 cells/well). The following day, 18.5 kBq/mL[^{125}I]IUdR-C_{18}-LIPs and 1U/mL esterase was added to the cells and incubated for 4, 7 or 24 h. After incubation, the cells were washed twice in PBS and twice in 5% trichloroacetic acid (TCA, Sigma-Aldrich). TCA fractions were collected to determine unincorporated [^{125}I]IUdR and cells were solubilized with 1 M sodium hydroxide and harvested to determine incorporated [^{125}I]IUdR. The amount of unincorporated and incorporated [^{125}I]IUdR was determined in a 2470 Wizard Automatic Gamma Counter (Perkin Elmer) and compared to total amount of added activity.

In vivo DNA incorporation and SPECT/SCT scan of C_{18}-125I-UdR in tumor-bearing mice Without other statements, all animal experiments were approved by the Experimental Animal Committee of The Danish Ministry of Justice (2022-15-0201-01159) and were performed at the animal core facility at the University of Southern Denmark, Denmark. Animals were housed under pathogen-free conditions with ad libitum food and water and acclimatized for a minimum of one week before used in experiments.

11 weeks old CB17 SCID mice (Janvier) were. For cell implantation, the mice were anesthetized with a mixture of hypnorm/midazolam subcutaneously. Animals were placed in a stereotactic frame (Model 900, David Kopf Instruments, Tujunga, USA) and a midline scalp incision was made and a burr hole was made one mm anteriorly and two mm laterally to bregma. A 2 µl cell suspension of 300,000 U87 cells in Hank's Balanced

Salt Solution (HBSS, Gibco) was slowly injected at a depth of 3.5 mm. Sixteen days after, the mice were anaesthetized and fixated as described above and the midline incision was re-incised and the burr hole was identified and 25 µl C_{18}-[^{125}I]IUdR-LIPs (approx. 9 MBq/mL) or *N*-(4-iodophenyl)stearaylamide (15 MBq/mL), a mock compound that cannot integrating to DNA (see SI for more information), was injected slowly. Tumors were homogenized and DNA was purified after 2 days and 5 days of injection using DNeasy Blood & Tissue (Qiagen). The standard protocol from the kit was followed. SPECT/SCT scans were conducted only with C_{18}-[^{125}I]IUdR-LIPs (approx. 9 MBq/mL) after 1, 48 and 120 hours of injection, animals were euthanized before scan due to the low amount of activity.

In vivo biodistribution 5-7 weeks old male athymic nude rats (rnu/rnu) (Charles River) were anesthetized with a mixture of hypnorm/midazolam subcutaneously. Animals were placed in a stereotactic frame (Model 900, David Kopf Instruments, Tujunga, USA) and a midline scalp incision was made and a burr hole was made one mm anteriorly and two mm laterally to bregma. A 2 µl cell suspension of 300,000 T87 cells (patient-derived cell line) in HBSS supplemented with 0.9% glucose (SAD 500 mg/ml) was slowly injected at a depth of 3.5 mm. Twenty days later, the rats were anaesthetized and fixated as described above and the midline incision was re-incised and the burr hole was identified and 25 µl C_{18}-[^{125}I]IUdR-LIPs (range: 62-92 kBq, average: 82.625 kBq). *In vivo* biodistribution was performed 6 h and 24 h post-injection (p.i.). Organs were measured with a 2470 Wizard Automatic Gamma Counter (Perkin Elmer).

3 Results and discussion

Synthesis of [^{125}I]IUdR lipidized prodrugs

The first step was to prepare the non-radioactive prodrug compounds **2** (**Scheme 1**). Here the 5'-hydroxyl group of the deoxyribose was functionalized with a fatty acid chain via an ester linkage. This was done by reacting commercially available iododeoxyuridine (IUdR) with the corresponding carboxylic acid under dehydrating conditions using dicyclohexanecarbodiimide (DCC) and sub-stoichiometric amounts of dimethylaminopyridine (DMAP) as base in DMF, giving 25-53% yield. With the reference compound **2** in hand, the iodine was converted to the corresponding tributylstannyl group, using 10 mol% $Pd(Ph_3P)_2Cl_2$ and *bis*(tributylstannane) in 1,4-dioxane at 120 °C. This gave compound **3** in a fairly straightforward manner, albeit in low yield (27-35%).

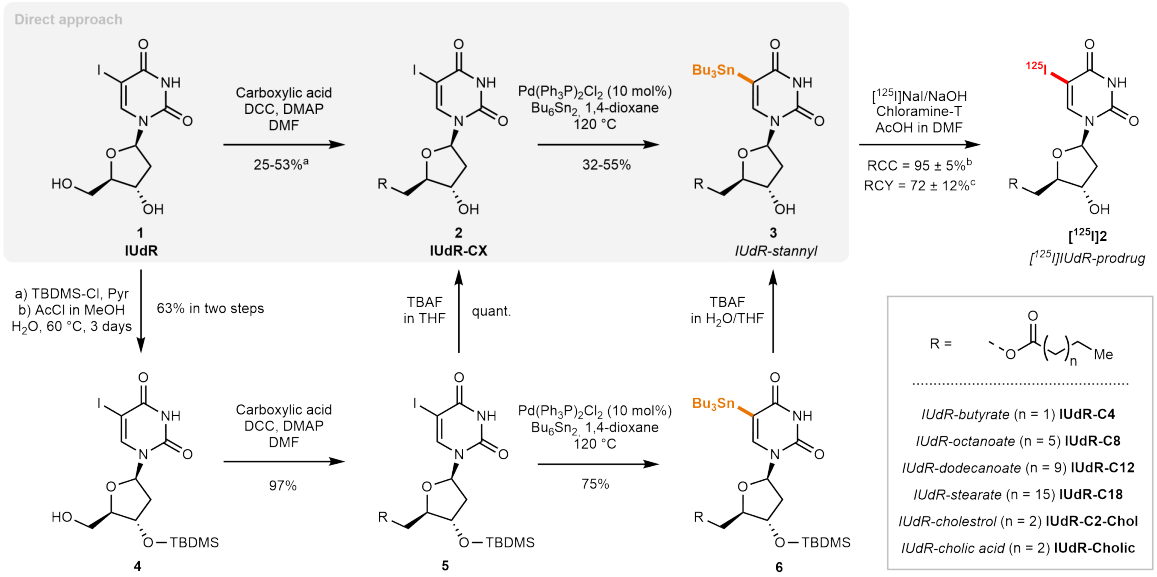

Scheme 1. Overview of chemical synthesis of the different IUdR derivatives. *Direct approach (highlighted box):* two-step preparation of IUdR non-radioactive references (**2a** – **2e**, IUdR-C_n) and the stannyl precursors (**3a** – **3e**, IUdR-stannyl). *Protecting group approach (non-highlighted):* multi-step protecting group preparation of IUdR non-radioactive references and the stannyl precursors (*vide infra*).

The yield in both steps were rather low (25-53% and 27-35%, respectively), and therefore an alternative route was carried out. Here, IUdR was first mono-protected on the 3'-hydroxyl group by a consecutive *bis*-protection of both hydroxyl groups, followed by a selective liberation of the 5'-hydroxyl group under mild anhydrous acidic conditions using sub-stoichiometric amounts of acetyl chloride in MeOH at 60 °C. This two-step procedure

gave easy access to mono-protected compound **4** (63% yield in two steps). Similarly, to above, compound **4** could then be functionalized with the lipid through an ester linkage, which afforded the desired product in excellent yield (97%). At this junction, the TBDMS protection group could be removed by treating compound **5** with TBAF in THF . This gave rise to compound **2** in much better overall yield than the above-mentioned procedure, albeit in more steps (61% overall yield in four steps). Alternatively, compound **5** can be used to prepare the stannyl derivative **3**. Subjecting **5** to catalytic amounts of $Pd(Ph_3P)_2Cl_2$ with *bis*(tributylstannane) in 1,4-dioxane at 120 °C gave stannyl **6** in good yield (75%). The TBDMS protecting group could now be removed which gave the final precursor **3** in much better yield than the earlier mentioned procedure (46% overall yield in five steps, as opposed to 12% overall yield in two steps). Arguably, the longer route is excessive when preparing only small amounts of reference and precursor compounds. However, the synthesis of alternative derivatives (see below) is greatly relieved using mono-protected compound **4** as the starting material, as opposed to the *direct* synthesis of the other prodrugs directly from IUdR.

With this framework in hand, the other IUdR derivatives (C_4, C_8, C_{12},C_{18}) could be prepared in a straightforward manner (Entries 2-5, **Table 1**). In addition, control compound **[^{125}I]IAn-C_{18}** ([^{125}I]4-iodophenyl-*N*-stearamide) was also prepared following the relevant synthetic steps (62% yield).

Table 1. Overview of IUdR prodrug synthesis, and radiochemistry

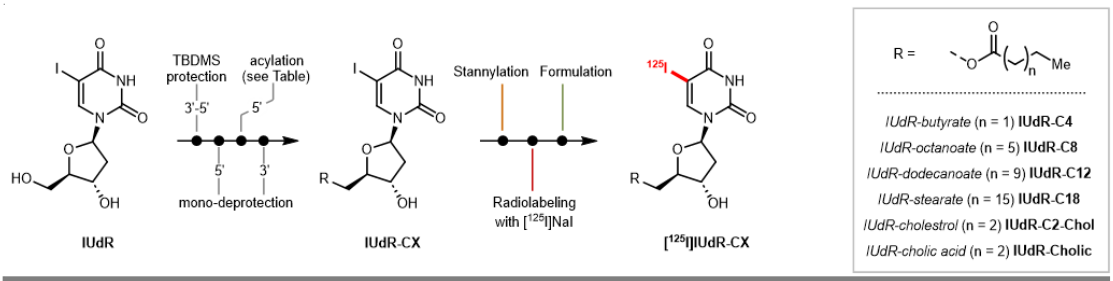

Entry[a]	Compound	Acylation		Stannylation		125I-iodination	
		Via **1**	Via **5**[b]	Via **2**	Via **6**[c]	RCC[d]	RCY[e]
1	C_0	-	-	-	-	99 ± 1% (n = 4)	96 ± 2% (n = 4)
2	C_4	45%	95% (71%)	55%	55%	96 ± 4% (n = 4)	94 ± 4% (n = 4)
3	C_8	23%	93% (70%)	45%	45%	97 ± 2% (n = 4)	83 ± 2% (n = 4)
4	C_{12}	35%	85% (64%)	32%	66%	99 ± 1% (n = 4)	64 ± 1% (n = 4)
5	C_{18}	53%	97% (73%)	35%	61%	99 ± 1% (n = 4)	71 ± 1% (n > 25)
6	IAn-C_{18}	n.a.	n.a.	n.a.	62%	98 ± 1% (n = 2)	95 ± 1% (n = 2)

[a]See methods section for full details on reagents and conditions. [b]Overall yield in four steps between parentheses. [c]Overall yield in five steps. [d]Radio chemical conversion (RCC) based on radio-TLC analysis (see SI). [e]Radio chemical yield (RCY) based on activity (MBq) after purification and reformulation (end of synthesis), and non-decay corrected (ndc). Abbreviations: n.a. = not applicable, because of different synthetic procedure.

Radioiodinationprocedures

The iodine-125 isotopologues of the IUdR-C_n derivatives were prepared using a standard [^{125}I]iododestannylation procedure. IUdR-stannyl precursor **3** (0.13 - 0.17 µmol, 0.1 mg in 100 µL DMF) was treated with chloramine-T in the presence of [^{125}I]NaI/NaOH (5.0 - 250 MBq, see SI for details), under acidic conditions in the presence of AcOH. This gave radio-iodinated **[^{125}I]2** in quantitative amounts with typical RCCs of 99 ± 1% (see **Table 1**). The radio-iodinated compound was then purified by trapping it on a Waters C_{18}-cartridge, with subsequent release using a variety of different elution mixtures of MeCN and H_2O, depending on compound polarity (see SI for details). This provided **[^{125}I]2** in RCYs of 71 ± 1% (n = 4) after reformulation, and RCP > 99%, as judged by radio-TLC and radio-HPLC (A_M = 0.03 - 1.67 GBq/µmol). The compound was then reformulated into EtOH for further use. This standardized procedure allowed us to prepare all radio-iodinated [^{125}I]IUdR-C_n derivatives (see **Table 1** for an overview of obtained RCYs) at activity levels (up to 250 MBq of [^{125}I]NaI) required for further studies. **Table 2** presented the lipophilicity properties of the [^{125}I]IUdR-C_n derivatives.

It should be noted that unreacted stannyl-IUdR precursor or activated [^{125}I]Iodine was sequestered by quenching the reaction mixture with aqueous non-radioactive potassium io-

Table 2. Lipophilicity parameters of [^{125}I]IUdR-C_n prodrugs and analogues

Entry[a]	Compound	pKa[a]	$LogD_{lit}$	$LogD_{comp}$	$LogD_{meas}$	LogM
			(pH = 7.4)	(pH = 7.4)	(pH = 7.4)	(cm s^{-1})
1	C0	7.7	-0.96	-0.60	-1.16 ± 0.05	-4.8
2	C_4	7.7	-	+0.98	+0.62 ± 0.02	-2.3
3	C_8	7.7	-	+2.76	+1.54 ± 0.05	-1.0
4	C_{12}	7.7	-	+4.54	+2.11 ± 0.02	-0.2
5	C_{18}	7.7	-	+7.21	+6.51 ± 0.07	+0.5

[a]$LogD_{lit}$, $LogD_{comp}$ and $LogD_{meas}$; are from literature (Ref.), calculated, or measured, respectively. [b]pKa are based on the most acidic proton. [c]Values between parentheses are estimated values. LogD values are taken or measured with a pH = 7.4 (PBS buffer). LogM values are calculated compound *lipid-permeability* (with COSMOS)

dide ([^{127}I]KI in H_2O) and aqueous sodium metabisulfite ($Na_2S_2O_5$), subsequently. This addition of non-radioactive iodide rendered the formal molar activity (A_M) modest (0.03 - 1.67 GBq/µmol). It is generally advantageous that radiopharmaceutical compounds possess a high A_M. This is required to avoid saturation of the target which would result in an higher degree of off-target dose. [52] Nevertheless, we believe this to be less relevant with [^{125}I]IUdR, since this compound is inserted into the DNA. Moderate A_M [^{125}I]IUdR-C_n (*vide infra*) was therefore considered effective enough for the planned *in vitro* and *in vivo* studies and was therefore used without further purification.

Loading of [^{125}I]IUdR-C_n prodrugs into liposomes

Upon obtaining the [^{125}I]IUdR-C_n prodrugs, we commenced with the insertion of these prodrugs into liposomes to produce the final product [^{125}I]IUdR-C_n-LIPs. We started with the evaluation of different loading strategies using Stealth liposomes as the nanocarriers. Liposomes were prepared using dehydration of premixed lipid powders (HSPC:CHOL:DSPE-PEG_{2000}, 3:1:1 mass ratio) at 65 °C for 1 hour then mechanically extruded to form the SUVs. It resulted in an average diameter of 120.45 ± 10.5 nm, a PDI of 0.085 ± 0.015, and a lipid content of 32.3 mM after extrusion. We studied two drug loading methods, pre-insertion, and post-insertion, with differences in incubation time and temperatures. The key difference between them is the timing of drug loading: pre-insertion occurs during liposome formation, while post-insertion occurs after liposome formation. With the pre-insertion strategy, a high drug-insertion yield (drug-loading, dl%) can be achieved. While for post-insertion, radiation exposure will be limited but the loading yield can be lower. Both methods were screened to establish a simple, fast, and safe way to load [^{125}I]IUdR-C_n prodrugs while maintaining a high drug loading. Post-insertion of [^{125}I]IUdR-C_n (10 MBq,) in the li-

posomal bilayer was performed at a temperature of 35 °C (**Figure 2a**). After 12 hours incubation, the mixture was purified using a PD-10 size-exclusion column to remove unincorporated [^{125}I]IUdR-C_n compound from the liposome mixture. [^{125}I]IUdR-C_4 and [^{125}I]IUdR-C_8 showed poor insertion and only 8 ± 1% and 18 ± 2% (n = 4) insertion was obtained for [^{125}I]IUdR-C_4 and [^{125}I]IUdR-C_8, respectively. Owning much lower lipophilicity than the other [^{125}I]IUdR derivatives with higher degree of carbon-chain length (**Table 2**, LogD < +2.7 for C_8 and C_4), it is reasonable to accommodate the low insertion to the poor lipophilicity of the [^{125}I]IUdR-C_4 and [^{125}I]IUdR-C_8 derivatives. However, the [^{125}I]IUdR-C_{12} and [^{125}I]IUdR-C_{18} derivatives yielded substantial drug insertion, 68 ± 5% and 78 ± 2% (n = 4) drug insertion respectively, warranting the continued use of the [^{125}I]IUdR-C_{12} and [^{125}I]IUdR-C_{18} derivatives for the post-insertion strategy.

A post-insertion strategy of [^{125}I]IUdR-C_n into liposomes was also carried out (**Figure 2b**). Typically, a homogeneous solution of [^{125}I]IUdR-C_n (0.5 MBq) with HSPC:CHOL:DSPE-PEG_{2000} (3:1:1 weight ratio) in DCM/MeOH was prepared, then evaporated to a uniform film under a flow of argon, and re-hydrated by adding ISO-HEPES (1 mL, pH = 7.4), and then stirred for an hour, subsequently. After extrusion, the loaded Stealth liposomes were purified using a PD-10 size-exclusion column. As depicted in **Figure 2b**, [^{125}I]IUdR-C_4, [^{125}I]IUdR-C_8 and [^{125}I]IUdR-C_{18}, resulted in low to average insertion at 7 ± 1%, 47 ± 4% and 49 ± 2% loading, respectively (n = 4). However, pre-insertion of [^{125}I]IUdR-C_{12} resulted in a more effective loading of 83 ± 6% (n = 4), approximating almost quantitative incorporation. Notably, pre-insertion of [^{125}I]IUdR-C_{18} showed significant lower insertion than post-insertion of [^{125}I]IUdR-C_{18} (49 ± 2% vs. 78 ± 2%, respectively), which might be related to the poor aqueous solubility of [^{125}I]IUdR-C_{18} (logD = +7.21), might form aggregates of [^{125}I]IUdR-C_{18} which result in *sluggish* liposome insertion. Moreover, [^{125}I]IUdR-C_{12} may have yielded better pre-insertion loading than [^{125}I]IUdR-C_{18} due low solubility of [^{125}I]IUdR-C_{18} in ISO-HEPES at room temperature.

Hereafter, we further screened the loading parameters at different temperatures (35 °C, 45 °C and 55 °C) and mixing time (6 and 12 hours) to determine more optimal conditions for post-insertion (**Figure 2c - 2d**). Under all tested conditions (temperature and time), the insertion efficiency of [^{125}I]IUdR-C_8 into Stealth liposomes was inefficient (dI% < 10%, see SI **Figure S4**). In contrast, as can been seen in **Figure 2c** and **2d**, loading of [^{125}I]IUdR-C_{12} and [^{125}I]IUdR-C_{18} prodrugs into liposomes under the same conditions was more efficient (up to 95% incorporation). Notably, for the [^{125}I]IUdR-C_{12} prodrug there was no significant

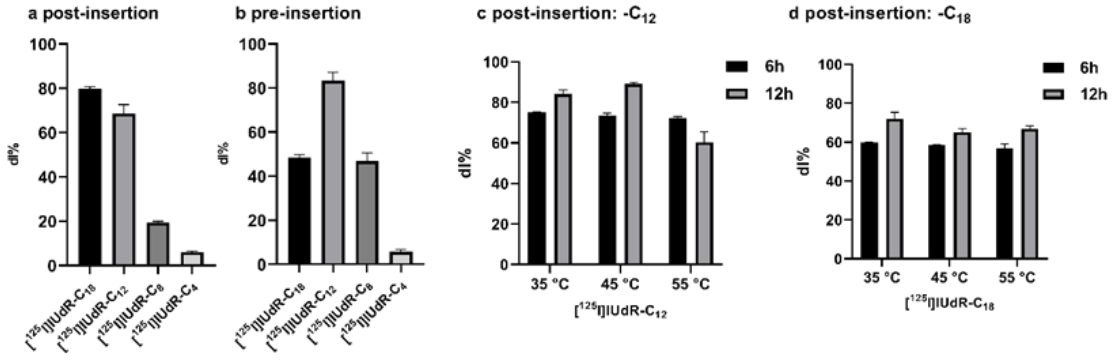

Figure 2. Loading efficiency (dl%) of [^{125}I]IUdR-C_n prodrugs into liposomes (n = 4, 8, 12 and 18). (a-b) Insertion efficiency of [^{125}I]IUdR-C_4, -C_8, -C_{12} and -C_{18}, pre-and post-insertion into liposomes, and post-insertion was conducted at 35 °C and incubation for 12 hours (see SI for more details). (c-d) Insertion efficiency of [^{125}I] IUdR-C_{12} and -C_{18}, by post-insertion into liposomes at different temperatures and incubation time (see SI for more details). Error bars shown are SD.

effect between the temperatures 35 °C and 45 °C (80 ± 5% and 82 ± 7%, respectively), and the loading at 55 °C was slightly lower (66 ± 6%). The post-insertion loading of [^{125}I]IUdR-C_{18} was similar at all tested temperatures (66 ± 7%, 62 ± 3% and 62 ± 5%, respectively at 35 °C, 45 °C and 55 °C). In contrast to temperature, time dependency was more noticeable (**Figure 2c - 2d**). The [^{125}I]IUdR-C_{12} prodrug showed an average increase of 12.5% in insertion efficiency after 12 hours compared to 6 hours, excluding the loading at 55 °C. The more lipophilic [^{125}I]IUdR-C_{18} prodrug exhibited an average increase of 10% in loading efficiency after 12 hours of incubation compared to 6 hours. It should be noted that an increased solubility of the [^{125}I]IUdR-C_n prodrug at higher temperatures may appear beneficial, the opposing loading-release kinetics (migration in between the buffer media, and the liposomal bilayer interface) at these temperatures may adversely hamper insertion efficiencies under post-insertion conditions.

Based on these results, we identified the optimal conditions for post-insertion of [^{125}I]IUdR-C_{12} and [^{125}I]IUdR-C_{18} as an incubation temperature of 35 °C for a duration of 12 hours. However, for the other compounds that were included in this study, this method was found to be unsuitable. The varying lipophilicity of the prodrugs may account for this discrepancy, indicating that alternative methods or approaches should be explored to reach high loading yields in future studies.

Based on these observations, pre- and post-insertion were not efficient enough for [^{125}I]IUdR-C_8 and C_4 insertion into liposomes (dl% < 25%). In contrast, both methods were effective for the more lipophilic compounds [^{125}I]IUdR-C_{12} and C_{18}. On average, the pre-insertion strategy was slightly less efficient than the post-insertion incorporation strategy (72 ± 20% and 74 ± 6%, respectively). Both methods provided similar drug insertion for [^{125}I]IUdR-C_{12} and [^{125}I]IUdR-C_{18}. On this basis, we chose to prepare [^{125}I]IUdR-C_n-LIPs by post-insertion due to its operational flexibility and ability to avoid radioactive mechanical extrusion during the procedure, and deemed easier to implement in the production of a radiopharmaceutical.

Esterase mediated in vitro release from [^{125}I]IUdR-C_n-LIPs

Liposomes containing [^{125}I]IUdR-C_4, -C_8, -C_{12}, and -C_{18} prodrugs were prepared using the post-insertion method described above. We investigated the release of [^{125}I]IUdR from [^{125}I]IUdR-C_n-LIPs in a HEPES buffer containing esterase as well as in HEPES buffer mixed with rat-brain homogenate in a 1:1 ratio. This study indicated that hydrolysis of the [^{125}I]IUdR-C_n prodrugs in PBS buffer without esterase was sluggish , indicating the necessity of esterase to enable the release of [^{125}I]IUdR. Consequently, *in vitro* release assays were conducted by mixing esterase (1.0 U/mL) with liposomes loaded with [^{125}I]IUdR-C_4, -C_8, -C_{12} and -C_{18}, dispersed in HEPES buffer. The release efficiency was evaluated according to the observed ratios of [^{125}I]IUdR-C_n, [^{125}I]IUdR and other unidentified ^{125}I-labeled species (“others”, green lines in **Figure 3**).

For liposomes loaded with [^{125}I]IUdR-C_8 and [^{125}I]IUdR-C_{12}, we observed them to have very similar esterase-meditated release rates (**Figure 3a** and **3b**). Both [^{125}I]IUdR-C_8 and [^{125}I]IUdR-C_{12} were completely consumed within the first 3 hours and [^{125}I]IUdR was the only release-product observed during this time. For [^{125}I]IUdR-C_{12}, after 6 hours we observed the presence of an unknown substance other than [^{125}I]IUdR (**Figure 3b**, green line). It was noticed that the increase of this unknown substance was correlated with a decrease in [^{125}I]IUdR. Overall, it is noteworthy that C_8 and C_{12} exhibited slower hydrolysis rates than C_4. However, the release rate of [^{125}I]IUdR was still fast as all the prodrugs were entirely hydrolysed within 3 hours of admission, which is too fast for glioblastoma cellular growth and isotope decay (*vide infra*). [^{125}I]IUdR has a relative short bio-survivability in blood, both in humans and in mice (5 and 7 minutes, respectively).[51–53] Consequently, when the release of [^{125}I]IUdR from C_8 or C_{12} approaches complete release within 3 hours, it can be inferred that a significant quantity of [^{125}I]IUdR will be eliminated from the target area before cellular uptake. In this case, the therapeutic efficiency will be diminished, highlighting the importance of a slower release rate.

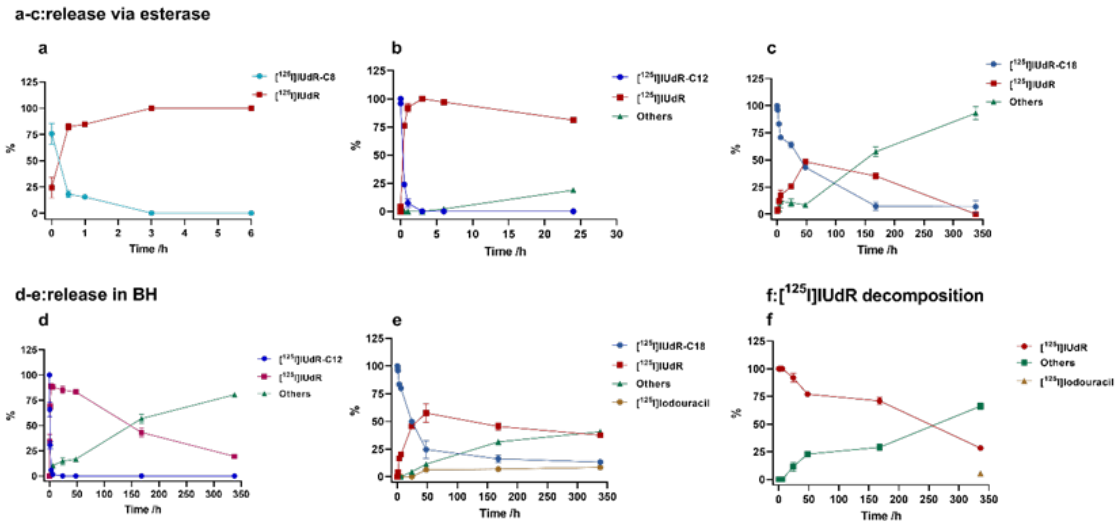

Figure 3. Release of [^{125}I]IUdR from [^{125}I]IUdR-C_n-LIPs (n = 0, 8, 12 and 18). a-c) Esterase mediated release and decomposition of [^{125}I]IUdR from [^{125}I]IUdR-C_n-LIPs. a) [^{125}I]IUdR-C_8-LIPs, b) [^{125}I]IUdR-C_{12}-LIPs, c) [^{125}I]IUdR-C_{18}-LIPs. d-e) Release and decomposition of [^{125}I]IUdR from [^{125}I]IUdR-C_n-LIPs in brain homogenate, d) [^{125}I]IUdR-C_{12}-LIPs. e) [^{125}I]IUdR-C_{18}-LIPs. and f) Decomposition of [^{125}I]IUdR. The time point for the termination of the release experiment was either when [^{125}I]IUdR is completely released or after 336 hours (14 days).

The most lipophilic compound, [^{125}I]IUdR-C_{18}, showed the slowest rate of [^{125}I]IUdR release (**Figure 3c**). Within the first 30 minutes, only 30% of [^{125}I]IUdR-C_{18} was hydrolyzed, which was significantly slower than for the C_8 and C_{12} prodrug loaded liposomes. Further incubation showed 60% [^{125}I]IUdR-C_{18} consumption after 2 days, and 92% after 7 days. Notably, the difference in the time to reach a [^{125}I]IUdR plateau (red line) for [^{125}I]IUdR-C_{18} hydrolysis was 16 times longer than for C_8 and C_{12}. This supports that [^{125}I]IUdR-C_{18} exhibits extended residence in the liposomal membrane due to the higher lipophilicity of the C_{18} prodrug-anchor. This therefore enables a more continuous release of [^{125}I]IUdR for a longer period of time. Gratifyingly, the [^{125}I]IUdR concentration reached a plateau at around 50% after 2 days and remained at an elevated concentration over the next 5 days (on average 35%, **Figure 3c**, red line). Similar to the C_{12} release profile (**Figure 3b**), an unknown radioactive compound emerged during the release from C_{18} loaded liposomes (**Figure 3c**, green line). Because of this observation, we speculated whether these unknown radioactive compounds were directly derived from [^{125}I]IUdR or a by-product of general degradation of the radioactive species. Therefore, a [^{125}I]IUdR degradation experiment in the presence of esterase was carried out to see whether these unknown radioactive compounds could emerge directly from [^{125}I]IUdR (**Figure 3f**). After two weeks, the same degradation products were observed and nearly 70% was detected after this time, with only 30% of [^{125}I]IUdR left (**Figure 3f)**. Accordingly, the observed degradation of released ^{125}I]IUdR was at least partially mediated by the esterase or impurities in the esterase. According to literature, a major decomposition product of IUdR, by X-ray induced radiolysis is deoxyuridine and iodouracil.[36,37] Iodouracil is similar to thymine and uracil, both of which still participate in DNA and RNA replication processes of cells, and can thus still have a cytotoxic effect.[57] Therefore, we assessed that one of the unknown radioactive compounds could be [^{125}I]iodouracil. Cross-validation of iodouracil and [^{125}I]iodouracil using radio-TLC indeed confirmed the presence of [^{125}I]iodouracil.

In summary, we demonstrated that [^{125}I]IUdR-C_n-LIPs are capable of releasing [^{125}I]IUdR. The rate of release of [^{125}I]IUdR from the different [^{125}I]IUdR-C_n-LIPs varies, depending on simulated biophysical environment (e.g. enzymes, or tissue homogenate), and by the lipophilicity of the prodrug-anchor (C_4, C_8, C_{12} and C_{18}).

Release from [^{125}I]IUdR-C$_n$-LIPs in rat brain homogenate

A range of endogenous enzymes, including esterases and phosphatases, are present in the brain tissue.[54] Accordingly, we used rat brain homogenate to simulate release conditions in the living brain. In the above-described esterase-meditated release assay we observed that [^{125}I]IUdR-C$_{18}$-LIPs and [^{125}I]IUdR-C$_{12}$-LIPs had the best suited release profiles. Consequently, we continued the [^{125}I]IUdR release study in rat brain homogenates for [^{125}I]IUdR-C$_{12}$-LIPs and [^{125}I]IUdR-C$_{18}$-LIPs (see SI for detailed descriptions). In rat brain homogenate mixed with HEPES buffer, we observed that liposomal [^{125}I]IUdR-C$_{12}$ was completely consumed within 24 hours, with more than 95% consumed within the first 6 hours **(Figure 3 d)**. At the same time, [^{125}I]IUdR increased at a rapid rate during the first hours and reached a plateau at 90% after 3 hours. After this, the [^{125}I]IUdR concentration declined steadily, as was also observed in the esterase studies described above. These results demonstrated that liposomal [^{125}I]IUdR-C$_{12}$ in brain homogenate resulted in release of [^{125}I]IUdR, albeit very rapid (90% in 3 hours).

However, in comparison to the earlier described esterase-mediated [^{125}I]IUdR release, it was noticed that the release of [^{125}I]IUdR peaked within the first 3 hours. With this observation, liposomes loaded with [^{125}I]IUdR-C$_{12}$ was not an optimal contender, due to this *burst-release* of [^{125}I]IUdR *in vivo*. Therefore, a more gradual release is vital to avoid unnecessary *in vivo* attrition of [^{125}I]IUdR in order to maintain its therapeutic effect. On the other hand, [^{125}I]IUdR-C$_{18}$-LIPs showed a slower release of [^{125}I]IUdR (**Figure 3e**). In the first 6 hours of incubation, only 40% of [^{125}I]IUdR was observed. Continued incubation revealed a steady release of [^{125}I]IUdR, with 60% released after 2 days, and 85% after 2 weeks. Moreover, [^{125}I]IUdR reached a plateau at around 60% [^{125}I]IUdR after 3 days and remained above 40% over 2 weeks (**Figure 3e**, red line). Compared with esterase-mediated hydrolysis of [^{125}I]IUdR-C$_{18}$, [^{125}I]IUdR release in brain homogenate had a similar and consistent pattern. An almost identical release rate of [^{125}I]IUdR in the first 2 days was observed, and maximal concentration of free [^{125}I]IUdR was also similar (50% to 60% released [^{125}I]IUdR). The difference was that [^{125}I]IUdR in BH was greater than in PBS with esterases. Notably, after 14 days, 40% of [^{125}I]IUdR was still present in homogenate. While in PBS with esterases [^{125}I]IUdR was completely degraded after 2 weeks. This release behaviour of [^{125}I]IUdR was considered preferable to the faster observed release from [^{125}I]IUdR-C$_{12}$-LIPs. Despite the lower plateau level for [^{125}I]IUdR, C$_{18}$ took longer to reach this plateau than C$_{12}$ (72 hours versus 3 hours, respectively).

Similar to our observations with esterase-mediated release experiments, we also observed radioactive substances that were not [^{125}I]IUdR-C_n, [^{125}I]IUdR, or [^{125}I]iodouracil in the brain homogenate release assays (**Figure 3d** and **3e**, green lines). These unknown substances reached activity ratios of 48% and 80% in 1 and 2 weeks, respectively. We cross-referenced radio-TLC R_f values of iodouracil and [^{125}I]iodouracil and quantified [^{125}I]iodouracil in the C_{18} brain homogenate release assay(**Figure 3e**, khaki line). After 14 days, [^{125}I]iodouracil reached about 10% abundancy. In brain homogenate, the appearance of additional radioactive species was also observed. The higher presence of various enzymes and cellular structures in brain homogenate as compared to esterase isolate, likely account for these additional [^{125}I]-species (others, **Figure 3f**).

Proposed mechanism of [^{125}I]IUdR release from liposomes

With the release studies conducted, we investigated the mode-of-release of [^{125}I]IUdR from the liposomes. Based on the stability analysis presented in **Figure S2**, only 3% of [^{125}I]IUdR was identified after 7 days from [^{125}I]IUdR-C_{18}-LIPs (no esterase added), indicated that the hydrolysis of the [^{125}I]IUdR-C_{18} in [^{125}I]IUdR-C_{18}-LIPs was limited and slow. On the other hand, esterase meditated release was reported to be notably rapid.[55] Therefore, we hypothesized that mode-of-release is a two-step process composed of (1) [^{125}I]IUdR-C_n leaving the lipid membrane and entering the surrounding medium, (2) hydrolysis by esterase (**Figure 4a**).

To elucidate this, we conducted a two-compartment release study. Here [^{125}I]IUdR-C_{18}-LIPs and esterase were separated by a dialysis membrane (30 kDa cut-off) with only the ester-prodrug small enough to cross the dialysis membrane **(Figure 4b)**. [^{125}I]IUdR-C_{18}-LIPs was placed inside the dialysis bag, with esterase only added to the compartment outside the dialysis bag. In this way, [^{125}I]IUdR-C_{18} would only be hydrolysed by the esterases when it escaped the liposome and crossed the dialysis membrane. During the course of this experiment, we measured the activity of both the inside and outside compartments **(Figure 4c)**. The activity in the outer compartment (containing esterases-PBS) progressively increased, from 40% in 24 hours and 82% after 7 days This indicated that [^{125}I]IUdR-C_{18} could indeed navigate itself crossing the dialysis membrane, reaching the outer chamber. This experiment suggested that hydrolysis of the prodrug takes place in the medium, and not near or on the surface of the liposome, making the affinity for the prodrug to the liposomal bilayer, and thereby the size of the lipid anchor, a key factor in the rate of [^{125}I]IUdR release.

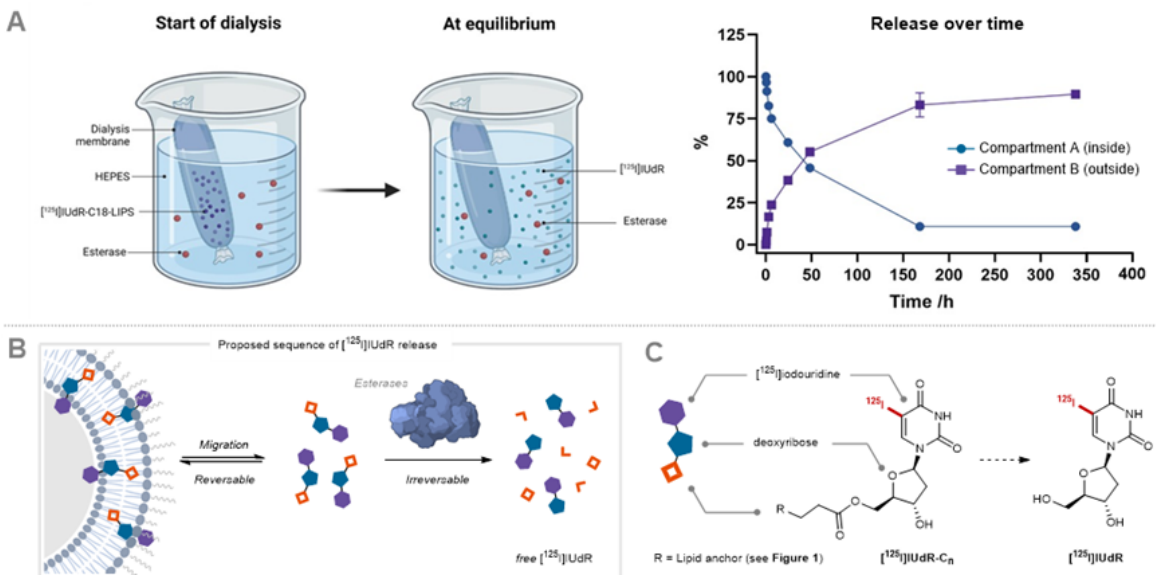

Figure 4 Release mechanism study of [^{125}I]IUdR-C_n-LIPs via the dialysis method. (a). Proposed mechanism of esterase mediated hydrolysis, (b) Illustration of experimental setup, (c) Radioactivity percentage in and outside of the dialysis bag.

Therapeutic efficacy in cell cultures

We investigated the in vitro efficacy of the liposomal delivery system in the LN229 cell line using the CellTiter-Blue assay. This study focused on four main treatment groups: (1) [^{125}I]IUdR-C_{18}-LIPs, (2) [^{125}I]IUdR-C_{18} prodrug, (3) [^{125}I]IUdR, and (4) IUdR-C_{18} prodrug. All groups, except for [^{125}I]IUdR, were tested both with and without esterase. The cell viability results were shown in **Figure 5**. As control experiments, we first investigated the influence of esterase when added to cells. As can be seen in **Figure 5a**, significant cell growth inhibition was found when the concentration was higher than 0.4 U/mL. Consequently, a non-cytotoxic concentration of 0.1 U/mL was selected for the subsequent cell studies. We have also studied the cytotoxicity of free iodine-125, which exhibited no noteworthy cell-killing ability up to 30 kBq/mL, indicating the longer ranges X-ray and electron emissions are not sufficient for cell killing (**Figure 5b**).

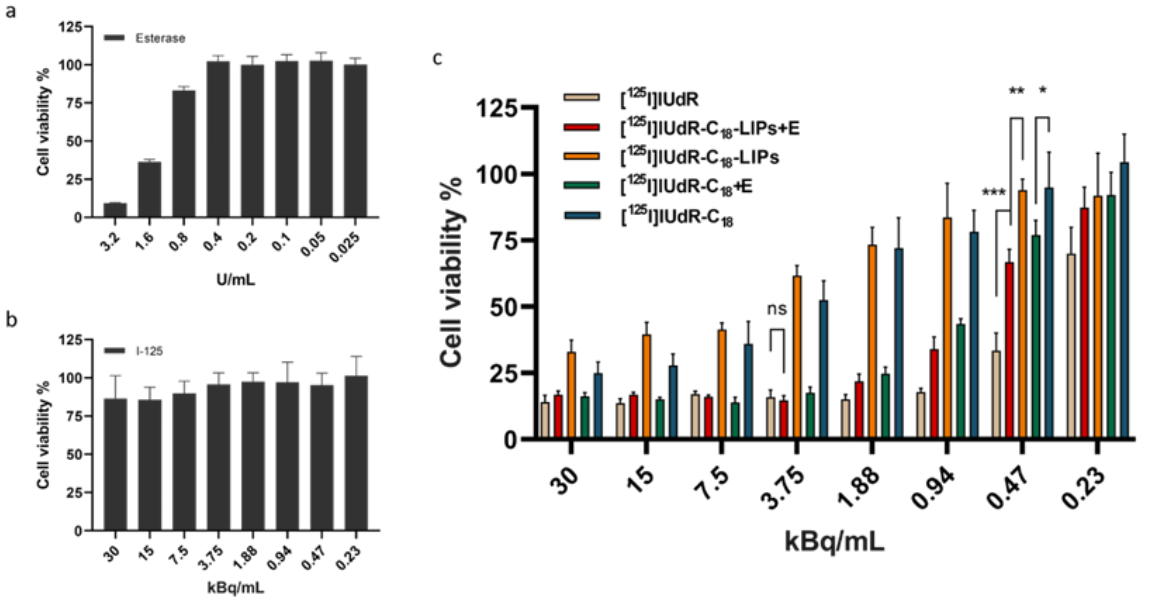

Figure 5 . Cell viability analysis based on CellTiter-Blue assay in LN229 cell line. (a), Control experiment. Viability of cells treated with varying concentrations of esterase, from 0.025 – 3.2 U/mL; (b), Control experiment. Viability of cells treated with different activities of free iodine-125, from 0.23 – 30 kBq/mL; and (c) Viability of cells treated with [^{125}I]IUdR-C_{18}-LIPs, [^{125}I]IUdR-C_{18} prodrug (with or without esterase), and [^{125}I]IUdR. Activities benchmarked against free iodine-125 levels. ”E” represents esterase, while ”LIPS” stands for liposomes. See SI for conditions and methods. Error bars shown are SD

In the next assay, **Figure 5c**, the radioactive groups, [^{125}I]IUdR-C_{18}-LIPs (with or without esterase), [^{125}I]IUdR-C_{18} prodrug (with or without esterase), and [^{125}I]IUdR were tested. Free [^{125}I]IUdR-C_{18} prodrug without liposomes (entry 5) showed a linear activity correlation, where lower radioactivity correlated with higher cell viability. A similar trend was also observed with the loaded liposomes without esterase, [^{125}I]IUdR-C_{18}-LIPs (entry 3). The release of [^{125}I]IUdR from liposomes has been demonstrated to be a two-step process, therefore after the prodrug had been entered the media, the gradual release of [^{125}I]IUdR persisted due to the slow hydrolysis of the ester bond in the aqueous media, subsequently leading to the descend of cell viability even in the absence of esterases. (**Figure S1**) In contrast to these entries, items with added esterases, [^{125}I]IUdR-C_{18}+E and [^{125}I]IUdR-C_{18}-LIPs+E (entries 4 and 2, respectively) showed a clear increase in efficacy and IC_{50} was 0.72 kBq/mL and 0.60 kBq/mL, respectively. When compared with [^{125}I]IUdR-C_{18} and [^{125}I]IUdR-C_{18}-LIPs, which had IC_{50} values of 2.10 kBq/mL and 2.96 kBq/mL, respectively, the esterase treated groups showed a roughly 4-fold increase in efficacy. This clearly demonstrated that the cell survival rate is correlated with the release amount of [^{125}I]IUdR. It was found that,

however, the efficacy of [^{125}I]IUdR-C_{18}-LIPs+E (entry 2), was slightly higher than [^{125}I]IUdR-C_{18}+E (entry 4), as one would expect the release from the liposomes to be slower than the rate of ester hydrolysis. However, this effect can also be attributed to the poor solubility of the C_{18} prodrug (LogD > 4, see table 2), which could slow dissolution and thereby release of the free [^{125}I]IUdR. Finally, the positive control, [^{125}I]IUdR (entry 1), showed the highest efficacy, with an IC_{50} of 0.33 kBq/mL. Accordingly, [^{125}I]IUdR-C_{18}-LIPs+E was observed to exhibit a similar efficiency to [^{125}I]IUdR at radioactivity levels of ≥1.88 kBq/mL. While the difference of viability at low activities may be attributed to the two-step release mechanism of [^{125}I]IUdR from the liposomes. Therefore this sequential release might not ensure consistent cellular uptake of [^{125}I]IUdR, resulting in insufficient cellular uptake of [^{125}I]IUdR, especially at low activities.

Additional control experiments in which nonradioactive IUdR-C_{18} prodrug or nonradioactive IUdR-C_{18}-LIPs were added, showed no significant cytotoxicity (**Figure S3**). This demonstrated that the mechanism of our nanoparticles is mediated by the release of free [^{125}I]IUdR, and the subsequent induction of lethal DNA double-strand breaks by the highly localized Auger cascade. [56]

Clonogenic assay

In addition to the cell viability assay, we conducted a clonogenic assay for [^{125}I]IUdR, [^{125}I]IUdR-C_{18}-LIPs+E and free iodine-125 to determine the effect on the proliferation of LN229 cells is by the nanoparticles. Cells were exposed to the radioactive compounds at the same radioactivity concentrations that ranging from 0.125 to 2 kBq/mL for 2 days, prior to being transferred to low cell density plates. Colonies were visualized by crystal violet staining after 12 days of incubation. As can be seen in **Figure 6a-b**, both [^{125}I]IUdR and [^{125}I]IUdR-C_{18}-LIPs+E showed significant capacity to reduce colony formation, with IC_{50} values of 0.21 kBq/mL and 0.29 kBq/mL, respectively. While free iodine-125 didn't show significant inhibition of colony formation. This demonstrated that [^{125}I]IUdR-C_{18}-LIPs+E has a comparable ability to inhibit the formation of colonies as free [^{125}I]IUdR, which is consistent with our previous cytotoxicity studies (**Figure 5**).

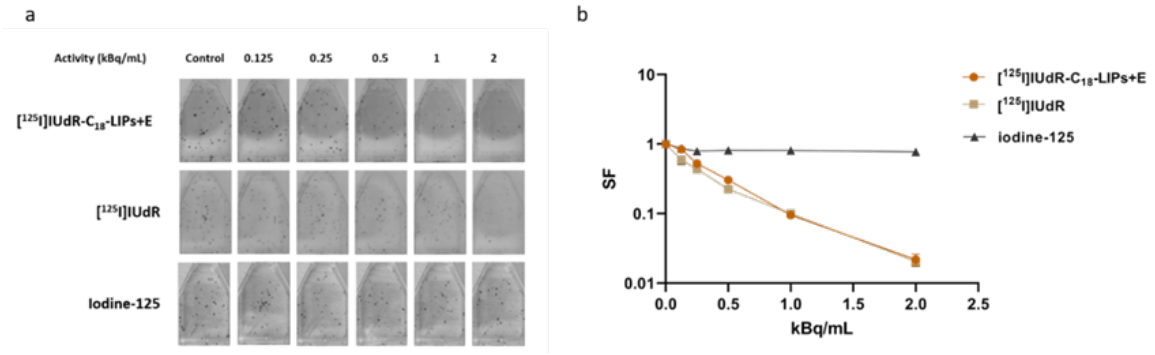

Figure 6. Clonogenic assay for [^{125}I]IUdR, [^{125}I]IUdR-C_{18}-LIPs+E and free iodine-125 in LN229 cells. (a). Representative images of plates at different radioactivities. The cells density in each plate can be seen in SI. (b). Quantification of the results shown in (a), SF represents survival factors. Data are presented as mean±SD (n=3).

In vitro and *in vivo* DNA incorporation

We firstly investigated the efficiency of incorporating [^{125}I]IUdR, obtained from [^{125}I]IUdR-C_{18}-LIPs+E, into the DNA in LN229 cells. The cells were exposed to [^{125}I]IUdR-C_{18}-LIPs+E for 4, 7, or 24 hours, and subsequently assessed the degree of integration at each time point. As can be seen in **Figure 7a**, it revealed an increase in the incorporation of [^{125}I]IUdR into DNA over time. the incorporation percentages were 3 % at 4 hours, 4.8 % at 7 hours and 11 % at 24 hours of total added [^{125}I]IUdR-C_{18}-LIPs (18.5 kBq). We also investigated the DNA incorporation efficiency of [^{125}I]IUdR-C_{18}-LIPs into the DNA in the tumor of mice,. Mice were injected with either [^{125}I]IUdR-C_{18}-LIPs and euthanized after 2 or 5 days or injected with mock solution and euthanized after 5 days. **Figure 7b** indicated an elevated incorporation of [^{125}I]IUdR in DNA after [^{125}I]IUdR-C_{18}-LIPs injection, with the highest incorporation after 5 days. In contrast, Injection of mock after 5 days demonstrated almost no incorporation. However, there was no statistical significance was obtained, possibly due to small group sizes (3+4+2 mice) and a large variance in same groups.

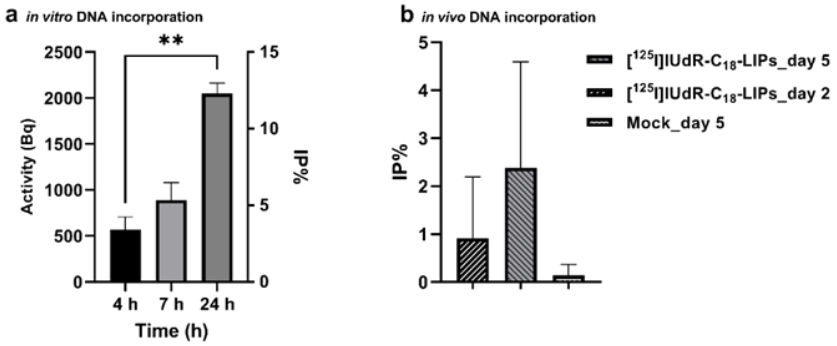

Figure 7. *In vitro* and *in vivo* DNA incorporation of [^{125}I]IUdR-C_{18}-LIPs. (a). DNA incorporation of [^{125}I]IUdR-C_{18}-LIPs in LN 229 cells after 4, 7, and 24 hours of incubation. (b) DNA incorporation in tumors of mice that were injected with either [^{125}I]IUdR-C_{18}-LIPs or mock and euthanized 2 or 5 days post-injection. Data was represented in terms of specific activities (Bq) or the percentage of incorporation (IP%), or both. Two-tailed paired Student *t*-test *P*-values indicate statistical significance (**P*<0.05, ***P*<0.01, ****P*<0.001). Error bars shown are SD

In vivo biodistribution

Biodistribution of [^{125}I]IUdR-C_{18}-LIPs was evaluated in rats bearing T87 xenografts at 6 and 24 h p.i.. **Figure 8** showed a fast clearance of [^{125}I]IUdR-C_{18}-LIPs from blood and normal-tissue. The (stomach) ventricle demonstrated a high uptake at 6 h p.i. and there was a significant decrease in the extent of uptake within a time frame ranging from 6 to 24 h p.i. Uptake in brain (left hemisphere, right hemisphere and cerebellum) exceed the uptake in normal-tissue at both time points. No significant difference in uptake was observed in brain and right hemisphere (site of tumor and injection), indicating retention, while uptake reduced in the left hemisphere and increased in cerebellum from 6 to 24 h p.i. After 6 h, 17.22% (average, n = 4) of injected activity (IA) was detected in the organs measured, which indicated a fast excretion of the remaining IA within the 6 h. The detected IA reduced to 7.20% (average, n = 4) of IA after 24 h. This indicated a further excretion from the rats from 6 h to 24 h.

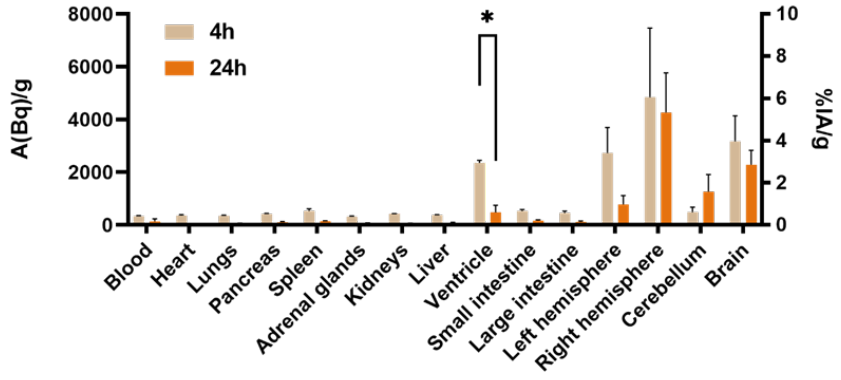

Figure 8. *In vivo* biodistribution of [^{125}I]IUdR-C_{18}-LIPs in glioblastoma-bearing athymic nude rats after 6 h (n = 4) and 24 h (n = 4) post-injection. Data was represented as activity (Bq) per gram of organ (left, A/g) and percentage of injected dose per gram of organ (right, %IA/g). Brain: left hemisphere, right hemisphere and cerebellum. Two-tailed paired Student *t*-test *P*-values indicate statistical significance (*P<0.05, **P<0.01, ***P<0.001). Error bars shown are SD

SPECT/SCT scans of [^{125}I]IUdR-C_{18}-LIPs in tumor-bearing mice

We also investigated the distribution of [^{125}I]IUdR-C_{18}-LIPs by performing SPECT/CT scans. The scans were performed in mice bearing U87 xenografts at 1, 48 and 120 h p.i. As shown in **Figure 9**, [^{125}I]IUdR-C_{18}-LIPs showed a fast clearance from blood and normal-tissue with a retention in brain at 1 and 48 h. Thyroid uptake was visible at 48 and 120 h, which was expected given that thyroid uptake was not blocked with potassium iodide, as in *ex vivo* biodistribution. The distribution in scans were comparable with the distribution observed in the previous *ex vivo* biodistribution (**Figure 8**).

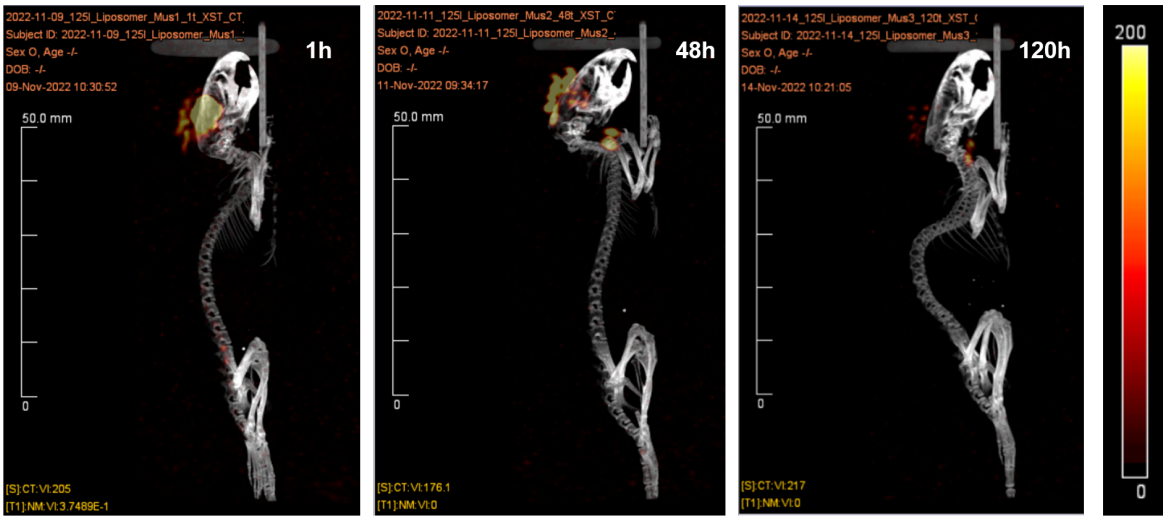

Figure 9. SPECT/CT scan of [^{125}I]IUdR-C_{18}-LIPs in tumor-bearing mice after 1, 48 and 120 h post-injection. Left: 1 h, middle: 48 h and right: 120 h.

Discussion

In order to achieve high and spatially well-distributed DNA uptake of [^{125}I]IUdR in glioblastoma cells, a simple but efficient multi-stage delivery system is desirable. Here we report a liposome based formulation of lipidized prodrugs of [^{125}I]IUdR to fulfil two separate roles. Liposomes were chosen because of their utility to achieve wide distribution in the brain upon administration by convection enhanced delivery (CED), as recently demonstrated by us (Chapter 5). As such, liposomes functioned solely as a carrier. PEG coated liposomes were chosen to minimize interaction with brain tissue and cells, to enable wide distribution and limit cellular uptake. [57,58]

To enable incorporation and release of [^{125}I]IUdR from liposomes, we designed and synthesized [^{125}I]IUdR modified in the 5' primary alcohol position on the deoxyribose with linear alkyl chains, as well as with cholesterol, via an ester bond. The hydrophobic alkyl chains functioned as anchors that facilitate immobilization of the prodrug inside the lipid-bilayer of the Stealth liposomes, as well as a mean to tune release from the bilayer, with smaller lipids effecting faster release, and vice versa. The Stealth liposomes used were composed of phospholipids, more specifically phosphatidylcholine (HSPC) and PEG-phosphatidylethanolamines (DSPE-PEG$_{2000}$) as well as cholesterol. Lipophilic compounds, therefore, could easily be immobilized inside the lipid compartment of these liposomes, due to the favourable polarity match. The next feature was the cleavable chemical linkage, that connects the lipid anchor to the [^{125}I]IUdR. Here we opted to utilize a simple ester linkage, as these can undergo hydrolysis by endogenous esterase that are present inside of brain, such as carboxyl esterase, which is reported to have 50–70 units in human brain, and can therefore function as a means of drug release. [54]

4 Summary and outlook

In summary, we demonstrated that [^{125}I]IUdR-C$_n$-LIPs can release [^{125}I]IUdR in brain homogenates. Moreover, [^{125}I]IUdR-C$_{18}$-LIPs was regarded to be the most promising choice since it had a slower release rate than -C$_{12}$ and had a greater retention of [^{125}I]IUdR within the 14 day window. Additionally, we have also demonstrated that [^{125}I]IUdR is most likely released in a two-step process. These findings are encouraging because they confirmed that [^{125}I]IUdR-C$_{18}$-LIPs is capable of releasing [^{125}I]IUdR in brain homogenates without the additional addition of esterase. This means that we can reasonably assume that after ad-

ministering [^{125}I]IUdR-C_{18}-LIPs into the rat brain, [^{125}I]IUdR can be released from [^{125}I]IUdR-C_{18}-LIPs with a rather slow release rate. Correspondingly, our treatment strategy of GBM will benefit from the slow release and long retention time of [^{125}I]IUdR, as they ensure the high therapeutic dose of [^{125}I]IUdR and hence the effectiveness of the treatment. Furthermore, we also demonstrated that [^{125}I]IUdR-C_{18}-LIPs exhibits a remarkable ability to induce cell death, according to its comparable IC_{50} values to [^{125}I]IUdR. The biodistribution in vivo demonstrated that [^{125}I]IUdR-C_{18}-LIPs had a retention of 2 days in the brain. These findings highlight the potential of [^{125}I]IUdR-C_{18}-LIPs as a promising therapeutic agent in terms of GBM treatment.

5 References

(1) Davis, M. E. Glioblastoma: Overview of Disease and Treatment. *Clinical Journal of Oncology Nursing* **2016**, *20* (5), 2–8. https://doi.org/10.1188/16.cjon.s1.2-8.

(2) Ostrom, Q. T.; Gittleman, H.; Farah, P.; Ondracek, A.; Chen, Y. W.; Wolinsky, Y.; Stroup, N. E.; Kruchko, C.; Barnholtz-Sloan, J. S. CBTRUS Statistical Report: Primary Brain and Central Nervous System Tumors Diagnosed in the United States in 2006-2010. *Neuro-Oncology* **2013**, *15*, 1–56. https://doi.org/10.1093/neuonc/not151.

(3) Ostrom, Q. T.; Gittleman, H.; Liao, P.; Vecchione-Koval, T.; Wolinsky, Y.; Kruchko, C.; Barnholtz-Sloan, J. S. CBTRUS Statistical Report: Primary Brain and Other Central Nervous System Tumors Diagnosed in the United States in 2010–2014. *Neuro-Oncology* **2017**, *19* (suppl_5), v1–v88. https://doi.org/10.1093/neuonc/nox158.

(4) Walker, E. V.; Davis, F. G.; Shaw, A.; Louchini, R.; Shack, L.; Woods, R.; Kruchko, C.; Spinelli, J.; Guiot, M. C.; Perry, J.; Melin, B.; Barnholtz-Sloan, J.; Turner, D.; King, M.; Hannah, H.; Bryant, H.; Cbtr Founding Affiliates. Malignant Primary Brain and Other Central Nervous System Tumors Diagnosed in Canada from 2009 to 2013. *Neuro-Oncology* **2019**, *21* (3), 360–369. https://doi.org/10.1093/neuonc/noy195.

(5) Gittleman, H.; Boscia, A.; Ostrom, Q. T.; Truitt, G.; Fritz, Y.; Kruchko, C.; Barnholtz-Sloan, J. S. Survivorship in Adults with Malignant Brain and Other Central Nervous System Tumor from 2000-2014. *Neuro-Oncology* **2018**, *20*, 6–16. https://doi.org/10.1093/neuonc/noy090.

(6) Brodbelt, A.; Greenberg, D.; Winters, T.; Williams, M.; Vernon, S.; Collins, V. P.; Natl Canc Information, N. Glioblastoma in England: 2007-2011. *European Journal of Cancer* **2015**, *51* (4), 533–542. https://doi.org/10.1016/j.ejca.2014.12.014.

(7) Stupp, R.; Mason, W. P.; van den Bent, M. J.; Weller, M.; Fisher, B.; Taphoorn, M. J. B.; Belanger, K.; Brandes, A. A.; Marosi, C.; Bogdahn, U.; Curschmann, J.; Janzer, R. C.; Ludwin, S. K.; Gorlia, T.; Allgeier, A.; Lacombe, D.; Cairncross, J. G.; Eisenhauer, E.; Mirimanoff, R. O. Radiotherapy plus Concomitant and Adjuvant Temozolomide for Glioblastoma. *N Engl J Med* **2005**, *352* (10), 987–996. https://doi.org/10.1056/NEJMoa043330.

(8) Paulmurugan, R.; Massoud, T. F. *Glioblastoma Resistance to Chemotherapy: Molecular Mechanisms and Innovative Reversal Strategies*; Academic Press, 2021.

(9) Prager, B. C.; Bhargava, S.; Mahadev, V.; Hubert, C. G.; Rich, J. N. Glioblastoma Stem Cells: Driving Resilience through Chaos. *Trends in Cancer* **2020**, *6* (3), 223–235. https://doi.org/10.1016/j.trecan.2020.01.009.

(10) Alifieris, C.; Trafalis, D. T. Glioblastoma Multiforme: Pathogenesis and Treatment. *Pharmacology & Therapeutics* **2015**, *152*, 63–82. https://doi.org/10.1016/j.pharmthera.2015.05.005.

(11) Sevastre, A. S.; Costachi, A.; Tataranu, L. G.; Brandusa, C.; Artene, S. A.; Stovicek, O.; Alexandru, O.; Danoiu, S.; Sfredel, V.; Dricu, A. Glioblastoma Pharmacotherapy: A Multifaceted Perspective of Conventional and Emerging Treatments (Review). *Experimental and Therapeutic Medicine* **2021**, *22* (6). https://doi.org/10.3892/etm.2021.10844.

(12) Di Nunno, V.; Franceschi, E.; Tosoni, A.; Gatto, L.; Lodi, R.; Bartolini, S.; Brandes, A. A. Glioblastoma: Emerging Treatments and Novel Trial Designs. *Cancers* **2021**, *13* (15). https://doi.org/10.3390/cancers13153750.

(13) Nam, J. Y.; De Groot, J. F. Treatment of Glioblastoma. *Journal of oncology practice* **2017**, *13* (10), 629–638.

(14) Wick, W.; Osswald, M.; Wick, A.; Winkler, F. Treatment of Glioblastoma in Adults. *Therapeutic advances in neurological disorders* **2018**, *11*, 1756286418790452.

(15) Stupp, R.; Hegi, M. E.; Mason, W. P.; van den Bent, M. J.; Taphoorn, M. J.; Janzer, R. C.; Ludwin, S. K.; Allgeier, A.; Fisher, B.; Belanger, K.; Hau, P.; Brandes, A. A.; Gijtenbeek, J.; Marosi, C.; Vecht, C. J.; Mokhtari, K.; Wesseling, P.; Villa, S.; Eisenhauer, E.; Gorlia, T.; Weller, M.; Lacombe, D.; Cairncross, J. G.; Mirimanoff, R.-O. Effects of Radiotherapy with Concomitant and Adjuvant Temozolomide versus Radiotherapy Alone on Survival in Glioblastoma in a Randomised Phase III Study: 5-Year Analysis of the EORTC-NCIC Trial. *The Lancet Oncology* **2009**, *10* (5), 459–466. https://doi.org/10.1016/S1470-2045(09)70025-7.

(16) Ostermann, S.; Csajka, C.; Buclin, T.; Leyvraz, S.; Lejeune, F.; Decosterd, L. A.; Stupp, R. Plasma and Cerebrospinal Fluid Population Pharmacokinetics of Temozolomide in Malignant Glioma Patients. *Clinical Cancer Research* **2004**, *10* (11), 3728–3736.

(17) Ortiz, R.; Perazzoli, G.; Cabeza, L.; Jiménez-Luna, C.; Luque, R.; Prados, J.; Melguizo, C. Temozolomide: An Updated Overview of Resistance Mechanisms, Nanotechnology Advances and Clinical Applications. *Current Neuropharmacology* **2021**, *19* (4), 513–537.

(18) Ashby, L. S.; Smith, K. A.; Stea, B. Gliadel Wafer Implantation Combined with Stan-

dard Radiotherapy and Concurrent Followed by Adjuvant Temozolomide for Treatment of Newly Diagnosed High-Grade Glioma: A Systematic Literature Review. *World journal of surgical oncology* **2016**, *14*, 1–15.

(19) Chowdhary, S. A.; Ryken, T.; Newton, H. B. Survival Outcomes and Safety of Carmustine Wafers in the Treatment of High-Grade Gliomas: A Meta-Analysis. *Journal of Neuro-Oncology* **2015**, *122* (2), 367–382. https://doi.org/10.1007/s11060-015-1724-2.

(20) Zhang, H.; Wang, R. Z.; Yu, Y. Q.; Liu, J. F.; Luo, T. M.; Fan, F. Glioblastoma Treatment Modalities besides Surgery. *Journal of Cancer* **2019**, *10* (20), 4793–4806. https://doi.org/10.7150/jca.32475.

(21) Stupp, R.; Taillibert, S.; Kanner, A.; Read, W.; Steinberg, D. M.; Lhermitte, B.; Toms, S.; Idbaih, A.; Ahluwalia, M. S.; Fink, K.; Di Meco, F.; Lieberman, F.; Zhu, J.-J.; Stragliotto, G.; Tran, D. D.; Brem, S.; Hottinger, A. F.; Kirson, E. D.; Lavy-Shahaf, G.; Weinberg, U.; Kim, C.-Y.; Paek, S.-H.; Nicholas, G.; Bruna, J.; Hirte, H.; Weller, M.; Palti, Y.; Hegi, M. E.; Ram, Z. Effect of Tumor-Treating Fields Plus Maintenance Temozolomide vs Maintenance Temozolomide Alone on Survival in Patients With Glioblastoma: A Randomized Clinical Trial. *JAMA* **2017**, *318* (23), 2306. https://doi.org/10.1001/jama.2017.18718.

(22) Kirson, E. D.; Gurvich, Z.; Schneiderman, R.; Dekel, E.; Itzhaki, A.; Wasserman, Y.; Schatzberger, R.; Palti, Y. Disruption of Cancer Cell Replication by Alternating Electric Fields. *Cancer Research* **2004**, *64* (9), 3288–3295. https://doi.org/10.1158/0008-5472.can-04-0083.

(23) Yan, G.; Wang, Y. F.; Chen, J. C.; Zheng, W. Z.; Liu, C. Z.; Chen, S.; Wang, L. R.; Luo, J.; Li, Z. Q. Advances in Drug Development for Targeted Therapies for Glioblastoma. *Medicinal Research Reviews* **2020**, *40* (5), 1950–1972. https://doi.org/10.1002/med.21676.

(24) Autier, L.; Clavreul, A.; Cacicedo, M. L.; Franconi, F.; Sindji, L.; Rousseau, A.; Perrot, R.; Montero-Menei, C. N.; Castro, G. R.; Menei, P. A New Glioblastoma Cell Trap for Implantation after Surgical Resection. *Acta Biomaterialia* **2019**, *84*, 268–279. https://doi.org/10.1016/j.actbio.2018.11.027.

(25) Piccirillo, S. G. M.; Dietz, S.; Madhu, B.; Griffiths, J.; Price, S. J.; Collins, V. P.; Watts, C. Fluorescence-Guided Surgical Sampling of Glioblastoma Identifies Phenotypically Distinct Tumour-Initiating Cell Populations in the Tumour Mass and Margin. *British Journal of Cancer* **2012**, *107* (3), 462–468. https://doi.org/10.1038/bjc.2012.271.

(26) Breznik, B.; Motaln, H.; Vittori, M.; Rotter, A.; Lah Turnšek, T. Mesenchymal Stem Cells Differentially Affect the Invasion of Distinct Glioblastoma Cell Lines. *Oncotarget; Vol 8, No 15* **2017**.

(27) Lemée, J.-M.; Clavreul, A.; Aubry, M.; Com, E.; de Tayrac, M.; Eliat, P.-A.; Henry, C.; Rousseau, A.; Mosser, J.; Menei, P. Characterizing the Peritumoral Brain Zone in Glioblastoma: A Multidisciplinary Analysis. *Journal of Neuro-Oncology* **2015**, *122* (1), 53–61. https://doi.org/10.1007/s11060-014-1695-8.

(28) Ku, A.; Facca, V. J.; Cai, Z.; Reilly, R. M. Auger Electrons for Cancer Therapy – a Review. *Ejnmmi Radiopharmacy and Chemistry* **2019**, *4* (1), 27. https://doi.org/10.1186/s41181-019-0075-2.

(29) Pirovano, G.; Jannetti, S. A.; Carter, L. M.; Sadique, A.; Kossatz, S.; Guru, N.; Demétrio De Souza França, P.; Maeda, M.; Zeglis, B. M.; Lewis, J. S.; Humm, J. L.; Reiner, T. Targeted Brain Tumor Radiotherapy Using an Auger Emitter. *Clin Cancer Res* **2020**, *26* (12), 2871–2881. https://doi.org/10.1158/1078-0432.CCR-19-2440.

(30) Bailly, C.; Vidal, A.; Bonnemaire, C.; Kraeber-Bodere, F.; Cherel, M.; Pallardy, A.; Rousseau, C.; Garcion, E.; Lacoeuille, F.; Hindre, F.; Valable, S.; Bernaudin, M.; Bodet-Milin, C.; Bourgeois, M. Potential for Nuclear Medicine Therapy for Glioblastoma Treatment. *Frontiers in Pharmacology* **2019**, *10*. https://doi.org/10.3389/fphar.2019.00772.

(31) Howell, R. W. Advancements in the Use of Auger Electrons in Science and Medicine during the Period 2015–2019. *International Journal of Radiation Biology* **2023**, *99* (1), 2–27. https://doi.org/10.1080/09553002.2020.1831706.

(32) Pirovano, G.; Wilson, T. C.; Reiner, T. Auger: The Future of Precision Medicine. *Nuclear Medicine and Biology* **2021**, *96–97*, 50–53. https://doi.org/10.1016/j.nucmedbio.2021.03.002.

(33) Pirovano, G.; Jannetti, S. A.; Carter, L. M.; Sadique, A.; Kossatz, S.; Guru, N.; Franca, P. D. D.; Maeda, M.; Zeglis, B. M.; Lewis, J. S.; Humm, J. L.; Reiner, T. Targeted Brain Tumor Radiotherapy Using an Auger Emitter. *Clinical Cancer Research* **2020**, *26* (12), 2871–2881. https://doi.org/10.1158/1078-0432.ccr-19-2440.

(34) Lehnert, S.; Li, Y.; Bump, E.; Riddoch, B.; Chenite, A.; Shive, M. 125I-Iododeoxyuridine for the Treatment of a Brain Tumor Model: Selection of Conditions for Optimal Effectiveness. *The Open Nuclear Medicine Journal* **2011**, *3* (1).

(35) Garrett, C.; Wataya, Y.; Santi, D. V. THYMIDYLATE SYNTHETASE - CATALYSIS OF DEHALOGENATION OF 5-BROMO-2'-DEOXYURIDYLATE AND 5-IODO-2'-DEOXYURIDYLATE. *Biochemistry* **1979**, *18* (13), 2798–2804. https://doi.org/10.1021/bi00580a017.

(36) Hampton, E. G.; Rich, M. A.; Eidinoff, M. L. INTRODUCTION OF THE 5-IODOURACIL MOIETY INTO DEOXYRIBONUCLEIC ACID OF MAMMALIAN CELLS. *Journal of Biological Chemistry* **1960**, *235* (12), 3562–3566.

(37) Thisgaard, H.; Halle, B.; Aaberg-Jessen, C.; Olsen, B. B.; Therkelsen, A. S. N.; Dam, J. H.; Langkjær, N.; Munthe, S.; Någren, K.; Høilund-Carlsen, P. F.; Kristensen, B. W. Highly Effective Auger-Electron Therapy in an Orthotopic Glioblastoma Xenograft Model Using Convection-Enhanced Delivery. *Theranostics* **2016**, *6* (12), 2278–2291. https://doi.org/10.7150/thno.15898.

(38) Miyata, S.; Kawabata, S.; Hiramatsu, R.; Doi, A.; Ikeda, N.; Yamashita, T.; Kuroiwa, T.; Kasaoka, S.; Maruyama, K.; Miyatake, S. I. Computed Tomography Imaging of Transferrin Targeting Liposomes Encapsulating Both Boron and Iodine Contrast Agents by Convection-Enhanced Delivery to F98 Rat Glioma for Boron Neutron Capture Therapy. *Neurosurgery* **2011**, *68* (5), 1380–1387. https://doi.org/10.1227/NEU.0b013e31820b52aa.

(39) Ksendzovsky, A.; Walbridge, S.; Saunders, R. C.; Asthagiri, A. R.; Heiss, J. D.; Lonser, R. R. Convection-Enhanced Delivery of M13 Bacteriophage to the Brain Laboratory Investigation. *Journal of Neurosurgery* **2012**, *117* (2), 197–203. https://doi.org/10.3171/2012.4.Jns111528.

(40) Debinski, W.; Tatter, S. B. Convection-Enhanced Delivery to Achieve Widespread Distribution of Viral Vectors: Predicting Clinical Implementation. *Current Opinion in Molecular Therapeutics* **2010**, *12* (6), 647–653.

(41) Zhan, W. B.; Wang, C. H. Convection Enhanced Delivery of Liposome Encapsulated Doxorubicin for Brain Tumour Therapy. *Journal of Controlled Release* **2018**, *285*, 212–229. https://doi.org/10.1016/j.jconrel.2018.07.006.

(42) Han, Y.; Park, J. H. Convection-Enhanced Delivery of Liposomal Drugs for Effective Treatment of Glioblastoma Multiforme. *Drug Delivery and Translational Research* **2020**, *10* (6), 1876–1887. https://doi.org/10.1007/s13346-020-00773-w.

(43) White, E.; Bienemann, A.; Pugh, J.; Castrique, E.; Wyatt, M.; Taylor, H.; Cox, A.; McLeod, C.; Gill, S. An Evaluation of the Safety and Feasibility of Convection-Enhanced

Delivery of Carboplatin into the White Matter as a Potential Treatment for High-Grade Glioma. *Journal of Neuro-Oncology* **2012**, *108* (1), 77–88. https://doi.org/10.1007/s11060-012-0833-4.

(44) Shi, M. H.; Anantha, M.; Wehbe, M.; Bally, M. B.; Fortin, D.; Roy, L. O.; Charest, G.; Richer, M.; Paquette, B.; Sanche, L. Liposomal Formulations of Carboplatin Injected by Convection-Enhanced Delivery Increases the Median Survival Time of F98 Glioma Bearing Rats. *Journal of Nanobiotechnology* **2018**, *16*. https://doi.org/10.1186/s12951-018-0404-8.

(45) Corem-Salkmon, E.; Ram, Z.; Daniels, D.; Perlstein, B.; Last, D.; Salomon, S.; Tamar, G.; Shneor, R.; Guez, D.; Margel, S.; Mardor, Y. Convection-Enhanced Delivery of Methotrexate-Loaded Maghemite Nanoparticles. *International Journal of Nanomedicine* **2011**, *6*, 1595–1602. https://doi.org/10.2147/ijn.S23025.

(46) Freeman, A. C.; Platt, S. R.; Holmes, S.; Kent, M.; Robinson, K.; Howerth, E.; Eagleson, J.; Bouras, A.; Kaluzova, M.; Hadjipanayis, C. G. Convection-Enhanced Delivery of Cetuximab Conjugated Iron-Oxide Nanoparticles for Treatment of Spontaneous Canine Intracranial Gliomas. *Journal of Neuro-Oncology* **2018**, *137* (3), 653–663. https://doi.org/10.1007/s11060-018-2764-1.

(47) Nordling-David, M. M.; Yaffe, R.; Guez, D.; Meirow, H.; Last, D.; Grad, E.; Salomon, S.; Sharabi, S.; Levi-Kalisman, Y.; Golomb, G.; Mardor, Y. Liposomal Temozolomide Drug Delivery Using Convection Enhanced Delivery. *Journal of Controlled Release* **2017**, *261*, 138–146. https://doi.org/10.1016/j.jconrel.2017.06.028.

(48) Inoue, T.; Yamashita, Y.; Nishihara, M.; Sugiyama, S.; Sonoda, Y.; Kumabe, T.; Yokoyama, M.; Tominaga, T. Therapeutic Efficacy of a Polymeric Micellar Doxorubicin Infused by Convection-Enhanced Delivery against Intracranial 9L Brain Tumor Models. *Neuro-Oncology* **2009**, *11* (2), 151–157. https://doi.org/10.1215/15228517-2008-068.

(49) Zhang, R.; Saito, R.; Mano, Y.; Sumiyoshi, A.; Kanamori, M.; Sonoda, Y.; Kawashima, R.; Tominaga, T. Convection-Enhanced Delivery of SN-38-Loaded Polymeric Micelles (NK012) Enables Consistent Distribution of SN-38 and Is Effective against Rodent Intracranial Brain Tumor Models. *Drug Delivery* **2016**, *23* (8), 2780–2786. https://doi.org/10.3109/10717544.2015.1081994.

(50) Lilius, T. O.; Mortensen, K. N.; Deville, C.; Lohela, T. J.; Stæger, F. F.; Sig-

urdsson, B.; Fiordaliso, E. M.; Rosenholm, M.; Kamphuis, C.; Beekman, F. J.; Jensen, A. I.; Nedergaard, M. Glymphatic-Assisted Perivascular Brain Delivery of Intrathecal Small Gold Nanoparticles. *Journal of Controlled Release* **2023**, *355*, 135–148. https://doi.org/10.1016/j.jconrel.2023.01.054.

(51) Lee, D.-J.; Prensky, W.; Krause, G.; Hughes, W. L. Blood Thymidine Level and Iododeoxyuridine Incorporation and Reutilization in DNA in Mice given Long-Acting Thymidine Pellets. *Cancer Research* **1976**, *36* (12), 4577–4583.

(52) Klecker Jr, R. W.; Jenkins, J. F.; Kinsella, T. J.; Fine, R. L.; Strong, J. M.; Collins, J. M. Clinical Pharmacology of 5□iodo□2□□deoxyuridine and 5□iodouracil and Endogenous Pyrimidine Modulation. *Clinical Pharmacology & Therapeutics* **1985**, *38* (1), 45–51.

(53) Bagshawe, K. D.; Sharma, K.; Southall, P. J.; Boden, J. A.; Boxer, G. M.; Patridge, T. A.; Antoniw, P.; Pedley, R. B. Selective Uptake of Toxic Nucleoside (125IUdR) by Resistant Cancer. *The British journal of radiology* **1991**, *64* (757), 37–44.

(54) Prabha, M.; Ravi, V.; Ramachandra Swamy, N. Activity of Hydrolytic Enzymes in Various Regions of Normal Human Brain Tissue. *Indian J Clin Biochem* **2013**, *28* (3), 283–291. https://doi.org/10.1007/s12291-012-0273-0.

(55) Ma, X.; Huang, X.; Huang, G.; Li, L.; Wang, Y.; Luo, X.; Boothman, D. A.; Gao, J. Prodrug Strategy to Achieve Lyophilizable, High Drug Loading Micelle Formulations Through Diester Derivatives of β-Lapachone. *Advanced Healthcare Materials* **2014**, *3* (8), 1210–1216. https://doi.org/10.1002/adhm.201300590.

(56) Bradley, E. W.; Chan, P. C.; Adelstein, S. J. The Radiotoxicity of Iodine-125 in Mammalian Cells: I. Effects on the Survival Curve of Radioiodine Incorporated into DNA. *Radiation Research* **1975**, *64* (3), 555–563.

(57) Li, M.; Jiang, S.; Simon, J.; Paßlick, D.; Frey, M.-L.; Wagner, M.; Mailänder, V.; Crespy, D.; Landfester, K. Brush Conformation of Polyethylene Glycol Determines the Stealth Effect of Nanocarriers in the Low Protein Adsorption Regime. *Nano Letters* **2021**, *21* (4), 1591–1598. https://doi.org/10.1021/acs.nanolett.0c03756.

(58) Suk, J. S.; Xu, Q.; Kim, N.; Hanes, J.; Ensign, L. M. PEGylation as a Strategy for Improving Nanoparticle-Based Drug and Gene Delivery. *Adv Drug Deliv Rev* **2016**, *99* (Pt A), 28–51. https://doi.org/10.1016/j.addr.2015.09.012.

Chapter 3

[^{125}I]IUdR-Iododeoxyuridine Prodrugs Loaded Polymeric Micelles: A Novel Approach for Glioblastoma Treatment via Auger Radiotherapy

---

Qing Tang[1], Alina Hossain[1], Natan Johannes Willem Straathof[1], Katharina Ravn,[1] Andreas Ingemann Jensen*,[1]

[1]DTU Denmark, Institut for Sundhedsteknologi, Risø Campus, Frederiksborgvej 399 (Bygning 202), 4000 Roskilde.

The work in this chapter will be represented as manuscript.

1 Introduction

Glioblastoma multiforme (GBM) is a highly aggressive and difficult-to-treat form of brain cancer that poses significant challenges in the field of neuro-oncology. Classified as a grade IV tumor, GBM is characterized by its rapid progression and ability to infiltrate healthy brain tissue.[1,2] The invasive nature of GBM cells makes it challenging to accurately diagnose and surgically remove the tumor completely.[3] Furthermore, GBM exhibits resistance to conventional treatment methods, leading to a median survival rate of approximately 15 months, with variations based on multiple factors.[2,4,5]

Nevertheless, the challenge of GBM's infiltrative cells extends beyond the realm of conventional methods. The extensive and frequently unnoticed infiltration of these cells into healthy brain tissue necessitates the development of novel therapeutic approaches that specifically target these elusive cells.[3,6,7] Polymeric micelles, also referred to as PMs, have recently emerged as a promising development at the intersection of nanotechnology and oncology.[8,9] These nanoscale drug carriers are formed through the self-assembly of amphiphilic block copolymers, offering potential advantages such as enhanced cellular uptake and effective solubilization of hydrophobic compounds.[10,11] Furthermore, their manufacturing process is relatively straightforward due to their core-shell structure. This makes them highly suitable for encapsulating therapeutic medicines, ensuring targeted delivery to infiltrative glioma cells, where their efficacy is most crucial.[12]For example, Quader et al. designed an epirubicin (Epi)-loaded polymeric (Acetal-PEG-b-PBLA) micelles delivery system that was surface-modified with the cyclic arginine-glycine-aspartic acid (cRGD) peptide.[13] The purpose of this formulation was to actively target αvβ3 and αvβ5 integrins overexpressed on the endothelial cells of GBM, with the ultimate goal of circumventing the blood-brain tumor barrier (BBTB) and facilitating the direct administration of therapeutic agents to GBM cells. [14,15]

In addition to active targeting GBM cells, a passive delivery method, Convection-Enhanced Delivery (CED), has garnered significant interest due to its potential to transform the administration of therapeutics to the brain by directly targeting GBM cells, therefore bypassing many of the limitations of systemic administration.[16–18] By employing a continuous pressure gradient, CED induces a bulk flow of agents, ensuring extensive dispersion of high drug concentrations within the brain tissue.[19] This method proves especially advantageous for substances of varying molecular weights, addressing the challenges associated with lim-

ited brain penetration. Examples of PMs utilized in CED for GBM treatment include those based on block copolymers like poloxamers and poly(ethylene glycol)-poly(ε-caprolactone) conjugates, which have shown promise in preclinical studies for their ability to deliver therapeutic agents effectively to the tumor site.[20–23]

The possibilities of radiopharmaceutical [^{125}I]5-Iodo-2'-deoxyuridine ([^{125}I]IUdR) as Auger radiotherapy agents have been widely explored.[24–26] Thisggard et.al demonstrated that [^{125}I]IUdR [^{125}I]IUdR markedly reduced the viability and migratory capabilities of GBM cells in vitro, this reduction was even more pronounced when cells were treated in combination with methotrexate (MTX) and/or temozolomide (TMZ).[27] Additionally, other studies have shown that when combined with thymidylate synthase inhibitors like MTX and 5-fluoro-2'-deoxyuridine (F-UdR), the uptake and therapeutic effect of [^{125}I]IUdR are enhanced.[28–30] This combined approach is believed to be due to an increase in DNA replication in tumor cells when exposed to MTX, along with a higher DNA incorporation of iodine-125 through thymidylate synthetase inhibition[24].

However, [^{125}I]IUdR undergoes intracellular catabolism rapidly, leading to its dehalogenation into free nucleotide and iodine, as well as a short biological half-life. Given these characteristics, a nanosized structure could be advantageous, as their larger size and special structures might be able to increase the retention time of the therapeutical drugs.[31,32] In section 2.2, we have synthesized a range of [^{125}I]IUdR carbolic derivatives and assessed their performance in liposomes. These liposome based formulations exhibited a controlled release and demonstrated substantial cytotoxic potential.

In this section, we explored the viability of using PMs (PLGA-mPEG) as a delivery platform for the same [125I]IUdR-Cn prodrugs, where n= 8,12 or 18. The formulated nanoparticles, so called [125I]IUdR-Cn-PMs, the formulation methods, encapsulation efficacy, and release study of the prodrug-loaded PMs, as well as in vitro cellular studies, have been invested in this section. The design of this project was illustrated in **Figure 1**.

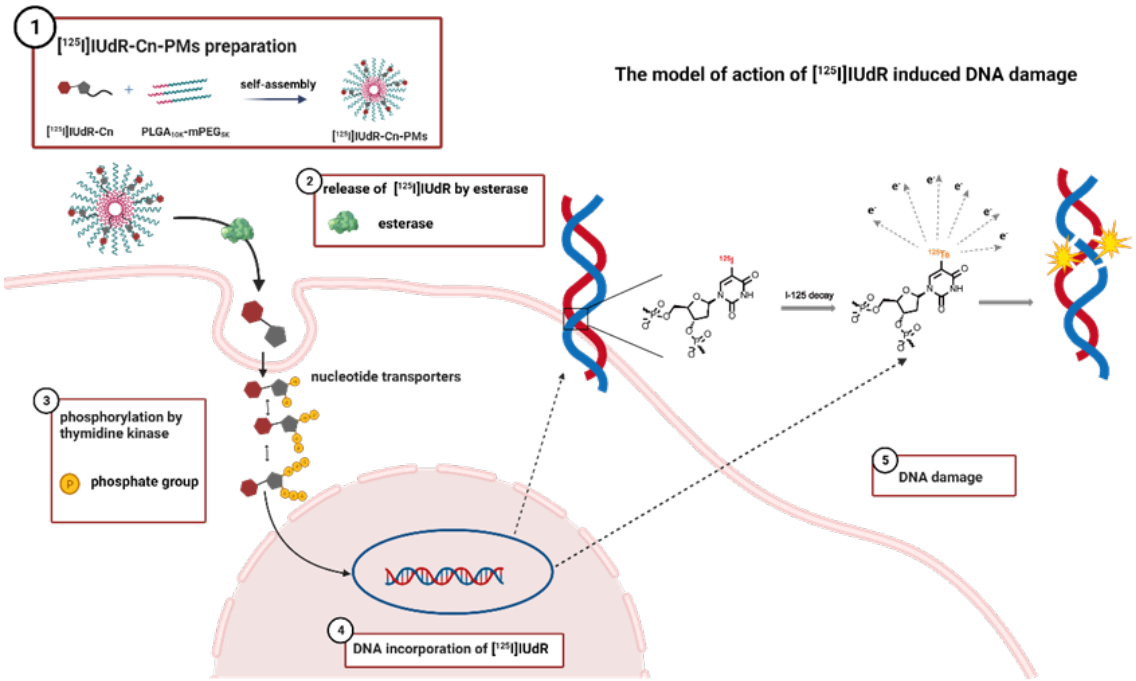

Figure 1. Illustration of the [125I]IUdR-Cn-PMs (n= 8,12 or 18) delivery system and the model of action in tumor cell.

2 Materials and methods

General considerations: All reagents and solvents were bought from commercial suppliers; Sigma-Aldrich, ABCR Chemicals, FluoroChem or TCI Chemicals, and were used as received. Milli-Q (MQ) water (18.2 MΩ × cm) was used for all micelles preparation steps. $PLGA_{10k}$-$mPEG_{5k}$ and $PLGA_{5k}$-$mPEG_{2k}$ were obtained from Nanosoft Polymers. Dulbecco's modified Eagle's medium (DMEM, high glucose) and fetal bovine serum (FBS) were obtained from Gibco and used as received. Celltiter Blue was purchased from Promega. Esterase from porcine liver was purchased from Merck. The [^{125}I]NaI was purchased from Perkin Elmer.

Radioactivity was measured on a dose calibrator (CRC-55tR). Radio TLC analysis was performed with a PerkinElmer Cyclone Plus phosphor imager on commercial pre-coated aluminium TLC sheets (4 x 10 cm, Merck Silica gel 60), and unless stated otherwise run in 10% MeOH in DCM and exposed overnight to a phosphor imaging plate. The particle size and zeta potential (DLS) of the self-assembled micelles were measured by dynamic light scattering on a Malvern Zetasizer NANO ZS (Malvern Instruments Limited, UK).

Radiolabelling of [^{125}I]IUdR-prodrugs ([^{125}I]IUdR-Cn)

The [^{125}I]IUdR-prodrugs were synthesized and purified in the same way as mentioned in **Chapter 2**. Briefly, a mixture of *Bu*$_3$Sn-IUdR derivative (0.5 mg, 0.6-0.97 µmol) in 100 µL DMF was added with chloramine-T solution (1 mg, 10 µL of H_2O), acetic acid (3 µL), and [^{125}I]NaI in 0.1 M NaOH (2-50 MBq) in a sequential manner. The vial was stirred for 30 min at 25 °C. Radio TLC was afterwards done to check the consumption of the [^{125}I]NaI. KI in H2O (10 µL, 0.1 M) was then added to the vial and was stirred for another 10 min. at 25 °C. The reaction was terminated using a sodium meta-bisulfite solution (2 mg in 20 µL of H_2O) and an aliquot was taken for radio-TLC analysis to give the radio chemical conversion of the reaction. For the purification step, the reaction mixture was diluted with MeCN (2 mL), taken up and filtered through a pre-activated SiO_2 cartridge (Sep-Pak Silica Plus Light Cartridge) to remove residual salts. The details of the synthesis, radiolabelling and purification steps can be found in **Chapter 2.**

Preparation of PMs

50 mg $PLGA_{10k}$-$mPEG_{5k}$ was weighed and dissolved in 5 mL of DMF to achieve a 10 mg/mL solution. After stirring for 15 minutes, MilliQ water was added dropwise to achieve DMF/H_2O ratios of 1:1, 1:2, 1:5, and 1:10, followed by another 15 minutes of stirring. The dispersions were then purified by dialysis with MWCO of 10 kDa.

Preparation of [^{125}I]IUdR-prodrugs loaded PMs ([^{125}I]IUdR-Cn-PMs)

Into a 10 mL vial, 100 µL of [^{125}I]IUdR-CX in MeCN was added and its radioactivity measured as 3 MBq. After evaporating the MeCN under Argon for 15 minutes, 100 µL of either $PLGA_{5k}$-$mPEG_{2k}$ or $PLGA_{10k}$-$mPEG_{5k}$ (both 10 mg/mL in DMF) solution was added and stirred for 10 minutes. Following the dropwise addition of 1 mL MilliQ water and 20 minutes of stirring, purification was achieved using centrifugal filters or PD-10 columns.

Esterase meditated release study in PBS buffer

Release studies were evaluated to monitor the release of [^{125}I]IUdR from [^{125}I]IUdR-Cn-PMs (n=8, 12, 18) in pH 7.4 PBS at 37°C with the addition of 10 µL of esterase (100 U/mL). Aliquots (5 µL) were taken after 0 h, 0.5h, 1h, 3h, 6h, 24h, 48h, 7 days and 14 days post-esterase addition. Immediately after collection, the aliquots were mixed with 15 µL of tetrahydrofuran (THF), then analyzed subsequently using Radio-TLC.

In vitro cell viability study

LN-229 cells were grown in Dulbecco's modified Eagle's medium (DMEM) growth medium with a pH= 7.4, supplemented with 10% fetal bovine serum (FBS), 100 U/mL of penicillin, 2 mM glutamine, and 100 µg/mL of streptomycin according to supplier instructions. Cell cultures were maintained in flasks and grown at 37 °C in a humidified atmosphere of 5% CO_2 in air.

In vitro cytotoxicity of [^{125}I]IUdR-C18-PMs against LN-229 cells was determined by a cell viability assay using CellTiter-Blue from Promega. Briefly, cells were seeded in 96-well plates, 300 cells/well, and incubated for 24 hours at 37 °C in an incubator. Samples were grouped to evaluate cytotoxicity as (1) [^{125}I]IUdR-C18-PMs with/without esterase, (2) [^{125}I]IUdR-C18 prodrug with/without esterase, (3) [^{125}I]IUdR and blank PMs. Appropriate

amounts of [^{125}I]IUdR-C18-PMs, [^{125}I]IUdR-C18 in DMSO and [^{125}I]IUdR were diluted with complete DMEM culture medium to achieve the desired final radioactivity of 0.12, 0.23, 0.49, 0.98, 1.97, 3.75, 7.5, and 15kBq/mL. All groups with added esterase (E) maintained a consistent concentration of 0.1 U/mL, introduced post sample preparation. The plates were incubated for 7 days before mixed with CellTiter-Blue solution (20 µL). After a 4 h incubation, the absorbance was recorded by microplate reader at 570 and 600 nm. The results were expressed as % cell viability = (mean optical density (OD) of treated cells/mean OD of untreated cells) × 100%.

DNAincorporation assay

Two 6-well plates, each containing 5x10^5 LN229 cells per well, were incubated for 24 hours at 37°C and 5% CO_2 atmosphere. Post incubation, the media was replaced with fresh media that contained either 30 kBq [^{125}I]IUdR-C18-PMs with 0.1 U/mL esterase or a control of 30 kBq [^{125}I]IUdR. One plate was incubated for 1 hour and the other one for 4 hours. Finally, genomic DNA was extracted using the E.Z.N.A. tissue DNA Kit from Omega BIO-TEK.

3 Results and discussion

Preparation of PMs

The nanoprecipitation method was chosen to prepare the PMs. In a typical procedure, the amphiphilic polymer was dissolved in organic solution (e.g., MeCN), then rapidly mixed with water. Previous research indicated that the miscibility of the organic solvent in water affects the size of nanoparticles in a given solvent-water system. Among the four different investigated solvent, DMF, MeCN, THF and Acetone, PMs prepared using DMF produced the smallest particles, which could be because of the solvent found to be most miscible with water. Therefore, we focused on the solvent:water ratio during the during the preparation of blank PMs , specifically when utilizing DMF as the solvent.

Two different polymer concentration, 5 mg/mL and 10 mg/mL, were tested with the DMF: H_2O ratio of 1:1, 1:2, 1:5, and 1:10. At 5 mg/mL (**Figure 2,** black), the PMs resulted in a size distribution between 71.11-120.96 nm, with PDI values of 0.053-0.157. Most nanoparticles remained consistent in the 1:10-1:2 range. However, the size increased from 71.11 ± 13.72 nm to 120.96 ± 14.68 nm when the ratio shifted from 1:2 to 1:1. At the higher polymer concentration (10 mg/mL, **Figure 2,** blue), the size of the PMs ranged from 42.66-83.90 nm with PDI values between 0.133-0.219. While the PMs were produced at 1:5 ratio were smaller than 1:10 ratio (42.66 ± 8.28 and 69.30 ± 9.17 nm, respectively).

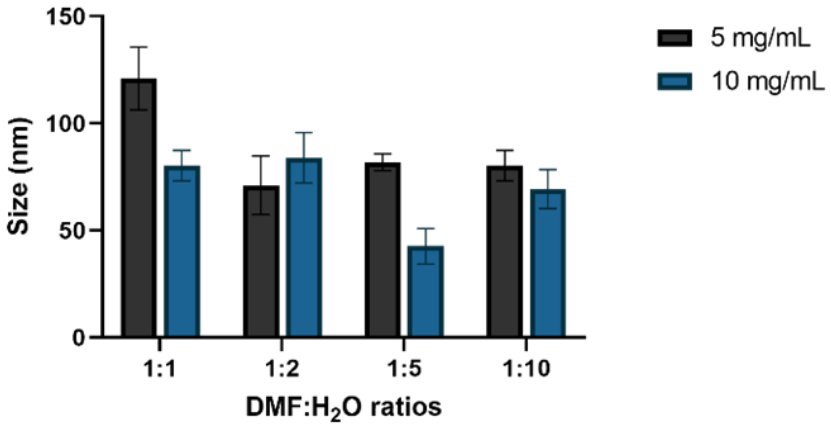

Figure 2. Influence of different DMF:H_2O ratios (1:1, 1:2, 1:5 and 1:10) on the size of PMs during PM preparation at two distinct polymer concentrations: 5 mg/mL and 10 mg/mL.

Comparing results across the DMF: H_2O ratios, no direct correlation between the size and the DMF:H_2O ratio was observed, which was aligned with findings from previously published research. Regarding the polymer concentrations, there was a general decrease in particle size for the 1:10, 1:5, and 1:1 ratios when shifting from 5 mg/mL to 10 mg/mL, the 1:2 ratio deviated from this pattern. This suggests that while increasing polymer concentration might generally lead to a reduction in particle size for certain solvent ratios, the behavior is not universally consistent across all ratios, indicating the intricate interplay between solvent ratio and polymer concentration in determining nanoparticle size. Nevertheless, the 10 mg/mL and 1:10 ratio were elected for the preparation of [^{125}I]IUdR-prodrugs loaded PMs for the expectation of a stable size and possible high drug encapsulation efficiency.

Preparation of [^{125}I]IUdR-prodrugs loaded PMs ([^{125}I]IUdR-CX-PMs)

Prodrugs [^{125}I]IUdR-C_8, -C_{12} and -C_{18} were loaded into PMs using nanoprecipitation method, also called pre-insertion method, which means the prodrugs were premixed with polymer in DMF solution before rapidly mixed with water. Whereafter the loaded [^{125}I]IUdR-C_n-PMs and unencapsulated prodrugs were removed using a PD-10 column. As shown in **Figure 3**, [^{125}I]IUdR-C_{18}-PMs showed the highest loading efficiency at 76% ± 4.04, [^{125}I]IUdR-C_8-PMs had the lowest at 50% ± 7.63, and [^{125}I]IUdR-C_{12}-PMs was intermediate at 65% ± 3.61. Therefore, the higher lipophilicity of [^{125}I]IUdR-C_{18} (LogD =)and resultant superior loading yield emphasized that more lipophilic compounds may integrate better into micelles' hydrophobic cores. These results demonstrated that the physicochemical properties of the prodrugs had significant influence in its encapsulation into PMs.

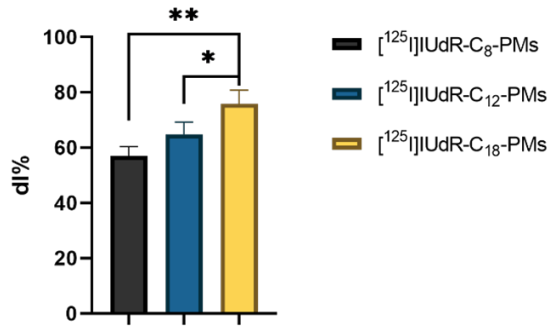

Figure 3. Loading efficiency (dl%) of [^{125}I]IUdR-C_8-PMs, [^{125}I]IUdR-C_{12}-PMs and [^{125}I]IUdR-C_{18}-PMs.

Esterases meditated release study

The release of [^{125}I]IUdR from [^{125}I]IUdR-C_n-PMs, n=8,12, and 18, was studied in PBS (pH 7.4) at 37°C using commercial esterase from porcine liver. This study simulated conditions that micelles might face in biological settings, especially in esterase-rich tissues. The release profile aimed to showcase a triggered release and to identify the best drug composition for in vitro cell studies. As shown in **Figure 4a** and **4b**, both [^{125}I]IUdR-C_8-PMs and [^{125}I]IUdR-C_{12}-PMs exhibited a rapid burst release, achieving 100% release of [^{125}I]IUdR within 30 minutes. In contrast, for [^{125}I]IUdR-C_{18}-PMs (**Figure 4c**), a more gradual release pattern was observed. In the first 3 hours, a burst release of [^{125}I]IUdR was also found, accounting for 87% of the total released [^{125}I]IUdR, leaving 13% of [^{125}I]IUdR-C_{18}. [^{125}I]IUdR-C_{18} was further hydrolyzed by esterase over the subsequent 2 days, but [^{125}I]IUdR was remained quite stable around 85%, and retained over 65% after 14 days. The plateau of [^{125}I]IUdR in the first 2 days can be attributed to the emergence of the unidentified others (**Figure 4c**, black line), these unknown species, have been demonstrated to be the decomposition products of [^{125}I]IUdR in the previous section. Overall, the differences in release speed of [^{125}I]IUdR from [^{125}I]IUdR-C_n-PMs could be because of the lipophilicity difference, therefore [^{125}I]IUdR-C_n-PMs was chosen for the subsequentially in vitro cell studies.

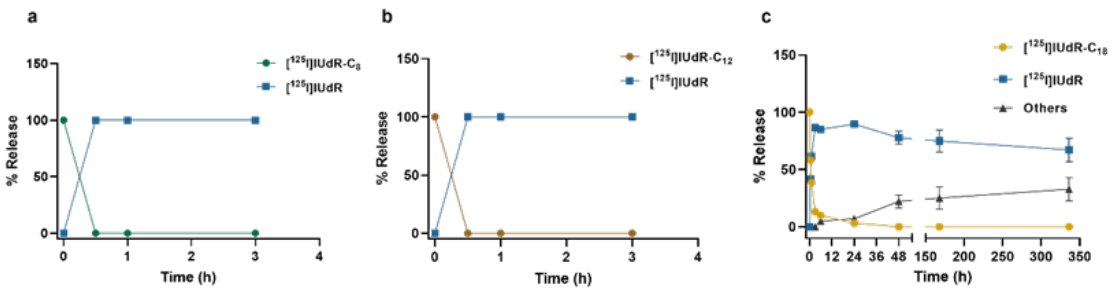

Figure 4. Esterase mediated release of [^{125}I]IUdR from: a) [^{125}I]IUdR-C_8-PMs, b) [^{125}I]IUdR-C_{12}-PMs and c) [^{125}I]IUdR-C_{18}-PMs. Esterase concentration in all release studies was 1 U/mL. The termination of the release study was either when [^{125}I]IUdR is completely released or after 336 hours (14 days). Error bars shown are SD, n=3.

In vitro cell viability study

The cell viability study was conducted using using the CellTiter-Blue assay, with concentrations ranging from 0.12 to 3.8 kBq/mL. The results of cell viability study was shown in **Figure 5.** LN-229 cells were exposed to five groups, [^{125}I]IUdR-C_{18}-PMs with esterase, [^{125}I]IUdR-C_{18}-PMs, [^{125}I]IUdR-C_{18} prodrug with esterase, [^{125}I]IUdR-C_{18}, and free [^{125}I]IUdR, for 7 days to evaluate their ability of cell viability inhibition.

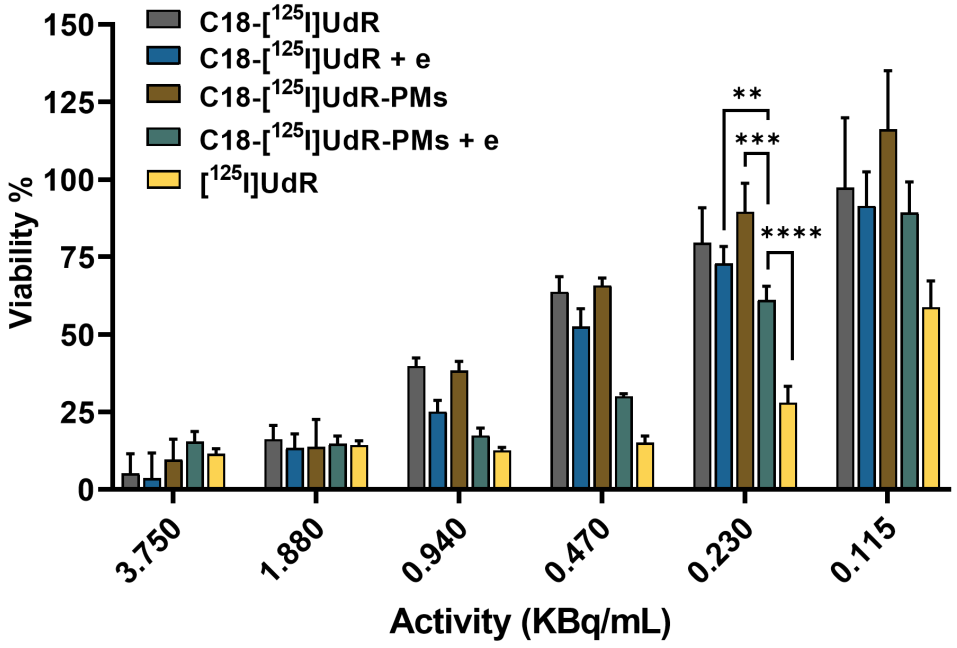

Figure 5. Viability of cells treated with [^{125}I]IUdR-C_{18}-PMs, [^{125}I]IUdR-C_{18} prodrug (with or without esterase), and free [^{125}I]IUdR based on CellTiter-Blue assay in LN229 cell line. Activity ranging from 0.115 – 3.8 kBq/mL. ”e” represents esterase, with the concentration of 0.1U/mL. Two-tailed paired Student *t*-test *P*-values indicate statistical significance (**P*<0.05, ***P*<0.01, ****P*<0.001, *****P*<0.0001). Error bars shown are SD.

Both free [^{125}I]IUdR-C_{18} prodrug and [^{125}I]IUdR-C_{18}-PMs (**Figure 5**, entries gray and brown) showed linear radioactivity correlations with cell viability, as indicated by their respective IC_{50} values of 1.35 kBq/mL and 1.09 kBq/mL. In other words, lower radioactivity was associated with higher cell viability. The potency of esterase-added [^{125}I]IUdR-C_{18} +e and [^{125}I]IUdR-C_{18}-PMs+e (entries blue and green, respectively) were significantly higher, with IC_{50} vslues of 0.86 kBq/mL and 0.51 kBq/mL, respectively. The efficacy of the esterase-treated groups were increased by approximately 2-fold compared to the related non-

esterase added groups. This significant difference was more pronounced in the lower concentration range (0.115-0.94 kBq/mL), while it gradually decreased or even disappeared at concentrations greater than 1.88 kbq/mL. This clearly indicated that cell survival was related to the amount of the released [^{125}I]IUdR. Finally, the positive control free [^{125}I]IUdR (entry yellow) showed the highest efficacy with an IC_{50} of 0.13 kBq/mL. Similarly, the efficiency of [^{125}I]IUdR-C_{18}-PMs+e was observed to be similar to that of free [^{125}I]IUdR at radioactivity levels ≥1.88 kBq/mL.

Negative control groups, such as free iodine-125, blank PMs and esterase were also tested and showed no significant cell killing efficacy. Therefore, this cell viability study demonstrated that [^{125}I]IUdR-C_{18}-PMs showed the possibility to be a candidate for GBM treatment.

DNA incorporation assay

The DNA incorporation assay was employed to investigate the integration of [^{125}I]IUdR-C_{18}-PMs with esterase added and free [^{125}I]IUdR into the DNA of proliferating LN229 cells. Both samples consisted activity of 30 kBq, and incubated with LN229 cells for either 1 or 4 hours. The results, presented **Figure 6**, showed that both groups experienced an increase in DNA uptake efficiency over time. Specifically, the cells exposed to free [^{125}I]IUdR incorporated 3.7% of the introduced activity after a 4-hour incubation, while the cells treated with [^{125}I]IUdR-C_{18}-PMs+e had around 0.5%. This difference in incorporate efficiency among there two groups was notable. However, when evaluating varying incubation durations for [^{125}I]IUdR-C_{18}-PMs+e, there was a significantly higher incorporation after 4 hours compared to 1 hour.

The fact that free [^{125}I]IUdR displayed a more immediate and marked DNA incorporation efficiency than [^{125}I]IUdR-C_{18}-PMs+e was aligned with our expectation. This difference could be traced to that, on one hand, the free [^{125}I]IUdR were integrated efficiently by proliferating cells as they were easily accessed in the media. On the other hand, the gradual release of [^{125}I]IUdR from [^{125}I]IUdR-C_{18}-PMs led to its reduced uptake efficiency.

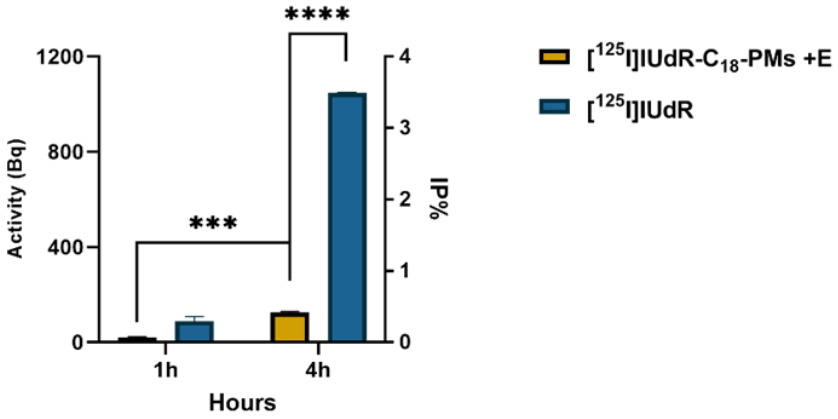

Figure 6. *In vitro* DNA incorporation of [^{125}I]IUdR-C_{18}-PMs with esterase (0.1U/mL) and free [^{125}I]IUdR after 1 or 4 hours of incubation. Data was represented in terms of the percentage of incorporation (IP%). Two-tailed paired Student *t*-test *P*-values indicate statistical significance (***P*<0.01, ****P*<0.001, *****P*<0.001). Error bars shown are SD.

Discussion

In our study, we described a polymeric micelles based delivery platform for the delivery of the Auger electron radiotherapeutic agent, [^{125}I]IUdR, for the purpose of targeting the infiltrative cells within glioblastoma.

Since micelles have different structures from liposomes, the size, formulation procedures, release rates, and cellular efficacy of drug-loaded micelles are also worthy of investigation. To ensure the effective incorporation of [^{125}I]IUdR into the micelles, we still focused on the previously investigated prodrugs of [^{125}I]IUdR, especially [^{125}I]IUdR-C_8, -C_{12}, and -C_{18}. These were strategically modified with linear alkyl chains at the 5' hydroxyl position of the deoxyribose via an ester bond. These lipophilic chains facilitated their insertion into the micelle's hydrophobic core, thus integrating [^{125}I]IUdR. Distinct from the post-insertion approach for liposomes, the nanoprecipitation or pre-insertion method proved superior for micelle drug encapsulation. A notable advantage was that hydrophobic radioactive prodrugs seamlessly self-assembled into micelles in aqueous solutions after the polymer had been pre-dissolved in an organic medium. This method was not only expedient but also streamlined. Conversely, the post-insertion technique demanded elevated micelle concentrations, and the micelle's hydrophilic PEG shell potentially impeded the lipophilic prodrug integration, compromising loading efficacy.

Upon evaluation, prodrug-loaded micelles, termed [^{125}I]IUdR-Cn-PMs, unveiled a fast release profile in the presence of esterases, with [^{125}I]IUdR-C_8, and -C_{12} being completely hydrolyzed in 30 mins.. This could be attributed to the relatively shorter lipophilic carbon chains, which might have compromised prodrug stability. Compared to liposomes containing 5% mol PEG_{2k}, which displayed a loose mushroom-like PEG layer that potentially allowing the reintroduction of free prodrugs, polymeric micelles derived from the $PLGA_{10K}$-$mPEG_{5k}$ polymer presented a dense brush-like surface. This tight configuration reduced the likelihood of liberated prodrugs re-entering the core, promoting their rapid enzymatic hydrolysis.

4 Summary and outlook

In conclusion, an approach based on [^{125}I]IUdR prodrugs loaded polymeric micelles ([^{125}I]IUdR-Cn-PMs) was successfully developed . The prodrugs, [^{125}I]IUdR-Cn, n = 4, 8, 12 and 18, were the same as the prodrugs used in chapter 2.2. The PMs were prepared using $PLGA_{10k}$-$mPEG_{5k}$ by nanoprecipitation method. A evaluation of the method was conducted using PMs, with the focus on solvent: water (DMF:H_2O) ratios (1:1, 1:2, 1:5, and 1:10, v/v) and polymer concentration (5 mg/mL and 10 mg/mL). At a polymer concentration of 5 mg/mL, the PMs exhibited a size distribution between 71.11-120.96 nm. When the polymer concentration was increased to 10 mg/mL, the size of the PMs ranged from 42.66-83.90 nm. However, no discernible relationship was identified between the solvent: water ratio or polymer concentration and the hydrodynamic size. Nevertheless, the 10 mg/mL and DMF: H_2O ratio (1:10) were elected for the preparation of [^{125}I]IUdR-Cn-PMs for the expectation of a reproduceable size and possible high drug encapsulation efficiency. [^{125}iIIUdR-C_8, -C_{12} and -C_{18} were loaded into PMs with a loading yield (dI%) of 50% ± 7.63, 65% ± 3.61 and 76% ± 4.04, respectively. Due to the poor lipophilicity of [^{125}I]IUdR-C_4, the production of [^{125}I]IUdR-C_4-PMs was unsuccessful (dI% < 5%). The release of [^{125}I]IUdR from [^{125}I]IUdR-Cn-PMs was conducted in PBS buffer (pH 7.4) at 37 ℃ with the addition of esterases (1 U/mL). Both [^{125}I]IUdR-C_8-PMs and [^{125}i]IUdR-C_{12}-PMs reached 100% release of [^{125}I]IUdR in 30 mins. For [^{125}i]IUdR-C_{18}-PMs, a burst 87% release of [^{125}iIIUdR was found in first 3 hours, and remained over 65% after 14 days. The viability study in LN229 cells demonstrated that with the addition of esterases, [^{125}I]IUdR-C_{18}-PMs showed significant cell killing ability compared to the [^{125}I]IUdR-C_{18}-PMs group with no esterases added.(P<0.001 at 0.23 kBq/mL). The DNA incorporation assay also showed increased incorporation with time (1h and 4h, P<0.001)

This work demonstrated that [^{125}I]IUdR-C_{18}-PMs is a possible candidate for GBM treatment. However, this system exhibited a faster release rate of [^{125}I]IUdR compared to [^{125}I]IUdR-C_{18}-LIPs. Therefore, the design of prodrugs for [^{125}I]IUdR can be further optimized, such as introducing long carbon chains containing ester bonds at both the 5' and 3'-OH sites. This means that the release of [^{125}I]IUdR requires two times of esterase hydrolysis, theoretically would slow down the release rate of [^{125}I]IUdR. Another possibility is to use isotopes with a shorter half-life, such as iodine-123 (half-life 13.2h). In this case, although the release rate is fast, the number of decay cycles of iodine-123 still increased compared to iodine-125, thus sufficient Auger electrons will be released to kill cancer cells.

5 References

(1) Alexander, B. M.; Cloughesy, T. F. Adult Glioblastoma. *Journal of Clinical Oncology* **2017**, *35* (21), 2402–2409. https://doi.org/10.1200/JCO.2017.73.0119.

(2) Alifieris, C.; Trafalis, D. T. Glioblastoma Multiforme: Pathogenesis and Treatment. *Pharmacology & Therapeutics* **2015**, *152*, 63–82. https://doi.org/10.1016/j.pharmthera.2015.05.005.

(3) Seker-Polat, F.; Pinarbasi Degirmenci, N.; Solaroglu, I.; Bagci-Onder, T. Tumor Cell Infiltration into the Brain in Glioblastoma: From Mechanisms to Clinical Perspectives. *Cancers* **2022**, *14* (2), 443. https://doi.org/10.3390/cancers14020443.

(4) Johnson, D. R.; O'Neill, B. P. Glioblastoma Survival in the United States before and during the Temozolomide Era. *J Neurooncol* **2012**, *107* (2), 359–364. https://doi.org/10.1007/s11060-011-0749-4.

(5) Furnari, F. B.; Cloughesy, T. F.; Cavenee, W. K.; Mischel, P. S. Heterogeneity of Epidermal Growth Factor Receptor Signalling Networks in Glioblastoma. *Nature Reviews Cancer* **2015**, *15* (5), 302–310.

(6) Cordova, J. S.; Shu, H.-K. G.; Liang, Z.; Gurbani, S. S.; Cooper, L. A.; Holder, C. A.; Olson, J. J.; Kairdolf, B.; Schreibmann, E.; Neill, S. G.; others. Whole-Brain Spectroscopic MRI Biomarkers Identify Infiltrating Margins in Glioblastoma Patients. *Neuro-oncology* **2016**, *18* (8), 1180–1189.

(7) El Kheir, W.; Marcos, B.; Virgilio, N.; Paquette, B.; Faucheux, N.; Lauzon, M.-A. Drug Delivery Systems in the Development of Novel Strategies for Glioblastoma Treatment. *Pharmaceutics* **2022**, *14* (6), 1189. https://doi.org/10.3390/pharmaceutics14061189.

(8) Zhang, Y.; Huang, Y.; Li, S. Polymeric Micelles: Nanocarriers for Cancer-Targeted Drug Delivery. *Aaps Pharmscitech* **2014**, *15*, 862–871.

(9) Alphandéry, E. Nano-Therapies for Glioblastoma Treatment. *Cancers* **2020**, *12* (1), 242.

(10) Torchilin, V. P. Micellar Nanocarriers: Pharmaceutical Perspectives. *Pharmaceutical research* **2007**, *24*, 1–16.

(11) Ma, X.; Huang, X.; Huang, G.; Li, L.; Wang, Y.; Luo, X.; Boothman, D. A.; Gao, J. Prodrug Strategy to Achieve Lyophilizable, High Drug Loading Micelle Formulations Through

Diester Derivatives of β-Lapachone. *Advanced Healthcare Materials* **2014**, *3* (8), 1210–1216. https://doi.org/10.1002/adhm.201300590.

(12) Matsumura, Y.; Maeda, H. A New Concept for Macromolecular Therapeutics in Cancer Chemotherapy: Mechanism of Tumoritropic Accumulation of Proteins and the Antitumor Agent Smancs. *Cancer research* **1986**, *46* (12_Part_1), 6387–6392.

(13) Quader, S.; Liu, X.; Chen, Y.; Mi, P.; Chida, T.; Ishii, T.; Miura, Y.; Nishiyama, N.; Cabral, H.; Kataoka, K. cRGD Peptide-Installed Epirubicin-Loaded Polymeric Micelles for Effective Targeted Therapy against Brain Tumors. *Journal of controlled release* **2017**, *258*, 56–66.

(14) Ahmed, M. H.; Canney, M.; Carpentier, A.; Thanou, M.; Idbaih, A. Unveiling the Enigma of the Blood–Brain Barrier in Glioblastoma: Current Advances from Preclinical and Clinical Studies. *Current Opinion in Oncology* **2023**. https://doi.org/10.1097/CCO.0000000000000990.

(15) Wolburg, H.; Noell, S.; Fallier-Becker, P.; Mack, A. F.; Wolburg-Buchholz, K. The Disturbed Blood–Brain Barrier in Human Glioblastoma. *Molecular aspects of medicine* **2012**, *33* (5–6), 579–589.

(16) Bobo, R. H.; Laske, D. W.; Akbasak, A.; Morrison, P. F.; Dedrick, R. L.; Oldfield, E. H. Convection-Enhanced Delivery of Macromolecules in the Brain. *Proceedings of the National Academy of Sciences* **1994**, *91* (6), 2076–2080.

(17) Autier, L.; Clavreul, A.; Cacicedo, M. L.; Franconi, F.; Sindji, L.; Rousseau, A.; Perrot, R.; Montero-Menei, C. N.; Castro, G. R.; Menei, P. A New Glioblastoma Cell Trap for Implantation after Surgical Resection. *Acta Biomaterialia* **2019**, *84*, 268–279. https://doi.org/10.1016/j.actbio.2018.11.027.

(18) Barua, N. U.; Gill, S. S.; Love, S. Convection-Enhanced Drug Delivery to the Brain: Therapeutic Potential and Neuropathological Considerations: Convection-Enhanced Drug Delivery to the Brain. *Brain Pathology* **2014**, *24* (2), 117–127. https://doi.org/10.1111/bpa.12082.

(19) Lonser, R. R.; Sarntinoranont, M.; Morrison, P. F.; Oldfield, E. H. Convection-Enhanced Delivery to the Central Nervous System. *Journal of neurosurgery* **2015**, *122* (3), 697–706.

(20) Kim, S.; Shi, Y.; Kim, J. Y.; Park, K.; Cheng, J.-X. Overcoming the Barriers in Micellar Drug Delivery: Loading Efficiency, in Vivo Stability, and Micelle–Cell Interaction. *Expert*

opinion on drug delivery **2010**, *7* (1), 49–62.

(21) Bernal, G. M.; LaRiviere, M. J.; Mansour, N.; Pytel, P.; Cahill, K. E.; Voce, D. J.; Kang, S.; Spretz, R.; Welp, U.; Noriega, S. E.; Nunez, L.; Larsen, G.; Weichselbaum, R. R.; Yamini, B. Convection-Enhanced Delivery and in Vivo Imaging of Polymeric Nanoparticles for the Treatment of Malignant Glioma. *Nanomedicine-Nanotechnology Biology and Medicine* **2014**, *10* (1), 149–157. https://doi.org/10.1016/j.nano.2013.07.003.

(22) Saucier-Sawyer, J. K.; Seo, Y.-E.; Gaudin, A.; Quijano, E.; Song, E.; Sawyer, A. J.; Deng, Y.; Huttner, A.; Saltzman, W. M. Distribution of Polymer Nanoparticles by Convection-Enhanced Delivery to Brain Tumors. *Journal of Controlled Release* **2016**, *232*, 103–112. https://doi.org/10.1016/j.jconrel.2016.04.006.

(23) Sawyer, A. J.; Saucier-Sawyer, J. K.; Booth, C. J.; Liu, J.; Patel, T.; Piepmeier, J. M.; Saltzman, W. M. Convection-Enhanced Delivery of Camptothecin-Loaded Polymer Nanoparticles for Treatment of Intracranial Tumors. *Drug Delivery and Translational Research* **2011**, *1* (1), 34–42. https://doi.org/10.1007/s13346-010-0001-3.

(24) Madsen, K. L.; Therkelsen, A. S. N.; Langkjær, N.; Olsen, B. B.; Thisgaard, H. Auger Electron Therapy of Glioblastoma Using [125I]5-Iodo-2′-Deoxyuridine and Concomitant Chemotherapy – Evaluation of a Potential Treatment Strategy. *Nuclear Medicine and Biology* **2021**, *96–97*, 35–40. https://doi.org/10.1016/j.nucmedbio.2021.03.001.

(25) Lehnert, S.; Li, Y.; Bump, E.; Riddoch, B.; Chenite, A.; Shive, M. 125I-Iododeoxyuridine for the Treatment of a Brain Tumor Model: Selection of Conditions for Optimal Effectiveness. *The Open Nuclear Medicine Journal* **2011**, *3* (1).

(26) Semnani, E.; Wang, K.; Adelstein, S.; Kassis, A. 5-[123I/125I]Iodo-2′-Deoxyuridine in Metastatic Lung Cancer: Radiopharmaceutical Formulation Affects Targeting. *Journal of nuclear medicine : official publication, Society of Nuclear Medicine* **2005**, *46*, 800–806.

(27) Thisgaard, H.; Halle, B.; Aaberg-Jessen, C.; Olsen, B. B.; Therkelsen, A. S. N.; Dam, J. H.; Langkjær, N.; Munthe, S.; Någren, K.; Høilund-Carlsen, P. F.; Kristensen, B. W. Highly Effective Auger-Electron Therapy in an Orthotopic Glioblastoma Xenograft Model Using Convection-Enhanced Delivery. *Theranostics* **2016**, *6* (12), 2278–2291. https://doi.org/10.7150/thno.15898.

(28) Dupertuis, Y. M.; Vazquez, M.; Mach, J.-P.; De Tribolet, N.; Pichard, C.; Slosman, D. O.; Buchegger, F. Fluorodeoxyuridine Improves Imaging of Human Glioblastoma Xenografts

with Radiolabelled Iododeoxyuridine. *Cancer research* **2001**, *61* (21), 7971–7977.

(29) Kassis, A. I.; Dahman, B. A.; Adelstein, J. S. In Vivo Therapy of Neoplastic Meningitis with Methotrexate and 5-[^{125} I]Iodo-2'-Deoxyuridine. *Acta Oncologica* **2000**, *39* (6), 731–737. https://doi.org/10.1080/028418600750063802.

(30) Armstrong, R. D.; Diasio, R. B. Metabolism and Biological Activity of 5'-Deoxy-5-Fluorouridine, a Novel Fluoropyrimidine. *Cancer Research* **1980**, *40* (9), 3333–3338.

(31) Aparicio-Blanco, J.; Torres-Suárez, A.-I. Glioblastoma Multiforme and Lipid Nanocapsules: A Review. *j biomed nanotechnol* **2015**, *11* (8), 1283–1311. https://doi.org/10.1166/jbn.2015.2084.

(32) Gharibkandi, N. A.; Gierałtowska, J.; Wawrowicz, K.; Bilewicz, A. Nanostructures as Radionuclide Carriers in Auger Electron Therapy. *Materials* **2022**, *15* (3), 1143. https://doi.org/10.3390/ma15031143.

Chapter 4

Continuous & Sustained Release of Cytotoxic [^{125}I]IUdR from a Modified Cyclononyne-Functionalized PeptoBrush for Auger-radiotherapy of Glioblastoma

---

Qing Tang,[1] Gabriela Schäfer,[3] Heyang Zhang,[3] Matthias Barz,[3*] Natan J.W. Straathof,[1,2,*] Andreas I. Jensen[1,2,*]

[1]DTU Denmark, Institut for Sundhedsteknologi, Risø Campus, Frederiksborgvej 399 (Bygning 202), 4000 Roskilde.

[2]DTU Denmark, Department of Health Technology, Lyngby Campus, Ørsteds Plads (building 345C), DK-2800 Kgs. Lyngby.

[3]Leiden Academic Centre for Drug Research (LACDR), Leiden University, Einsteinweg 55, 2333, CC, Leiden, the Netherlands

*corresponding author: atije@dtu.dk, njwst@dtu.dk and m.barz@lacdr.leidenuniv.nl

The work in this chapter will be represented as full manuscript.

1 Introduction

Glioblastoma, often referred to as glioblastoma multiforme (GBM), is an aggressive, highly malignant and the most lethal primary brain tumour that originates in the glial cells of the central nervous system.[1–3] These tumours are marked by genetic and molecular heterogeneity, which contributes to their aggressive behaviour and resistance to therapies.[3–5] Common genetic alterations observed in glioblastoma include mutations in genes such as EGFR (epidermal growth factor receptor), TP53 (tumour protein 53), and IDH1 (isocitrate dehydrogenase 1), among others.[6–9]

This complex and challenging tumour is characterized by its rapid growth, infiltrative nature, and resistance to traditional treatment approaches, including surgery, radiation therapy, and chemotherapy.[10–12] However, due to the tumour's infiltrative nature, it is often challenging to remove all cancerous cells, and recurrence is therefore very common, leading to an average medium survival rate of 5% in 18 months.[13,14] Research efforts are therefore focusing on alternative more effective treatment strategies, including targeted radiotherapies,[15,16] immunotherapies,[17–19] and personalized medicine approaches tailored to the genetic profile of individual tumours. [20–22]

Drug delivery to the brain, particularly in the context of treating glioblastoma, presents a myriad of challenges that stem from the intricate nature of the central nervous system and the unique characteristics of the tumour itself.[23,24] Overcoming the obstacles associated with delivering therapeutic agents effectively to this challenging environment is crucial for improving patient outcomes. One of the most common, but significant, challenges is the presence of the blood-brain barrier, a specialized barrier that tightly regulates the passage of substances between the bloodstream and the brain.[25] While it serves to protect the brain from harmful agents, it also impedes the delivery of therapeutic drugs. GBM further disrupts the BBB, causing increased permeability, but this phenomenon is often heterogeneous and not uniform throughout the tumour.[26,27] Even if drugs can breach the blood-brain barrier, they often have limited penetration into the tumour tissue due to its complex microenvironment. The dense extracellular matrix and interstitial fluid pressure within the tumour can hinder uniform drug distribution.[28] Another challenge is tumour heterogeneity, which means GBM are genetically and phenotypically diverse, thereby drugs may not effectively target all aspects of the tumour and therefore contributing to treatment resistance.[29,30] Most notably, GBM cells infiltrate surrounding brain tissue, making

it difficult to remove the tumour entirely through surgery and challenging to deliver drugs specifically to tumour cells without affecting healthy brain tissue.[31,32] The infiltrative nature of the GBM is imaginably the greatest challenge to effectively combat this cancer type, and demands a targeted and localized drug delivery approach to minimize collateral healthy cell damage.[33,34]

[^{125}I]Iododeoxyuridine, also referred to as [^{125}I]IUdR, is a radiolabelled nucleoside analogue of deoxyuridine that contains a 125-iodine isotope (**Figure 1**, Bottom Right-side). This compound serves as a valuable tool for labelling DNA or DNA precursors within cells, enabling the study of DNA synthesis and metabolism.[35] This property also makes it effective in impairing the growth of cancer cells, especially tracking down and compromising the effects of infiltrating glioblastoma stem-cells.[35,36] When [^{125}I]IUdR is incorporated into DNA, the radioactive decay of iodine-125 emits Auger electrons (with a half-life of 59.8 days). These high-energy Auger electrons (ranging from 4 to 25 keV/µm) cause disruption to the DNA's chemical bonds in the nearby vicinity, ultimately resulting in cellular death. Through this mechanism, [^{125}I]IUdR has demonstrated remarkable efficacy in eliminating glioblastoma cancer cells and retarding the metastatic processes.[37,38]

Certain therapeutic agents, including [^{125}I]IUdR, inherently face challenges due to their instability or rapid metabolism, posing difficulties in achieving effective delivery to and within the brain over extended periods.[39] Ensuring drug stability and sustained release within the brain environment becomes imperative. This critical task can be achieved through the utilization of polymer based nanocarriers, which have demonstrated remarkable success in drug delivery. Polymer based nanocarriers, specifically liposomes and polymeric micelles, are at the forefront of revolutionizing drug delivery systems.[34,40,41] They enable precise transportation and targeted release of therapeutic agents. These carriers possess minuscule dimensions (ranging from 40 to 120 nm) and customizable characteristics, providing innovative solutions to issues such as limited drug penetration and unintended cytotoxic side effects (as depicted in **Figure 1**).[42,43] One of the key features of these nanocarriers is their enhanced bioavailability, through means of a polyethylene glycol (PEG) surface modification. In brief, a PEG surface (modification) increases systemic circulation by reducing the recognition and clearance by the reticuloendothelial system (RES). To illustrate this further, several PEG-modified lipid formulations such as Doxil, Onivyde, Onpattro, Comirnaty, and Spikevax have attained FDA approval.[44,45] While this achievement is noteworthy, there have emerged certain instances raising concerns in the realm of toxicology and immunol-

ogy linked to PEG-modified drugs, encompassing phenomena like auto-immune response and accelerated blood clearance.[46–48] Of particular note is the undesirable effect of the latter, as it diminishes the therapeutic impact of nanocarriers, thereby necessitating more frequent administrations. This contradicts a primary advantage of nanocarriers – their capacity to prolonged sustainably deliver therapeutic agents.

This said, an alternative polymer featuring similarities, are polypeptides and polypeptoids, containing base amino acids, and polysarcosine (N-methylated). These novel nanostructures, polypept(o)ides, have been defined as hybrid materials consisting of polypeptides and polypeptoids.[49–51] They, also known as PeptoBrush (PB), have recently emerged as an alternative to substitute PEG in protein conjugates, drug formulations, drug-delivery systems, imaging or theragnostic applications, since they are able to combine synthetic precision and high functionality of synthetic materials.[52,53] (e.g. unnatural amino acids). For this purpose, PeptoBrushes appear to be ideal (alternative) candidate for drug delivery in the brain. They can be used to build up core–shell structures that allow for high loading of lipophilic compounds, including chemical moieties that can *connect* the drug load to the polymer, without the risk of aggregation and with the possibility to protection these moieties against degradation. They intrinsically combine a 3D structure and the multi-functionality of polypeptides with structural flexibility and “stealth-like” properties of polysarcosine. Moreover, these types of polymers are reported to be highly biocompatible (nontoxic and nonimmunogenic) and have been demonstrated for EPR-mediated tumour targeting due to their smaller size (<40 nm, see **Figure 1**, Top).[53] The latter is especially advantageous as smaller nanocarriers will have a much better distribution when administered in the cerebral region, leading to increased therapeutic effectiveness, while covering a larger section of the cerebral tissue. From this, it is clear that PeptoBrush offers different and unique opportunities through its design as opposed to the aforementioned nanocarriers, such as liposomes and polymeric micelles (see also **Figure 1** Bottom Box). We propose that a continuous and sustained release of [^{125}I]IUdR could present a more potent strategy for glioblastoma treatment, opposed to (or combined with) the current treatment strategy. Hence the use of a grafted drug to a polymer could be highly beneficial as opposed to a *loaded* nano-particles due to a dissimilar load-and-release methodology.

With this in mind, the research design aims to investigate the potential synergistic effects of combining [^{125}I]IUdR and PeptoBrush as a novel therapeutic approach for glioblastoma treatment. This study seeks to leverage the distinct attributes of both [^{125}I]IUdR, an Auger-

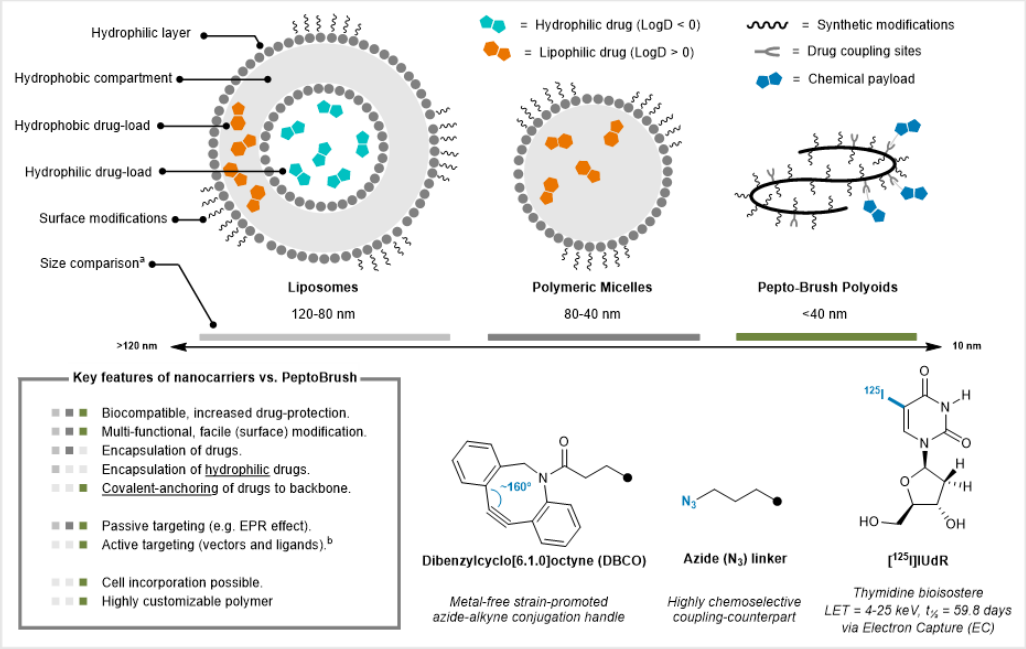

Figure 1. Comparison of different nano-carriers as drug delivery systems (liposomes, polymeric micelles and the PeptoBrush). Top: different structure, drug-loading capacity, features and size (non-uniform representation done for clarity). [a]Note to size comparison: described sizes are generalized but not limited to these sizes. Bottom Box: summary of key features, compared. [b]Note: while active targeting with NPs is possible its usually applied with pretargeting strategy. Bottom Right-side: chemical components for [^{125}I]IUdR drug loading of the PeptoBrush.

therapeutic agent capable of high DNA damage to glioblastoma cells, and the PeptoBrush, a polypeptoid nanocarrier which allows precise synthetic pre-functionalization. The PeptoBrush will be functionalized with a bio-conjugative coupling handle, while [^{125}I]IUdR will be functionalized with the concomitant coupling partner. This strategic approach will enable the direct covalent loading of [^{125}I]IUdR onto the PB polymer. Notably, the linker that connects [^{125}I]IUdR to its coupling partner will contain an ester linkage. Which possesses the capability to undergo *in vivo* hydrolysis through various mechanisms of action, including esterases. Esterase-mediated hydrolysis serves as a remarkable pathway for drug activation and controlled release. When prodrugs or drug carriers are designed as such, they remain inert until encountering esterases *in vivo*. These enzymes trigger the hydrolysis of the ester bond, leading to the release of [^{125}I]IUdR into its active form. This process is highly advantageous, as it allows for the precise modulation of drug activity and localized therapeutic effects. Other enzymes, such as amidases and lipases, can also contribute to the breakdown of specific chemical bonds. Hence, the diverse array of these enzymes facilitates the targeted release and activation of [^{125}I]IUdR *in vivo* from the PB in a facile manner.

2 Materials and methods

Chemicals and reagents. All reagents and solvents were bought from commercial suppliers; VWR International, Sigma-Aldrich, ABCR Chemicals, FluoroChem or TCI Chemicals, and were used as received. Dry dimethylformamid (DMF) was degassed by three freeze-pump thaw cycles to remove residual dimethyllamine before using. Tetrahydrofuran (THF) and n-hexane were dried over sodium and THF was freshly distilled before use. N,N-Diisopropylethylamine (DIPEA), N,N-triethylamine (TEA) and neopentylamine were dried over sodium hydroxide and distilled on molecular sieves. Iodine-125 (^{125}I) was bought from PerkinElmer (NEZ0330##MC, where ## is the amount of mCi, e.g. 10 mCi = 10, NEZ033010MC) as a [^{125}I]NaI/NaOH in H_2O solution (Specific Activity: 1□7 Ci/mg, 0.1M NaOH, pH = 12–14). Deuterated solvents were obtained from Deutero GmbH or VWR. Dialysis was carried out using Spectra/Por membranes (Roth) with 6-8 kDa molecular weight cut-off.

Equipment and analysis. The hydrodynamic diameter ($Ø_{hyd}$) and zeta potential of the prepared nanoparticles (NPs) were measured by dynamic light scattering (DLS) on a ZetaPALS (Brookhaven Instruments Limited, USA). Unless stated otherwise, $Ø_{hyd}$ and analysis were performed in isotonic HEPES buffer (150 mM NaCl, 10 mM HEPES, pH 7.4) at 25°C, and were done in quintuplets. Osmolarity was measured on a Gonotec Osmomat 010/030-D (Gonotec Gmbh, Germany). Radio-HPLC was performed on a Hitachi Chromaster equipped with a Hitachi 5160 manual purge quaternary gradient pump, coupled to a Hitachi 5260 thermostat loop autosampler, a Hitachi 5310 column oven, a Hitachi 5430 UV-Vis multichannel detector and a radio-detector (gamma) with analogue output and ca. 0.2 min signal delay. Unless stated otherwise, routine HPLC analysis was performed using a Luna C18(2) (Ø = 2.5 µm, 100 Å) column using a 20 min program, with a 0-100 H_2O/MeCN + 0.1% TFA gradient. Routine quantification of radioactivity was performed on a Capintec CRC-55tR dose calibrator (DoseCall), and reported in Becquerel (Bq). If applicable, liquid scintillation counting (LSC) measurements were performed on a HIDEX 425-034 LSC for routine analysis, or on a HIDEX 300-SL LSC for large batch analysis, and reported in Becquerel (Bq), or counts per minute (cpm). Radio-TLC analysis was performed with a PerkinElmer Cyclone Plus phosphor imager on commercially TLC pre-coated aluminium sheets (4 x 10 cm, Merck Silica gel 60), and unless stated otherwise run in 10% MeOH in DCM. Radio chemical conversion (RCC) is always based on the relative converted substance, judged by

Radio-TLC. Radio chemical yield (RCY) is based on the collected activity of the radiolabeled product, judged by DoseCall or LSC, and (if stated) decay corrected. Metal content (ICP) was performed on an ICP-OES iCAP 7000 Plus Series (Thermo Fisher Scientific), using the relevant reference metal standard curve, prepared with metal-free 1% HCl in H_2O. Size exclusion purification was performed on DP-10 (PD MidiTrap G-25 columns contain Sephadex G-25 resin) bought from Cytiva Sweden, using the relevant buffer (e.g., PBS (pH = 7.4), or HEPES (pH = 7.3) at 25 °C in MiliQ-H_2O (18.2 MΩ·cm).

Analytical gel permeation chromatography (GPC) was carried out at 40 °C with a flow rate of 1.0 mL/min using hexafluoroisopropanol (HFIP) as eluent, equipped with 3 g/L potassium trifluoroacetate. Column material was modified silica gel (PFG columns, particle size: 7 µm, porosity: 100 100 Å and 4000 Å). The system was equipped with a UV detector (Jasco UV-2075 plus) set at a wavelength of 230 nm (unless otherwise mentioned) and an RI detector (Jasco RI-2031). Molecular weights were determined by using a calibration with poly(methyl methacrylate) (PMMA) standards (Polymer Standards Services GmbH, Germany) and toluene as an internal standard. The elution diagram was evaluated with PSS WinGPC (Polymer Standard Service GmbH, Germany). Degree of polymerization (DP) of polysarcosine (pSar) was determined by calibration of apparent Mn against a series of pSar standards characterized by static light scattering to obtain absolute molecular weights. The samples were filtered through polytetrafluoroethylene (PTFE) syringe filters with a pore size of 0.2 µm.

Synthesis of ((2R,3S,5R)-3-hydroxy-5-(5-iodo-2,4-dioxo-3,4-dihydropyrimidin-1(2H)-yl)tetrahydrofuran-2-yl)methyl 4-azidobutanoate (IUdR-N_3). A round-bottom flask was equipped with a stirring bar and charged with 3'-TBDMS-5'-C4-Azide-IUdR (250 mg, 0.44 mmol), from the previous step, and dissolved into dry THF (10 mL). The mixture was cooled down to 0 °C, using an ice-bath. To this mixture was added dropwise a solution of TBAF in THF (1M, 1 mL, 1 mmol) while stirring at 0 °C. After 10 minutes, the ice-bath was removed, and the mixture was allowed to warm up to room temperature. The reaction was monitored by TLC (10% MeOH in DCM), until all starting material was consumed. If full consumption was not reached after 2 hours stirring at room temperature, an extra portion of TBAF in THF (1 M, 0.25 mL, 0.25 mmol) was added dropwise. After complete consumption of the starting material, the reaction mixture was diluted with EtOAc (25 mL) and transferred into an extraction funnel. The organic mixture was washed consecutively

with 1 M HCl, sat. $NaHCO_3$ in H_2O and brine. The combined organic layers were collected and dried over MgSO4, filtered, and concentrated in vacuo. The crude product was then further purified by SiO_2 column chromatography (5% MeOH in DCM) to give the title product as a glassy substance (200 mg, 95% yield). The compound can be crystallized using $CHCl_3$, to give a clear white solid powder.

Synthesis of Homopolymers

Poly(g-benzyl-l-glutamic acid)(pGlu(OBn). The synthesis was adapted from literature.[1] Prior to solvation in dry dimethylformamide (DMF) (5 mL) *g*-benzyl-l-glutamate (Glu(OBn)) N-Carboxyanhydride (NCA) (480 mg, 1.82 mmol) was transferred into a predried Schlenk-flask equipped with a stir bar under nitrogen counter flow. The NCA was dried under high vacuum, dissolved and a stock solution of neopentylamine (1.59 mg, 0.02 mmol, 1 eq) in absolute DMF (500 mL) was added to the solution to initiate the polymerization. The mixture was allowed to stir at 0 °C under nitrogen atmosphere for 72 h. Progress of the reaction was monitored by. FTIR Spectroscopy and showed disappearance of the NCA peaks (1855 and 1788 cm^{-1}). After completion of the polymerization the amine end group was capped by adding acetic anhydride (26.9 mg, 0.09 mmol, 5 eq) and triethylamine (18.5 mg,0.18 mmol, 10 eq) to the solution and allowed to stir overnight at room temperature. The polymer was precipitated into diethyl ether and centrifuged (5000 rpm at 4 °C for 10 min). After the liquid fraction was discarded the polymer was resuspended in diethyl ether and centrifuged again. This step was repeated one more time and the polymer was dried under high vacuum to afford a colorless solid (362 mg, 90% yield).

^{1}H NMR (400 MHz, CD2Cl2) δ 8.42 (s, 60H), 7.58 – 7.04 (m, 435H), 5.08 (s, 170H), 4.01 (s, 82H), 2.50 (d, J = 136.3 Hz, 327H), 0.94 (d, J = 11.0 Hz, 9H).

Polyglutamic Acid. $pGlu(OBn)_{100}$ (263 mg) was transferred in a Schlenk flask equipped with a stir bar and dissolved in trifluoroacetic acid (TFA) (2.5 mL). Hydrobromic acid (HBr, 48% v/v) (240 mL, 2 eq) was added to the mixture dropwise and the solution was allowed to stir overnight at room temperature. The polymer was precipitated into cold diethyl ether and centrifuged (5000 rpm at 4 °C for 10 min). After the liquid fraction was discarded the polymer was resuspended in diethyl ether and again centrifuged. This step was repeated one more time. The crude product was dissolved in water and lyophilized to obtain a col-

orless solid (105 mg, 92% yield).

^{1}H NMR (400 MHz, D2O) δ 4.18 (dd, J = 9.0, 5.5 Hz, 112H), 2.13 (tdd, J = 15.3, 12.2, 7.9 Hz, 232H), 1.97 – 1.72 (m, 233H), 0.75 (s, 9H).

Polysarcosine. Synthesis was carried out according to literature in a similar way as previously described.[1] Sarcosine NCA (1077.3 mg, 9.36 mg) was transferred into a predried Schlenk flask equipped with a stir bar under nitrogen counter flow. The NCA was dried under high vacuum and dissolved in absolute DMF (mL). A stock solution of neopentylamine (8.2 mg, 0.09 mmol, 1 eq) in DMF (10 mL) was added to the NCA to initiate the polymerization. Progress of the reaction was detected by FTIR Spectroscopy and showed disappearance of the NCA peaks (1855 and 1788 cm^{-1}). After completion of the polymerization the mixture was precipitated into diethyl ether and centrifuged (5000 rpm at 4 °C for 10 min). The crude product was resuspended in diethyl ether and again centrifuged. This procedure was repeated for one more time. The polymer was dried, dissolved in water and lyophilized to obtain a colorless fluffy polymer (662.5 mg, 98 % yield).

^{1}H NMR (400 MHz, DMSO) δ 4.51 – 3.81 (m, 215H), 3.17 – 2.56 (m, 331H), 0.85 (d, J = 9.6 Hz, 9H).

DBCO Functionalization

DBCO-pGlu(OBn). In a Schlenk flask equipped with a stir bar pGlu(OBn)$_{100}$ (88.3 mg, 0.01 mmol, 1 eq) was dissolved in MQ water (8 mL) and $NaHCO_3$ (339.9 mg, 3.39 mmol, 5 eq) as well as 4-(4,6-dimethoxy-1,3,5-triazin-2-yl)-4-methyl morpholinium chloride (DMTMMCl) (187.9 mg, 0.67 mmol, 1 eq) were added to the solution. Prior to the addition of dibenzocyclooctin (DBCO) to the mixture it was dissolved in dimethylsulfoxid (DMSO) (1.6 mL). The solution was allowed to stir at room temperature for 24 h before adding additional DMTMMCl (187.9 mg, 0.67 mmol, 1 eq). The crude product was purified using dialysis against a 6 – 8 kDa molecular weight cutoff (MWCO) for 3 days against DMSO with daily change of the solvent. After 3 days the product was dialysed against MQ water for one day and lyophilized under obtaining a colorless solid (180.6 mg, 83 % yield).

^{1}H NMR (600 MHz, DMSO) δ 7.77 – 6.90 (m, 134H), 5.33 (s, 2H), 5.02 (d, J = 15.4 Hz, 8H), 4.01 (d, J = 95.3 Hz, 20H), 2.28 – 1.62 (m, 68H), 0.93 – 0.72 (m, 9H).

Polysarcosinylation

PeptoBrush. DBCO-pGlu(OBn) functionalized backbone (22.7 mg, 0.001 mmol, 1 eq), polysarcosine (357.9 mg, 0.04 mmol, 0.4 eq) and $NaHCO_3$ (85.8 mg, 1.02 mmol, 10 eq) were transferred into a Schlenk flask equipped with a stir bar and dissolved in a mixture of MQ water (7 mL) and DMSO (1.4 mL). To the solution DMTMMCl (28.3 mg, 0.12 mmol, 1 eq) was added and the mixture was allowed to stir at room temperature for 24 h. After 24 h, additional DMTMMCl (28.3 mg, 0.12 mmol, 1 eq) was added and stirred overnight. Progress of the reaction was monitored by size exclusion chromatography (SEC) analysis. The solution was purified using spinfiltration (MWCO of 20 kDa, volume of 2 mL, 2 x 30 min, 5000 rpm). After centrifugation steps the filtrates were removed and the crude concentrated product was redissolved in MQ water until the volume of 2 mL and centrifuged again. The procedure was repeated for 10 times. The product was lyophilized under obtaining the purified final PeptoBrush (120 mg, 60 % yield).

Synthesis of [^{125}I]IUdR-PB Radiolabelling of [^{125}I]IUdR labelled Peptobrush- dibenzoazacyclooctyne (PB-DBCO) via Copper-free click reaction. 3MBq of [^{125}I]IUdR-N3 in 200µL MeCN was transferred to a HPLC vial and dried down under argon flow, then 50 µL of DMSO was added to the HPLC vial and vomit gently. 2mg of PB-DBCO in 200 µL PBS was added to the reaction vial. The vial was then incubated at 40℃ degrees for 60 min. Withdraw an aliquot (1 µL) from the crude product and apply it onto a TLC plate that using 10%MeOH in DCM as mobile phase. The TLC plate was then analysed using the Cyclone. After 1h, 300µL of PBS was added to the crude reaction before applied to a size exclusion Minitrap column. Fractions were collected every 0.5 mL, for a total of 5mL. Fractions 2 and 3 were pulled together as the final product. Activity of each fraction was measures using dose calibrator, the click efficiency was determinized using the following equation:

Yield= (Activity of Fractions 2 and 3)/(total activity)*100%

Radio purity was measured by aliquoting 1 µL of the final product and apply to radio-TLC.

Esterase mediated release of [^{125}I]IUdR from [^{125}I]IUdR-PB in PBS buffer

Three HPLC vials containing [^{125}I]IUdR-PB dispersion (50 kBq, 1.0 mL) in PBS buffer were continuously stirred at 37 ℃. Esterase powder derived from porcine liver (1 mg, 20 Units) was dissolved in PBS (200 µL) to create a stock solution with a concentration of 100 U/mL.

Subsequently, 10 µL of the esterase stock solution was added to each vial, resulting in a final concentration of 1 U/mL. At various time intervals, 0, 0.5, 1, 3, 6, 24, 48, 120, and 480 hours, aliquots of 5 µL were extracted from the vials. These aliquots were immediately mixed with 15 µL of tetrahydrofuran (THF) to halt the enzymatic hydrolysis and disrupt the brush structure. The resulting mixture was then subjected to analysis using radio-TLC to quantify the ratios of [^{125}I]IUdR and [^{125}I]IUdR-PB.

DNA incorporation assay

LN-229 cells were grown in Dulbecco's modified Eagle's medium (DMEM) growth medium with a pH = 7.4, supplemented with 5% fetal bovine serum (FBS), 100 U/mL of penicillin, 2 mM glutamine, and 100 µg/mL of streptomycin according to supplier instructions. Cell cultures were maintained in flasks and grown at 37 °C in a humidified atmosphere of 5% CO2 in air. LN229 cells were seeded on 6-well plates at a density of 0.5×10^6 cells per well before placed in an incubator for 24 hours incubation. Following this, 3 mL of PB-[^{125}I]IUdR (5 kBq/mL) and esterase-containing PB-[^{125}I]IUdR (5 kBq/mL, 0.1 U/mL of esterase) were added to each plate in triplicate. The plates were subsequently incubated for either 4 or 24 hours. At the end of the incubation period, the cellular DNA was collected using the DNA isolation protocol provided by the E.Z.N.A.® Tissue DNA Kit. A 20 µL aliquot of each DNA solution was then utilized for liquid scintillation counting (LSC) measurements.

Cell viability study

To assess the cytotoxicity of PB-[^{125}I]IUdR against LN-229 cells, an in vitro cell viability assay was performed using CellTiter-Blue from Promega. LN-229 cells were seeded in 96-well plates at a density of 300 cells per well and incubated for 24 hours at 37 °C. The samples were divided into five groups for cytotoxicity evaluation: (1) PB-[^{125}I]IUdR, (2) PB-[^{125}I]IUdR+esterase, (3) [^{125}I]IUdR-N_3, (4) [^{125}I]IUdR, and (5) PB. Appropriate amounts of PB-[^{125}I]IUdR, [^{125}I]IUdR-N_3 (dissolved in DMSO), and [^{125}I]IUdR were diluted with complete DMEM culture medium to achieve the desired final radioactivity levels of 0.23, 0.49, 0.98, 1.97, 3.75, 7.5, 15, and 30 kBq/mL. The esterase concentration in group (2) was 0.1 U/mL. The PB group had concentrations of 0.0156, 0.0312, 0.0625, 0.125, 0.25, 0.5, 1, and 2 mg/mL. The plates were incubated for 7 days before being mixed with CellTiter-Blue solution (20 µL per well). Following a 4-hour incubation, the absorbance was measured using a

microplate reader at 570 and 600 nm. The results were expressed as the percentage of cell viability, calculated as (mean optical density (OD) of treated cells/mean OD of untreated cells) × 100%.

3 Results and discussion

Chemistry

PeptoBrush **8** were prepared by grafting DBCO-amine and pSar polymers onto a pGlu acid **4** backbone (**Figure 2**). The hydrophobic pGlu acid backbone (PGlu(OBn)) was prepared by nucleophilic ring-opening polymerization of (S)-benzoic-(S)-3-(2,5-dioxooxazolidin-4-yl)propanoic anhydride **1** and initiated by neopentylamine. Following was a capping and concomitant acidic removal of the benzyl protecting group, to obtain polymer **4** in a yield of 97% (see methods section for details). The chain length of **4** consisted of 100 ± 5 monomer units, which was determined by proton nuclear magnetic resonance spectroscopy (see SI for spectral data). Having the backbone in hand, we incorporated the DBCO functionality. Polymer **4** was mixed with 10% w/w DBCO-amine **5**, under alkaline dehydrating amide coupling conditions, affording intermediate DBCO polymer **6**. The corresponding polymer was further purified by dialysis and subsequent lyophilization. The degree of DBCO functionalization was determined by NMR through quantification of the alkene protons (5.4 - 5.8 ppm) against the original protons, and showed that a 13 DBCO groups were conjugated per polymer. At the same time, pSar-amine **7** was prepared by ring-opening polymerization using N-carboxyanhydride and neopentylamine. The polymer was isolated in a yield of 98%, and the degree of polymerization (D_P) was determined to be 82 and a dispersity value (Đ) of 1.10 was detected by size exclusion chromatography (SEC) using hexafluoroisopropanol (HFIP). Polymer **7** was then reacted with the remaining carboxylic acids of the pGlu acid backbone *via* amide coupling, using DMTMM and $NaHCO_3$ to give the final DBCO-functionalized PeptoBrush **8**. The resulting PeptoBrush were successfully purified by spin-filtration, lyophilized, and analyzed via SEC and DLS. (see **Table 1** and methods section for details). **Table 1** displays a summary of the characteristics for the synthesized PGlu(OBn) (**4**), pSar-amine (**7**), and PeptoBrush (**8**).

Table 1. Characteristics of prepared polymers.

Entry	Polymer	Yield	DP	M_n (kg mol^{-1})	Đ	DLS (nm)	Zeta (mV)
1	PGlu(OBn) **4**	92%	100	13	1.13	n.d.	n.d.
2	pSar **7**	98%	82	5.9	1.10	n.d.	n.d.
3	PB **8**	60%	100/82	250	1.2	7.07 ± 2.01	-21.9±4.13

Next, was the preparation of [^{125}I]IUdR-Azide ([^{125}I]IUdR-N_3). Based on prior studies, it was prevalent that the 5'-hydroxyl group of IUdR can be functionalized with a small ester-linkage, which is labile enough for facile release of [^{125}I]IUdR under enzymatic conditions (see Ref.). This linker will also contain a terminal primary azide moiety (**Figure 2**, compound **2**), which will be used to graft the prodrug to the PeptoBrush. Briefly, previously prepared 3'-TBDMS-IUdR **10** (see SI for details) was mixed with 4-azidobutanoic acid (1.5 equiv.) under amide coupling conditions (DCC, DMAP in DMF), giving us a TBDMS protected IUdR-azide derivative **11** (75% yield). This intermediate was then subjected to TBDMS deprotection conditions, using TBAF in THF, to give **12** (99% yield). Finally, the iodine, on the iodouridine, was replaced with a tri-butylstannyl moiety, using Bu_6Sn_2 (1.5 equiv.), $Pd(Ph_3P)Cl_2$ (20 mol%), in 1,4-dioxane at 130 °C, to give the final precursor **13** for radiochemistry (*vide infra*, see SI for full details). After this, the IUdR-N_3 stannyl derivative **13** (1 mg) was mixed with [^{125}I]NaI, AcOH and Chloramine-T as the oxidant, in DMF at room temperature for 30 minutes, to give [^{125}I]IUdR-Azide, **[^{125}I]12**, in RCC = 99 ± 1%, and with a final RCY = 67 ± 2% after purification and reformulation (n = 4, A_M = 0.03 - 1.67 GBq/µmol)

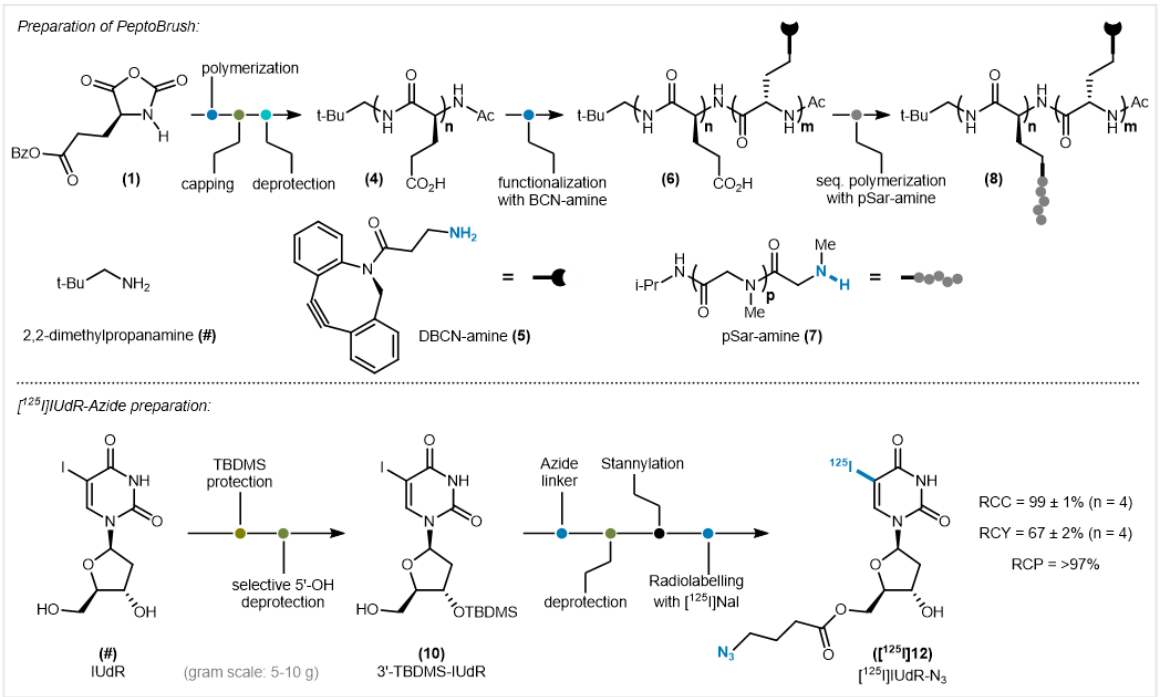

Figure 2. Synthetic overview of DBCO-PeptoBrush synthesis and preparation of [^{125}I]IUdR-N_3 (see Supporting Information for experimental details). Notes and abbreviations: DBCO = dibenzoazacyclooctyne, pSar = polysarcosine, IUdR = iododeoxyuridine.

Synthesis of[^{125}I]IUdR-PB

With [^{125}I]IUdR-N_3 in hand we commenced with the optimization for the *loading* of the PB-DBCO with [^{125}I]IUdR (**Figure 3**).The introduction or loading of [^{125}I]IUdR onto the PB was accomplished by the additive and copper free click reaction, between the azide ([^{125}I]IUdR-N_3) and the DBCO moiety. The formed radiolabelled polymer was refer to as [^{125}I]IUdR-PB. Initially, a test labelling was conducted at room temperature with 0.3 mg of PB-DBCO in 100 µL PBS:MeCN (1:1, v/v), which resulted in 36% RCY (Entry 1). Following this, we increased the temperature during the click reaction, to 37 °C and 40 °C, and changed the solvent system to 10% DMSO in 200 µL PBS (Entry 2 and 3). Meanwhile, amount of PB-DBCO was also increased to 2 mg. The highest loading efficiency was 68 ± 11% at 40 °C (n = 2), while the loading efficiency increased with higher amounts of PB-DBCO polymer concentration (from 41% to 79%, see SI for details). Overall, [^{125}I]IUdR-N_3 was successfully conjugated to PB via the copper free click reaction, and the efficiency was primarily governed by the PB-DBCO polymer amount, and by the increased temperature (**Figure 3**, table).

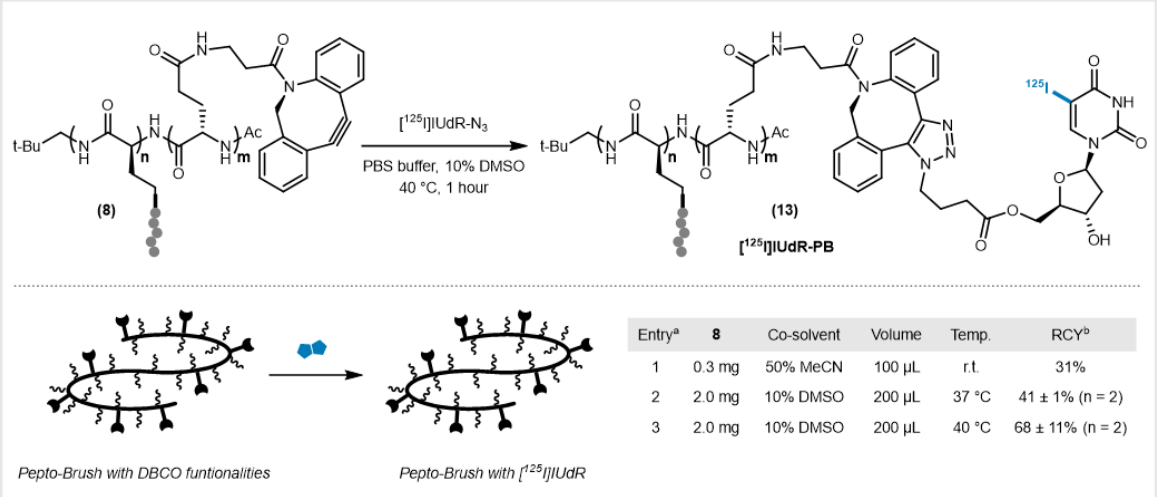

Entry[a]	8	Co-solvent	Volume	Temp.	RCY[b]
1	0.3 mg	50% MeCN	100 µL	r.t.	31%
2	2.0 mg	10% DMSO	200 µL	37 °C	41 ± 1% (n = 2)
3	2.0 mg	10% DMSO	200 µL	40 °C	68 ± 11% (n = 2)

Figure 3. Radiolabelling procedure and illustration of the preparation of [^{125}I]IUdR-PB via copper free click reaction between PB-DBCO and [^{125}I]IUdR-N_3. (see SI for more details). [a]Unless stated otherwise (see table in Figure 3), reagents and conditions: PB-DBCO, [^{125}I]IUdR-N_3, PBS buffer (pH = 7.4), MeCN or DMSO co-solvent, for 1 hour. Analyzed by Rad-TLC (RCC, see SI) and measured by Dose-CAL (RCY, activity yield of the final product). [b]RCY = Radio chemical yield of the final product, calculated by: RCY = A_{prod} / A_{start} (non-decay corrected).

Post synthesis of PB and [^{125}I]IUdR-PB, the number average molecular weight(Mn) of the polymer was measured by SEC using HFIP (**Figure 4A** and **Table 1**). As shown in **Figure 4A**, the differences of elution time of pGlu(OBn)$_{100}$ and PB indicated the different Mn (13 kg/mol and 250 kg/mol, respectively), the larger the Mn the shorter elution. However, the insignificant changes of the structures of PB and [^{125}I]IUdR-PB or IUdR-PB, the Mn measurement was not utilized with [^{125}I]IUdR-PB. The changes of PB and [^{125}I]IUdR-PB can still be recognized by their hydrodynamic size, zeta potential of them(**Figure 4B**). Post radiolabelling synthesis, the diameter of [^{125}I]IUdR-PB increased from 7.07±2.01 nm (PB) to 12.13±1.93 nm, zeta potential also increased from -21.9± 4.1 mV to −4.0± 1.4 mV.

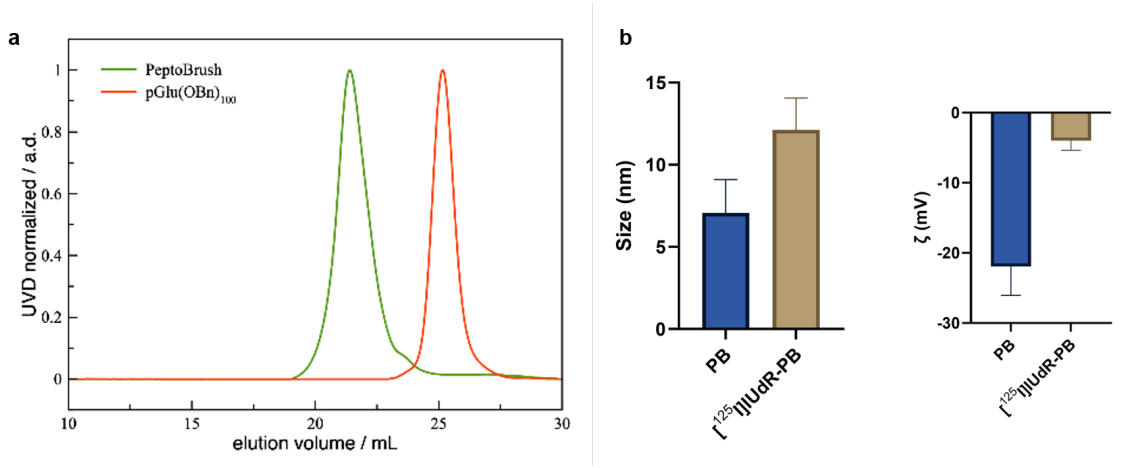

Figure 4. Analysis of PB. (A) SEC characterization of pGlu(OBn)$_{100}$, and PB. (B) DLS and Zeta potential (ζ) results of PB (blue entries) and [^{125}I]IUdR-PB (light brown entries).

Esterase mediated release of [^{125}I]IUdR from [^{125}I]IUdR-PB

The release of [^{125}I]IUdR from [^{125}I]IUdR-PB was conducted in PBS buffer(pH= 7.4) at 37 °C with the addition of esterases. The releasing percentage of [^{125}I]IUdR was analysed using MeOH/DCM(1:9, v/v) as eluent with Radio-TLC at each timepoint. (See SI for details.) As shown in Figure 5a, in the first 24 hours, 4.4 % of [^{125}I]IUdR was released from [^{125}I]IUdR-PB, though there was no release of it in the first 6 hours. This release of [^{125}I]IUdR continued increasing to 52.5% by the end of 480 hours. On the other hand, the release of [^{125}I]IUdR from [^{125}I]IUdR-PB without esterase in PBS buffer, was also investigated (Figure 5b). The initial 24 hours showed a 1.9% release of [^{125}I]IUdR from [^{125}I]IUdR-PB. By the 480-hour mark, the release of [^{125}I]IUdR had reached to 22.8%, indicating a more gradual release of the drug from [^{125}I]IUdR-PB.

Comparatively, the presence of esterase significantly expedited the release of [125I]IUdR from [125I]IUdR-PB. The difference was not significant enough in the first 24 hours, this could be attributed to the brush-like structure of the nanocarrier. The densely packed "brush" structure can introduce steric hindrance, which acted as a physical barrier, potentially limited or slowed down the access of esterase to the ester linker of [125I]IUdR. Over the 480-hour period, the amount of released [125I]IUdR in esterase-rich environment was more than 2 times of the non-esterase group.

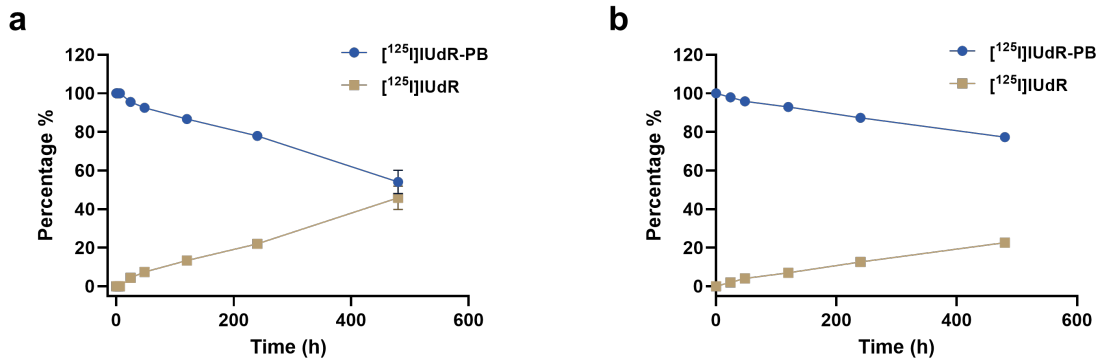

Figure 5. Release of [125I]IUdR-PB in PBS buffer(pH= 7.4) at 37 ℃ with or without esterases, the concentration of esterases is 1 U/mL. a) Esterases mediated release of [125I]IUdR from [125I]IUdR-PB. b) Release of[125I]IUdR from [125I]IUdR-PB in the absence of esterases. The time point for the termination of the release experiment was either when [125I]IUdR is completely released or after 480 hours (20 days). Error bars shown are SD, n=3.

DNA incorporation efficiency of [125I]IUdR-PB

We explored the efficiency of integrating [125I]IUdR, released from [125I]IUdR-PB with (-) and without (+) esterase (E), into the DNA of LN229 cells, referred to as IP% (**Figure 6**). The cells were exposed to [125I]IUdR-PB with and without esterase and after 4 hours and 24 hours of incubation. The cells were harvested with trypsin and washed with cold PBS. The DNA from the cells was isolated following the E.Z.N.A.® Tissue DNA Kit and assessed to quantify the degree of integration based on radioactivity that was measured by LSC. The results, as illustrated in **Figure 6**, showed that even in the absence of esterase, [125I]IUdR-PB still showed a significant increase of [125I]IUdR incorporation to DNA after 24 hours when compared to 4 hours.(0.53% and 0.22%, respectively). Meanwhile, the IP% of[125I]IUdR-PB+E also increased to 1.0% after 24 hours of incubation, which could be because of the acerated release of [125I]IUdR from [125I]IUdR-PB with esterase addition. Moreover, a comparison between the groups with and without esterase revealed a notice-

able difference in IP% after 24 hours, whereas no distinction was observed at the 4-hour interval. In general, these results suggested that the incorporation of [^{125}I]IUdR into DNA had an increase over time in both test groups. While the IP% difference between groups with and without esterase could be become increasingly distinct as time progressed, possibly due to the expanding gap in [^{125}I]IUdR release over time(**Figure 5**).

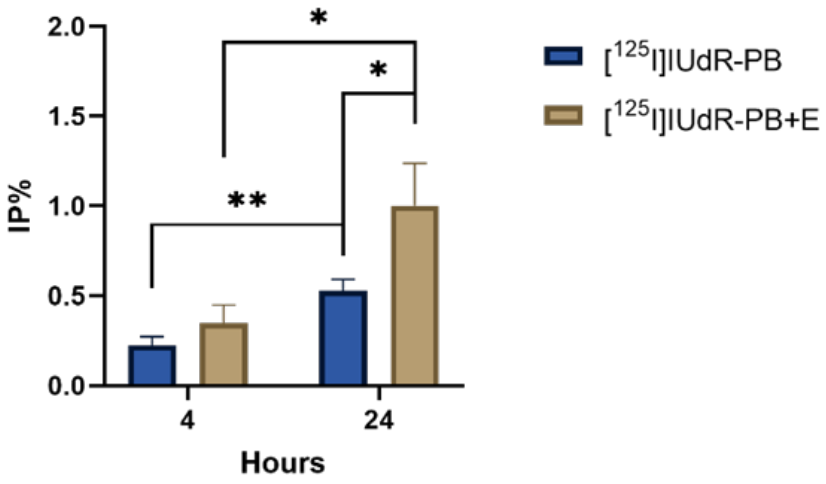

Figure 6. *In vitro* DNA incorporation of [^{125}I]IUdR-PB with or without esterase in LN229 cells after 4 and 24 hours of incubation. Data was represented in terms of the percentage of incorporation (IP%) based on the total added activity. Two-tail unpaired t-test P-values indicate statistical significance (*P<0.05, **P<0.01). Error bars shown are SD.

In vitro cell viability study

The cell viability study was conducted to investigate the ability of cell proliferation inhibition of by [^{125}I]IUdR released from [^{125}I]IUdR-PB against LN229 cells via Celltiter Blue assay. Similar to the prior studies, [^{125}I]IUdR-PB was tested with and without the addition of esterase, moreover, [^{125}I]IUdR-N_3 prodrug and free [^{125}I]IUdR were also included in the assay as controls. Each entry was prepared in different concentrations and incubated with 300 of cells per well for 7 days, in 6-fold (n = 6).

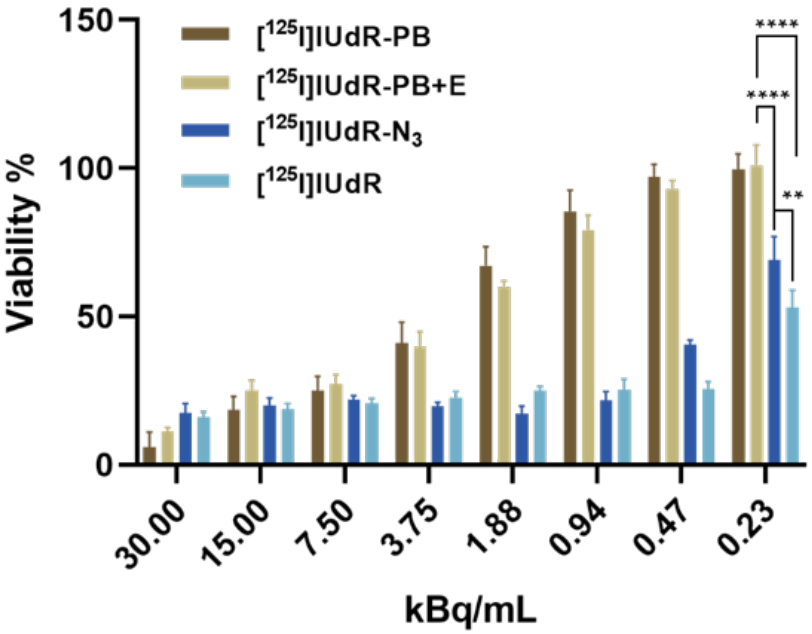

Figure 7. Viability of LN229 cells treated with [125I]IUdR-PB (with or without esterase), [125I]IUdR-N_3, and free [125I]IUdR. Activities ranged from 0.23-30 KBq/mL. "E" represents esterase, 0.1 U/mL. Two-tailed unpaired t-test P-values indicate statistical significance (**P<0.01, ****P<0.0001). Error bars shown are SD.

As shown in **Figure 7**, the positive control group, free [125I]IUdR (light blue), showed the highest inhibitory ability to cell growth even at the lowest level of 0.23 kBq/mL, with viability of 54 ± 4%. While [125I]IUdR-N_3 (blue), also displayed commendable efficacy, although there was a certain difference with [125I]IUdR in the low intensity region (0.23 to 0.47 kBq/mL), this disparity disappeared in ranges exceeding 0.94 kBq/mL. This might be because of the minimal difference in their solubilities ($LogD_{pH=7.4}$), which are -0.7 and +0.29, respectively. Consequently, [125I]IUdR-N_3 could potentially be integrated into cells by slow hydrolysis of ester bond even in the absence of esterase. For [125I]IUdR-PB, with and without esterase groups (brown and khaki, respectively), they both showed a linear activity correlation, that was, as radioactivity decreased, cell viability increased. Their ability to inhibit cells was significantly different from free [125I]IUdR when activity was less than 3.75 kBq/mL. This difference could be attributed to the release of [125I]IUdR from [125I]IUdR-PB, which is required to see any effect on cell viability. The two groups, [125I]IUdR-PB + E and [125I]IUdR-PB, did not show significant differences across any activity, even though while the release of [125I]IUdR was confirmed in the release study (**Figure 5**). This inconsistency might be due to our choice of using an esterase concentration of 0.1 U/mL for cell study,

as opposed to the 1 U/mL used in release study.

In a different study (Chapter 2), 1U/mL of esterase was found to be detrimental to cells, whereas 0.1u/ mL was not only benign but also ensured effective [^{125}I]IUdR release from [^{125}I]IUdR-Cn-LIPs. However, given the brush-like structure of PB, esterase required more time to hydrolyze the prodrug, leading to slow release of [^{125}I]IUdR compared to [^{125}I]IUdR-Cn-LIPs. Therefore, chosen the same esterase concentration (0.1U/mL) as liposomal system, possibly made the release of [^{125}I]IUdR potentially even more suboptimal, resulted in nonsignificant difference between [^{125}I]IUdR-PB +E and [^{125}I]IUdR-PB. Despite this, we still observed a pronounced inhibition in cell viability, similar to the positive control [^{125}I]IUdR, at active concentrations ≥ 7.5 kbq/mL.

Discussion

Polypept(o)ides, particularly PeptoBrushes, have emerged as a promising candidate in the fields of drug delivery and medical imaging. These hybrid constructs merge the characteristics of peptides with peptide-mimetic structures, resulting in a unique design that boasts a hydrophilic brush shell and a hydrophobic core. Such a design not only facilitates the encapsulation of a diverse range of therapeutic agents but also possibly offer prolonged in vivo retention due to their brush-like structures.

In our research, we successfully synthesized and grafted [^{125}I]IUdR -N_3, a prodrug with an ester bond suitable for click reactions, onto PB via the grafted DBCO arms on the backbone. The release of [^{125}I]IUdR from [^{125}I]IUdR-PB was also confirmed in esterase-rich environment. However, the rate of release was considerably slower than the liposome-based platform (with 24-hour release rates of 5% and 25%, respectively). This disparity could be attributed to the structural variances between the two nanocarriers (PeptoBrush vs. liposomes). The morphology and topology of PB, combined with its surface pSar brush-layer, arguably introduces significant steric hindrance to the cleavable ester bonds, hindering the esterases hydrolysis. This could indicate that the rate of IUdR release might be dictated by the changes of the morphology and topology of the PB.

Additionally, the different methods of loading prodrugs to nanocarriers could played as another important role. While the post-insertion method was utilized for prodrug([^{125}I]IUdR-C_{18}) loading in liposomes, click reaction was applied for prodrug ([^{125}I]IUdR -N_3) conjugation on PB. The formed liposomes, [^{125}I]IUdR-C_{18}-LIPs, the prodrug can be liberated from the liposome's bilayer membrane, making them easier accessible to esterase. In contrast, [^{125}I]IUdR -N_3 integrated via click reaction on PB remained grafted, making the prodrug theologically cannot leave the nanocarrier, therefore, a slower [^{125}I]IUdR release rate from [^{125}I]IUdR-PB compared to [^{125}I]IUdR-C_{18}-LIPs was not surprised.

Another notable difference was the prodrugs used in these two systems, while [^{125}I]IUdR -C_{18} for liposomes, [^{125}I]IUdR -N_3 for PB. The length of the carbon chain between the two prodrugs might also cause influence in release rate. Because after grafting [^{125}I]IUdR -C_4-N_3 into PB, the distance between the ester linker to the backbone is related to the length of the carbon chain in [^{125}I]IUdR -N_3. Utilizing a longer carbon chain in the prodrug might increase the distance of ester linker from PB, potentially accelerating the [^{125}I]IUdR release rate.

4 Summary and outlook

Overall, we have successfully synthesized the brush-shaped nanocarrier PB, and conjugated [^{125}I]IUdR- N_3 to the nanoparticle with high yield(reaching 79%) via copper-free click reaction. The release of [^{125}I]IUdR from [^{125}I]IUdR-PB was demonstrated in esterase-rich PBS buffer at 37 °C. A consistent release was observed with more than 50% of [^{125}I]IUdR was identified over 20 days. Moreover, the DNA incorporation efficiency of [^{125}I]IUdR-PB with or without the addition of esterases were conducted. The results demonstrated that the increased release of [^{125}I]IUdR in esterases- added group can lead to a higher DNA incorporation efficiency. Moreover, the in vitro efficacy study, the efficacy of [^{125}I]IUdR-PB did not significantly differ between the groups with and without esterases, which could be attributed to the use of the improper esterases concentration. However, [^{125}I]IUdR-PB stilled behaved similar killing ability as free [^{125}I]IUdR when radioactivity was ≥ 7.5 kbq/mL.

Additionally, PB's utility as a drug carrier was accentuated by its high loading efficiency and short drug loading duration. This stands in contrast to the two-step drug loading process of liposomes, where liposomes are first produced followed by prodrug insertion. This efficiency could significantly enhance production efficiency, making it more viable for potential clinical applications. With further strategic prodrug design, [^{125}I]IUdR-PB could become a promising therapeutic candidate for GBM treatments.

5 References

(1) Chen, L.; Ma, J.; Zou, Z.; Liu, H.; Liu, C.; Gong, S.; Gao, X.; Liang, G. Clinical Characteristics and Prognosis of Patients with Glioblastoma: A Review of Survival Analysis of 1674 Patients Based on SEER Database. *Medicine* **2022**, *101* (47), e32042. https://doi.org/10.1097/MD.0000000000032042.

(2) Kawauchi, D.; Ohno, M.; Honda-Kitahara, M.; Miyakita, Y.; Takahashi, M.; Yanagisawa, S.; Tamura, Y.; Kikuchi, M.; Ichimura, K.; Narita, Y. Clinical Characteristics and Prognosis of Glioblastoma Patients with Infratentorial Recurrence. *BMC Neurol* **2023**, *23* (1), 9. https://doi.org/10.1186/s12883-022-03047-9.

(3) Alexander, B. M.; Cloughesy, T. F. Adult Glioblastoma. *Journal of Clinical Oncology* **2017**, *35* (21), 2402–2409. https://doi.org/10.1200/JCO.2017.73.0119.

(4) Hasanzadeh, N.; Niknejad, A. Cerebral Glioblastoma: A Review on Genetic Alterations, Signaling Pathways, and Clinical Managements. *Jentashapir Journal of Cellular and Molecular Biology* **2021**, *12* (4).

(5) Patil, V.; Pal, J.; Somasundaram, K. Elucidating the Cancer-Specific Genetic Alteration Spectrum of Glioblastoma Derived Cell Lines from Whole Exome and RNA Sequencing. *Oncotarget* **2015**, *6* (41), 43452–43471. https://doi.org/10.18632/oncotarget.6171.

(6) Appin, C. L.; Brat, D. J. Molecular Genetics of Gliomas. *The Cancer Journal* **2014**, *20* (1), 66–72. https://doi.org/10.1097/PPO.0000000000000020.

(7) Cantero, D.; Mollejo, M.; Sepúlveda, J. M.; D'Haene, N.; Gutiérrez-Guamán, M. J.; Rodríguez De Lope, Á.; Fiaño, C.; Castresana, J. S.; Lebrun, L.; Rey, J. A.; Salmon, I.; Meléndez, B.; Hernández-Laín, A. TP53, ATRX Alterations, and Low Tumor Mutation Load Feature IDH-Wildtype Giant Cell Glioblastoma despite Exceptional Ultra-Mutated Tumors. *Neuro-Oncology Advances* **2020**, *2* (1), vdz059. https://doi.org/10.1093/noajnl/vdz059.

(8) Labussiere, M.; Boisselier, B.; Mokhtari, K.; Di Stefano, A.-L.; Rahimian, A.; Rossetto, M.; Ciccarino, P.; Saulnier, O.; Paterra, R.; Marie, Y.; Finocchiaro, G.; Sanson, M. Combined Analysis of TERT, EGFR, and IDH Status Defines Distinct Prognostic Glioblastoma Classes. *Neurology* **2014**, *83* (13), 1200–1206. https://doi.org/10.1212/WNL.0000000000000814.

(9) Lobbous, M.; Tucker, Z.; Coffee, E.; Nabors, L. PATH-35. RETROSPECTIVE ANALYSIS OF 145 PATIENTS WITH GLIOBLASTOMA; CORRELATING MOLECULAR ALTERATION INCIDENCE

WITH DEMOGRAPHICS, TUMOR LOCATION, AND PROGNOSIS. *Neuro-Oncology* **2019**, *21* (Supplement_6), vi150–vi151. https://doi.org/10.1093/neuonc/noz175.631.

(10) Roth, P.; Weller, M. Challenges to Targeting Epidermal Growth Factor Receptor in Glioblastoma: Escape Mechanisms and Combinatorial Treatment Strategies. *Neuro-Oncology* **2014**, *16* (suppl 8), viii14–viii19. https://doi.org/10.1093/neuonc/nou222.

(11) Chuang, D. F.; Lin, X. Targeted Therapies for the Treatment of Glioblastoma in Adults. *Curr Oncol Rep* **2019**, *21* (7), 61. https://doi.org/10.1007/s11912-019-0807-1.

(12) Cha, G. D.; Jung, S.; Choi, S. H.; Kim, D.-H. Local Drug Delivery Strategies for Glioblastoma Treatment. *Brain Tumor Res Treat* **2022**, *10* (3), 151. https://doi.org/10.14791/btrt.2022.0017.

(13) Wick, W.; Osswald, M.; Wick, A.; Winkler, F. Treatment of Glioblastoma in Adults. *Therapeutic advances in neurological disorders* **2018**, *11*, 1756286418790452.

(14) Desjardins, A.; Gromeier, M.; Herndon, J. E.; Beaubier, N.; Bolognesi, D. P.; Friedman, A. H.; Friedman, H. S.; McSherry, F.; Muscat, A. M.; Nair, S.; Peters, K. B.; Randazzo, D.; Sampson, J. H.; Vlahovic, G.; Harrison, W. T.; McLendon, R. E.; Ashley, D.; Bigner, D. D. Recurrent Glioblastoma Treated with Recombinant Poliovirus. *N Engl J Med* **2018**, *379* (2), 150–161. https://doi.org/10.1056/NEJMoa1716435.

(15) Laine, A. L.; Huynh, N. T.; Clavreul, A.; Balzeau, J.; Bejaud, J.; Vessieres, A.; Benoit, J. P.; Eyer, J.; Passirani, C. Brain Tumour Targeting Strategies via Coated Ferrociphenol Lipid Nanocapsules. *European Journal of Pharmaceutics and Biopharmaceutics* **2012**, *81* (3), 690–693. https://doi.org/10.1016/j.ejpb.2012.04.012.

(16) Arranja, A. G.; Pathak, V.; Lammers, T.; Shi, Y. Tumor-Targeted Nanomedicines for Cancer Theranostics. *Pharmacological Research* **2017**, *115*, 87–95. https://doi.org/10.1016/j.phrs.2016.11.014.

(17) Chen, K. S.; Mitchell, D. A. MONOCLONAL ANTIBODY THERAPY FOR MALIGNANT GLIOMA. In *Glioma: Immunotherapeutic Approaches*; Yamanaka, R., Ed.; 2012; Vol. 746, pp 121–141.

(18) Majc, B.; Novak, M.; Kopitar-Jerala, N.; Jewett, A.; Breznik, B. Immunotherapy of Glioblastoma: Current Strategies and Challenges in Tumor Model Development. *Cells* **2021**, *10* (2), 265. https://doi.org/10.3390/cells10020265.

(19) Medikonda, R.; Dunn, G.; Rahman, M.; Fecci, P.; Lim, M. A Review of Glioblastoma Immunotherapy. *Journal of Neuro-Oncology* **2021**, *151* (1), 41–53. https://doi.org/10.1007/s11060-020-03448-1.

(20) Coleman, N.; Ameratunga, M.; Lopez, J. Development of Molecularly Targeted Agents and Immunotherapies in Glioblastoma: A Personalized Approach. *Clin Med Insights Oncol* **2018**, *12*, 117955491875907. https://doi.org/10.1177/1179554918759079.

(21) Lin, C. Y.; Li, R. J.; Huang, C. Y.; Wei, K. C.; Chen, P. Y. Controlled Release of Liposome-Encapsulated Temozolomide for Brain Tumour Treatment by Convection-Enhanced Delivery. *Journal of Drug Targeting* **2018**, *26* (4), 325–332. https://doi.org/10.1080/1061186x.2017.1379526.

(22) Sassi, K.; Nury, T.; Samadi, M.; Fennira, F. B.-A.; Vejux, A.; Lizard, G. Cholesterol Derivatives as Promising Anticancer Agents in Glioblastoma Metabolic Therapy. In *Gliomas*; Brain Tumor Center of Excellence, Wake Forest Baptist Medical Center Comprehensive Cancer Center, Winston Salem, NC, USA, Debinski, W., Eds.; Exon Publications, 2021; pp 97–120. https://doi.org/10.36255/exonpublications.gliomas.2021.chapter6.

(23) Wang, K.; Zhang, F.; Wen, C.; Huang, Z.; Hu, Z.; Zhang, Y.; Hu, F.; Wen, L. Regulation of Pathological Blood-Brain Barrier for Intracranial Enhanced Drug Delivery and Anti-Glioblastoma Therapeutics. *Oncology Research* **2021**, *29* (5), 351–363. https://doi.org/10.32604/or.2022.025696.

(24) Ahmed, M. H.; Canney, M.; Carpentier, A.; Thanou, M.; Idbaih, A. Unveiling the Enigma of the Blood–Brain Barrier in Glioblastoma: Current Advances from Preclinical and Clinical Studies. *Current Opinion in Oncology* **2023**. https://doi.org/10.1097/CCO.0000000000000990.

(25) Abbott, N. J.; Patabendige, A. A.; Dolman, D. E.; Yusof, S. R.; Begley, D. J. Structure and Function of the Blood–Brain Barrier. *Neurobiology of disease* **2010**, *37* (1), 13–25.

(26) Inda, M.-M.; Bonavia, R.; Seoane, J. Glioblastoma Multiforme: A Look inside Its Heterogeneous Nature. *Cancers* **2014**, *6* (1), 226–239.

(27) Wolburg, H.; Noell, S.; Fallier-Becker, P.; Mack, A. F.; Wolburg-Buchholz, K. The Disturbed Blood–Brain Barrier in Human Glioblastoma. *Molecular aspects of medicine* **2012**, *33* (5–6), 579–589.

(28) Giles, B.; Nakhjavani, M.; Wiesa, A.; Knight, T.; Shigdar, S.; Samarasinghe, R.

M. Unravelling the Glioblastoma Tumour Microenvironment: Can Aptamer Targeted Delivery Become Successful in Treating Brain Cancers? *Cancers* **2023**, *15* (17), 4376. https://doi.org/10.3390/cancers15174376.

(29) Aum, D. J.; Kim, D. H.; Beaumont, T. L.; Leuthardt, E. C.; Dunn, G. P.; Kim, A. H. Molecular and Cellular Heterogeneity: The Hallmark of Glioblastoma. *Neurosurgical focus* **2014**, *37* (6), E11.

(30) Furnari, F. B.; Cloughesy, T. F.; Cavenee, W. K.; Mischel, P. S. Heterogeneity of Epidermal Growth Factor Receptor Signalling Networks in Glioblastoma. *Nature Reviews Cancer* **2015**, *15* (5), 302–310.

(31) Cordova, J. S.; Shu, H.-K. G.; Liang, Z.; Gurbani, S. S.; Cooper, L. A.; Holder, C. A.; Olson, J. J.; Kairdolf, B.; Schreibmann, E.; Neill, S. G.; others. Whole-Brain Spectroscopic MRI Biomarkers Identify Infiltrating Margins in Glioblastoma Patients. *Neuro-oncology* **2016**, *18* (8), 1180–1189.

(32) Seker-Polat, F.; Pinarbasi Degirmenci, N.; Solaroglu, I.; Bagci-Onder, T. Tumor Cell Infiltration into the Brain in Glioblastoma: From Mechanisms to Clinical Perspectives. *Cancers* **2022**, *14* (2), 443. https://doi.org/10.3390/cancers14020443.

(33) El Kheir, W.; Marcos, B.; Virgilio, N.; Paquette, B.; Faucheux, N.; Lauzon, M.-A. Drug Delivery Systems in the Development of Novel Strategies for Glioblastoma Treatment. *Pharmaceutics* **2022**, *14* (6), 1189. https://doi.org/10.3390/pharmaceutics14061189.

(34) Alphandéry, E. Nano-Therapies for Glioblastoma Treatment. *Cancers* **2020**, *12* (1), 242.

(35) Bloomer, W. D.; Adelstein, S. J. 5-125I-Iododeoxyuridine as Prototype for Radionuclide Therapy with Auger Emitters. *Nature* **1977**, *265* (5595), 620–621.

(36) Bagshawe, K. D.; Sharma, K.; Southall, P. J.; Boden, J. A.; Boxer, G. M.; Patridge, T. A.; Antoniw, P.; Pedley, R. B. Selective Uptake of Toxic Nucleoside (125IUdR) by Resistant Cancer. *The British journal of radiology* **1991**, *64* (757), 37–44.

(37) Madsen, K. L.; Therkelsen, A. S. N.; Langkjær, N.; Olsen, B. B.; Thisgaard, H. Auger Electron Therapy of Glioblastoma Using [125I]5-Iodo-2□-Deoxyuridine and Concomitant Chemotherapy – Evaluation of a Potential Treatment Strategy. *Nuclear Medicine and Biology* **2021**, *96–97*, 35–40. https://doi.org/10.1016/j.nucmedbio.2021.03.001.

(38) Thisgaard, H.; Halle, B.; Aaberg-Jessen, C.; Olsen, B. B.; Therkelsen, A. S. N.; Dam, J. H.; Langkjær, N.; Munthe, S.; Någren, K.; Høilund-Carlsen, P. F.; Kristensen, B. W. Highly Effective Auger-Electron Therapy in an Orthotopic Glioblastoma Xenograft Model Using Convection-Enhanced Delivery. *Theranostics* **2016**, *6* (12), 2278–2291. https://doi.org/10.7150/thno.15898.

(39) Bodei, L.; Kassis, A. I.; Adelstein, S. J.; Mariani, G. Radionuclide Therapy with Iodine-125 and Other Auger–Electron-Emitting Radionuclides: Experimental Models and Clinical Applications. *Cancer Biotherapy and Radiopharmaceuticals* **2003**, *18* (6), 861–877. https://doi.org/10.1089/108497803322702833.

(40) Chen, P. Y.; Ozawa, T.; Drummond, D. C.; Kalra, A.; Fitzgerald, J. B.; Kirpotin, D. B.; Wei, K. C.; Butowski, N.; Prados, M. D.; Berger, M. S.; Forsayeth, J. R.; Bankiewicz, K.; James, C. D. Comparing Routes of Delivery for Nanoliposomal Irinotecan Shows Superior Anti-Tumor Activity of Local Administration in Treating Intracranial Glioblastoma Xenografts. *Neuro-Oncology* **2013**, *15* (2), 189–197. https://doi.org/10.1093/neuonc/nos305.

(41) Mangraviti, A.; Tzeng, S. Y.; Kozielski, K. L.; Wang, Y.; Jin, Y.; Gullotti, D.; Pedone, M.; Buaron, N.; Liu, A.; Wilson, D. R.; Hansen, S. K.; Rodriguez, F. J.; Gao, G.-D.; DiMeco, F.; Brem, H.; Olivi, A.; Tyler, B.; Green, J. J. Polymeric Nanoparticles for Nonviral Gene Therapy Extend Brain Tumor Survival in Vivo. *Acs Nano* **2015**, *9* (2), 1236–1249. https://doi.org/10.1021/nn504905q.

(42) Biddlestone-Thorpe, L.; Marchi, N.; Guo, K.; Ghosh, C.; Janigro, D.; Valerie, K.; Yang, H. Nanomaterial-Mediated CNS Delivery of Diagnostic and Therapeutic Agents. *Advanced Drug Delivery Reviews* **2012**, *64* (7), 605–613. https://doi.org/10.1016/j.addr.2011.11.014.

(43) Li, J.; Zhao, J.; Tan, T.; Liu, M.; Zeng, Z.; Zeng, Y.; Zhang, L.; Fu, C.; Chen, D.; Xie, T. Nanoparticle Drug Delivery System for Glioma and Its Efficacy Improvement Strategies: A Comprehensive Review. *International Journal of Nanomedicine* **2020**, 2563–2582.

(44) Bi, D.; Unthan, D. M.; Hu, L.; Bussmann, J.; Remaut, K.; Barz, M.; Zhang, H. Polysarcosine-Based Lipid Formulations for Intracranial Delivery of mRNA. *Journal of Controlled Release* **2023**, *356*, 1–13.

(45) Gaudin, A.; Song, E.; King, A. R.; Saucier-Sawyer, J. K.; Bindra, R.; Desmaele, D.; Couvreur, P.; Saltzman, W. M. PEGylated Squalenoyl-Gemcitabine Nanoparticles for the Treatment of Glioblastoma. *Biomaterials* **2016**, *105*, 136–144.

https://doi.org/10.1016/j.biomaterials.2016.07.037.

(46) Mohamed, M.; Abu Lila, A. S.; Shimizu, T.; Alaaeldin, E.; Hussein, A.; Sarhan, H. A.; Szebeni, J.; Ishida, T. PEGylated Liposomes: Immunological Responses. *Science and Technology of Advanced Materials* **2019**, *20* (1), 710–724. https://doi.org/10.1080/14686996.2019.1627174.

(47) Shiraishi, K.; Yokoyama, M. Toxicity and Immunogenicity Concerns Related to PEGylated-Micelle Carrier Systems: A Review. *Science and Technology of Advanced Materials* **2019**, *20* (1), 324–336. https://doi.org/10.1080/14686996.2019.1590126.

(48) Tenchov, R.; Sasso, J. M.; Zhou, Q. A. PEGylated Lipid Nanoparticle Formulations: Immunological Safety and Efficiency Perspective. *Bioconjugate Chemistry* **2023**.

(49) Klinker, K.; Barz, M. Polypept(o)Ides: Hybrid Systems Based on Polypeptides and Polypeptoids. *Macromol. Rapid Commun.* **2015**, *36* (22), 1943–1957. https://doi.org/10.1002/marc.201500403.

(50) Bauer, T. A.; Eckrich, J.; Wiesmann, N.; Kuczelinis, F.; Sun, W.; Zeng, X.; Weber, B.; Wu, S.; Bings, N. H.; Strieth, S.; others. Photocleavable Core Cross-Linked Polymeric Micelles of Polypept (o) Ides and Ruthenium (Ii) Complexes. *Journal of Materials Chemistry B* **2021**, *9* (39), 8211–8223.

(51) Skoulas, D.; Stuettgen, V.; Gaul, R.; Cryan, S.-A.; Brayden, D. J.; Heise, A. Amphiphilic Star Polypept (o) Ides as Nanomeric Vectors in Mucosal Drug Delivery. *Biomacromolecules* **2020**, *21* (6), 2455–2462.

(52) García-Vázquez, R.; Battisti, U. M.; Shalgunov, V.; Schäfer, G.; Barz, M.; Herth, M. M. [11C] Carboxylated Tetrazines for Facile Labeling of Trans-Cyclooctene-Functionalized PeptoBrushes. *Macromolecular rapid communications* **2022**, *43* (12), 2100655.

(53) Stéen, E. J. L.; Jørgensen, J. T.; Johann, K.; Nørregaard, K.; Sohr, B.; Svatunek, D.; Birke, A.; Shalgunov, V.; Edem, P. E.; Rossin, R.; others. Trans-Cyclooctene-Functionalized Peptobrushes with Improved Reaction Kinetics of the Tetrazine Ligation for Pretargeted Nuclear Imaging. *ACS nano* **2019**, *14* (1), 568–584.

Chapter 5

The influence of size on the intracranial distribution of biomedical nanoparticles administered by convection enhanced delivery in pigs

---

Mahsa Amirrashedi [a,b,c], Andreas Ingemann Jensen [d*], Qing Tang [d], Natan Johannes Willem Straathof [d], Katharina Ravn [d], Christian G.T. Pedersen [a], Louise Langhorn [e], Frantz R. Poulsen [f,g], Max Woolley [h], David Johnson [h], Julia Williams [h], Helge Thisgaard [a,f*], Bo Halle [f,g*]

[a] Department of Nuclear Medicine, Odense University Hospital, Odense, Denmark

[b] Department of Applied Mathematics and Computer Science, Technical University of Denmark, Kgs. Lyngby, Denmark

[c] Danish Research Centre for Magnetic Resonance, Centre for Functional and Diagnostic Imaging and Research, Copenhagen University Hospital Amager and Hvidovre, Copenhagen, Denmark

[d] The Hevesy Laboratory, Department of Health Technology, Technical University of Denmark, Roskilde, Denmark

[e] Biomedical Laboratory, University of Southern Denmark, Odense, Denmark

[f] Department of Clinical Research, University of Southern Denmark, Odense, Denmark

[g] Department of Neurosurgery, Odense University Hospital, Odense, Denmark

[h] Renishaw Neuro Solutions Ltd (RNS), Gloucestershire GL12 8JR, United Kingdom

*Corresponding authors: atije@dtu.dk, Helge.Thisgaard@rsyd.dk, Bo.Halle@rsyd.dk

The work in this chapter will be represented as manuscript.

1 Introduction

It is widely acknowledged that effective drug delivery to the brain is often hindered by the blood-brain barrier (BBB). This anatomical hurdle renders systemic drug administration futile against a vast spectrum of central nervous system (CNS) disorders and associated pathologies[1]. In severe medical conditions (e.g., glioblastoma multiforme, diffuse intrinsic pontine glioma, Parkinson's disease, etc.), direct administration of therapeutics into the affected regions of the brain, thereby bypassing the BBB, is highly desirable. One plausible remedy is to employ bulk convective flow at the infusion site, using so-called convection-enhanced delivery (CED). CED relies on the direct delivery of high drug concentrations using a hydrostatic pressure gradient generated through microcatheters implanted intracerebrally. Opposed to diffusion-driven strategies, CED allows for the expansive distribution of therapeutic agents within the brain parenchyma, thereby reaching a larger volume of distribution and potentially covering more of the affected brain regions[2,3].

The efficacy of CED is reliant upon several factors; chief among them being the optimal design and size of the infusate [4-6]. Small molecule therapeutic agents typically have short half-lives in the brain, leading to their swift elimination immediately after infusion. This limitation can be addressed using nanoencapsulation, in this way artificially increasing the size of the administered compounds and protecting them from rapid clearance. Biomedically relevant nanoparticles (NPs) such as gold nanoparticles (AuNPs)[7], polymeric micelles [8,9], dendrimers[10], and liposomes (LIPs)[11-13] may in this way minimize systemic toxicity, improve intracranial retention, and facilitate sustained release of their therapeutic cargo[5]. Once administered via CED, NPs must navigate through the brain's extracellular matrix (ECM). Their physiochemical properties, notably their size and surface architecture, are believed to play critical roles in determining their distribution within the brain. These properties are therefore central to aspects like penetration depth, distribution volume, and intracranial retention. As such, the size dependency of NPs on CED can be thought of as relating both to an initial distribution phase, as well as a retention phase, once the infusion has been terminated. Studies suggest that NPs exceeding diameters of 100 nm face challenges when moving through the brain's ECM, which typically display openings of 38-64 nm in healthy tissue[14] but which can fluctuate between 7–100 nm in tumor-affected areas[15]. As such, larger NPs would be expected to show limited distribution but increased retention within the brain, given that their size would hinder swift removal, whether through cellular absorption, glymphatic clearance, transit through perivascular routes, or clearance via cap-

illaries. Conversely, smaller NPs might penetrate and distribute more extensively but might not remain in the tissue for as long. The small dimensions of such particles may accelerate their removal through clearance mechanisms or diffusive exit from the target. In this way, the dimension of NPs is likely to be a strategic variable that can be fine-tuned to optimize the effectiveness of NP delivery via CED, a topic that warrants deeper exploration. In addition, the surface architecture of the NPs is expected to be of key importance. Previous reports support that NPs with neutral or slightly negative surface charge (zeta potential) and coating with hydrophilic polymers such as polyethylene glycol (PEG) facilitate passage through the cerebral interstitium. This is in line with established nanomedicine, in which such coatings are employed to limit the interaction of NPs with biological materials in the living organism.

In addition to delivering drugs, NPs can also serve as tracers during the infusion process[16,17]. This feature is of utmost importance in CED, which relies on precise and targeted infusion. By attaching suitable radionuclides to the NPs, the entire infusion process can be tracked and monitored noninvasively via nuclear imaging. This provides not only valuable real-time feedback on the effectiveness of the delivery method but also permits prompt identification of suboptimal infusion and enables on-the-fly modulation of infusion parameters. Despite the wealth of studies utilizing gadolinium(Gd)-enhanced magnetic resonance imaging (MRI) to characterize the distribution achieved via CED[18-25], the potential of nuclear imaging modalities such as positron emission tomography (PET) remains largely untapped and has not yet been fully elucidated in the context of image-guided intracranial drug delivery. PET provides an exquisitely sensitive alternative to MRI contrast for tracking and monitoring the spatiotemporal distribution of radiolabelled therapeutics during CED. Moreover, PET-guided delivery provides invaluable insight into the pharmacokinetics of the infused substance, including its dispersion and elimination, adding an additional layer of quantitative information to the delivery process.

Motivated by the promise of using NPs for drug delivery via CED and the need for optimized strategies for this, we here report an investigation of PET-guided intracranial CED of NPs of three different sizes. The central objective was to evaluate the impact of NP size on the two crucial delivery aspects of CED in the brain: volume of distribution (VD) and intracranial retention. As the largest NP type (1□30 nm), we used liposomes (LIPs). LIPs are biocompatible and biodegradable lipid-based, spherical NPs, which can be readily manufactured by established method in sizes of around or slightly above 100 nm. In addition, LIPs can be

readily labeled with PET radionuclides in the lipid bilayer membrane as well as in the inner aqueous compartment and used for in vivo PET imaging. However, LIPs are challenging to prepare in small sizes. For this reason we used AuNPs for the two smaller NP designs (6□ nm and 4□0 nm). AuNPs are biocompatible gold spheres which can be readily synthesized in tailored sizes in the 5-50 nm range using reported procedures . We recently reported a practical method for surface labeling of AuNPs with radiometals for PET imaging, which was also used in the current study. All three NP designs were coated with PEG, ensuring that their interaction with biological matter in the brain would be similar between them, and were labeled with the positron-emitting radionuclide copper-64 (^{64}Cu) for quantitative PET imaging. The concept of this study was illustrated in **Figure 1.**

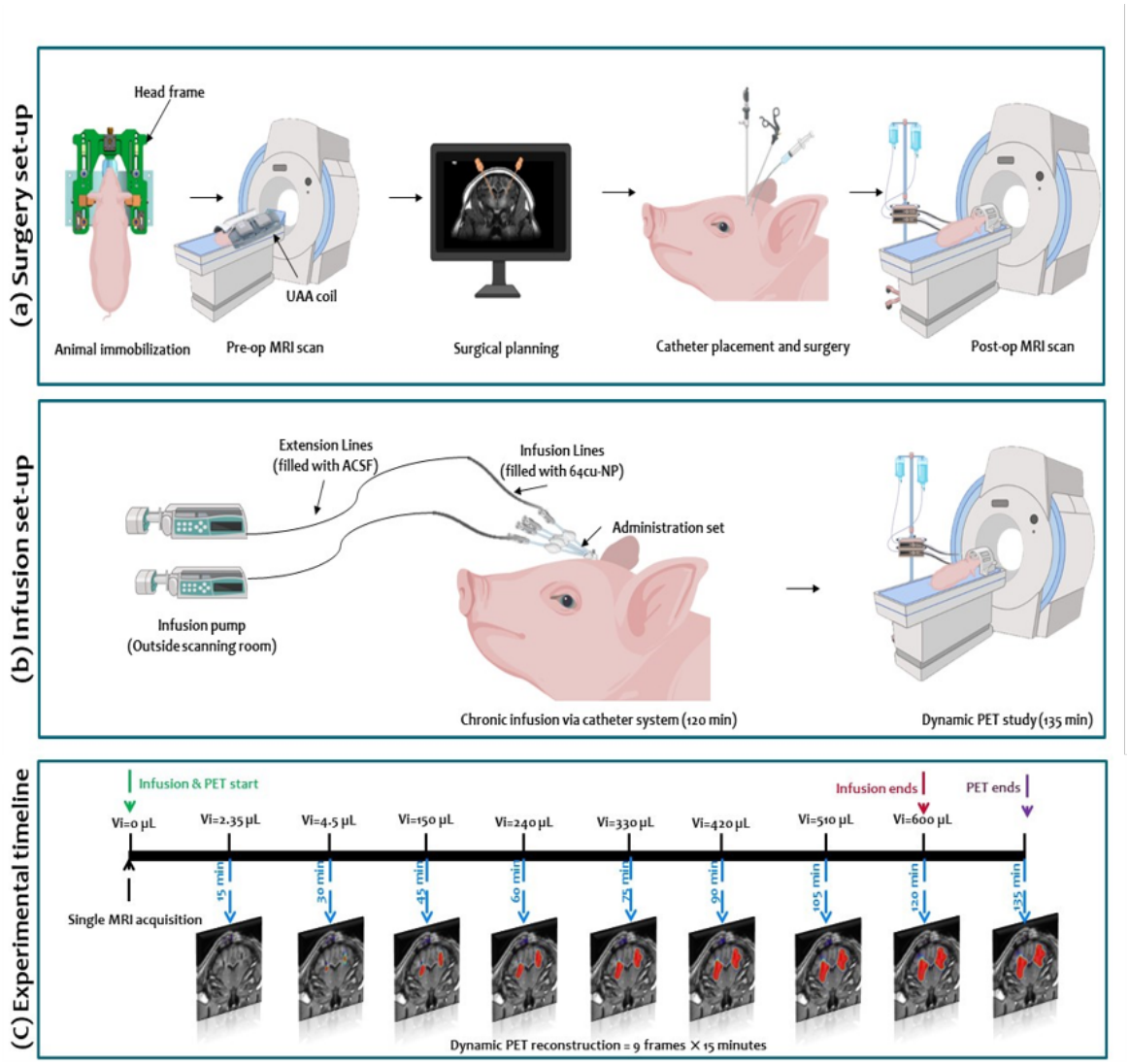

Figure 1. (a) Experimental set-up on the surgery day: the anesthetized animal was immobilized in an MRI-compatible head frame, followed by a pre-catheter implantation MRI scan. The MRI scan was then transferred into Neuroinspire software to plan the implantation trajectories of two infusion catheters within the putaminal region. Postoperative MRI was performed immediately after surgery to confirm the accuracy of targeting and placement of the catheters. (b) The infusion procedure for administering ^{64}Cu-NP: 300 µL tubes were filled with radioactivity and connected to the delivery channel in the Neuroinfuse application set. The other end was attached to a 6 m extension line which allowed infusion from a syringe pump outside the scanning unit. (c) Experimental timeline for each infusion: after securing the infusion lines to the application set, the animal was positioned inside a head coil for PET/MRI studies. Each infusion lasted 120 minutes, and emission data were collected over 135 minutes, beginning at the start of the infusion. Dynamic PET data was then reframed into nine frames of 15 minutes and reconstructed. MRI scan was acquired on each infusion session as an anatomical guide for PET data and quantitative analysis. Abbreviations: PET, Positron emission tomography; MRI, Magnetic resonance imaging; UAA, Upper anterior array; ^{64}Cu-NP, radiolabelled nanoparticles with copper-64; aCSF, Artificial cerebrospinal fluid; Gd, Gadolinium; V_i, Volume of infusion at specific time point.

2 Materials and methods

Materials

All reagents and solvents were bought from commercial suppliers; VWR International, Sigma-Aldrich, ABCR Chemicals, FluoroChem or TCI Chemicals, and were used as received. Technical solvents were bought from VWR International and used as received. Isotonic HEPES buffer (Iso-HEPES, 10 mM HEPES, 150 mM NaCl, pH 7.4) was prepared by dissolving HEPES free acid (2.38 g), HEPES-Na (6.60 g), and NaCl (17.54 g) in MiliQ-H_2O (2.0 L). Pre-mixed, custom-prepared lipid powder (3:1:1, HSPC:Chol:DSPE-PEG_{2k}) was bought from Lipoid GmbH. DSPE-PEG_{1k}-DOTA was purchased from Xi'an Ruixi Biological Technology Co., Ltd. China (Catalogue number: R-0225). TA-DOTA was purchased from CheMatech macrocycle design technologies, France (Catalogue number: C128). $HAuCl_4$ $3H_2O$ was bought from Sigma-Aldrich (> 99.9%, CAS: 16961-25-4, Prod. No.: 520918). Copper-64 chloride ($[^{64}Cu]CuCl_2$, dry) was produced on-site at the Hevesy Laboratory (0.3 - 1.5 GBq, ^{64}Cu-radionuclidic purity > 99%, molar activity (M_A) > 1 TBq/µmol).

Equipment & analysis

The hydrodynamic diameter ($Ø_{hyd}$) and zeta potential (ζ) of the prepared NPs were measured by dynamic light scattering (DLS) on a ZetaPALS (Brookhaven Instruments Limited, USA). Unless stated otherwise, $Ø_{hyd}$ and ζ analyses were performed at 0.1 mg/mL NP concentration in iso-HEPES buffer at 25°C and were done in quintuplets. Osmolarity was measured on a Gonotec Osmomat 010/030-D (Gonotec Gmbh, Germany). Radio-HPLC was performed on a Hitachi Chromaster equipped with a Hitachi 5160 manual purge quaternary gradient pump, coupled to a Hitachi 5260 thermostat loop autosampler, a Hitachi 5310 column oven, a Hitachi 5430 UV-Vis multichannel detector and a radio-detector (gamma) with analog output and ca. 0.2 min signal delay. Unless stated otherwise, routine HPLC analysis was performed using a Luna C18(2) (Ø = 2.5 µm, 100 Å) column using a 20 min program, with a gradient of 0-100% MeCN in water, both eluents with 0.1% TFA. Routine quantification of radioactivity was performed on a Capintec CRC-55tR dose calibrator (DoseCall). If applicable, liquid scintillation counting (LSC) measurements were performed on a HIDEX 425-034 LSC for routine analysis, or on a HIDEX 300-SL LSC for large batch analysis and reported in becquerel (Bq) or counts per minute (cpm). Radio-TLC analysis was performed with a PerkinElmer Cyclone Plus phosphor imager on commercial pre-coated aluminum TLC sheets (4 x 10 cm, Merck Silica gel 60), and unless stated otherwise, run in 10% MeOH

in DCM. Free ^{64}Cu was quantified as ^{64}Cu-EDTA (Rf = 0.7) by adding EDTA to the reaction mixture prior to analysis. Radiochemical conversion (RCC) was always based on the relative converted substance, judged by radio-TLC. Radiochemical yield (RCY) was based on the collected activity of the radiolabelled product, judged by DoseCall or LSC, and decay corrected (dc) unless otherwise stated. Metal content was performed on an ICP-OES iCAP 7000 Plus Series (ICP, Thermo Fisher Scientific), using the relevant reference metal standard curve, prepared with metal-free 1% HCl in H_2O. Size exclusion chromatography (SEC) was performed on PD-10 cartridges (PD MidiTrap^{TM} G-25, containing sephadex G-25 resin) bought from Cytiva Sweden, using the relevant elution buffer (e.g., PBS (pH = 7.4) or iso-HEPES at 25°C.

Synthesis of 8 nm gold nanoparticles, AuNPs(8).

All glassware and magnets were cleaned by treating it with *aqua regia* (65% HNO_3 in H_2O/37% HCl in H_2O, 1:3, v/v) to remove residual metal. To a glass 100 mL round bottom-flask, containing a stirring bar, was added an aq. trisodium citrate solution (74 mg in 7.5 mL H_2O, 0.25 mmol). This was then mixed with metal-free water (30 mL), aq. potassium carbonate (5.3 mg in 0.25 mL H_2O, 38 µmol) and aq. tannic acid (128 µg in 30 µL H_2O, 75 nmol). The resulting solution was then stirred while heated to 70 °C. Then aq. $HAuCl_4$ $3H_2O$ (2.57 mg in 0.25 mL, 6.25 µmol) was added, resulting in a grey color, followed by a gradual change to light red. The mixture was stirred at 70 °C for 15 minutes and then allowed to cool down to room temperature, furnishing small **AuNP(8)** (ICP-OES: 0.032 mg Au/mL,).

Synthesis of 40 nm gold nanoparticles, AuNPs(40).

All glass was cleaned by treating it with *aqua regia* (65% HNO_3 in H_2O/37% HCl in H_2O, 1:3, v/v) to remove any residual metal contaminations. In a glass 100 mL round bottom-flask, with a stirring bar (also cleaned with *aqua regia*), was added $HAuCl_4$ 3 H_2O (7.4 mg, 18 µmol) in MiliQ-H_2O (50 mL). The mixture was then heated up to 75 °C, and stirred vigorously, followed by the addition of an aqueous trisodium citrate solution (48.5 mg in 4 mL H_2O, 165 µmol, pH = 7.0), and then stirred for 1 hour at 75 °C. The resulting *dark red* suspension was then heated up to 85 °C for 30 minutes, and then allowed to cool down to room temperature, furnishing the medium **AuNP(40**) (ICP-OES: 0.066 mg/mL)

Synthesis of [^{64}Cu]Cu-TA-DOTA

To an acid-washed, glass 10 mL vial, containing dry [^{64}Cu]$CuCl_2$ (0.1 – 1.0 GBq, see Table S1, page S26 in the SI) was added a stirring bar and aq. NH_4OAc (1.12 mg, 0.5 mL, pH = 6.8). The vial was sealed, heated up to 40 °C, and stirred for 10 minutes. To this stirring mixture was added aq. TA-DOTA stock solution (3.2 mg, 10 µL). The pH was measured using a pH-indicator (pH = 6.0). The mixture was then stirred for 20 minutes at 40 °C. Hereafter, an aliquot was taken from the reaction mixture and analyzed with radio-TLC, with elution in 5% NH_4OAc in H_2O:MeOH (1:1, v/v, RCC_1). The resulting [^{64}Cu]Cu-TA-DOTA in aq. NH_4OAc (**2**) was used directly in the following steps.

Radiolabelling of AuNPs with [^{64}Cu]Cu-TA-DOTA ([^{64}Cu]Cu-AuNPs)

Prior to use, all glass was cleaned by treating it with *aqua regia* (65% HNO_3 in H_2O/37% HCl in H_2O, 1:3, v/v) to remove any residual metal contaminations. To a 50 mL glass round-bottom flask equipped with a stirring bar was added AuNP dispersion, prepared as described above (20 mL). To this was added [^{64}Cu]Cu-DOTA complex, prepared as described above (1.0 mL, 1100 MBq, Table S1, page S26 in the SI), transferring all the activity into the reaction vial containing the AuNPs (A_{trans} > 95%). Then the mixture was stirred for 20 minutes at room temperature. Hereafter, an aliquot was taken and analyzed by radio-TLC (5% NH_4OAc in H_2O:MeOH, 1:1, v/v) to confirm the successful attachment of the [^{64}Cu]Cu-TA-DOTA to the AuNPs (RCC_2). Following this, the surface of the AuNPs was further decorated by adding a freshly prepared aqueous solution of MeO-PEG_{2K}-SH (2.1 mg, 100 µL), and the resulting mixture was stirred for 15 minutes at room temperature. Hereafter, an aliquot was taken and analyzed by radio-TLC (5% NH_4OAc in H_2O:MeOH,1:1, v/v, RCC_3) to confirm the continued surface attachment of the [^{64}Cu]Cu-TA-DOTA. A size-exclusion column (Cytiva PD MiniTrap G-25) was equilibrated with saline (5 mL) prior to sample application. A dispersion of AuNPs in saline (100 µL) was applied to the column and then eluted with saline, and fractions (14 fractions of 200 µL, depending on loading and column size) were collected. Once all the fractions were collected, they were analyzed for activity. The mixture was transferred into a centrifugation filter (MWCO = 30 kDa) and spun to remove the aqueous buffer (4400 rpm). Hereafter, the [^{64}Cu]Cu-DOTA-PEG-AuNPs were redispersed in sterile saline (15 mL) and the filter cartridge was centrifuged again to remove the saline (4400 rpm). The purified [^{64}Cu]Cu-DOTA-PEG-AuNPs were then resuspended in sterile saline (6 mL) and transferred into a 20 mL glass vial. The activity of the vial was measured (RCY_1) and an aliquot (1 mL) was immediately removed for analysis by DLS and size exclusion chro-

matography (**Table 1**). The remaining [^{64}Cu]Cu-DOTA-PEG-AuNPs dispersion (5 mL) was then sterile filtered (Acrodisc syringe filter, 13 mm Ø, 0.2 µm) into a sterile septum sealed 10 mL vial, which afforded the final product [^{64}Cu]Cu-AuNP (RCY_2).

Preparation of DOTA-LIPs

In a 10mL metal-free vial, was added pre-mixed lipid powder HSPC:CHOL:DSPE-PEG_{2k} (44.0 mg, 53.4 µmol, 3:1:1, mass ratio), then DSPE-PEG_{1k}-DOTA (1.28 mg, 6.0 µmol) to reach <10 mol% of DOTA in the resulting lipid mixture. t-BuOH:H_2O (3.0 mL, 9:1 v/v) was added and the solids were dissolved by sonication. The resulting solution was aliquoted into three vials separately (1.0 mL each) and freeze-dried. The obtained lyophilizate was hydrated with metal-free iso-HEPES (1.0 mL) buffer at 65 °C, followed by manual extrusion in an Avanti mini extruder with a 100 nm filter. The resulting liposomes are in the following referred to as DOTA-LIPs. Hereafter, the lipid dispersion was transferred to a glass vial and stored in the refrigerator for further use and analysis.

Preparation of [^{64}Cu]Cu-DOTA-LIPs

To a metal-free vial containing dry [^{64}Cu]$CuCl_2$ (360 MBq), DOTA-liposomes (20 mM lipid, 750 µL, see below) were added. The reaction mixture was magnetically stirred at 55 °C for 2 h. After this, 1 µL of the reaction solution was aliquoted and mixed with EDTA in iso-HEPES (100 µL, 20 nmol) and analyzed by radio-TLC (5% NH_4OAc in H_2O:MeOH, 1:1) (RCC_1). After 30 minutes, EDTA (50 µL) was added to the entire reaction mixture and stirred for 10 minutes while cooling down to room temperature and analyzed by radio-TLC (RCC_2). The [^{64}Cu]Cu-DOTA-LIPs were then purified by elution through a PD-10 size-exclusion column. The final product was then passed through a sterilized Millex-HV 0.45 µm filter. An aliquot of the product (1 mL) was removed for analysis, including radio-TLC (RCC_3), DLS and ICP-OES.

Characterization of [^{64}Cu]Cu-AuNPs and [^{64}Cu]Cu-DOTA-LIPs

The final dispersions of NPs all the different prepared (**[^{64}Cu]Cu-AuNPs** and **[^{64}Cu]Cu-DOTA-LIPs**) were characterized. Total activity was measured by dose-calibrator and purity was determined radio-TLC using a mixture of (5 % NH_4OAc in H_2O:MeOH, 1:1 v/v). Size and polydispersity index (PDI) were determined by DLS, UV-Vis, and TEM using the methods described in the Supporting Information. ICP-OES was used to determine the gold and phosphorus concentration using a predetermined standard, respectively. **Table 1** outlines a summary of the data for all the different prepared NPs (see Results section below).

The numbers of liposomes (*n*) in the final product were calculated using the following equation, adapted from the literature.[26] In which: *d* is the DLS volume-weighted diameter of the measured liposomes.

Animals and housing

Three Göttingen female-minipigs (Ellegaard Göttingen Minipigs A/S, Dalmose, Denmark) weighing on average 9.3 ± 0.4 kg (ranging from 8.9-9.6 kg) and approximately two months old were included in the present study. Minipigs were used due to their slow growth rate, making them optimal for long-term CED studies. Prior to the initiation of experimental procedures, the animals were allowed to acclimatize for one month at the animal facility of the Biomedical Laboratory, University of Southern Denmark. The animals were kept in communal enclosures with sawdust bedding and fed twice daily with a standard minipig diet (Altromin 9069, Altromin, Germany) and free access to water. Enrichment was provided in the form of hay, toys, and daily human interaction. The animals were attended to at least twice daily and monitored for general well-being, physical activity, and food consumption. Body weight was monitored weekly.

Anesthesia, analgesia, and perioperative procedures

For all surgical and imaging procedures, pigs were premedicated in a calm environment with an intramuscular injection of medetomidine 0,03 mg/kg (Cepetor Vet., 10 mg/mL, ScanVet Animal Health, Fredensborg, Denmark), midazolam 0,25 mg/kg (Midazolam 5 mg/mL, hameln pharma GmbH, Hameln, Germany), ketamine 5 mg/kg (Ketaminol Vet., 100 mg/mL, MSD Animal Health, Copenhagen, Denmark) and butorphanol 0,2 mg/kg (Butomidor Vet. 10 mg/mL, Salfarm Danmark A/S, Kolding, Denmark). Two IV accesses and a urinary catheter size six were placed before general anesthesia (GA) was induced with propofol (Propomitor Vet., 10 mg/mL, Orion Pharma Animal Health, Copenhagen, Denmark), and the pig was intubated with a cuffed orotracheal tube size 5,5. For surgical procedures, the animal was moved to the operating table and GA was maintained by a constant rate infusion of propofol 10 mg/kg/h and fentanyl 20 µg/kg/h while being mechanically ventilated with a tidal volume of 7-8 mL/kg and a respiratory frequency of 22-26 per minute. During surgical procedures, non-invasive blood pressure, electrocardiogram, body temperature, heart rate, oxygen saturation and capnography was continuously monitored. To prevent postoperative pain, pigs were administered an intramuscular injection of meloxicam 0,4 mg/kg (Metacam 5 mg/mL, Boehringer Ingelheim Vetmedica GmbH, In-

gelheim/Rhein, Germany) at the day of surgery. For antibiotic prophylaxis, an intravenous infusion of Cefuroxime 375 mg (Cefuroxime 'Fresenius Kabi', 750 mg, Fresenius Kabi AB, Uppsala, Sweden) was administered preoperatively in combination with an intramuscular injection of Amoxicillin 20 mg/kg (Noromox Prolongatum Vet., 150 mg/ml, ScanVet Animal Health, Fredensborg, Denmark). For imaging procedures, the anesthetized animal was transported to the imaging facility while maintaining anesthesia with propofol 2 mg/kg/h and manually ventilating the animal using a hand-held infant resuscitator (Ambu® SPUR II, Ambu A/S, Ballerup, Denmark) with a constant oxygen supply. During transport, heart rate and peripheral oxygen saturation (SpO_2) were continuously monitored with pulse oximetry and rectal body temperature was monitored regularly. During all imaging sessions, minipigs were mechanically ventilated, and GA was maintained as during surgical procedures. Hypothermia was prevented during all procedures using heated blankets and heated infusion bags.

Head immobilization and pre-catheter implantation MRI

A dedicated MRI-compatible head frame[27,28] was mounted on the anesthetized animal using two zygomatic arc screws, a moldable palate tray, and a snout strap. A fiducial arc was attached onto the frame and the animal was transferred in the prone position to the scanner bed of a GE SIGNA PET/MRI scanner with a magnetic field strength of 3 T (GE Healthcare, Waukesha, WI, USA). The upper anterior array (UAA) coil was attached around the fiducial arc. The step-by-step overview of all procedures involved on the surgery day is summarized in Figure 1.a. 3D MRI scans consisting of T1-weighted BRAVO (Repetition time = 8.8 ms, Echo time = 3.45 ms, Inversion time = 450 ms, Number of averages = 3, Flip angle= 12, Matrix size = 256 × 256 × 150, in-plane resolution = 0.8 mm × 0.8 mm, Slice thickness = 0.8 mm) and T2-weighted (Repetition time = 2742 ms, Echo time = 139.16 ms, Inversion time = 450 ms, Number of averages = 2, Flip angle = 12, Matrix size = 512 × 512 × 200, in-plane resolution = 0.39 mm × 0.39 mm, Slice thickness = 0.6 mm) sequences were obtained. For MRI acquisition, an Upper Anterior Array (UAA) providing a superior-inferior(S/I) coverage of 54 cm and right-left(R/L) coverage of 50 cm was employed. The preoperative MRI scans were then loaded into the neurosurgical planning software Neuroinspire™ (Renishaw Plc, Wotton-under-Edge, Gloucestershire, UK) to plan the implantation trajectories of two infusion catheters within the putaminal targets. Immediately after surgery, 22 µL of a mixture of Gd (Gadovist 1mmol/mL, Bayer Healthcare, Germany) and sterile artificial cerebrospinal fluid (aCSF, Torbay Pharmaceutical Manufacturing Unit, Paignton, UK) in a concentration of

2mM Gd were infused into the implanted catheters and a T1-weighted MRI was performed to confirm the targeting accuracy and verify proper catheter placement. For postoperative MRI scans, 8 channel high resolution brain array was utilized.

Ethical approval

All animal procedures were conducted in accordance with the obtained approval from the Danish Animal Experiments Inspectorate (license no. 2020-15-0201-00553). The experiments were conducted according to the EU directive 2010/63/EU on the protection of animals used for scientific purposes.

Implantation of Neuroinfuse chronic drug delivery system

To enable CED the Neuroinfuse chronic drug delivery system[29] developed by Renishaw Inc. was implanted. Following the preoperative MRI scans the animal was transferred from the scanner unit to the operation theatre. With the head still fixated in the dedicated head frame the animal was placed in a prone position. An 8-10 cm midline incision was made on the top of the skull. Periosteum was separately elevated.

The skin incision was closed in two layers with interrupted Vicryl 2-0 subcutaneously and continuous Monocryl 4-0 intracutaneously. The zygomatic wounds were closed with interrupted Ethilon 3-0 sutures.

Postoperative recovery and follow-up

A postoperative MRI was commenced to confirm adequate catheter placement. After this, the animal was referred to the animal facility for postoperative recovery and care. Special attention was drawn towards the awakening phase to ensure that the animals would avoid head traumas due to anesthetic side effects. Until full recovery, animals were closely monitored. In the subsequent period, animals were inspected minimum twice daily and assessed for neurological deficits and abnormal behavior. Wounds were inspected daily for signs of infection, and the skin/bone-anchored port interface was cleaned with sterile water when necessary.

Euthanasia

On the last day of the study, pigs were euthanized with an intravenous overdose of pentobarbital 100 mg/kg (Exagon Vet., 400 mg/mL, Salfarm Danmark, Kolding, Denmark) while in general anesthesia.

Infusion of nanoparticles The administration of ^{64}Cu-labeled NPs (^{64}Cu-NPs) commenced seven days after catheter implantation by connecting the application set to the transcutaneous port (as depicted in figure 1. B.). Infusions were repeated at weekly intervals for a total of four weeks. Each week a different type of nanocarrier was synthesized and infused into the subjects. Briefly, for each infusion, two 300 µL tubes were filled with dispersions of radiolabelled NPs at specific size. One end of the infusion tubes was connected to the corresponding delivery channel in the application set, while the other end was attached to a 6 m extension line which in turn connected to standard syringes pre-filled with artificial CSF (Figure 1.b). The extension lines were utilized to allow infusions from a syringe pump located outside the MRI scanning room. Once the application set was secured to the transcutaneous bone-anchored port, the infusion was initiated with 40-minute ramps. The infusion rate was gradually increased to a maximum rate of 3 µL/min per catheter with a total volume of 600 µL of ^{64}Cu-NPs delivered per infusion. Once the infusion was finished, the catheters were left in situ for an additional 15 minutes, and the pump rate gradually decreased to stabilize the pressure before disconnecting the infusion lines. The application set was then removed from the port.

Positron Emission Tomography (PET)

After attaching the infusion lines to the application set, the animal was positioned inside an 8-channel high-resolution brain array coil providing (S/I) coverage of 24 cm and (R/L) coverage of 22 cm for PET/MRI studies. PET emission data were collected dynamically over a 135-minute period, beginning at the start of the infusion. To facilitate quantitative analysis and to study the biodistribution of ^{64}Cu-NPs at different time points, list-mode emission files were re-binned into nine frames of 15 minutes each to produce dynamic PET scans and were reconstructed into a 256 × 256 × 89 matrix size (1.1718 mm × 1.1718 mm × 2.78 mm) using GE's Time of Flight Bayesian penalized reconstruction algorithm (Q.clear) with β=100. Quantitative corrections including detector geometry modeling, normalization, attenuation, scattering, decay, and dead time were considered inside the iterative loop. Of note, an MRI-based attenuation correction (MRAC) method was applied to correct attenuated annihilation photons. Additionally, we acquired a single MRI scan in each session to serve as an anatomical guide for defining the Volume of Interests (VOIs). MRI acquisitions were performed using the same setup and protocols described in the previous section. The experimental timeline is also shown in Figure 1.c.

PET Data analysis

Image analysis was carried out using GE's PET4D workstation, Image J, and Amide v1.0.4 software. Data visualization and a part of the image processing were performed in MATLAB R2023a.

Iso-contour plots

We studied the anisotropy in the spatial dispersion of NPs using iso-contour plots. To this end, three consecutive cross-sectional slices with the highest uptake value surrounding the left catheter from the same animal were selected, averaged, and then normalized to the maximum value in the image. The final image matrix was resampled to a finer grid of 1024 × 1024, and a contour plot was generated based on the processed image using an integrated program in MATLAB. The filled contour plot represents iso-lines obtained from an image and fills the areas between these isolines with consistent colors that correspond to the final image matrix values.

Statistics

Data were reported as mean values ± standard error of the mean (SEM), unless otherwise mentioned. All statistical testing was performed using GraphPad Prism (San Diego, CA, USA). One-way analysis of variance (ANOVA) followed by Tukey's Honestly Significant Difference (HSD) test was selected to compare the AUC results (FWHM, TAC, and VD) among different groups of NP with $P < 0.05$ considered significant. Significant difference was defined as $^{*}P < 0.05$, $^{**}P < 0.01$, $^{***}P < 0.001$, $^{****}P < 0.0001$.

3 Results and discussion

Synthesis and characterization of nanoparticles

To investigate the influence of NPs size on CED, we prepared two different types of ^{64}Cu-NPs in three different sizes: small and medium AuNPs: **NP(8)** and **NP(40)**, and large liposomal-NPs: **NP(130)**. Briefly, the synthesis of the [^{64}Cu]Cu-AuNPs began with the preparation of AuNPs from commercially available, high purity, $HAuCl_4$ 3□H_2O in a buffer solution at an elevated temperature (75 °C). Using different amounts of $AuCl_3$, with and without trisodium citrate buffer (pH = 7.0) yielded different sizes, small and medium, of AuNPs (see SI for details), with sizes of 5.42 ± 0.9 nm and 13.37 ± 0.83 nm, respectively (**Table 1**). Next, the freshly prepared AuNPs were treated with ^{64}Cu-DOTA-TA (a DOTA chelator linked to a 1,2-dithiolane functionality, see SI for structure), which was obtained quantitively from complexing [^{64}Cu]$CuCl_2$ and DOTA-TA using standard conditions, as described in the SI (RCC = 97.4 ± 0.4%, n = 4). In all cases, both the medium and small AuNPs were successfully coated with the ^{64}Cu-DOTA-TA complex with good radiochemical conversions (RCC = 83.5 ± 9.5%, n = 4). The radiolabelled AuNPs were then treated with a final coating of MeO-PEG_{2000}-SH in sufficient amounts to fully decorate the surface with a protective layer. The PEG-coating was not observed to displace the ^{64}Cu-DOTA-TA. The PEG-coated ^{64}Cu-AuNPs were then reformulated into saline by consecutive filtration, followed by redispersion in saline, then sterile filtered, and characterized to give the final ^{64}Cu-AuNPs ready for the *in vivo* studies (RCY = 57.0 ± 1.0%, n = 2, **Table 1** and **Table S1** in the SI).

Table 1. Properties of NPs administered intracranially to pigs. Reported data are given as mean ± SD (n = 5).

	^{64}Cu-AuNP(40)	^{64}Cu-AuNP(8)	^{64}Cu-LIPs(130)	^{64}Cu-LIPs(130)
Size classification	*medium*	*small*	*large*	*large*
$Ø_{hyd}$ DLS untr. AuNPs (nm)	13.37 ± 0.83	5.42 ± 0.9	n.a.	n.a.
$Ø_{hyd}$ DLS (nm)	39.84 ± 6.89	7.53 ± 0.36	134 ± 9	127 ± 10
Ø TEM (nm)	14.2 ± 1.3	4.8 ± 0.8	n.a.	n.a.
ζ (mV)	-4.86	-9.55	-4.89	-2.45
Ø UV-Vis (nm)	68 ± 8.0	6.6 ± 0.6	n.a.	n.a.
ICP-OES	Au = 0.18 mg/mL	Au = 0.12 mg/mL	P = 3.14 mM	P = 2.55 mM
Number of NPs			2.70 x 10^{+13} (4 mL)	2.76E x 10^{+13} (4 mL)
Total activity (A_{yield})	480 MBq	487 MBq		
Specific Activity (ndc.)	10.50 GBq/µmol	15.99 GBq/µmol		
RCY (ndc.)	43%	45%	48%	45%

Abbreviations: untr., untreated; ICP-OES, Inductively coupled plasma optical emission spectroscopy; DLS, Dynamic light scattering analysis; TEM, Transmission electron microscopy; RCY, Radiochemical yield; ndc., Non-decay corrected; A_{Final}, Final activity; ζ, Zeta potential; $Ø_{vol}$, Diameter measured by DLS; SD, Standard deviation.

Next, [^{64}Cu]Cu-LIPs were prepared as the *large* size-classified NPs for this study. First, stealth liposomes were prepared from a lipid mixture of SPC:Chol:DSPE-PEG_{2k} (44 mg, 3:1:1, mass ratio) and 1% DSPE-PEG_{1k}-DOTA (1.28 mg, 6.0 µmol) in tert-BuOH:H_2O (3.0 mL, 9:1 v/v) followed by freeze-drying and hydration with metal-free iso-HEPES (1.0 mL) at 65 °C, yielding the desired DOTA-decorated stealth liposomes (DOTA-LIPs, see SI page S26 for details). Next, the DOTA-LIPs were directly mixed with [^{64}Cu]$CuCl_2$ (0.1 - 1.5 GBq) at 55 °C for 2 h, which provided the radiolabelled [^{64}Cu]Cu-LIPs (RCC = 90 ± 1%, n = 2). The ^{64}Cu-labeled liposomes were then further purified by size exclusion chromatography using a PD-10 size exclusion column, with iso-HEPES (pH = 7.4), followed by filtration (0.45 µm) to give the final [^{64}Cu]Cu-LIPs for the *in vivo* studies (A = 374.5 ± 85.5 MBq, RCY = 54.0 ± 1.0% (dc.), n = 2, **Table 1**).

All NPs prepared in this study were analyzed for gold, or phosphorous content by ICP-OES (AuNPs or LIPs, respectively). Moreover, we also conducted a stability assay in order to determine the NPs potential fate after 24 hours, subsequent to preparation. After 24 hours, the NPs were resubjected to size exclusion chromatography to separate the NPs from potential degraded material, characterizing both the size and decomposition of the NPs (**Figure 2**, graphs 1B, 2B, and 3B).

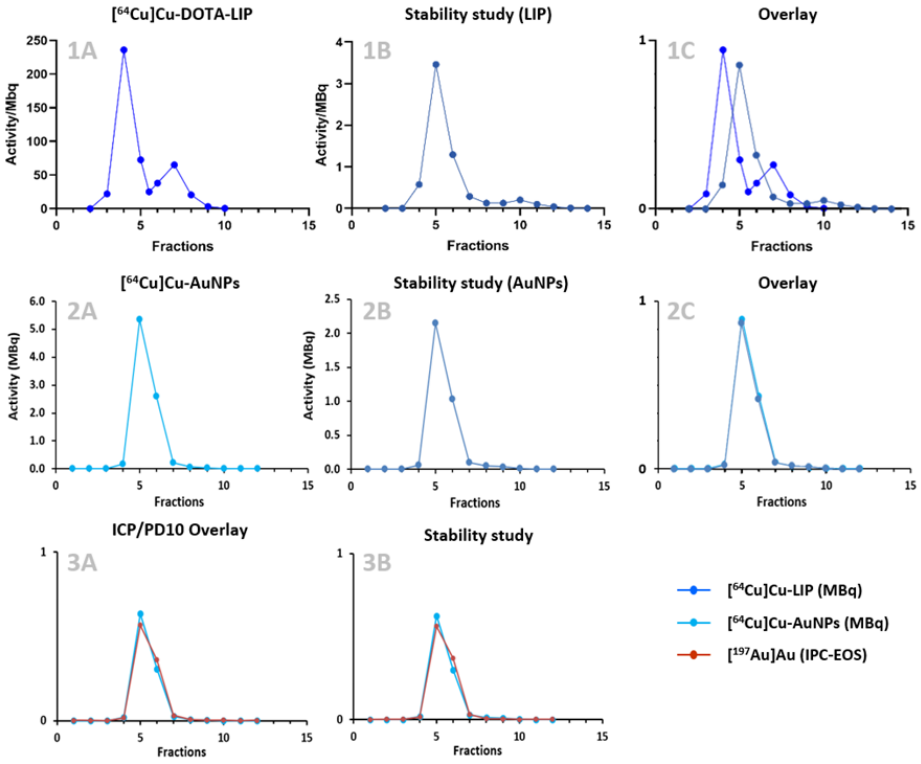

Figure 2. Size exclusion, stability, and ICP-EOS characterization of the different NPs in this study. (1A) ^{64}Cu-activity (MBq) analysis of [^{64}Cu]Cu-LIPs PD-10 size exclusion fractions. (1B) ^{64}Cu-activity (MBq) analysis of [^{64}Cu]Cu-LIPs PD-10 size exclusion fractions after 24 hours (stability assay). (1C) Overlay of 1A and 1B. (2A) ^{64}Cu-activity (MBq) analysis of [^{64}Cu]Cu-AuNPs PD-10 size exclusion fractions. (2B) ^{64}Cu-activity (MBq) analysis of [^{64}Cu]Cu-AuNPs PD-10 size exclusion fractions after 24 hours (stability assay). (2C) Overlay of 2A and 2B. (3A) ^{64}Cu-AuNPs ICP-OES analysis of the PD-10 size exclusion fraction, showing the overlap of ^{64}Cu activity (MBq) and ICP Au (mg/mL). (3B) ^{64}Cu-AuNPs ICP-OES analysis of the PD-10 size exclusion fraction, overlap, after 24 hours (stability study). *Abbreviations:* ICP-OES, inductively coupled plasma optical emission spectroscopy; ^{64}Cu, copper-64; NPs, nanoparticles; LIP, liposome; AuNPs, gold nanoparticles.

For the AuNPs, this, in conjunction with the size-exclusion chromatography ^{64}Cu-activity result, would confirm the interconnection of the ^{64}Cu activity with the gold, of the NPs (**Figure 2**, graphs 3A and 3B). This depicts a clear overlap of the ^{64}Cu activity (light blue line), and the gold content measured per fraction as judged by ICP-EOS (red line), which indicates the interconnection between the gold and the ^{64}Cu activity.

CED of radiolabelled nanoparticles in the minipig brain

We conducted PET imaging to track the real-time distribution kinetics of ^{64}Cu-labeled gold nanoparticles and liposomes following their direct infusion into the minipig brain. PET/MRI scans obtained from each subject at different infusion sessions were rigidly registered to a standard coordinate system through Amide software to facilitate visualization. Sagittal and transverse PET/MRIs of a representative minipig brain illustrating the distribution of three distinct NPs following 120-minute CED infusion are shown in **Figure 3**. The administered ^{64}Cu-NPs were easily distinguishable as a region of high signal intensity in the acquired PET images (Figure 3).

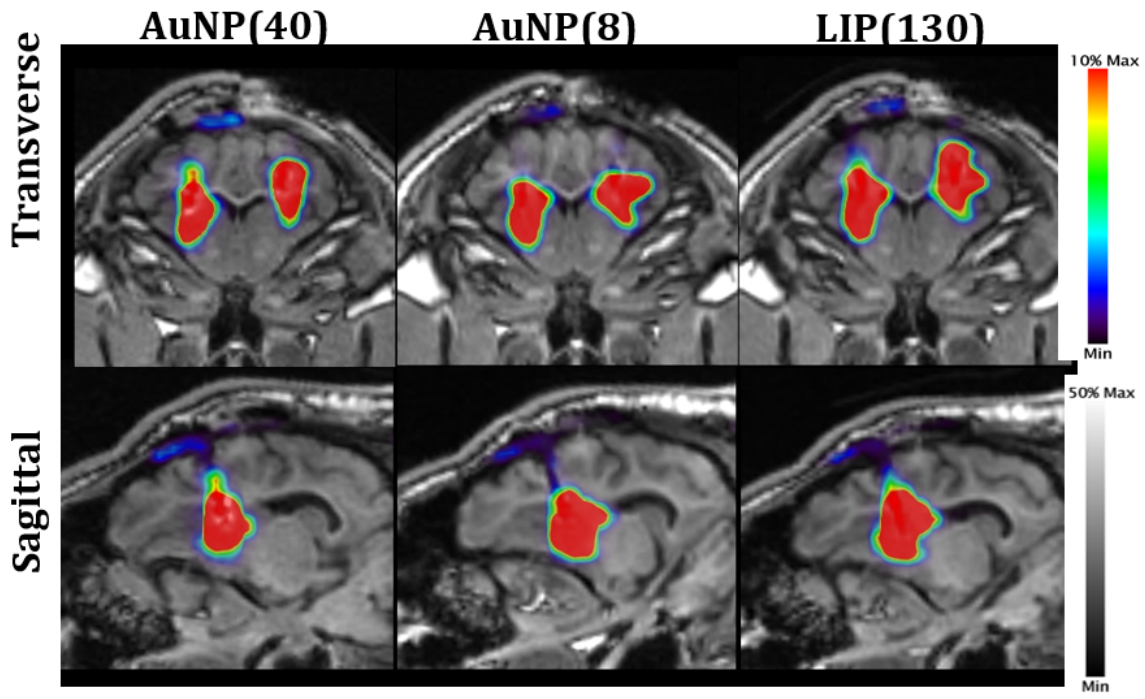

Figure 3. From left to right: representative PET/MRI scans of a minipig brain received ^{64}Cu labeled AuNP(40), AuNP(8), LIP(130) upon completion of two hours infusion from transverse (upper panel) and sagittal views (lower panel). Administration of nanoparticles was performed through two catheters implanted bilaterally within the putaminal regions. Abbreviations: PET, Positron emission tomography; MRI, Magnetic resonance imaging; AuNP(40), radiolabelled gold nanoparticles with an average diameter of 40 nm; AuNP(8), radiolabelled gold nanoparticles with an average diameter of 8 nm; LIP(130), radiolabelled liposomes with an average diameter of 130 nm.

Detailed presentation of dynamic PET frames and real-time tracking of ^{64}Cu-NP infusions can be found in **Figure S1**. During the infusion of all three types of ^{64}Cu-NPs, the distribution volumes demonstrated a gradual increase in size over time without reaching a steady state

even after a 120-minute infusion (Figure S1). As evidenced by Figure 3, LIP(130) exhibited a broader distribution compared to those achieved with the AuNPs and covered a more significant portion of the brain from both sagittal and transverse views. Moreover, medium-sized AuNP(40) penetrated less than small-sized AuNP(6).

We also assessed iso-contours for a single catheter infused with different NPs to explore directional bias in the distribution cloud generated following infusion. As depicted in **Figure 4**, isodose lines elicited slightly anisotropic dispersion of NPs. This can be attributed to both intrinsic properties of the infused NPs as well as the complex and intricate architecture of the targeted region. Brain parenchyma is notorious for its heterogeneous cellular density, extracellular space, uneven portion of white and gray matter, and tissue elasticity across various regions. These disparities contribute to a non-uniform and asymmetric distribution of the infusate around the cannula tip, even in healthy brain tissue[30]

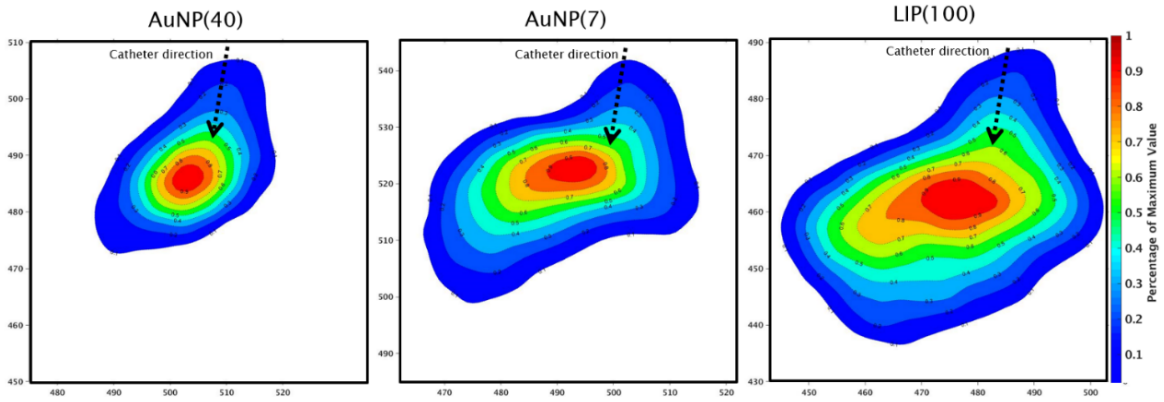

Figure 4. From left to right: iso-contours and iso-lines for a single catheter infused with ^{64}Cu-labeled AuNP(40), AuNP(6), and LIP(130) at the end of a 120-minute infusion. The process involved averaging three consecutive slices (target slice where the catheter is clearly visible plus two adjacent slices), normalizing to the maximum value, resampling to a finer sample size with a pixel size of 0.29 mm × 0.29 mm, and generating iso-contours based on the processed image. Pixels receiving the same percentage of infusion activity are shown with the same color (e.g., an area with 0.5 to 0.6 of the maximum value is shown with green color). Areas receiving < 0.1 maximum value are masked out and shown in white. Black arrows indicating catheter direction. Abbreviations: PET, Positron emission tomography; AuNP(40), radiolabelled gold nanoparticles with an average diameter of 40 nm; AuNP(8), radiolabelled gold nanoparticles with an average diameter of 8 nm; LIP(130), radiolabelled liposomes with an average diameter of 130 nm.

Discussion

On-going studies are unraveling the potential of locally administered NPs , which were loaded with a combination of cargos and imaging probes[9,11,13,31-35]. To ensure efficient transport of NP-encapsulated agents using CED, several key properties have been highlighted[5]; For example, NPs must seemingly possess a size smaller than 100 nm to effectively navigate the ECM. Further, to minimize the likelihood of non-specific binding to negatively charged components in the brain parenchyma, and enable wide distribution, the surface charge should be neutral or negatively charged[12,35,36]. With this in mind, this study investigated the biodistribution of nanoparticles by CED in a large animal model. Two different types of NPs, specifically stealth liposomes and AuNPs, with different sizes of small AuNPs (8□ nm), medium AuNPs (4□0 nm), and large LIPs (1□30 nm), all radiolabelled with ^{64}Cu, enabling their monitoring through PET imaging. To quantify the distribution of NPs within the brain, we performed a comprehensive analysis of the acquired PET scans in terms of isocontours.

The AuNPs administered by CED displayed a size-dependent diffusion and retention profile. We observed that smaller-sized AuNP(8) navigated the brain's ECM more efficiently and reached a larger volume of distribution and retention time. This could be attributed to the dense meshwork of glycoproteins and proteoglycans of ECM, which pose significant barriers to the diffusion of larger AuNPs(40). However, the larger LIP(130) significantly outperformed the two AuNPs, both in terms of distribution range and retention. This inconsistency may be related to the characteristics of the two types of nanoparticles. AuNP are dense, solid particles, while liposomes are 'soft' lipid nanoparticles. The patterns of movement of these two particles under the continuous pressure of CED are not yet fully understood. Therefore, to gain a deeper understanding of the relationship between size and distribution, it would be more beneficial to compare particles of the same nature, such as smaller-sized liposomes or micelles.

The present study is not without its limitations as it primarily focused on investigating the CED distribution NPs in healthy minipigs, and thus, distribution properties are not entirely applicable to a tumorous milieu. Brain tumors like GBM are marked by a heterogeneous landscape, characterized by varying cellular compositions, necrotic zones, hemorrhage, and distinct growth dynamics. Consequently, different regions within the tumor may exhibit varying capabilities for penetration and distribution of NPs administered directly into tumoral zones. Therefore, though our isodose evaluation showed that the distribution of

NPs is not entirely homogenous, this result didn't fully reflect the actual behavior of NPs in cancer-affected brains, especially in GBM. Consequently, additional studies in large animal tumor models to shed light on this would be highly relevant.

Our findings support the potential of integrating NPs and localized delivery methodologies as a promising therapeutic platform for addressing CNS-related disorders. However, before this approach can be translated into clinical practice, more in-depth investigations should be conducted to verify its reliability and robustness. Moreover, clinical implementation would require additional studies to optimize multiple attributes in relation to the NPs design such as size, shape, surface properties, and cargo loading capacity, in order to enhance their ability to penetrate greater distances effectively.

4 Summary and outlook

This study presents a pioneering effort in conducting PET-guided intracranial CED of three differently sized ^{64}Cu-labeled NPs, ranging in diameters from 8 to 130 nm. The aim was to investigate the impact of NPs size on the distribution volume and brain retention in a minipig model during CED administration. The comprehensive analysis of PET scans yielded substantial advantages for larger liposomes (LIPs) over smaller gold nanoparticles (AuNPs), evident in distribution volumes, penetration distance, and intracranial retention. Moreover, we observed slightly reduced penetration and retention of medium-sized AuNP(40) compared to small-sized AuNP(8). These findings underscore the superior performance of larger sized liposomes and highlight the crucial role of NPs size and physicochemical properties in shaping the efficacy of intracranial drug delivery strategies.

5 References

1 Samal, J., Rebelo, A. L. & Pandit, A. A window into the brain: Tools to assess pre-clinical efficacy of biomaterials-based therapies on central nervous system disorders. *Adv Drug Deliv Rev* **148**, 68-145 (2019). https://doi.org:10.1016/j.addr.2019.01.012

2 Bobo, R. H., Laske, D. W., Akbasak, A., Morrison, P. F., Dedrick, R. L. & Oldfield, E. H. Convection-enhanced delivery of macromolecules in the brain. *Proc Natl Acad Sci U S A* **91**, 2076-2080 (1994). https://doi.org:10.1073/pnas.91.6.2076

3 Groothuis, D. R. The blood-brain and blood-tumor barriers: a review of strategies for increasing drug delivery. *Neuro Oncol* **2**, 45-59 (2000). https://doi.org:10.1093/neuonc/2.1.45

4 Sampson, J. H. *et al.* Poor drug distribution as a possible explanation for the results of the PRECISE trial. *J Neurosurg* **113**, 301-309 (2010). https://doi.org:10.3171/2009.11.Jns091052

5 Allard, E., Passirani, C. & Benoit, J. P. Convection-enhanced delivery of nanocarriers for the treatment of brain tumors. *Biomaterials* **30**, 2302-2318 (2009). https://doi.org:10.1016/j.biomaterials.2009.01.003

6 Halle, B., Mongelard, K. & Poulsen, F. R. Convection-enhanced Drug Delivery for Glioblastoma: A Systematic Review Focused on Methodological Differences in the Use of the Convection-enhanced Delivery Method. *Asian J Neurosurg* **14**, 5-14 (2019). https://doi.org:10.4103/ajns.AJNS_302_17

7 Georgiou, C. J. *et al.* Treatment of Orthotopic U251 Human Glioblastoma Multiforme Tumors in NRG Mice by Convection-Enhanced Delivery of Gold Nanoparticles Labeled with the β-Particle-Emitting Radionuclide, (177)Lu. *Mol Pharm* **20**, 582-592 (2023). https://doi.org:10.1021/acs.molpharmaceut.2c00815

8 Inoue, T. *et al.* Therapeutic efficacy of a polymeric micellar doxorubicin infused by convection-enhanced delivery against intracranial 9L brain tumor models. *Neuro Oncol* **11**, 151-157 (2009). https://doi.org:10.1215/15228517-2008-068

9 Gleason, J. M. *et al.* Intrinsically Disordered Protein Micelles as Vehicles for Convection-Enhanced Drug Delivery to Glioblastoma Multiforme. *ACS Appl Bio Mater* **5**, 3695-3702 (2022). https://doi.org:10.1021/acsabm.2c00215

10 Wu, G., Barth, R. F., Yang, W., Kawabata, S., Zhang, L. & Green-Church, K. Targeted delivery of methotrexate to epidermal growth factor receptor-positive brain tumors by means of cetuximab (IMC-C225) dendrimer bioconjugates. *Mol Cancer Ther* **5**, 52-59 (2006). https://doi.org:10.1158/1535-7163.MCT-05-0325

11 Saito, R. *et al.* Gadolinium-loaded liposomes allow for real-time magnetic resonance imaging of convection-enhanced delivery in the primate brain. *Exp Neurol* **196**, 381-389 (2005). https://doi.org:10.1016/j.expneurol.2005.08.016

12 MacKay, J. A., Deen, D. F. & Szoka, F. C., Jr. Distribution in brain of liposomes after convection enhanced delivery; modulation by particle charge, particle diameter, and presence of steric coating. *Brain Res* **1035**, 139-153 (2005). https://doi.org:10.1016/j.brainres.2004.12.007

13 Mamot, C. *et al.* Extensive distribution of liposomes in rodent brains and brain tumors following convection-enhanced delivery. *J Neurooncol* **68**, 1-9 (2004). https://doi.org:10.1023/b:neon.0000024743.56415.4b

14 Thorne, R. G. & Nicholson, C. In vivo diffusion analysis with quantum dots and dextrans predicts the width of brain extracellular space. *Proc Natl Acad Sci U S A* **103**, 5567-5572 (2006). https://doi.org:10.1073/pnas.0509425103

15 Hobbs, S. K. *et al.* Regulation of transport pathways in tumor vessels: role of tumor type and microenvironment. *Proc Natl Acad Sci U S A* **95**, 4607-4612 (1998). https://doi.org:10.1073/pnas.95.8.4607

16 Desai, P. *et al.* Radiolabelled Nanocarriers as Theranostics-Advancement from Peptides to Nanocarriers. *Small* **18**, e2200673 (2022). https://doi.org:10.1002/smll.202200673

17 Farzin, L., Sheibani, S., Moassesi, M. E. & Shamsipur, M. An overview of nanoscale radionuclides and radiolabelled nanomaterials commonly used for nuclear molecular imaging and therapeutic functions. *J Biomed Mater Res A* **107**, 251-285 (2019). https://doi.org:10.1002/jbm.a.36550

18 Richardson, R. M. *et al.* Interventional MRI-guided putaminal delivery of AAV2-GDNF for a planned clinical trial in Parkinson's disease. *Mol Ther* **19**, 1048-1057 (2011). https://doi.org:10.1038/mt.2011.11

19 Su, X. *et al.* Real-time MR imaging with Gadoteridol predicts distribution of trans-

genes after convection-enhanced delivery of AAV2 vectors. *Mol Ther* **18**, 1490-1495 (2010). https://doi.org:10.1038/mt.2010.114

20 Christine, C. W. *et al.* Magnetic resonance imaging-guided phase 1 trial of putaminal AADC gene therapy for Parkinson's disease. *Ann Neurol* **85**, 704-714 (2019). https://doi.org:10.1002/ana.25450

21 Stiles, D. (Google Patents, 2015).

22 Yao, Y., Ding, X., Qi, Y., Qi, M. & Jones, A. Using MRI to determine gadolinium contrast agent concentration in convection-enhanced delivery. *Brain Tumor Res Treat* **10** (2022). https://doi.org:https://doi.org/10.14791/btrt.2022.10.F-2562

23 Salegio, E. A. *et al.* Feasibility of Targeted Delivery of AAV5-GFP into the Cerebellum of Nonhuman Primates Following a Single Convection-Enhanced Delivery Infusion. *Hum Gene Ther* **33**, 86-93 (2022). https://doi.org:10.1089/hum.2021.163

24 Spinazzi, E. F. *et al.* Chronic convection-enhanced delivery of topotecan for patients with recurrent glioblastoma: a first-in-patient, single-centre, single-arm, phase 1b trial——. *Lancet Oncol* **23**, 1409-1418 (2022). https://doi.org:10.1016/S1470-2045(22)00599-X

25 Salegio, E. A., Campagna, M. V., Allen, P. C., Stockinger, D. E., Song, Y. & Hwa, G. G. C. Targeted Delivery and Tolerability of MRI-Guided CED Infusion into the Cerebellum of Nonhuman Primates. *Hum Gene Ther Methods* **29**, 169-176 (2018). https://doi.org:10.1089/hgtb.2018.049

26 Mozafari, M., Mazaheri, E. & Dormiani, K. Simple equations pertaining to the particle number and surface area of metallic, polymeric, lipidic and vesicular nanocarriers. *Sci. Pharm* **89**, 15 (2021). https://doi.org:https://doi.org/10.3390/scipharm89020015

27 Bienemann, A. *et al.* The development of an implantable catheter system for chronic or intermittent convection-enhanced delivery. *J Neurosci Methods* **203**, 284-291 (2012). https://doi.org:10.1016/j.jneumeth.2011.10.002

28 White, E. *et al.* A robust MRI-compatible system to facilitate highly accurate stereotactic administration of therapeutic agents to targets within the brain of a large animal model. *J Neurosci Methods* **195**, 78-87 (2011). https://doi.org:10.1016/j.jneumeth.2010.10.023

29 Barua, N. U. *et al.* A novel implantable catheter system with transcutaneous port for

intermittent convection-enhanced delivery of carboplatin for recurrent glioblastoma. *Drug Deliv* **23**, 167-173 (2016). https://doi.org:10.3109/10717544.2014.908248

30 Healy, A. T. & Vogelbaum, M. A. Convection-enhanced drug delivery for gliomas. *Surg Neurol Int* **6**, S59-67 (2015). https://doi.org:10.4103/2152-7806.151337

31 Wang, Y. *et al.* Nanoparticle-mediated convection-enhanced delivery of a DNA intercalator to gliomas circumvents temozolomide resistance. *Nat Biomed Eng* **5**, 1048-1058 (2021). https://doi.org:10.1038/s41551-021-00728-7

32 Stephen, Z. R. *et al.* Time-Resolved MRI Assessment of Convection-Enhanced Delivery by Targeted and Nontargeted Nanoparticles in a Human Glioblastoma Mouse Model. *Cancer Res* **79**, 4776-4786 (2019). https://doi.org:10.1158/0008-5472.CAN-18-2998

33 Finbloom, J. A. *et al.* Evaluation of Three Morphologically Distinct Virus-Like Particles as Nanocarriers for Convection-Enhanced Drug Delivery to Glioblastoma. *Nanomaterials (Basel)* **8** (2018). https://doi.org:10.3390/nano8121007

34 Josowitz, A. D., Bindra, R. S. & Saltzman, W. M. Polymer nanocarriers for targeted local delivery of agents in treating brain tumors. *Nanotechnology* **34**, 072001 (2022). https://doi.org:10.1088/1361-6528/ac9683

35 Zhou, J. *et al.* Highly penetrative, drug-loaded nanocarriers improve treatment of glioblastoma. *Proc Natl Acad Sci U S A* **110**, 11751-11756 (2013). https://doi.org:10.1073/pnas.1304504110

36 Phillips, W. T., Bao, A., Brenner, A. J. & Goins, B. A. Image-guided interventional therapy for cancer with radiotherapeutic nanoparticles. *Adv Drug Deliv Rev* **76**, 39-59 (2014). https://doi.org:10.1016/j.addr.2014.07.001

37 Saito, R. *et al.* Distribution of liposomes into brain and rat brain tumor models by convection-enhanced delivery monitored with magnetic resonance imaging. *Cancer Res* **64**, 2572-2579 (2004). https://doi.org:10.1158/0008-5472.can-03-3631

38 Nance, E. A. *et al.* A dense poly(ethylene glycol) coating improves penetration of large polymeric nanoparticles within brain tissue. *Sci Transl Med* **4**, 149ra119 (2012). https://doi.org:10.1126/scitranslmed.3003594

39 Birzu, C. *et al.* Recurrent Glioblastoma: From Molecular Landscape to New Treatment Perspectives. *Cancers (Basel)* **13** (2020). https://doi.org:10.3390/cancers13010047

Chapter 6

Summary and Outlook

In recent years, significant progress has been made in the field of nanomedicine, which has provided innovative solutions for drug delivery and therapeutic applications. Innovative drug delivery systems, diagnostic tools, and therapeutic agents based on nanoparticles have been successfully produced, such as Doxil®. These advancements are particularly crucial when dealing with complex and aggressive diseases like GBM. As a high-grade glioma that is notorious for its rapid growth and highly infiltrative nature, GBM is one of the most challenging brain cancers to treat. Traditional treatment modalities, including surgery, radiation, and chemotherapy, often fall short in eradicating the disease completely, primarily due to the tumor's ability to infiltrate surrounding healthy brain tissue.

To address these challenges, Auger radiotherapy has gained attention as a promising therapeutic approach. Unlike conventional radiotherapy, which relies on high-energy photons or particles to kill cancer cells, Auger radiotherapy employs low-energy Auger electrons. These electrons have a very short range, typically less than a few nanometers, making them ideal for localized cellular damage. Therefore, by delivering Auger electrons directly to these infiltrative cells, it is possible to induce significant cellular damage while sparing adjacent healthy tissues. However, the effectiveness of Auger radiotherapy largely depends on the precise delivery and retention of the therapeutic agents in the target tissue.

Therefore, nanocarriers, such as liposomes and micelles, have demonstrated significant potential in augmenting the efficacy of Auger radiotherapy. These nanocarriers offer advantages such as increased drug loading capacity and stability, and enhanced retention time, making them well-suited for delivering Auger emitters specifically to infiltrative cells.

In this thesis we presented research focusing on the treatment of GBM via [^{125}I]IUdR loaded nanocarriers. The research begins with an deep exploration of liposomal drug delivery systems, which was presented in Chapter 2. [^{125}I]IUdR, as a potential candidate for Auger radiotherapy, has been proven effective in treating GBM.[50] However, free [^{125}I]IUdR degrades quickly in the body. Therefore, in this chapter, we firstly modified the structure of [^{125}I]IUdR. The introduction of an ester linker was a strategic design choice. By introducing different lengths of carbon chains at the 5' primary alcohol position on the deoxyribose with

linear alkyl chains through an ester linker, namely [^{125}I]IUdR-C_4, -C_8, -C_{12}, and -C_{18}, these prodrugs were loaded into liposomes via post or pre insertion method. The differences in the length of the linear alkyl chains also allowed us to control the rate of the release of [^{125}I]IUdR by esterase hydrolysis. Different release rates were confirmed in in vitro release experiments, including ISO-HEPES buffer with added esterase and in rat brain homogenate. Prodrugs with shorter chains resulted in faster release rates, especially for [^{125}I]IUdR-C_4 and -C_8, while longer chains had slower release rates. Among them, [^{125}I]IUdR-C_{18}-LIPs was elected for *in vitro* and *in vivo* tests, which showed DNA incorporation capabilities both in vivo and in vitro, as well as in vitro cell-killing ability. *In vivo* distribution of [^{125}I]IUdR-C_{18}-LIPs showed a 48-hour retention in the brain. These findings demonstrated that [^{125}I]IUdR-C_{18}-LIPs could be a promising candidate for GBM treatment, therefore, the *in vivo* efficacy study will be beneficial and will be carried out in the next stage.

In addition to liposomes, the same prodrugs, [^{125}I]IUdR-C_4, -C_8, -C_{12}, and -C_{18}, wereinvestigated for drug loading, release, and efficacy studies based on micelle-based nanocarriers. We successfully prepared [^{125}I]IUdR-Cn prodrugs loaded polymeric micelles with a high yield, especilly for [^{125}I]IUdR-C_{18}. The release study meditated by esterase showed that [^{125}I]IUdR can released from [^{125}I]IUdR-C_n-PMs, but with relative fast speed when compared to [^{125}I]IUdR-C_{18}-LIPs. The in vitro DNA incorporation and efficacy studies showed with this system, [^{125}I]IUdR was able to integrated into DNA and then kill the cells. However, due to the fast release rate, using isotopes with a shorter half-life like iodine-123 would be interesting to investigate.

The third part turned to explore the potential of brush-shaped nanocarriers (PB) for Auger radiotherapy in GBM and presented in Chapter 4. This brush-shaped nanocarrier has a very small size and does not contain PEG, which can avoid immune responses such as ABC effect that may be caused by PEG. The alkyne DBCO was grafted into the side chain of PB for click reactions, and then the azide-functionalized prodrug [^{125}I]IUdR-C_4-N_3 with an ester bond was conjugated onto PB through copper-free click reaction, leading to a high loading efficiency that up to 79%. This was very interesting because it provided a effective alternative to traditional drug loading methods and may accelerate the transition from research to clinical applications in the terms of production. The release rate of [^{125}I]IUdR from [^{125}I]IUdR-PB was slower than that of liposomes and other nanosystems, releasing about 25% within 2 days. This is partly due to the spatial configuration of PB and may also be due to the shorter carbon chain of the prodrug [^{125}I]IUdR-C_4-N_3. They both may possibly

contribute to the slow release of [^{125}I]IUdR from [^{125}I]IUdR-PB, as the results of condense brush layer and close distance to the PB skeleton. *In vitro* cell experiments, including DNA incorporation and cell viability assays, demonstrated the effectiveness of [^{125}I]IUdR-PB as therapeutical agent for GBM. However, investigation on more rationally designed prodrugs loaded PB will further enhance the possibility of PB as a carrier for GBM treatment.

The forth part (Chapter 5) studied how the size of nanoparticles affect drug distribution and retention in the brain through PET-guided intracranial CED administration. CED, as a potential local administration method, can not only bring larger distribution volume (V_d) compared to diffusion, but also bypass the BBB and directly deliver drugs to the lesion site. Therefore, in this chapter, the behaviors of two nanoparticles, liposomes (130 nm) and gold nanoparticles (8 and 40 nm), were studied in the brains of pigs via CED administration. We found that liposomes (130) showed a better distribution than AuNP (8) and AuNP (40). This could be of high interest. Because the lipid composition of liposomes (130) was the same as that of [^{125}I]IUdR-C_{18}-LIPs, the differences were the labeling method (^{64}Cu-DOTA surface conjugation verse. post insertion of [^{125}I]IUdR-C_{18}) and lipids concentration (3 mM and roughly 15mM, respectively). Therefore, in the next stage, the study of the brain distribution of IUdR-C_{18}-LIPs labelled with iodine-124 ([^{124}I]IUdR-C_{18}-LIPs) that has similar lipids concentration to [^{125}I]IUdR-C_{18}-LIPs will further reveal and predict the characteristics of [^{125}I]IUdR-C_{18}-LIPs in the brain, and then further provide insight on the optimization of the *in vivo* efficacy study.

In summary, this thesis has conducted in-depth research in the field of targeted drug delivery systems, especially in Auger radiotherapy for GBM. Through the refinement of nanocarrier platforms for drug delivery, we have broadened the horizons for targeted GBM treatments.

References

1. Davis ME. Glioblastoma: overview of disease and treatment. Clinical Journal of Oncology Nursing 2016;20:S2.
2. Ostrom QT, Gittleman H, Liao P, et al. CBTRUS Statistical Report: Primary brain and other central nervous system tumors diagnosed in the United States in 2010–2014. Neuro-Oncology 2017;19:v1–v88.
3. Chen B, Chen C, Zhang Y, and Xu J. Recent incidence trend of elderly patients with glioblastoma in the United States, 2000–2017. BMC Cancer 2021;21:54.
4. Stupp R, Mason WP, Bent MJ van den, et al. Radiotherapy plus Concomitant and Adjuvant Temozolomide for Glioblastoma. New England Journal of Medicine 2005;352:987–96.
5. Louis DN, Perry A, Reifenberger G, et al. The 2016 World Health Organization Classification of Tumors of the Central Nervous System: a summary. Acta Neuropathologica 2016;131:803–20.
6. Stupp R, Hegi ME, Mason WP, et al. Effects of radiotherapy with concomitant and adjuvant temozolomide versus radiotherapy alone on survival in glioblastoma in a randomised phase III study: 5-year analysis of the EORTC-NCIC trial. The Lancet Oncology 2009;10:459–66.
7. Sampson JH, Heimberger AB, Archer GE, et al. Immunologic Escape After Prolonged Progression-Free Survival With Epidermal Growth Factor Receptor Variant III Peptide Vaccination in Patients With Newly Diagnosed Glioblastoma. Journal of Clinical Oncology 2010;28:4722–9.
8. Desjardins A, Gromeier M, Herndon JE, et al. Recurrent Glioblastoma Treated with Recombinant Poliovirus. New England Journal of Medicine 2018;379:150–61.
9. Weller M, Butowski N, Tran DD, et al. Rindopepimut with temozolomide for patients with newly diagnosed, EGFRvIII-expressing glioblastoma (ACT IV): a randomised, double-blind, international phase 3 trial. The Lancet Oncology 2017;18:1373–85.
10. Anton K, Baehring JM, and Mayer T. Glioblastoma Multiforme. Hematology/Oncology Clinics of North America 2012;26:825–53.
11. Janjua TI, Rewatkar P, Ahmed-Cox A, et al. Frontiers in the treatment of glioblastoma: Past, present and emerging. Advanced Drug Delivery Reviews 2021;171:108–38.
12. Angelucci C, Lama G, and Sica G. Multifaceted Functional Role of Semaphorins in Glioblastoma. International Journal of Molecular Sciences 2019;20:2144.
13. Pandey N, Anastasiadis P, Carney CP, et al. Nanotherapeutic treatment of the invasive glioblastoma tumor microenvironment. Advanced Drug Delivery Reviews 2022;188:114415.
14. Bailly C, Vidal A, Bonnemaire C, et al. Potential for Nuclear Medicine Therapy for Glioblastoma Treatment. Frontiers in Pharmacology 2019;10.
15. Majkowska-Pilip A, Gawęda W, Żelechowska-Matysiak K, Wawrowicz K, and Bilewicz A. Nanoparticles in Targeted Alpha Therapy. Nanomaterials 2020;10:1366.
16. Goel M, Mishra MK, and Kumar D. Recent advances in Targeted Radionuclide therapy for Cancer treatment. Chemical Biology Letters 2023;10:544–4.
17. Zukotynski K, Jadvar H, Capala J, and Fahey F. Targeted Radionuclide Therapy: Practical Applications and Future Prospects: Supplementary Issue: Biomarkers and their Essential Role in the Development of Personalised Therapies (A). Biomarkers in cancer 2016;8. Publisher: SAGE Publications Sage UK: London, England:BIC–S31804.

18. Nelson BJ, Andersson JD, and Wuest F. Targeted Alpha Therapy: Progress in Radionuclide Production, Radiochemistry, and Applications. Pharmaceutics 2021;13. Publisher: Multidisciplinary Digital Publishing Institute:49.

19. Chamarthy MR, Williams SC, and Moadel RM. Radioimmunotherapy of non-Hodgkin's lymphoma: from the 'magic bullets' to 'radioactive magic bullets'. The Yale journal of biology and medicine 2011;84. Publisher: Yale Journal of Biology and Medicine:391.

20. Bolcaen J, Gizawy MA, Terry SY, et al. Marshalling the Potential of Auger Electron Radiopharmaceutical Therapy. Journal of Nuclear Medicine 2023;64:1344–51.

21. Parker C, Lewington V, Shore N, et al. Targeted alpha therapy, an emerging class of cancer agents: a review. JAMA oncology 2018;4. Publisher: American Medical Association:1765–72.

22. Salih S, Alkatheeri A, Alomaim W, and Elliyanti A. Radiopharmaceutical Treatments for Cancer Therapy, Radionuclides Characteristics, Applications, and Challenges. Molecules 2022;27:5231.

23. Choi J and Kang JO. Basics of particle therapy II: relative biological effectiveness. Radiation Oncology Journal 2012;30:1.

24. Iliakis G, Mladenov E, and Mladenova V. Necessities in the Processing of DNA Double Strand Breaks and Their Effects on Genomic Instability and Cancer. Cancers 2019;11:1671.

25. Poty S, Francesconi LC, McDevitt MR, Morris MJ, and Lewis JS. α-Emitters for Radiotherapy: From Basic Radiochemistry to Clinical Studies—Part 1. Journal of Nuclear Medicine 2018;59:878–84.

26. Liu W, Ma H, Liang R, et al. Targeted Alpha Therapy of Glioma Using ^{211} At-Labeled Heterodimeric Peptide Targeting Both VEGFR and Integrins. Molecular Pharmaceutics 2022;19:3206–16.

27. Deshayes E, Roumiguie M, Thibault C, et al. Radium 223 dichloride for prostate cancer treatment. Drug design, development and therapy 2017;11. Publisher: Dove Press:2643.

28. Hagemann UB, Wickstroem K, Hammer S, et al. Advances in Precision Oncology: Targeted Thorium-227 Conjugates As a New Modality in Targeted Alpha Therapy. Cancer Biotherapy and Radiopharmaceuticals 2020;35:497–510.

29. Tafreshi NK, Doligalski ML, Tichacek CJ, et al. Development of Targeted Alpha Particle Therapy for Solid Tumors. Molecules 2019;24:4314.

30. Albertsson P, Bäck T, Bergmark K, et al. Astatine-211 based radionuclide therapy: Current clinical trial landscape. Frontiers in Medicine 2023;9:1076210.

31. Mezni E, Vicier C, Guerin M, Sabatier R, Bertucci F, and Gonçalves A. New Therapeutics in HER2-Positive Advanced Breast Cancer: Towards a Change in Clinical Practices? Cancers 2020;12:1573.

32. Mladenova V, Mladenov E, Stuschke M, and Iliakis G. DNA Damage Clustering after Ionizing Radiation and Consequences in the Processing of Chromatin Breaks. Molecules 2022;27:1540.

33. Haberkorn U, Giesel F, Morgenstern A, and Kratochwil C. The Future of Radioligand Therapy: α, β, or Both? Journal of Nuclear Medicine 2017;58:1017–8.

34. Brady D, O'Sullivan JM, and Prise KM. What is the Role of the Bystander Response in Radionuclide Therapies? Frontiers in Oncology 2013;3.

35. Stokke C, Kvassheim M, and Blakkisrud J. Radionuclides for Targeted Therapy: Physical Properties. Molecules 2022;27:5429.

36. Sgouros G, Bodei L, McDevitt MR, and Nedrow JR. Radiopharmaceutical therapy in cancer: clinical advances and challenges. Nature Reviews Drug Discovery 2020;19:589–608.

37. Gharibkandi NA, Gierałtowska J, Wawrowicz K, and Bilewicz A. Nanostructures as Radionuclide Carriers in Auger Electron Therapy. Materials 2022;15:1143.

38. Pirovano G, Wilson TC, and Reiner T. Auger: The future of precision medicine. Nuclear Medicine and Biology 2021;96-97:50–3.

39. Ku A, Facca VJ, Cai Z, and Reilly RM. Auger electrons for cancer therapy – a review. Ejnmmi Radiopharmacy and Chemistry 2019;4:27.

40. Idrissou MB, Pichard A, Tee B, Kibedi T, Poty S, and Pouget JP. Targeted Radionuclide Therapy Using Auger Electron Emitters: The Quest for the Right Vector and the Right Radionuclide. Pharmaceutics 2021;13:980.

41. Santoro L, Boutaleb S, Garambois V, et al. Noninternalizing monoclonal antibodies are suitable candidates for 125I radioimmunotherapy of small-volume peritoneal carcinomatosis. Journal of Nuclear Medicine 2009;50. Publisher: Soc Nuclear Med:2033–41.

42. Paillas S, Ladjohounlou R, Lozza C, et al. Localized Irradiation of Cell Membrane by Auger Electrons Is Cytotoxic Through Oxidative Stress-Mediated Nontargeted Effects. Antioxidants & Redox Signaling 2016;25:467–84.

43. Pedersen KS, Deville C, Søndergaard U, Jensen M, and Jensen AI. Improved procedures for production and purification of 135La from enriched [135Ba]BaCO3 on a 16.5 MeV cyclotron. Applied Radiation and Isotopes 2023;192:110612.

44. Aluicio□Sarduy E, Thiele NA, Martin KE, et al. Establishing Radiolanthanum Chemistry for Targeted Nuclear Medicine Applications. Chemistry – A European Journal 2020;26:1238–42.

45. Costa IM, Siksek N, Volpe A, et al. Relationship of In Vitro Toxicity of Technetium-99m to Subcellular Localisation and Absorbed Dose. International Journal of Molecular Sciences 2021;22:13466.

46. Pirovano G, Jannetti SA, Carter LM, et al. Targeted Brain Tumor Radiotherapy Using an Auger Emitter. Clinical cancer research : an official journal of the American Association for Cancer Research 2020;26:2871–81.

47. Madsen KL, Therkelsen ASN, Langkjær N, Olsen BB, and Thisgaard H. Auger electron therapy of glioblastoma using [125I]5-iodo-2□-deoxyuridine and concomitant chemotherapy – Evaluation of a potential treatment strategy. Nuclear Medicine and Biology 2021;96-97:35–40.

48. Kiess AP, Minn I, Chen Y, et al. Auger Radiopharmaceutical Therapy Targeting Prostate-Specific Membrane Antigen. Journal of Nuclear Medicine 2015;56:1401–7.

49. Krenning E, De Jong M, Kooij P, et al. Radiolabelled somatostatin analogue(s) for peptide receptor scintigraphy and radionuclide therapy. Annals of Oncology 1999;10:S23–S30.

50. Wei S, Li C, Li M, et al. Radioactive Iodine-125 in Tumor Therapy: Advances and Future Directions. Frontiers in Oncology 2021;11:717180.

51. Lehnert S, Li Y, Bump E, Riddoch B, Chenite A, and Shive M. 125I-Iododeoxyuridine for the Treatment of a Brain Tumor Model: Selection of Conditions for Optimal Effectiveness. The Open Nuclear Medicine Journal 2011;3.

52. Kassis AI, Sastry KSR, and Adelstein SJ. Kinetics of Uptake, Retention, and Radiotoxicity of 125 IUdR in Mammalian Cells: Implications of Localized Energy Deposition by Auger Processes. Radiation Research 1987;109:78.

53. Thisgaard H, Halle B, Aaberg-Jessen C, et al. Highly Effective Auger-Electron Therapy in an Orthotopic Glioblastoma Xenograft Model using Convection-Enhanced Delivery. Theranostics 2016;6. Place: Australia:2278–91.

54. Zeituni CA, Souza CD, Moura ES, et al. Theoretical, manufacturing and clinical application aspects of a prostate brachytherapy I-125 source in Brazil. 2012. Publisher: InTech: Open Access.

55. Klecker RW, Jenkins JF, Kinsella TJ, Fine RL, Strong JM, and Collins JM. Clinical pharmacology of 5-iodo-2□-deoxyuridine and 5-iodouracil and endogenous pyrimidine modulation. Clinical Pharmacology and Therapeutics 1985;38:45–51.

56. Rösler TW, Matusch A, Librizzi D, et al. Diesterified Derivatives of 5-Iodo-2□-Deoxyuridine as Cerebral Tumor Tracers. PLoS ONE 2014;9. Ed. by Deli MA:e102397.

57. Daems N, Michiels C, Lucas S, Baatout S, and Aerts A. Gold nanoparticles meet medical radionuclides. Nuclear Medicine and Biology 2021;100-101:61–90.

58. Pallares RM and Abergel RJ. Nanoparticles for targeted cancer radiotherapy. Nano Research 2020;13:2887–97.

59. Gaudin A, Song E, King AR, et al. PEGylated squalenoyl-gemcitabine nanoparticles for the treatment of glioblastoma. Biomaterials 2016;105. ISBN: 0142-9612:136–44.

60. Toyohara J, Hayashi A, Sato M, et al. Rationale of 5-125I-Iodo-4'-Thio-2'-Deoxyuridine as a Potential Iodinated Proliferation Marker. Journal of Nuclear Medicine 2002;43. Publisher: Society of Nuclear Medicine _eprint: https://jnm.snmjournals.org/content/43/9/1218.full.pdf:1218–26.

61. Poletto G, Evangelista L, Venturini F, et al. Nanoparticles and Radioisotopes: A Long Story in a Nutshell. Pharmaceutics 2022;14:2024.

62. Liao W, Fan S, Zheng Y, et al. Recent advances on glioblastoma multiforme and nano-drug carriers: A review. Current Medicinal Chemistry 2019;26. Publisher: Bentham Science Publishers:5862–74.

63. Yalamarty SSK, Filipczak N, Li X, et al. Mechanisms of Resistance and Current Treatment Options for Glioblastoma Multiforme (GBM). Cancers 2023;15:2116.

64. Filipczak N, Pan J, Yalamarty SSK, and Torchilin VP. Recent advancements in liposome technology. Advanced Drug Delivery Reviews 2020;156:4–22.

65. Sporer E, Poulie CBM, Bäck T, et al. Covalent core-radiolabeling of polymeric micelles with ^{125} I/ ^{211} At for theranostic radiotherapy. Nanotheranostics 2022;6:388–99.

66. Kumar V. Diagnostic and therapeutic applications of smart nanocomposite dendrimers. Frontiers in Bioscience 2021;26:518–36.

67. Zhao L, Zhu M, Li Y, Xing Y, and Zhao J. Radiolabeled Dendrimers for Nuclear Medicine Applications. Molecules 2017;22:1350.

68. Shi L, Zhang J, Zhao M, et al. Effects of polyethylene glycol on the surface of nanoparticles for targeted drug delivery. Nanoscale 2021;13:10748–64.

69. Veronese FM and Mero A. The Impact of PEGylation on Biological Therapies: BioDrugs 2008;22:315–29.

70. Dang Y and Guan J. Nanoparticle-based drug delivery systems for cancer therapy. Smart Materials in Medicine 2020;1:10–19.

71. Lombardo D, Kiselev MA, and Caccamo MT. Smart Nanoparticles for Drug Delivery Application: Development of Versatile Nanocarrier Platforms in Biotechnology and Nanomedicine. Journal of Nanomaterials 2019;2019:1–26.

72. Bobo D, Robinson KJ, Islam J, Thurecht KJ, and Corrie SR. Nanoparticle-Based Medicines: A Review of FDA-Approved Materials and Clinical Trials to Date. Pharmaceutical Research 2016;33:2373–87.

73. Tenchov R, Sasso JM, and Zhou QA. PEGylated Lipid Nanoparticle Formulations: Immunological Safety and Efficiency Perspective. Bioconjugate Chemistry 2023. Publisher: ACS Publications.

74. Wang H, Wang Y, Yuan C, et al. Polyethylene glycol (PEG)-associated immune responses triggered by clinically relevant lipid nanoparticles. preprint. Immunology, 2022. doi: 10.1101/2022.11.24.516986. url: http://biorxiv.org/lookup/doi/10.1101/2022.11.24.516986 (visited on 09/21/2023).

75. Benasutti H, Wang G, Vu VP, et al. Variability of Complement Response toward Preclinical and Clinical Nanocarriers in the General Population. Bioconjugate Chemistry 2017;28:2747–55.

76. Klinker K and Barz M. Polypept(o)ides: Hybrid Systems Based on Polypeptides and Polypeptoids. Macromolecular Rapid Communications 2015;36:1943–57.

77. Skoulas D, Stuettgen V, Gaul R, Cryan SA, Brayden DJ, and Heise A. Amphiphilic star polypept (o) ides as nanomeric vectors in mucosal drug delivery. Biomacromolecules 2020;21. Publisher: ACS Publications:2455–62.

78. Johann K, Bohn T, Shahneh F, et al. Therapeutic melanoma inhibition by local micelle-mediated cyclic nucleotide repression. Nature Communications 2021;12:5981.

79. Bhattacharyya S, Kudgus RA, Bhattacharya R, and Mukherjee P. Inorganic Nanoparticles in Cancer Therapy. Pharmaceutical Research 2011;28:237–59.

80. Lemaître TA, Burgoyne AR, Ooms M, Parac-Vogt TN, and Cardinaels T. Inorganic Radiolabeled Nanomaterials in Cancer Therapy: A Review. ACS Applied Nano Materials 2022;5:8680–709.

81. Chakravarty R, Goel S, Dash A, and Cai W. Radiolabeled inorganic nanoparticles for positron emission tomography imaging of cancer: an overview. The Quarterly Journal of Nuclear Medicine and Molecular Imaging 2017;61.

82. Cai Z, Chattopadhyay N, Yang K, et al. 111In-labeled trastuzumab-modified gold nanoparticles are cytotoxic in vitro to HER2-positive breast cancer cells and arrest tumor growth in vivo in athymic mice after intratumoral injection. Nuclear Medicine and Biology 2016;43:818–26.

83. Clanton R, Gonzalez A, Shankar S, and Akabani G. Rapid synthesis of 125I integrated gold nanoparticles for use in combined neoplasm imaging and targeted radionuclide therapy. Applied Radiation and Isotopes 2018;131:49–57.

84. Enrique MA, Mariana OR, Mirshojaei SF, and Ahmadi A. Multifunctional radiolabeled nanoparticles: strategies and novel classification of radiopharmaceuticals for cancer treatment. Journal of Drug Targeting 2015;23:191–201.

85. Pellico J, Gawne PJ, and T. M. De Rosales R. Radiolabelling of nanomaterials for medical imaging and therapy. Chemical Society Reviews 2021;50:3355–423.

86. Varani M, Bentivoglio V, Lauri C, Ranieri D, and Signore A. Methods for Radiolabelling Nanoparticles: SPECT Use (Part 1). Biomolecules 2022;12:1522.

87. Coenen HH, Mertens J, and Mazieère B, eds. RADIOIONIDATION REACTIONS FOR RADIO PHARMACEUTICALS. Dordrecht: Springer Netherlands, 2006. doi: 10.1007/1-4020-4561-1. url: http://link.springer.com/10.1007/1-4020-4561-1 (visited on 09/29/2023).

88. Frausto Da Silva JJR. The chelate effect redefined. Journal of Chemical Education 1983;60:390.

89. Van Der Geest T, Laverman P, Metselaar JM, Storm G, and Boerman OC. Radionuclide imaging of liposomal drug delivery. Expert Opinion on Drug Delivery 2016;13:1231–42.

90. Marik J, Tartis MS, Zhang H, et al. Long-circulating liposomes radiolabeled with [18F]fluorodipalmitin ([18F]FDP). Nuclear Medicine and Biology 2007;34:165–71.

91. Man F, Gawne PJ, and T.M. De Rosales R. Nuclear imaging of liposomal drug delivery systems: A critical review of radiolabelling methods and applications in nanomedicine. Advanced Drug Delivery Reviews 2019;143:134–60.

92. Petersen AL, Binderup T, Rasmussen P, et al. 64Cu loaded liposomes as positron emission tomography imaging agents. Biomaterials 2011;32:2334–41.

93. Ashique S and Anand K. Radiolabelled Extracellular Vesicles as Imaging Modalities for Precise Targeted Drug Delivery. Pharmaceutics 2023;15:1426.

94. Tang WL, Chen WC, Roy A, Undzys E, and Li SD. A Simple and Improved Active Loading Method to Efficiently Encapsulate Staurosporine into Lipid-Based Nanoparticles for Enhanced Therapy of Multidrug Resistant Cancer. Pharmaceutical Research 2016;33:1104–14.

95. Engudar G, Schaarup-Jensen H, Fliedner FP, et al. Remote loading of liposomes with a ^{124}I-radioiodinated compound and their *in vivo* evaluation by PET/CT in a murine tumor model. Theranostics 2018;8:5828–41.

96. Danhier F, Feron O, and Préat V. To exploit the tumor microenvironment: Passive and active tumor targeting of nanocarriers for anti-cancer drug delivery. Journal of Controlled Release 2010;148:135–46.

97. Wu J. The Enhanced Permeability and Retention (EPR) Effect: The Significance of the Concept and Methods to Enhance Its Application. Journal of Personalized Medicine 2021;11:771.

98. Bazak R, Houri M, Achy SE, Hussein W, and Refaat T. Passive targeting of nanoparticles to cancer: A comprehensive review of the literature. Molecular and Clinical Oncology 2014;2:904–8.

99. Hagaman DE, Damasco JA, Perez JVD, Rojo RD, and Melancon MP. Recent Advances in Nanomedicine for the Diagnosis and Treatment of Prostate Cancer Bone Metastasis. Molecules 2021;26:384.

100. Huynh NT, Roger E, Lautram N, Benoît JP, and Passirani C. The rise and rise of stealth nanocarriers for cancer therapy: passive versus active targeting. Nanomedicine 2010;5:1415–33.

101. Shi P, Cheng Z, Zhao K, et al. Active targeting schemes for nano-drug delivery systems in osteosarcoma therapeutics. Journal of Nanobiotechnology 2023;21:103.

102. Martín-Sabroso C, Torres-Suárez AI, Alonso-González M, Fernández-Carballido A, and Fraguas-Sánchez AI. Active Targeted Nanoformulations via Folate Receptors: State of the Art and Future Perspectives. Pharmaceutics 2021;14:14.

103. Kim J, Nam HY, Kim Ti, et al. Active targeting of RGD-conjugated bioreducible polymer for delivery of oncolytic adenovirus expressing shRNA against IL-8 mRNA. Biomaterials 2011;32:5158–66.

104. Quader S, Liu X, Chen Y, et al. cRGD peptide-installed epirubicin-loaded polymeric micelles for effective targeted therapy against brain tumors. Journal of controlled release 2017;258. Publisher: Elsevier:56–66.

105. Daniels TR, Bernabeu E, Rodríguez JA, et al. The transferrin receptor and the targeted delivery of therapeutic agents against cancer. Biochimica et Biophysica Acta (BBA) - General Subjects 2012;1820:291–317.

106. Miyata S, Kawabata S, Hiramatsu R, et al. Computed Tomography Imaging of Transferrin Targeting Liposomes Encapsulating Both Boron and Iodine Contrast Agents by Convection-Enhanced Delivery to F98 Rat Glioma for Boron Neutron Capture Therapy. Neurosurgery 2011;68. ISBN: 0148-396X:1380–7.

107. Costa SA, Mozhdehi D, Dzuricky MJ, Isaacs FJ, Brustad EM, and Chilkoti A. Active Targeting of Cancer Cells by Nanobody Decorated Polypeptide Micelle with Bio-orthogonally Conjugated Drug. Nano Letters 2019;19:247–54.

108. Wu X, Chen J, Wu M, and Zhao JX. Aptamers: Active Targeting Ligands for Cancer Diagnosis and Therapy. Theranostics 2015;5:322–44.

109. Rosenblum D, Joshi N, Tao W, Karp JM, and Peer D. Progress and challenges towards targeted delivery of cancer therapeutics. Nature Communications 2018;9:1410.

110. Peltek OO, Muslimov AR, Zyuzin MV, and Timin AS. Current outlook on radionuclide delivery systems: from design consideration to translation into clinics. Journal of Nanobiotechnology 2019;17:90.

111. Mathew EN, Berry BC, Yang HW, Carroll RS, and Johnson MD. Delivering Therapeutics to Glioblastoma: Overcoming Biological Constraints. International Journal of Molecular Sciences 2022;23:1711.

112. Liu Z, Ji X, He D, Zhang R, Liu Q, and Xin T. Nanoscale Drug Delivery Systems in Glioblastoma. Nanoscale Research Letters 2022;17:27.

113. Daneman R and Prat A. The Blood–Brain Barrier. Cold Spring Harbor Perspectives in Biology 2015;7:a020412.

114. Bolcaen J, Kleynhans J, Nair S, et al. A perspective on the radiopharmaceutical requirements for imaging and therapy of glioblastoma. Theranostics 2021;11:7911–47.

115. Cha GD, Jung S, Choi SH, and Kim DH. Local Drug Delivery Strategies for Glioblastoma Treatment. Brain Tumor Research and Treatment 2022;10:151.

116. Van Solinge TS, Nieland L, Chiocca EA, and Broekman MLD. Advances in local therapy for glioblastoma — taking the fight to the tumour. Nature Reviews Neurology 2022;18:221–36.

117. Ruiz-Garcia H, Ramirez-Loera C, Malouff TD, Seneviratne DS, Palmer JD, and Trifiletti DM. Novel Strategies for Nanoparticle-Based Radiosensitization in Glioblastoma. International Journal of Molecular Sciences 2021;22:9673.

118. Barua NU, Miners JS, Bienemann AS, et al. Convection-Enhanced Delivery of Neprilysin: A Novel Amyloid-beta-Degrading Therapeutic Strategy. Journal of Alzheimers Disease 2012;32. WOS:000309518600006:43–56.

119. Nwagwu CD, Immidisetti AV, Jiang MY, Adeagbo O, Adamson DC, and Carbonell AM. Convection Enhanced Delivery in the Setting of High-Grade Gliomas. Pharmaceutics 2021;13:561.

120. Naidoo J, Fiandaca M, Lonser RR, and Bankiewicz K. Convection-Enhanced Drug Delivery in the Central Nervous System. In: *Nervous System Drug Delivery*. Elsevier, 2019:335–50. doi: 10.1016/B978-0-12-813997-4.00016-5. url: https://linkinghub.elsevier.com/retrieve/pii/B9780128139974000165 (visited on 09/29/2023).

121. D'Amico RS, Aghi MK, Vogelbaum MA, and Bruce JN. Convection-enhanced drug delivery for glioblastoma: a review. Journal of Neuro-Oncology 2021;151:415–27.

122. Jahangiri A, Chin AT, Flanigan PM, Chen R, Bankiewicz K, and Aghi MK. Convection-enhanced delivery in glioblastoma: a review of preclinical and clinical studies. Journal of Neurosurgery 2017;126:191–200.

123. Halle B, Mongelard K, and Poulsen F. Convection-enhanced drug delivery for glioblastoma: A systematic review focused on methodological differences in the use of the convection-enhanced delivery method. Asian Journal of Neurosurgery 2019;14:5–14.

124. Papademetriou IT and Porter T. Promising approaches to circumvent the blood–brain barrier: progress, pitfalls and clinical prospects in brain cancer. Therapeutic Delivery 2015;6:989–1016.

125. Shi MH, Anantha M, Wehbe M, et al. Liposomal formulations of carboplatin injected by convection-enhanced delivery increases the median survival time of F98 glioma bearing rats. Journal of Nanobiotechnology 2018;16. ISBN: 1477-3155.

126. Cikankowitz A, Clavreul A, Tétaud C, et al. Characterization of the distribution, retention, and efficacy of internal radiation of 188Re-lipid nanocapsules in an immunocompromised human glioblastoma model. Journal of Neuro-Oncology 2017;131:49–58.

127. Seo YE, Bu T, and Saltzman WM. Nanomaterials for convection-enhanced delivery of agents to treat brain tumors. Current Opinion in Biomedical Engineering 2017;4:1–12.

128. Allard E, Passirani C, and Benoit JP. Convection-enhanced delivery of nanocarriers for the treatment of brain tumors. Biomaterials 2009;30:2302–18.

129. MacKay JA, Deen DF, and Szoka FC. Distribution in brain of liposomes after convection enhanced delivery; modulation by particle charge, particle diameter, and presence of steric coating. Brain Research 2005;1035:139–53.

130. Fleisher M, Patrick H, and Sherman JH. The role of convection-enhanced delivery in the treatment of GBM. In: *New Targeting in the Reversal of Resistant Glioblastomas*. Elsevier, 2021:145–60. doi: 10.1016/B978-0-12-822527-1.00004-6. url: https://linkinghub.elsevier.com/retrieve/pii/B9780128225271000046 (visited on 09/22/2023).

Appendix A

Supporting information:

Tuneable release of [^{125}I]-UdR-deoxyuridine from liposomes administered by convection enhanced delivery for Auger radiotherapy of glioblastoma

Qing Tang[1], Natan Johannes Willem Straathof[1], Aaraby Yoheswaran Nielsen[2], Katharina Ravn,[1] Vigga Sand Gammelsrød[2,3], Mikkel C Schou Andersen[3,4,5], Fedor Zhuravlev[1], Bo Halle[6], Helge Thisgaard*[,2], Andreas Ingemann Jensen*[,1]

[1]DTU Denmark, Institut for Sundhedsteknologi, Risø Campus, Frederiksborgvej 399 (Bygning 202), 4000 Roskilde.

[2]Department of Nuclear Medicine, Odense University Hospital, Odense, Denmark

[3]Department of Clinical Research, University of Southern Denmark, Odense, Denmark

[4]Department of Neurosurgery, Odense University Hospital, Odense, Denmark

[5]BRIDGE (Brain Research - Inter Disciplinary Guided Excellence), University of Southern Denmark, Odense, Denmark

[6]The Danish Neurosurgical Society, Odense University Hospital Dept. of Neurosurgery, Odense C

Table of contents

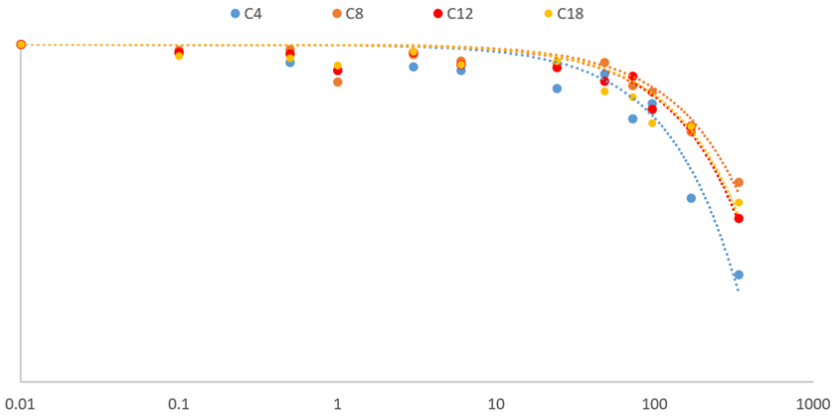

Figure s1. IUdR-prodrug compound stability in PBS at 37 °C

Stability of [^{125}I]IUdR-derivative in PBS buffer without esterase. In a 2 mL HPLC vial equipped with a stirring bar, containing the [^{125}I]IUdR-derivative (100-200 kBq) was dissolved in PBS (1 mL). The mixture was stirred at 37 °C and monitored by radio-TLC (10 cm SiO_2, 10% MeOH in DCM).

Samples were taken at different time intervals (0, 0.5, 1, 3, 6, 24, 48, 72, 96, 168 and 338 hours).

Notes: all compounds *show good stability against hydrolysis in PBS at 37 °C. Relative halve-life were calculated and are as follows; for C4* $t_{1/2}$ *= 192 ± 1 hours (n = 2) and for C8/C12/C18* $t_{1/2}$ *= 307* ± 23 hours (n = 2), respectively.

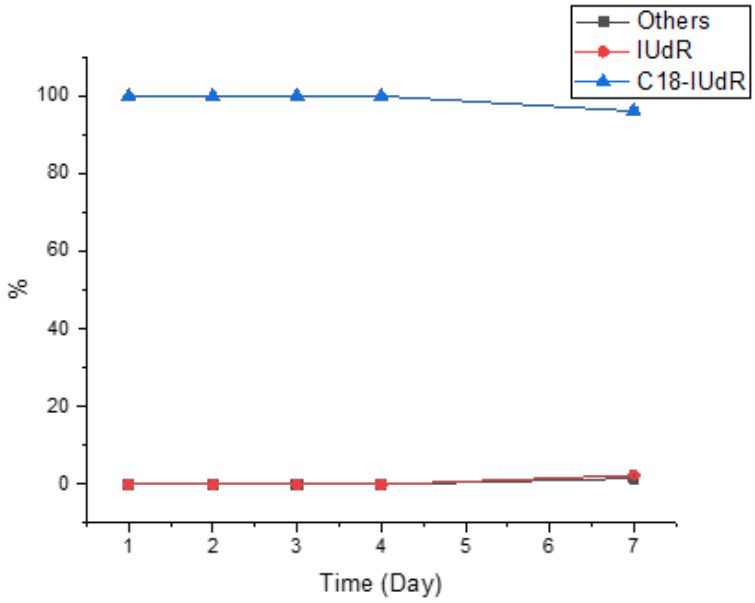

Figure s2. Stability test of [^{125}I]IUdR-C18-LIPs in PBS at 37 °C, no esterase added.

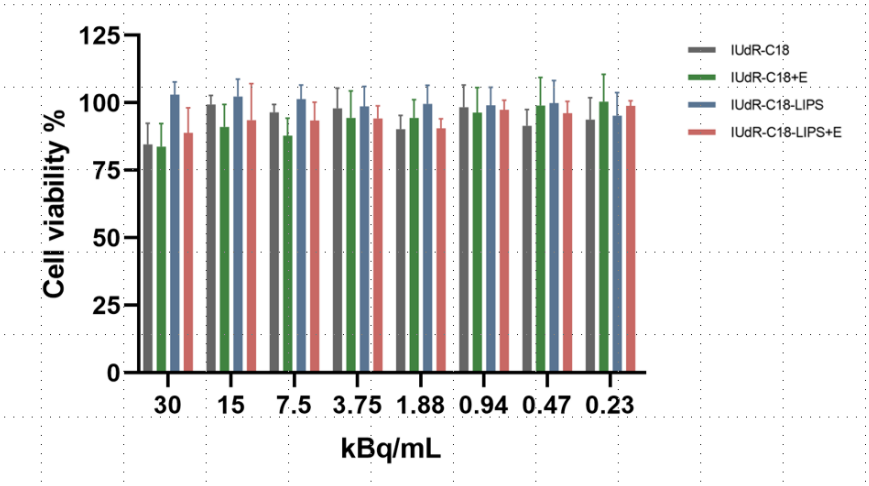

Figure s3. Viability of non-radiolabelled groups

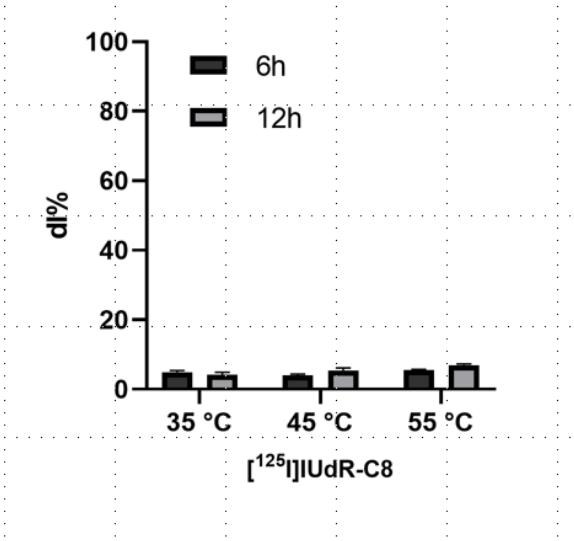

Figure s4. Loading efficiency of [^{125}I]IUdR-C8 at different times and temperatures.

Appendix B

Supporting information:

Continuous & Sustained Release of Cytotoxic [125I]IUdR from a Modified Cyclononyne-Functionalized PeptoBrush for Auger-radiotherapy of Glioblastoma

Qing Tang,[1] Gabriela Schäfer,[3] Heyang Zhang,[3] Matthias Barz,[3] Natan J.W. Straathof,[1,2], Andreas I. Jensen[1,2,]

1DTU Denmark, Institut for Sundhedsteknologi, Risø Campus, Frederiksborgvej 399 (Bygning 202), 4000 Roskilde.
2DTU Denmark, Department of Health Technology, Lyngby Campus, Ørsteds Plads (building 345C), DK-2800 Kgs. Lyngby.
3Leiden Academic Centre for Drug Research (LACDR), Leiden University, Einsteinweg 55, 2333, CC, Leiden, the Netherlands

Table of contents

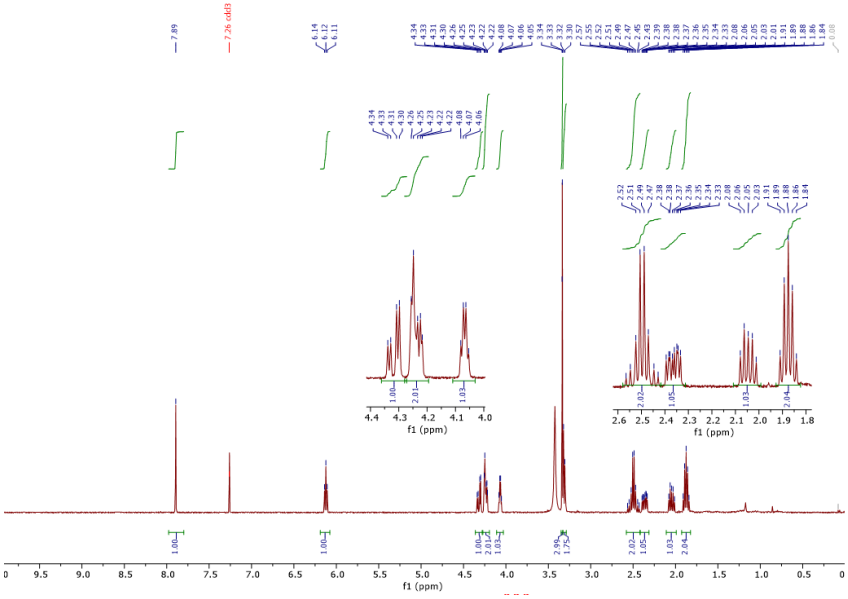

Figure S1. 1H-NMR spectrums of [^{125}I]IUdR-C_4- N_3

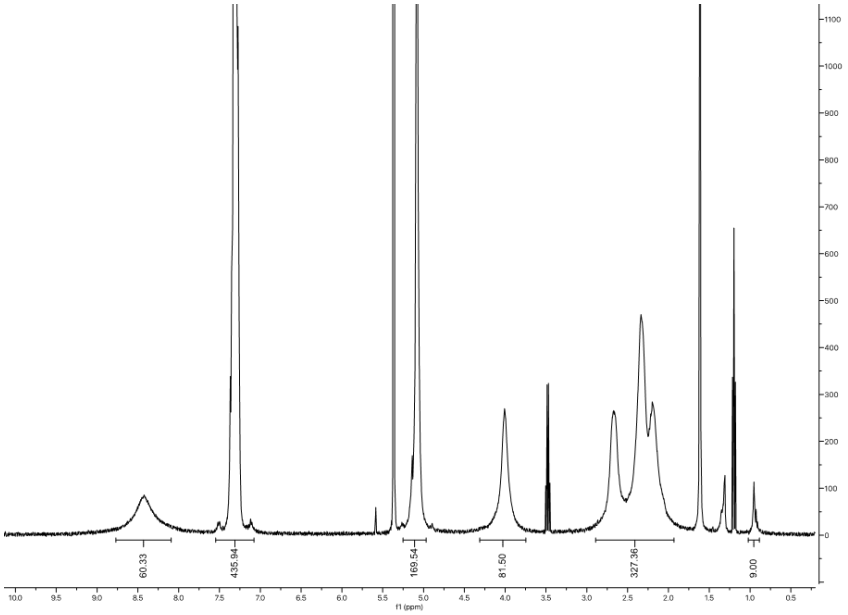

Figure s2. 1H-NMR spectrums of pGlu(OBn)

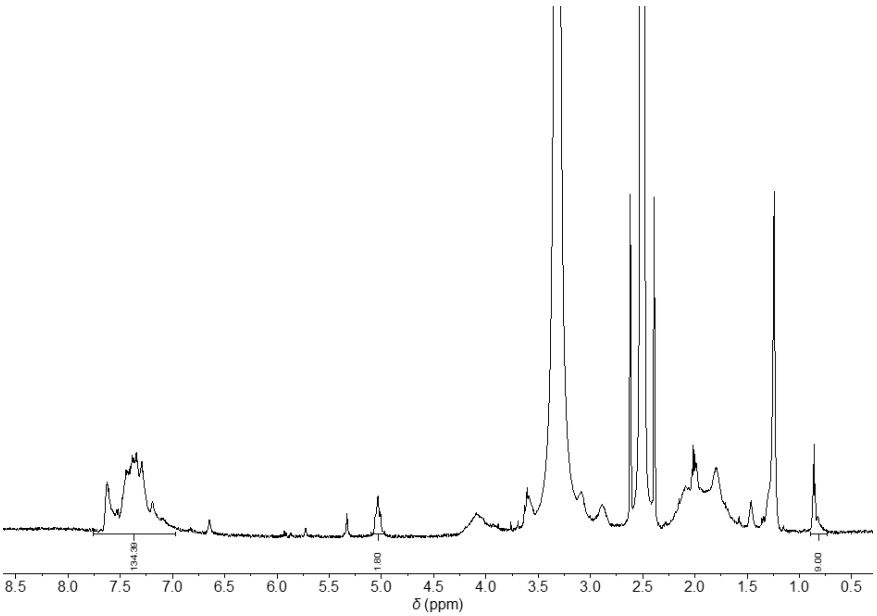

Figure 1. Figure s3. 1H-NMR spectrums of PB

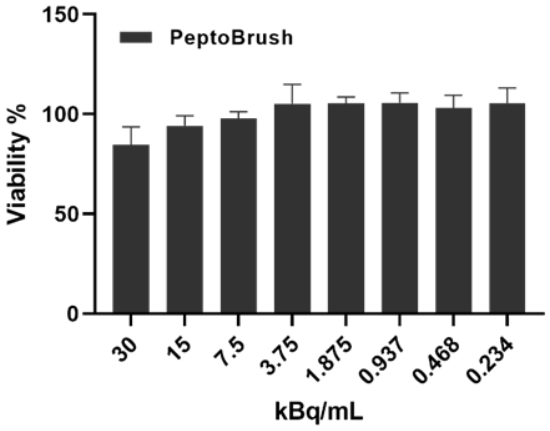

Figure S4. Viability of PeptoBrush against LN229 cells

Table S1. Overview of screening conditions of the [^{125}I]IUdR-N_3/PeptoBrush copper-free click-reaction.

	Weight (mg)	PBS (µL)	Solvent (µL)	Time (h)	Temp. (°C)	Activity (MBq)	Product (MBq)	Yield
1	0.3	50	50, MeCN	1	r.t	0.38	0.12	31%
2	2	200	20, DMSO	1	37	3.42	1.41	41%
3	1.2	200	20, DMSO	1	37	2.26	0.96	42%
4	2	200	20, DMSO	1	40	4.19	3.32	79%
5	2	200	20, DMSO	1	40	2.35	1.31	56%